The Development of MEMS-based Biodegradable Strain Sensors and Energy Sources for Monitoring Bone Healing

A Dissertation
Presented to
The Academic Faculty

By

Melissa Tsang

In Partial Fulfillment
Of the Requirements for the Degree
Doctor of Philosophy in
School of Electrical and Computer Engineering

Georgia Institute of Technology
August 2018

The Development of MEMS-based Biodegradable Strain Sensors and Energy Sources for Monitoring Bone Healing

Approved by:

Dr. Mark G. Allen, Advisor
School of Electrical & Computer Engineering
Georgia Institute of Technology

Dr. Oliver Brand
School of Electrical & Computer Engineering
Georgia Institute of Technology

Dr. Farrokh Ayazi
School of Electrical & Computer Engineering
Georgia Institute of Technology

Dr. Robert E. Guldberg
George W. Woodruff School of Mechanical Engineering
Georgia Institute of Technology

Dr. Johnna S. Temenoff
Coulter Department of Biomedical Engineering
Georgia Institute of Technology

Date Approved: May 18, 2018

To my grandma,

ACKNOWLEDGEMENTS

This research was made possible through an interdisciplinary collaboration between Dr. Mark Allen's MicroSensors and MicroActuators Research Group and Dr. Robert Guldberg's Musculoskeletal Research Laboratory, as well as research funding by both the National Science Foundation and National Institutes of Health.

What a tumultuous journey this graduate experience has been. I complete this degree with a different perspective on my education, my career and my life than when I began. Not that this was unexpected, but still I marvel at the evolution of a mind. I am both grateful and truly humbled; my graduate journey has and will forever be a formidable experience in shaping who I am. To those whom I wish to acknowledge, whose support have been an integral undercurrent driving my success, you know who you are. I'd like to take a less conventional path. Rather than identify those individuals, I'd prefer to share just what your support has meant to me. Because, chances are, I've thanked you at one point in time, but likely never elaborated on your significance, your impact. Academic cultivation, mental guidance and emotional support—the three pillars from which I was able to grow and to carve out an educational journey that has been uniquely mine.

Prior to graduate school, the term "academic" conjured an image of a classroom. But now, as I write, my mind flashes past many lessons learned in the lab, in the cleanroom, in conference rooms and in impromptu meetings no matter the location. I think that captures the essence of a Ph.D. in ways; being able to walk into your lab mate's office or vice versa and ask, "Do you have a minute?" only for that conversation to evolve into a 2-hour discussion, trying to make sense of unexpected results or troubleshoot a current problem. It's rarely scheduled and never ends quickly. Yet, those engaged dive right in with an open mind and an earnestness to think and to help. This

scenario has happened numerous times while waiting for a tool to pump down, working at a fume hood and even via text messages after hours, when maybe it would've been healthier to stop thinking about research. I've been very fortunate at Georgia Tech and at UPenn to have so many people to contemplate research with. Not only my own lab mates, but also with professors, cleanroom staff and fellow peers.

If ever you've heard me say that pursuing a Ph.D. is incredibly character-building, then I hope you also caught the dry humor. You confront many challenges throughout your thesis, but the majority of them take place in your mind; for me, at least. I don't want to downplay all the agonizing moments in the lab or the cleanroom; as an experimentalist, I dare not. But even in those moments, the greatest challenge that limited me was my own mental state—the futility, desperation, exasperation, fatigue and self-doubt. The ability to shrug it off and reset, to identify resources and brainstorm new ideas, and to problem solve and troubleshoot—these are the skills that I most cherish from my graduate training. A bit taboo, but these mental exercises only became more difficult the further I delved into my degree. I realized how much I still didn't know and I struggled with the uncertainty of both my near- and longer-term future. I didn't know if my research approach would ever pan out, I didn't know if my degree would ever come to fruition and I absolutely didn't know whether I could even find a job; one that would make me happy and render this entire Ph.D. experience worthwhile. In my lowest moments, I even asked those close to me whether they would still love me if I ended up working at Walmart. My mind became particularly cloudy in those months preceding my decision to switch programs and my final year in Philly. I am so grateful for all the mentors, friends and family in my life. Those who saw the uglier, weaker sides of me and nonetheless walked alongside me. The wave of mental guidance arrived in many forms. Whether a hug or a conversation over coffee (or beer or whiskey), the

encouragement to seek counseling and pursue outlets in painting and saxophone, the patience to listen and the integral advice to be patient with myself, your support painted these moments with light, love and strength.

Emotional support—a warm and serious topic, but one that oftentimes manifested in the most whimsical and light-hearted expressions. I have literally come home to a dozen whoopie pies delivered from a famous bakery in Portland, Maine as an express attempt to extinguish sadness. Also, a pound of rainbow cookies triple packaged in Ziploc bags from Veneiro's in New York. To be honest, I should probably thank all the local sushi restaurants near me; if they only knew the emotional support that I found in their yellowtail-scallion and spicy tuna rolls. And I have quite possibly received more than 1000 videos capturing daily glimpses of my nieces and nephew growing up that have never ceased to plant a smile from deep within me. My favorite remains a letter from my father; it bore merely 5 Chinese characters jotted on scrap paper: 女兒當自強. For these and all the moments in between, your support has kept me company throughout this tumultuous ride. They have kept me laughing and smiling, and most importantly, reminded me to stay true to myself.

I thank you all so much. I look back and I realize how colorful this journey has been. It's been beautiful.

TABLE OF CONTENTS

LIST OF TABLES

LIST OF FIGURES

LIST OF SYMBOLS AND ABBREVIATIONS

Symbol	Definition
Y	Young's modulus
P	Electrical resistivity
CTE	Coefficient of thermal expansions
CR	Corrosion rate
WVTR	Water vapor transport rate
CPE	Constant phase element
R	Resistance
L	Inductance
σ	Reaction rate
k	Rate constant
c	Concentration
G	Free energy
k_B	Boltzmann constant
T	Temperature
E	Electrical potential
β	Fraction of potential difference impacting activation energy of a cathodic reaction
F	Faraday's constant
i	Current density
η_S	Surface overpotential
I	Electrical current
PI	Pitting Index
Σ	Standard deviation
B	Stern-Geary coefficient
α	Electrochemical transfer coefficients
Z	Impedance

Φ	Power spectral density
BW	Bandwidth
q	Charge
f	Frequency
Λ	Weibull scale factor
ƙ	Weibull shape factor
M	Rank of data (for an empirical CDF)
N	Length of data (for an empirical CDF)
V	Volume
MW	Molecular weight
δ	Density
z	Charge equivalence
Pit_{max}	Maximum pit radius
S	Sorption coefficient
p	Partial pressure
a, g	Adsorbate-surface system parameters
H_a	Heat of adsorbate
U	Universal gas constant
J	Flux
Symbol	**Definition**
D	Diffusion coefficient
t	Time
Q	Total mass of transmitted permeate
l	Length
n	Number of layers
P	Permeation coefficient
A	Area
d	Diameter

r	Radius
BIF	Barrier improvement factor
Ψ	Volume fraction
m	Mass
e	Charge of an electron
h	Planck's constant
ξ	Height of potential barrier to electrical tunneling
ζ	Width of potential barrier to electrical tunneling
s	Distance
ℓ	Number of particles forming a conductive path
N	Number of conductive paths
GF	Gauge factor
ν	Poisson's ratio
ε	Strain
$\varkappa$	Non-linear factor
w	Width
Γ	Thickness
C	Specific capacity
Po	Power

SUMMARY

This thesis explores the development of MEMS-based biodegradable strain sensors and energy sources for monitoring bone fracture healing. The primary objective was to expand the arsenal of biodegradable materials that are biocompatible, can be micropatterned based on conventional CMOS-based fabrication technologies and whose degradation characteristics can be predictably harnessed for the design of MEMS-based, biodegradable devices. Towards these goals, the development of fabrication technologies for the micropatterning of biodegradable materials and extensive electrochemical characterization of their biodegradability are elaborated in Chapter 2. The exploration of biodegradable materials culminated in their integration towards and design of biodegradable strain sensors and energy sources, as elaborated in Chapter 3. Biodegradable strain sensors comprising electroplated magnesium as the primary conductor demonstrated a strain sensitivity of up to 0.1 $\mu V/\mu\varepsilon/V_{ex}$ and a functional lifetime of 4 days under physiological conditions. In turn, electroplated magnesium energy sources, which harnessed the galvanic corrosion of magnesium in physiological electrolyte, exhibited an energy density of approximately 700 WA/kg and stable discharge potential of 0.7 V within a volumetric constraint of 0.02 cm^3.

As a preamble, this thesis also elaborated on the design, fabrication and characterization of an analogously non-degradable strain sensor. The development of the non-degradable device analogue, as detailed in Chapter 3, furthered the quantitative understanding of the proposed application space and corresponding design constraints. The functional lifetime and, therefore, transience of a non-degradable device established an upper limit in the target functional lifetime of an analogous biodegradable device; despite the broader selection of materials available to

designing non-degradable devices, functional longevity under physiological conditions and electrical powering are nonetheless a challenge. Further, the demonstration and *in vivo* deployment of a non-degradable strain sensor for monitoring femoral segmental bone defects in rodents served as a proof-of-concept that MEMS technology can not only support medical interrogations in the clinical realm, but also expand fundamental biological research in small animal models. As the field of biodegradable MEMS is less established, the research on biodegradable strain sensors and energy sources concluded with *in vitro* device testing and cytotoxicity studies (Chapter 4) in accordance with international and FDA-recommended standards. Functional device testing and cellular toxicity results supported the use of electroplated Mg and biodegradable passivation schemes, such as pulse-plated zinc, fluorinated hydroxyapatite and multi-layer barrier films, for biodegradable orthopedic devices.

The research in this thesis addressed the direct application of monitoring mechanical strain across a rodent femoral bone defect, but also aimed to expand the general field of biodegradable MEMS research. The microfabrication technologies and passivation schemes developed can be applied to a broad class of devices and to achieve a spectrum of functional lifetimes. From materials to component devices, the results of this thesis serve as a trajectory towards an integrated biodegradable strain sensing system.

CHAPTER 1

INTRODUCTION

1.1 Overview

A sensor that lasts forever is not always desirable. This applies to longevity both in the functionality and the physical form of a sensor. A well-designed sensor should suit the intended application not only in terms of sensing modality, detection range and sensitivity, but also in functional lifetime and longevity. While hermeticity has been a hallmark of modern electronics, protecting circuitry and devices from the external environment and, thereby, ensuring their long-term performance, the transience of certain medical conditions and the desire to reduce environmental waste underscore the utility of a new class of devices—biodegradable sensors.

The present work identifies bone healing as an opportune application for introducing biodegradable, implantable sensors. Bone healing is a transient disease state and, even though it has been widely accepted that mechanical cues govern the dynamic processes of bone regeneration and remodeling, few devices have been developed to provide *in situ*, real time monitoring. This dissertation explores the development of biodegradable strain sensors and energy sources, along with non-degradable analogues, for the *in vivo* monitoring of bone healing. The engineering challenge presented is to build stable devices using materials that are intrinsically unstable in the intended operating environment and, perhaps, to do so using clever design schemes that harness the biodegradable nature of the material sets. The ensuing introduction reviews bone mechanobiology, implantable MEMS technology, and biodegradable materials and devices to establish the framework necessary for the development of biodegradable strain sensors and energy sources for monitoring bone fracture healing.

1.2 Bone Mechanobiology

1.2.1 Bone Regeneration and Remodeling

Bone regeneration is a dynamic process. The loading distribution across the healing bone, implanted structural devices, and adjacent tissue may evolve throughout the time course of bone healing [1]–[4]. Bone regeneration features the organized formation and remodeling of multiple tissue phenotypes. Figure 2 illustrates the timescale of the various phases of bone healing varies from hours and days to months and years, during which the interfragmentary strain, local pH and oxygen tension change over time. The four phases of bone regeneration are: (1) acute inflammation and hematoma (hours to days), (2) callus formation (days to weeks), (3) woven bone (weeks to months) and (4) lamellar bone (months to years). A callus is a soft tissue matrix that primarily comprises collagen; subsequent mineralization then leads to woven and lamellar bone with increasing mechanical stiffness. Woven bone features an unorganized matrix of collagen and hydroxyapatite, as well as a disorganized vascular network. Bone remodeling gradually restores the vascular and skeletal structure to its full functionality [5], [6]. From the initial empty defect through to regenerated and mineralized bone, the mechanical properties of healing bone and the corresponding load sharing between a bone defect and fixation plate result in a large dynamic range in mechanical strain throughout the time course of bone healing. The ability to quantitatively monitor mechanical loading continuously *in situ* would promote current understanding of the mechanical basis of bone regeneration, as well as inform the development of regenerative medicine therapies for bone-loading tissues.

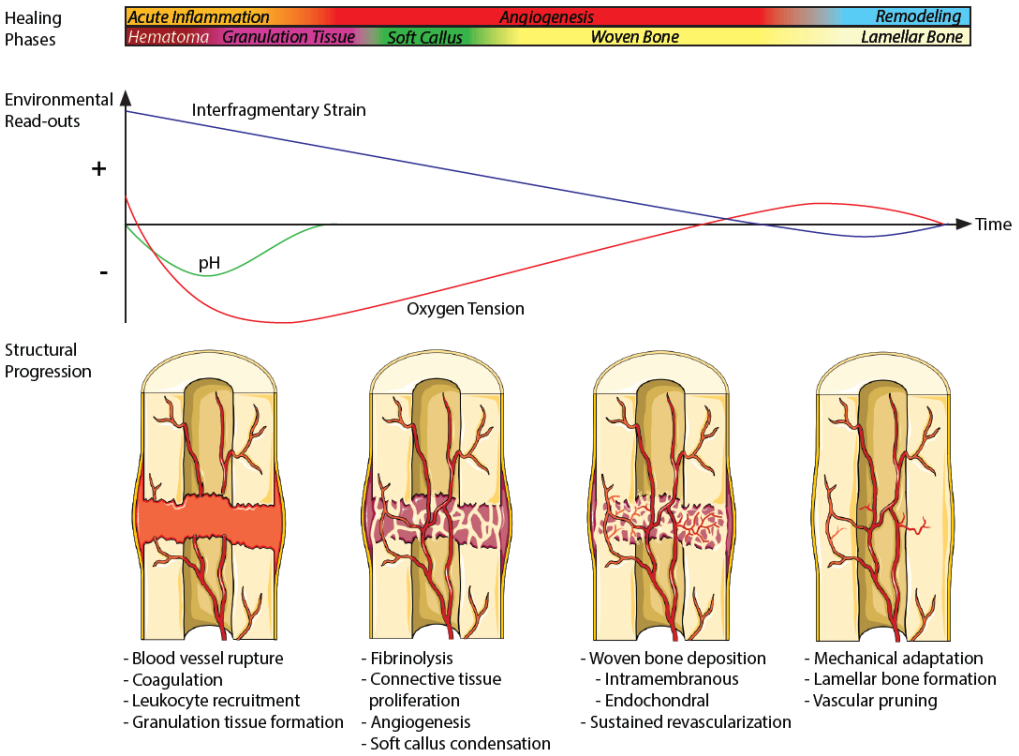

Figure 1 Schematic outlining the temporal profile of bone regeneration, illustrating phases of healing, structural progression in the defect, and qualitative estimates of environmental parameter profiles. Non-destructive, quantitative measurements of these environmental cues would significantly enhance fundamental understanding of the temporal progression of the bone healing environment as well as many other diseases of interest, providing a better foundation to develop and evaluate effective regenerative therapies [5].

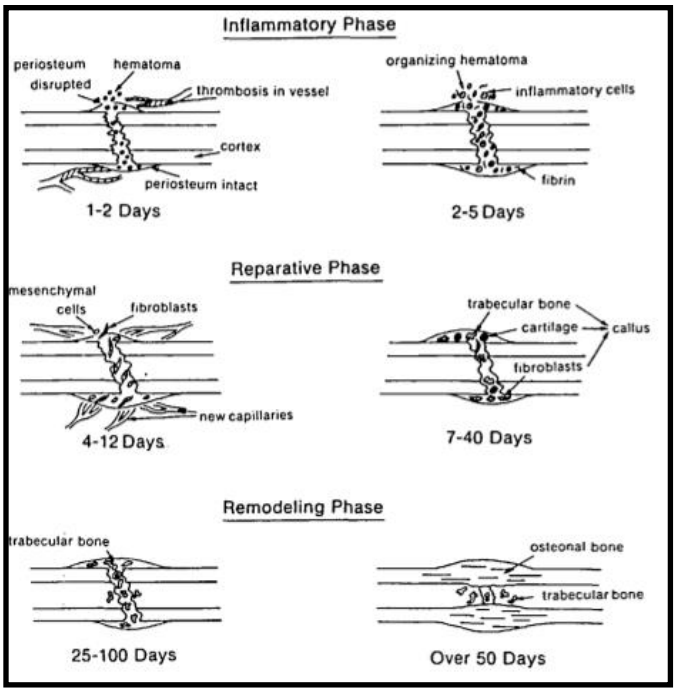

Figure 2 Schematic illustrating the biological changes during the inflammatory, reparative (i.e., regeneration) and remodeling phases of bone healing [6].

Clinically, bone fracture progress is largely determined by manual examination and radiographic evaluation of mineralization, as shown in Figure 3 [7]. In the latter case, fracture healing is considered complete when the mechanical properties of the callus formation match that of normal bone [8], [9]. Although these assessments determine the time course until fixation removal, progression of weight bearing, and diagnosis of delayed or non-uniform healing, these assessments are subjective and do not directly measure the mechanical properties of bone [7]. X-ray examination, for example, can only indicate bone healing once calcification begins at the callus site or the fracture line is lost. Further, callus formation visualized through X-ray correlates poorly with estimation of osseous union because the images indicate the quantity, but not the quality of the callus and are insufficient for evaluating fracture strength [10]. Dual-energy X-ray absorptiometry (DEXA) scans can determine bone mineral density (BMD) and bone mineral content (BMC), but surrounding fats and tissues can give rise to erroneous results [11]. Quantitative computed tomography (QCT) offers higher quality imaging than X-ray and DEXA, as well as assesses BMD. However, QCT is not suitable for areas with metallic implants and exposes the patient to higher

doses of radiation [12]. Quantitative ultrasound (QUS) can evaluate bone stiffness and healing, but can only access peripheral skeletal sites [9], [13], [14]. Local interrogation of the bone fracture site, such as with the *in situ* monitoring of mechanical strain, would further support clinical assessment of fracture progress.

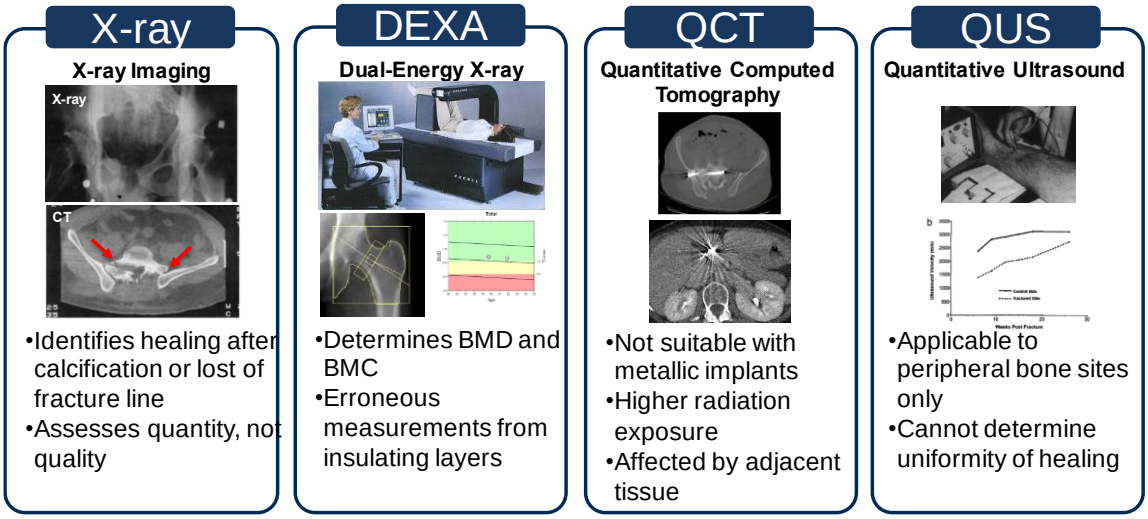

Figure 3 Comparison of various non-invasive imaging techniques clinically employed for monitoring bone fracture healing [7].

Large bone defects, characterized by segmental gaps greater than 3 cm in length, present a clinical challenge to physicians [3], [15]. Typically caused by trauma, fracture non-union or tumor resection, large bone defects are typically treated with bone grafts. It has been reported that over 500,000 and 2.2 million bone grafts are performed annually in the United States and worldwide, respectively [16]. This amounts to over $2.5 billion in annual medical expenses for large bone defect treatments [3]. The ability to quantitatively monitor mechanical strain during the acute phase of fracture healing would critically support both academic and clinical endeavors. Biomechanical factors, such as load magnitude, rate, mode and frequency, have been reported to influence the fracture healing process [17]–[20]. For example, moderate levels of compressive loading have been shown to stimulate bone remodeling along stress lines by promoting blood flow and callus formation at the fracture line; excessive strain, however, may result in non-union and prevent capillary formation at the injury site [6], [8], [21]. Tissue ingrowth increases the stiffness of the gap and reduces interfragmentary strain, enabling further differentiation of tissue with lower

failure strain and higher elastic modulus. In this manner, the fracture site progresses from granulation tissue and cartilage to fibrocartilage and remodeled bone. As can be observed, the healing bone responds dynamically to mechanical stimuli [3], [6].

1.2.2 Mechanical Regulation of Bone Healing

In 1987, Harold M. Frost proposed that the mechanical regulation of bone is directed by an inherent "mechanostat"—a window of strain stimuli that maintains healthy bone mass. As shown in Figure 4, exceeding this range might result in increased cortical bone mass due to overuse and physiological overload (i.e., 1500-5000 με), whereas insufficient strain would induce bone resorption (i.e., >200 με) [1], [2]. Subsequent studies have expanded upon Frost's findings on load-induced adaption (Figure 5). First, bone adapts to dynamic, rather than to static strains [22], [23]. Second, bone adaptation exhibits the principle of diminishing returns, wherein bone formation response tends to plateau with increasing loading duration [4]. Third, bone adaption is error-driven and responds to abnormal changes in strain [18], [19], [24]. While studies have cultivated our scientific understanding of the mechanical cues regulating healthy bone, research on the mechanical environment during bone fracture healing has been limited by appropriate *in vivo* models. In addition, clinical assessment of fracture healing progress has similarly been limited by appropriate interrogation techniques.

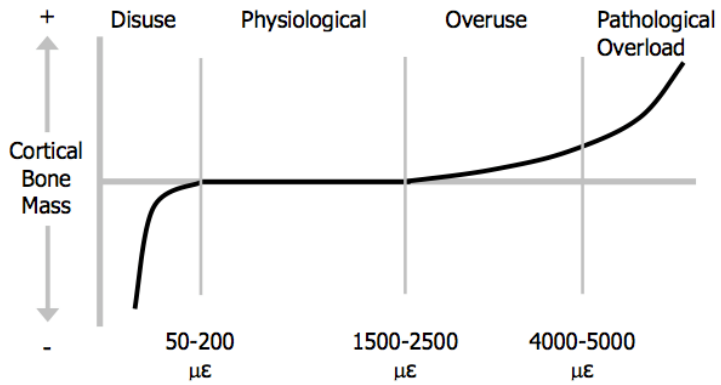

Figure 4 Schematic illustrating how mechanical stimulation triggers functional remodeling [23], [25].

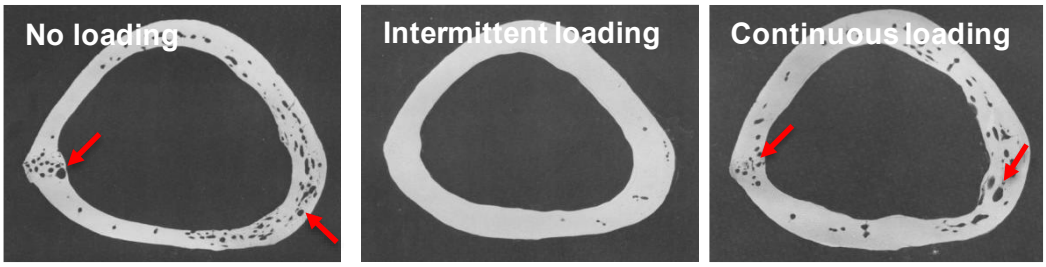

Figure 5 Cross-sectional images of avian ulna after various extents of dynamic loading for 8 weeks. Daily compressive loading triggered promoted bone remodeling. Specifically, micrographs show a 24% increase in cross-sectional area with intermittent loading (i.e., 100 cycles per day) due to new bone formation. For reference, ulna were fixated with stainless steel pins and external fixators. Spring-loaded compression of 525 N was delivered dynamically with an Instron mechanical testing frame at 1 Hz [26].

Researchers have been interested in the mechanical and biochemical cues regulating bone healing, where implantable strain sensors would enable *in situ* measurements throughout the various stages of bone regeneration and remodeling [5], [6], [14], [27], [28]. Current methods for investigating the effect of mechanical loading on bone fracture healing are limited to imaging techniques, and biomechanical analysis and histology of excised bone. Whereas radiographic methods do not directly measure the mechanical properties of bone or the local mechanical cues mediating regeneration, *ex vivo* biomechanical analysis does not allow for continuous monitoring within a given animal. As bone regeneration is a dynamic process, the loading distribution among

the healing bone, implanted structural devices, and adjacent tissue may evolve throughout the time course of bone healing. Neither techniques enable longitudinal studies and direct assessment of the mechanical environment *in vivo* [3], [15], [29].

Computational modeling, such as finite element models and computational fluid dynamics, provide spatial information and the ability to perform parametric analysis to evaluate the importance of model variables. However, the results of a computational model heavily depend on the input boundary conditions. As the boundary conditions are oftentimes approximated and premised on simplifying assumptions, this can significantly limit the accuracy of the model [5].

As such, current *in vivo* models cannot dually capture the complex 3D physiology and the mechanical environment local to the fracture site. The ability to quantitatively monitor mechanical loading continuously *in situ* would promote current understanding of the mechanical basis of bone regeneration.

1.3 Implantable MEMS Technologies

1.3.1 Review of Current Technologies

A large body of research has been demonstrated on various biomedical applications of sensors, but most efforts have focused on clinical monitoring rather than TE/RM or preclinical applications[30], [31]. Implantable sensors differ significantly in their designs and fabrication techniques, but the endpoint sensing modalities include biopotential[32], electrical impedance[33], pressure[34], [35], flow[36], [37], strain[38], oxygen[39], pH[33] and glucose[40], [41].

Clinical diagnostics have greatly benefited from implantable sensors, as it enables *in situ* monitoring of physiological metrics to track the progression of or recovery from a disease. Sensing

mechanisms for implantable MEMS sensors include mechanical[34], optical[35], magnetic[42], and electrochemical detection methods[39], as well as combinations thereof, while maintaining compact form factors, underscoring the appeal of MEMS technology; implantable MEMS can transduce a physiological input into an electrical output, oftentimes requiring only a small sample or stimulus. Despite the formidable challenges of avoiding adverse tissue response to implants, the goal of *in vivo* sensing has largely been achieved for a subset of clinical applications. Pressure sensors are a wonderful example of such, as they have been extensively demonstrated for arterial[43]–[45], intraocular[46] and intracranial[47], [48] pressure monitoring. Pressure sensors have further been presented to indirectly detect aneurysms[49] and restenosis[50], as well as to identify optimal settings for pacemakers[51]. Flow and glucose sensors have been investigated for diagnosing cardiovascular diseases[37] and continuous glucose monitoring[52], respectively. Due to continued advancements in clinical sensing, we see an exciting opportunity to leverage and adapt implantable sensors to enhance the pre-clinical development and evaluation of novel TE/RM therapies for a number of relevant diseases.

Oftentimes, multiple conditions or cues, such as physical, chemical, and biological, are relevant in evaluating how tissue engineered constructs perform *in vivo*. MEMS offers notable advantages over alternative types of implantable systems for tissue engineering and regenerative medicine due to the spectrum of supported sensing modalities, compactness of size, and amenability to integration[53]–[55]. For example, the role the local environment in bone healing could be more deeply understood by longitudinal monitoring of strain, oxygen tension, and pH within the defect. This could be enabled by the development of a multi-modal sensor system designed for a preclinical animal model. Strain sensors have previously been deployed to evaluate mechanical strains on internal and external fixation instrumentation in humans and sheep, which

show promise for clinical monitoring[27], [56]–[58]; however, implementations have primarily been limited to long bones of the leg where there is a substantial hardware footprint for sensor integration. The role of local oxygen tension is of particular interest to fracture healing. In 1972, Brighton and Krebs measured oxygen tension in a rabbit fibular fracture using platinum microelectrodes which were not implanted but inserted at each time point[59]. They noted marked differences and temporal trends of the oxygen tension in the hematoma, woven bone, and intact diaphyseal bone. Epari *et al.* revisited this approach with new technology in 2008, utilizing a percutaneously mounted, commercial multi-modal catheter probing the fracture gap to simultaneously measure pressure, oxygen tension, and temperature in a sheep tibial defect over a 10 day period [60]. While larger canine and ovine models are preferable to assess human-scale orthopedic and spine implants due to improved biomechanical similarity, small animal models possess important relative cost and throughput advantages, which makes them better suited for investigating newer and less-established therapeutic strategies for a wide range of diseases. Miniaturization of sensors and telemetry sufficient for small animal models, which are the primary test-bed for novel tissue engineering therapies, has not been demonstrated. Continued efforts toward pre-clinical sensors for bone healing and a host of other relevant injury and disease models would substantially inform a more quantitative understanding of the healing environment encountered *in vivo* and help to elucidate mechanistic reasons when different healing outcomes are observed between pre-clinical models.

Reactive oxygen species and inflammation (nitric oxide and pH) can also be monitored by electrochemical or optical sensors[61]. All sensors mentioned above can be integrated into one intelligent system for data collection and transmission. The use of multiple detection mechanisms, such as electrochemical and optical, can minimize crosstalk between different types of sensors or

validation and calibration for sensors of the same modality. This illustrates that certain attributes of MEMS, in this case their ability to detect and transduce various mechanical and chemical cues mediating bone healing into electrical signals, can be leveraged and applied towards a broad spectrum of tissue engineering and regenerative medicine applications. The microscale nature of MEMS devices can be designed to meet the physical constraints of preclinical animal models, which are oftentimes rodents or other small animals, to enable *in situ*, real-time sensing of physiological cues continuously within an animal and, thus, overcome the limitations of *ex vivo* endpoint measurements. Alternatively, the trend towards more biomimetic and physiologically-inspired devices supports their integration with TE/RM constructs to enable local evaluation of the therapeutic efficacy of TE/RM constructs in preclinical and clinical settings.

It is critical that sensors disturb the natural healing environment as little as possible to ensure that valid measurements are acquired. To ensure that novel implantable devices do not prompt fibrous encapsulation or actively irritate the tissue to a degree that alters the course of healing, the host response should be rigorously validated by histological evaluations against "sensor-free" controls for increased fibrous tissue growth and for localization of pro-inflammatory immune cells within the tissue of interest at the conclusion of the study. Additionally, sensors should be characterized under controlled *ex vivo* conditions before and after implantation to ensure their sensitivity or functionality does not drift over time due to interactions with the surrounding tissue. Migration of the sensor within the tissue is another factor that could potentially compromise the validity of the resultant data. Thus, TE/RM applications where a structural implant is used (e.g. orthopedic fixation hardware, vascular stent, tissue scaffold, etc.) are advantageous since they can act as a foundation to anchor the sensor in the healing environment. Including specific attachment features in the device design such as loops to accommodate sutures may be required. Additionally,

longitudinal radiography could serve as a valuable tool to track implant migration throughout a study.

In the design of an implantable system that facilitates tissue regeneration, a pivotal factor is the interplay between the targeted tissue and the implant. The integration of implantable sensors with TE/RM technologies can support this endeavor by providing a closed loop system for customizing regenerative therapies. A common example is the incorporation of a sensor into a drug delivery system so that the timing and rate of drug delivery can be tuned by changes in certain local physiological conditions. The integration of sensing components into responsive polymeric systems for controlled drug release has been the subject of extensive research[62]. Reports in the literature include systems triggered by the application of ultrasound[63], changes in pH[64], [65], temperature[66], analyte concentrations[67], [68], and electric[69] or magnetic[70] fields. The delivered molecules are diverse, including low molecular weight drugs, nucleic acids, peptides, and proteins, for the accelerated regeneration of tissues [71], [72].

As the fields of TE/RM and implantable sensors continue to grow, emerging technologies should consider the union of these two areas for smart, multi-functional regenerative therapies and preclinical tools for better understanding and modulating the complex biological world.

1.3.2 Assessment of Current Technologies

While significant strides have been made in the field of implantable sensors, key challenges and opportunities remain in developing implantable devices for continuous, *in vivo* monitoring. Whereas the early incarnations of implantable sensors were technology-driven devices, enabled by traditional CMOS-based materials and microfabrication technologies, recent developments in implantable MEMS highlight a trend towards more application-driven device design. Figure 6

illustrates this progression in implantable sensors, where direct offshoots of traditional CMOS technology included silicon microelectrode arrays for neuromodulation and ceramic-based pressure sensors for cardiac monitoring that are commercially available. In fact, most sensing modalities have corresponding commercial or near-commercial devices featuring traditional CMOS materials and processing. The implementation of sensors in TE/RM applications will significantly benefit from the advances in implantable sensors research. These can be grossly categorized into a bottom-up versus a top-down change in the sensor design. Specifically, recent developments in flexible, biodegradable and biomimetic sensors were mainly designed from a bottom-up, materials-level approach. Whether the goal was to minimize the deleterious response to the device, to overcome the negative effects of permanent implants or to better emulate the physiological tissue, the underlying motivation in these cases was to develop more physiologically compatible devices. The critical advancements to achieve this goal were primarily the introduction of new materials, as well as the development of corresponding fabrication technologies for the micropatterning and integration of these materials with standard MEMS processing. This application-driven approach has been a stark departure from early iterations of implantable sensors, which were largely technology-driven. Further support of this application-driven endeavor is the emphasis on multi-sensing or multi-functional devices to detect multiple cues and/or dually sense and actuate, thereby providing both monitoring and treatment. These efforts towards smart therapies and preclinical tools can be classified as top-down, systems integration approaches.

Lastly, the road to next-generation regenerative therapies and preclinical tools must tailor device design towards physiological constraints. This final thrust would ensure that the device addresses the real, physiological challenges and constraints of the design space. These include

physical size and footprint, dynamic range, biostability and pertinent testing. While most implantable strain sensors were designed to satisfy the physical constraints of a human body, sensors used for the preclinical models face more stringent size constraints because preclinical animal models are often conducted in rodents or small animals. Second, the dynamic range of a sensing parameter may either be very large or unknown. To the sensor engineer, a working range is necessary for device design. However, this information may be unknown and, hence, motivate the need for the device. For example, the mechanical stiffness of bone may change across orders of magnitude throughout the time course of bone regeneration and remodeling. For a segmental bone defect model, where the fracture gap in a rodent femur is 5-8 mm, the transition from an empty gap to mineralized bone would span a large range in mechanical stiffness. Consequently, a strain sensor monitoring the deformation across a fixation plate must vary strains across orders of magnitude due to the extent of load sharing between the bone defect and the plate. Together with the desired strain resolution when operating at the lower spectrum of the dynamic range, these constraints point towards the challenges of design for preclinical *in vivo* models. Further, whether for clinical or preclinical applications, next generation sensors for TE/RM must directly address biostability and functionality by moving beyond benchtop to *in vivo* testing as the endpoint for device characterization. A majority of the established literature in implantable sensors does not pursue *in vivo* device characterization even though the variability associated with a full animal system and host inflammatory response are just as important as the device specifications for designing an implantable system.

The development of smart, regenerative therapies and better investigatory tools for understanding tissue regeneration presents an exciting future for implantable sensors. The recognition of a need for more physiologically-motivated technology, whether pursued from a

bottom-up materials or top-down systems approach, has been a major step towards these goals. However, to realize these technologies for preclinical and clinical uses, more integrative and collaborative efforts must be established between biology and engineering in order to design not only for a specific sensing modality, but to design specifically for an *in vivo* system.

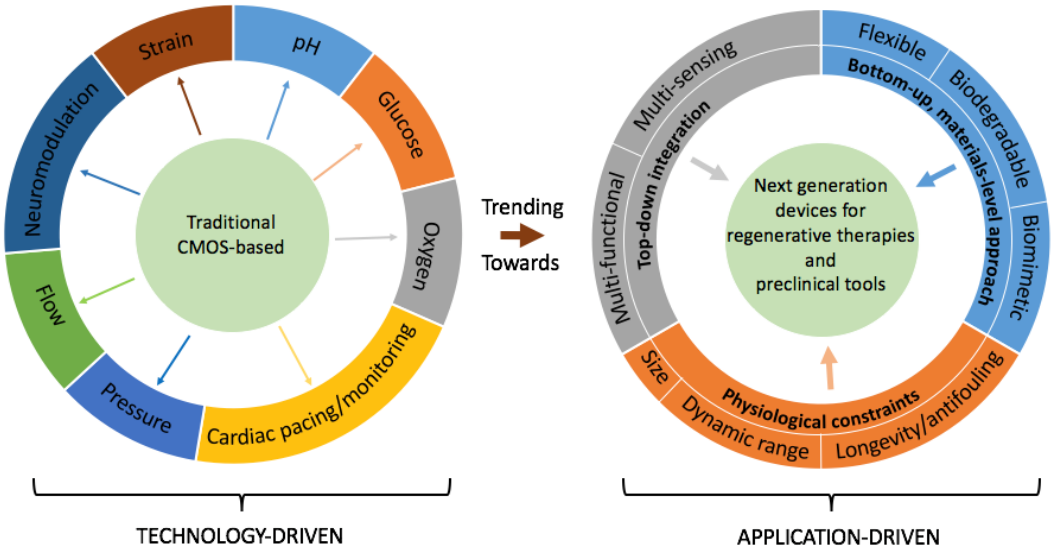

Figure 6 Advancements in implantable sensors. Early iterations of implantable sensors featured materials and design approaches that were direct outgrowth from traditional CMOS processing, as denoted by the outward-oriented arrows. However, research developments at the materials-, device- and systems-level have paved the road toward more application- driven, physiologically motivated designs. The integration of these approaches, along with addressing physiological constraints and representative testing, will be necessary for the development of next-generation, implantable sensors for smart regenerative therapies and preclinical tools [5].

1.4 Biodegradable MEMS Devices

In recent years, the development of biodegradable MEMS devices has populated literature. From temperature, pressure, strain, acceleration, flow rate and pH sensors to energy devices, such as

electrochemical cells, batteries, energy harvesters, the rise and prevalence of biodegradable devices in the past 8 years underscore a mindfulness for reducing waste, or residual material that no longer serves a function [73]–[81]. Whereas environmentally-degradable devices tackle the ever-growing accumulation of consumer electronic waste products with designs that decompose under ambient environmental conditions, biodegradable research advocates reducing waste by monitoring and treating transient disease states with similarly transient devices. In this manner, patients do not harbor an implanted device after device functionality is no longer clinically needed. Biodegradable devices avoid the negative effects commonly associated with permanent implants and the burden of a secondary procedure for device removal [82]–[84].

Biodegradable sensors have largely comprised resistive and wireless resonant devices. The simplicity of design in resistive-based sensors have motivated their development as thermal, strain and pressure sensors [73], [77], [80], [85]. Salvatore *et al.* demonstrated a biodegradable temperature sensor featuring Mg-based serpentine resistors as the sensing element and Peano-like structures to achieve strain-insensitive interconnects. The authors argued that hitherto the primary limitation to biodegradable devices have been the narrow selection of materials and the inefficient fabrication schemes for processing such materials. As a solution, the study implemented Ecoflex, a commercial biodegradable material manufactured by BASF, as the encapsulating polymer [73]. However, the limited data available on Ecoflex suggests that the polymer is biodegradable under ambient environmental conditions (i.e., climate, soil quality and population of micro-organisms) and shows limited results on its cytotoxicity for use in biomedical applications. Further, the fabrication approach presented was no less costly or laborious than Rogers *et al.* (i.e., transfer molding on SOI wafers, where the entire SOI wafer is sacrificially removed) because silicon wafers and two layers of polyimide were deposited only to be completed removed by plasma dry etching [76]. Given these caveats, the functional and degradation lifetime of the Ecoflex-based temperature sensors were 24 hours and 67 days, respectively, in 0.15 M NaCl. It should be noted that silicon dioxide and silicon nitride, deposited by chemical vapor deposition, were implemented as passivation schemes to hinder degradation. Within the functional lifetime, sensor performance was comparable to

conventional thermistors (i.e., 0.2%/K), but in spite of being flexible, the strain-referenced error was high for medical applications (i.e., 0.7% when folded and 0.2% at 10% ε) [73].

Kang *et al.* demonstrated intracranial pressure (ICP) sensors based on silicon nanomembranes (Si-NM). Thermal and ICP sensors featured Si-NM patterned to serpentine resistors on rigid substrate and on a membrane above an air cavity, respectively. The device was encapsulated with PLGA and polyanhydride, and passivated with silicon dioxide, to achieve a functional lifetime of 3 days *in vivo*. Degradation was accelerated in an alkaline environment (pH = 12); under these conditions, the degradation lifetime was 30 hours [77]. Although the accelerated degradation possesses less practicality because it cannot be compared with other devices in literature, it confirmed the degradability of the selected materials. Additional proof-of-concept demonstrations were shown for acceleration, flow rate and pH sensors that relied on a PLGA cantilever as the test mass, dual heating elements and temperature sensors to exploit thermal conductivity and diffusivity principles, and electrostatic gating of transport with Si-NM, respectively. The success of this study premised on the use of effective biodegradable materials. Silicon nanomembranes are biodegradable in a controlled manner because their breakdown does not proceed by galvanic corrosion, which can be stochastic [76], [85]. The reported degradation rate of the Si-NM and nano-porous Si (70% porosity; 80 μm thickness) were 23 nm/day and 9 μm/day, respectively, in cerebral spinal fluid [77]. In turn, polyanhydrides are unique because they are biodegradable polymers that break down by uniform degradation, provide excellent design control [81].

The study by Kang *et al.* comes 4 years after the same group published a paper in Science on transient electronics. Although the Science paper by Hwang *et al.* was not the first demonstration of biodegradable MEMS devices, its high impact was pivotal in bringing biodegradable devices to the research forefront. Hwang *et al.* introduced silicon nanomembranes as biodegradable materials and implemented Si-NM in tandem with magnesium, magnesium oxide and silk to build transient electronics feature passive components (e.g., resistors), as well as active components (e.g., transistors). The authors argued, from an engineering more so than a biomedical perspective, that silicon is a biodegradable material because it breaks

down in water, albeit at very slow rates of <3.5 nm/day. The paper also similarly argued traditional CMOS materials, such as silicon dioxide and silicon nitride, as biodegradable. These claims were perhaps the most impactful elements of this publication because it expanded the material sets available to biodegradable device design to encompass standard microfabrication materials and processes. In the proof-of-concept Science paper, the functional lifetime of the transient system was 10 minutes, but could be tuned to 2 days with 800 nm of sputtered MgO. Although 2 days was no slight feat, the general approach by Hwang *et al.* entailed laborious designs. For example, the deposition rate of RF sputtered MgO is rather slow (i.e., approximately 0.5 nm/min), the study implemented 800-nm-thick MgO in order to achieve functionality on the timescale of days [85].

Analogous to resistive-based sensors, biodegradable resistive heaters have also been demonstrated. Tamayol *et al.* developed a drug delivery system with on-demand release based on integrated heaters. The heaters were resistive elements patterned by sputter deposition of Mg through a shadow mask and encapsulated with electrospun sheets of PGS and PCL. Pegylated chitosan served as the nanocarrier for the delivery of antibiotics. Drug release was initiated by the application of 18 V across the Mg resistor, which elevated local temperatures by Joule heating. The on-off transition governing drug release was 33^{o}C to 37^{o}C, which was a narrow window for dermal applications where temperature profiles ranging from ambient environmental temperatures to elevated body temperatures due to exercise can occur. Further, the amount of released drug was inconsistent with cyclic release experiments [78].

An alternative approach to biodegradable MEMS sensors is wireless resonant devices. The wireless design is particularly advantageous in biodegradable devices because solder joints and non-degradable wire connections can present galvanic coupling that accelerates device degradation. Further, resonant devices whose measurement output is the resonant frequency or quality factor of the device provide a simple detection scheme. Luo *et al.* demonstrated a wireless RF pressure sensor comprising electroplated zinc as the conductive element and PLLA as the encapsulation material and pressure-sensitive membrane. The pressure sensor demonstrated a sensitivity of 39 kHz/kPa across a range of 0-20 kPa. As the degradation

lifetime of Zn exceeded the device functional lifetime, Zn/Fe bilayers were implemented to controllably expedite Zn corrosion through galvanic coupling with Fe [79]. In this manner, degradation of the metallic conductor was observed in 0.9 wt.% NaCl at 37°C after 300 hours. The sensor exhibited an initial stabilization period of 21 hours, after which the device demonstrated stable performance for 86 hours before loss of functionality. Hence, the use of Zn/Fe bilayers effectively reduced the functional lifetime to degradation lifetime ratio [80].

Biodegradable energy devices tend to feature larger footprints. This has been observed in electrochemical cells and batteries that feature Mg as sacrificial anode. For example, Yin *et al.* reported a series of biodegradable batteries with Mg as the anode and iron (Fe), molybdenum (Mo) or tungsten (W) as the cathode. The devices utilized commercial foil for the electrodes, phosphate-buffered saline (PBS) as the electrolyte and polyanhydride as the encapsulation to support the serial connection of electrochemical cells to achieve a higher voltage; serial connection of 4 cells reached a steady state voltage of 1.6 V. The authors reported that a single cell possessed a footprint of 3.9 cm^2 in and an electrode spacing of 4 mm. Taken together, this would correspond to a minimum thickness of 1.6 cm, excluding the thickness of the electrodes (tens-of-microns thickness per electrode) and polyanhydride encapsulation (hundreds-of-microns thickness per wall) [81].

Taking a different approach, Kim *et al.* demonstrated an ingestible sodium ion electrochemical cell comprising manganese oxide (MnO_2) and activated carbon (AC) as the electrodes. The MnO_2 and AC were deposited onto a conductive polymer that consisted of silver nanowires dispersed in PGS. The use of silver nanowires limited complete degradability, but the device nonetheless demonstrated a discharge voltage of 0.6 V at discharge currents of up to 20 μA [86]. Melanin and MnO_2 electrodes were implemented in a later study by the authors to improve energy density of the electrochemical cell [87].

The triboelectric effect was harnessed in a study by Zheng *et al.* to develop biodegradable energy harvesters. The authors designed a triboelectric nanogenerator (TENG) with biodegradable polymers (e.g., PLGA, PVA, PCL and PHB) as the frictional and encapsulating layers and sputtered Mg as the

electrodes. The frictional layers featured nanoscale surface topography that was formed by chemical treatment of polymeric films with sodium hydroxide. Devices achieved an open circuit potential of 40 V and a short circuit current of 1.2 μA. Using a linear motor operating at 20 Hz, the rectified output of the TENG was sufficient to power interdigitated electrodes and, ultimately, to stimulate the selective alignment and growth of neuronal cell cultures. Device functionality, evaluated by monitoring the open circuit potential of devices implanted in rats, persisted for 3 days. The degradation lifetime *in vitro* was 90 days [74]. Although the biodegradable TENG represented a new avenue to biodegradable energy devices, contrasting the electrochemical approaches previously discussed, it will be difficult to identify consistent physiological motion at the frequencies needed to power stimulation electrodes; this limitation has been characteristic to many biomedical energy harvester and more modest, alternative applications may be necessary.

Table 1 summarizes a selection of the biodegradable devices discussed in this section. Despite the diverse array of sensors, drug delivery systems and energy devices examined, the functional lifetime of all devices did not exceed a few days, whereas the degradation lifetime was typically 1-2 orders of magnitude higher. As Salvatore *et al.* had highlighted, the advancement of biodegradable devices is limited by its materials and fabrication [73]. The current review further supported this assessment.

Table 1 Overview of select biodegradable MEMS devices from literature.

Device Type	Materials	Functional Lifetime	Degradation Lifetime	Ref.
Thermistor	Ecoflex, CVD oxide and nitride, and sputtered Mg	20 h	67 days	[73]
ICP, pH, flow rate, acceleration and temperature sensors	Nanoporous Si, polyanhydride, PLGA, oxide	3 days	30 h (pH 12)	[77]
Heat-induced drug delivery system	PGS-PCL mesh, sputtered Mg and Zn	<1 h, Mg 2 days, Zn	4 days, Mg 20 days, Zn	[78]
Pressure sensor	Zn/Fe bilayers, PLLA and PCL	86 h	> 300 h	[79], [80]
Strain and temperature sensors	Silk, Si-NM, Mg, MgO	<2 days	n/a	[85]

1.5 Overview of the Present Research

This thesis harnesses bone fracture healing as an application platform for the development of biodegradable MEMS devices. The experimental chapters of this thesis are organized hierarchically from materials to devices to understanding *in vivo* performance. Specifically, chapter 2 focuses on the identification, microfabrication and characterization of biodegradable materials that are suitable for orthopedic devices. Chapter 3 presents the development of biodegradable strain sensors and energy sources, as well as explores the design of a non-degradable strain sensor for comparison. Lastly, chapter 4 discusses the *in vivo* deployment of a non-degradable strain sensing system in a critically-sized segmental bone defect model and characterizes the cellular toxicity of the biodegradable materials examined in this body of work. As biodegradable materials are less developed in their clinical and regulatory pathway, it was decided that cytotoxicity was critical to assessing *in vivo* pertinence. This work will not culminate in the animal deployment of a fully biodegradable system, as the requisites are (e.g., biodegradable circuitry and packaging) is beyond the scope of this research. The objective of this thesis is to further the field of biodegradable MEMS by introducing new approaches to fabrication and passivation, as well as to establish

more thorough characterization (at both the materials and device level) to support future work in an entirely biodegradable, implantable system.

CHAPTER 2

MICROFABRICATION AND CHARACTERIZATION OF BIODEGRADABLE MATERIALS

2.1. The Micropatterning of Magnesium for Biodegradable Applications

2.1.1. Introduction

The element magnesium (Mg) offers a unique combination of mechanical, electrochemical, electrical, and physiological properties that are attractive for biomedical applications. Magnesium is commonly alloyed with aluminum for structural applications in the automotive and aerospace industries due to its high modulus-to-density ratio [88]–[91]. Table 2 summarizes select material (e.g., mechanical, electrical, and physical) properties of biodegradable materials. The material properties of bone are provided as a reference. The data suggests that Mg possess mechanical and physical properties most similar to cortical bone, as compared to other biodegradable metals (e.g., Zn and Fe). Magnesium is also the fourth-most common cation found in the human body and an essential mineral nutrient. For example, adenosine triphosphate (ATP), the main energy source in biological cells, requires a bound Mg ion to be biologically active. Magnesium also plays a critical role in stabilizing polyphosphate compounds involved in DNA and RNA synthesis [92], [93]. Further, Mg is an electronegative element with a standard electrode potential of -2.34 V vs. SHE, a theoretical capacity of 2200 mAh/g, and naturally corrodes within a physiological environment [7-9]. These unique properties promote the use of Mg for biomedical applications, such as for the development of biodegradable implantable technologies. Biodegradable Mg implants would be advantageous for the treatment and monitoring of transient disease states, such as for monitoring bone fracture healing.

Table 2 Properties of cortical bone, fixation plate, and select biodegradable materials

Material	Young's Modulus (GPa)	Yield Stress (MPa)	Resistivity (Ω·cm)	Coefficient of Thermal Expansion ($\mu\varepsilon \cdot K^{-1}$)	Corrosion Rate	Water Vapor Transport Rate ($g \cdot m^2 day^{-1}$)	Source
Bone	20	130	7.00E+06	---	---	---	[97], [98]
Mg	45	65	4.40E-06	25	22.3 mil·yr^{-1}	---	[84], [96], [99]
Zn	90	---	5.90E-06	30.2	14.4 mil·yr^{-1}	---	
Fe	210	---	9.71E-06	12	7.48 mil·yr^{-1}	---	[99], [100]
PCL (60 kDa)	0.33	10	1.25E+12	122	>24 mo.	177	[101]–[105]
PLA (220 kDa)	1.30	---	5E+16	---	12-16 mo.	172	[101]–[103]
PLGA (75/25) (15 kDa)	0.2.0	---	---	---	2-5 mo.	---	[102], [106]
PLGA (50/50) (110 kDa)	2.0	---	---	---	0.5-4 mo.	---	[102], [107]
PSU	2.57	95.8	1.02E-01	56	---	14	[108]

To date, biomedical use of Mg has been demonstrated in structural devices, such as biodegradable stents and bone screws, as well as for transient implantable electronics [96], [99], [109]–[112]. The structural devices are typically machined from commercial extruded or cold-rolled Mg, such as with the laser micromachining of Mg foil for biodegradable stents [96], [99]. Fabrication of transient electronics containing Mg relies on the bulk micromachining of commercial Mg and physical vapor deposition (PVD) of thin-film Mg (i.e., <1 μm). However, these current methods of fabricating and patterning Mg for transient electronics have their respective limitations that preclude the full exploitation of Mg for clinically-targeted biodegradable microelectronics. Physical vapor deposition techniques, such as sputtering and evaporation, produce high quality Mg thin films with nanoscale grain size and high purity due to the vacuum deposition conditions. Further, the crystal orientation and morphology, ranging from columnar to granular structure, are tunable based on deposition conditions. Studies have demonstrated the enhanced corrosion resistance of Mg thin films in comparison to bulk commercial cold-rolled Mg [91], [113]. While these positive qualities render thin-film Mg a good candidate for corrosion resistant coatings, films deposited by PVD

methods are typically limited to submicron thicknesses. Due to the kinetics of Mg corrosion in physiological fluids, submicron, unpassivated Mg films biodegrade on the timescale of hours in physiological solutions. Hwang *et al.* demonstrated that 150-nm-thick Mg resistors completely dissolve in deionized water after 3 hours. Protection of the Mg with barrier oxide (e.g., MgO) and polymeric encapsulation extended longevity of the Mg to approximately 90 hours, though the degradation rate is expected to increase in physiological fluid [111]. Consequently, biodegradable devices comprising thin-film Mg may be restricted to clinical applications that require a monitoring and/ or treatment window of only several days, unless longer-lasting passivation schemes that simultaneously contemplate biodegradation are demonstrated.

The bulk micromachining of commercial Mg overcomes the thickness limitation of PVD methods, but is, in turn, limited in geometry and MEMS-integration. Common methods for the micropatterning of commercial Mg include photochemical etching, laser micromachining, and electric discharge machining (EDM). D.M. Allen *et al.* demonstrated 300-µm-wide feature and millimeter-scale spacing from the photochemical etching of Mg foil (250 µm thickness) in nitric acid solution, but showed no MEMS integration [114]. We previously demonstrated finer feature width and spacing (i.e., 100 µm) by confining photochemical etching to the top surface of Mg foil mounted onto a carrier substrate and the use of dilute hydrochloric acid. However, the isotropic nature of the chemical etchants limited the minimum feature size for a given thickness of Mg foil, and produced non-vertical sidewalls [115]. In contrast to wet chemical etching techniques, laser micromachining of commercial Mg achieved finer feature size, with 80-µm-wide lines and 20-µm-wide gaps demonstrated from 70-µm-thick Mg foil. However, the redeposition of debris and oxidation on the sidewall of laser-cut structures required post-process chemical treatment. In our previous study, citric acid was used to remove the redeposited material because the etchant preferentially removes metal oxides. However, citric acid will also etch magnesium isotropically via an oxidative mechanism, which, ultimately, reduced the Mg thickness by 15% and increased surface roughness threefold [115]. Boutry *et al.* utilized EDM to fabricate RLC resonators from 3-mm-thick commercial Mg that featured a width of 1 cm and a gap of 0.6 mm [14], [18]. As shown, the bulk micromachining of

commercial Mg is limited in minimum attainable feature size, amenability to three-dimensional multi-layered structures, and post-process integration with other MEMS. While these subtractive microfabrication approaches may be sufficient for certain applications, further advances in Mg microfabrication and integration would support the development of more sophisticated biodegradable devices and systems.

2.1.2. Laser Micromachining of Commercial Magnesium

Magnesium is an alkaline earth metal with attractive mechanical and electrochemical properties for biomedical and energy storage applications. However, current methods for the microfabrication of magnesium have mainly concentrated on the micropatterning of thin (i.e., submicron) films with sputtering and evaporation. The patterning of thicker Mg film (i.e., micron to hundreds-of-microns thickness) have been limited in feature size and MEMS integration. This section presents a subtractive approach to the microfabrication of commercial magnesium on the order of tens of microns in thickness.

Laser micromachining was investigated for the fabrication of high density, micron-scale magnesium microstructures and their integration into MEMS processes. Figure 7 Fabrication scheme for the laser micromachining of 50-μm-thick commercial Mg. presents the fabrication process for polydimethylsiloxane (PDMS) to demonstrate the compatibility of laser micromachining with MEMS integration. Laser micromachining was performed on commercially-available 70-μm-thick magnesium foil (99.9% pure) using an infrared laser (Resonetics, Nd:YLF 1047 nm) operating at 180 ns pulses and a power density of 30×10^{12} W/m^2. Magnesium foils were cleaned in 15% citric acid and laminated onto a glass substrate with adhesive prior to laser micromachining. Samples were cut at a cutting velocity of 1 mm/sec for 3 to 5 passes. Laser cutting conditions and post-processing treatment with citric acid were optimized to minimize the amount of redeposited material onto the surfaces and sidewalls of the fabricated structures. The samples were then cast with polydimethylsiloxane (PDMS) and immersed in acetone to release the PDMS-embedded magnesium microstructures from the glass substrate.

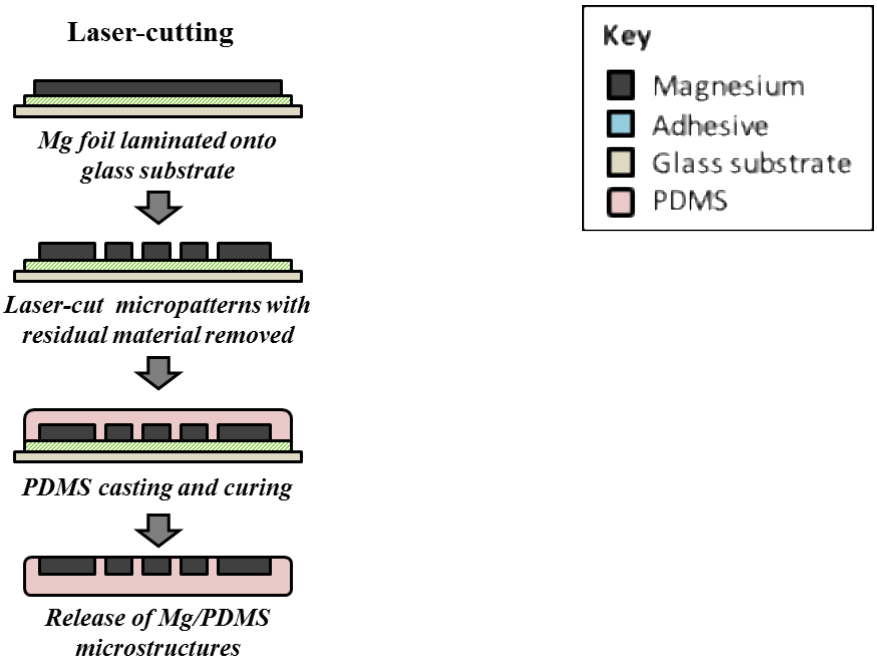

Figure 7 Fabrication scheme for the laser micromachining of 50-µm-thick commercial Mg.

Planar spiral and interdigitated comb geometries fabricated from laser micromachining (Figure 8) featured a minimum line width and gap of 80 µm and 20 µm, respectively, with variations of +5 µm. The surface roughness of the magnesium microstructures after post-process chemical treatment was 1.4 µm. The minimum gap obtained may be attributed to the redeposition of debris and oxidation that occurs at the sidewall of laser-cut structures. Multiple passes were required to maintain a clear, continuous spacing between adjacent turns. Magnesium microstructures were treated with citric acid after laser-cutting to remove redeposited materials from the surface and sidewall. Although citric acid preferentially removes metal oxides (e.g., MgO), it will also etch magnesium isotropically via an oxidative mechanism. Figure 8 presents a comparison of laser-cut microstructures before and after citric acid treatment. As shown, treatment with citric acid reduces the sidewall roughness attributed to redeposition, but also reduces the thickness and increases the surface roughness of the laser-cut magnesium microstructures.

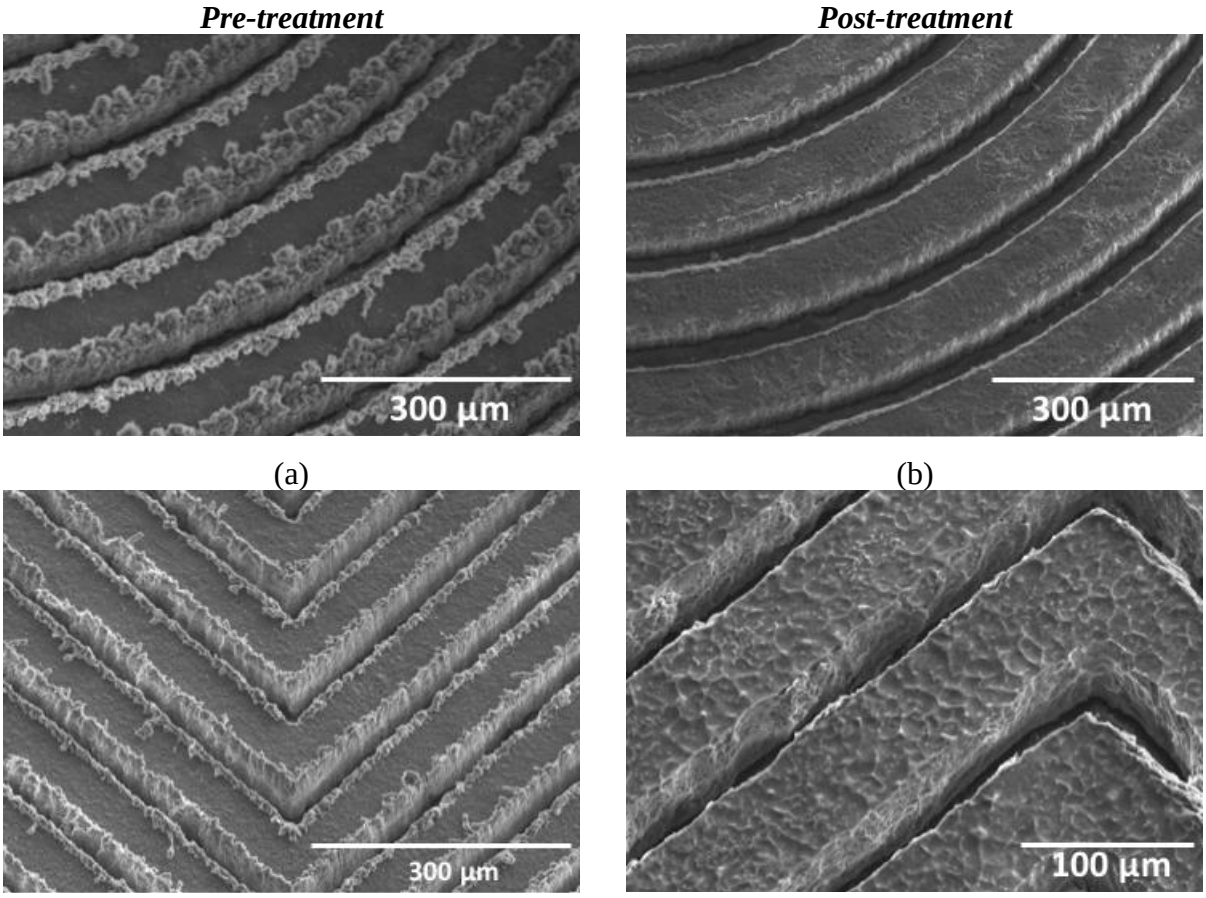

Figure 8 Laser machined magnesium microstructures (a, c) before and (b, d) after post-process treatment with citric acid and sonication to remove sidewall redeposition.

2.1.3. Chemical Wet Etching of Commercial Magnesium

The chemical etching of magnesium was explored as a subtractive, batch-scale approach for the micropatterning of MEMS-relevant geometries. Previous study on the photochemical etching of magnesium demonstrated features that were hundred-of-microns wide and separated by millimeter-scaled gaps [3]. Improvement upon the minimum achievable feature sizes (i.e., width and spacing) would promote the use of chemical etching for the micropatterning of thick magnesium structures for MEMS. Figure 9 illustrates the fabrication process for the chemical etching of magnesium microstructures on PDMS substrates. Chemical etching was performed in a 1:50 (v/v) solution of hydrochloric acid in water and through a micropatterned photoresist mold. Commercial magnesium foils (70-µm-thick) were cleaned with

solvent and citric acid to remove surface residues and oxides. Prior to photoresist patterning, the backside of the magnesium foils was spin-coated with PDMS and mounted onto a glass substrate to confine etching to one side and to serve as a backing layer for the etched structures. Planar circular coils were fabricated by the chemical etching of magnesium foil through a photoresist mask (Microposit S1813 positive resist) featuring 50-µm-wide gaps and 250–µm-wide lines. The measured etch rate was 7.5 µm/min. Etched samples were immersed in acetone to remove the photoresist mask and released from the underlying substrate.

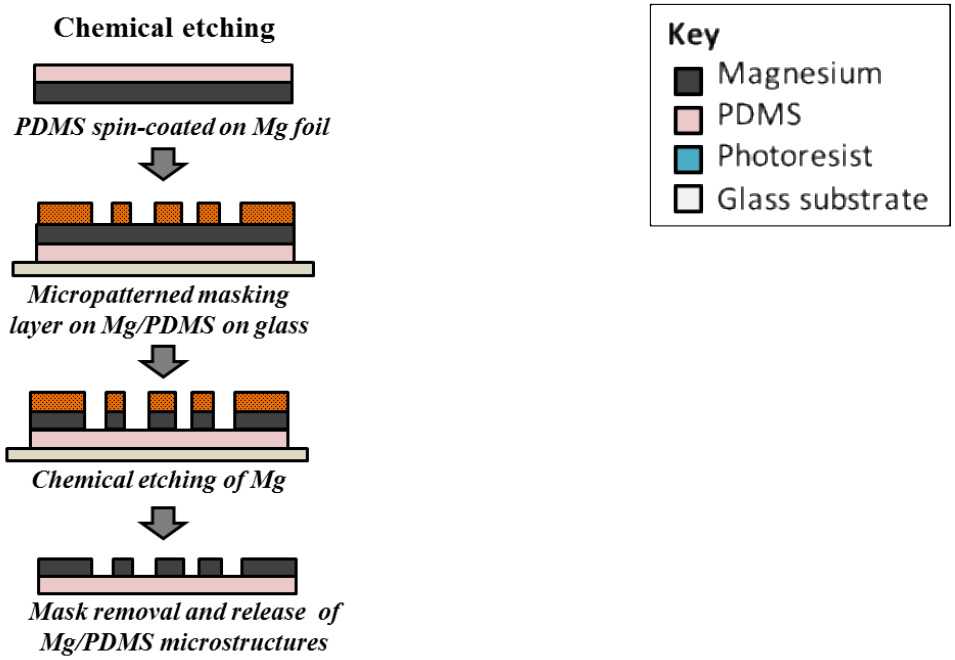

Figure 9 Fabrication process for the chemical wet etching of magnesium foil through a lithographically-defined etch mask and the embedding of chemically-etched Mg microstructures in PDMS.

Magnesium microstructures patterned by chemical etching featured line widths and gaps of 150 µm + 10 µm (Figure 11). Structures etched with dilute hydrochloric acid demonstrated greater uniformity, with reduced undulations along the sidewalls and less surface roughness (<1 µm), than magnesium structures treated with citric acid. The magnesium microstructures fabricated using hydrochloric acid exhibited finer feature sizes than previously-reported results with photochemical etching of magnesium with nitric acid

[3].

As hydrochloric acid etches isotropically, the fabricated structures were narrower than the designed patterns (Figure 11). Although the mask design may compensate for lateral etching, this strategy was limited by the challenge of etching through photomask features that were narrower than 30 μm in width. However, the extent of lateral etching was less than that of vertical etching. Specifically, the vertical etch rate of 1:50 (v/v) hydrochloric acid was 7.5 μm/min, whereas the lateral etch rate was 5.5 μm/min. Figure 11b shows the sloped sidewalls consistent with these etch rates, with greater undercut at the surface than the bottom of the etched structure. The outermost features (i.e., outer turns of a planar coil) and sharp corners also etched faster than inner features, resulting in over-etching in the outer regions. Another limitation to chemical etching is its dependence on the starting quality of the commercial magnesium foil. Although mechanical polishing and chemical cleaning removed surface residues and oxides, these approaches also reduced the thickness of the magnesium foil.

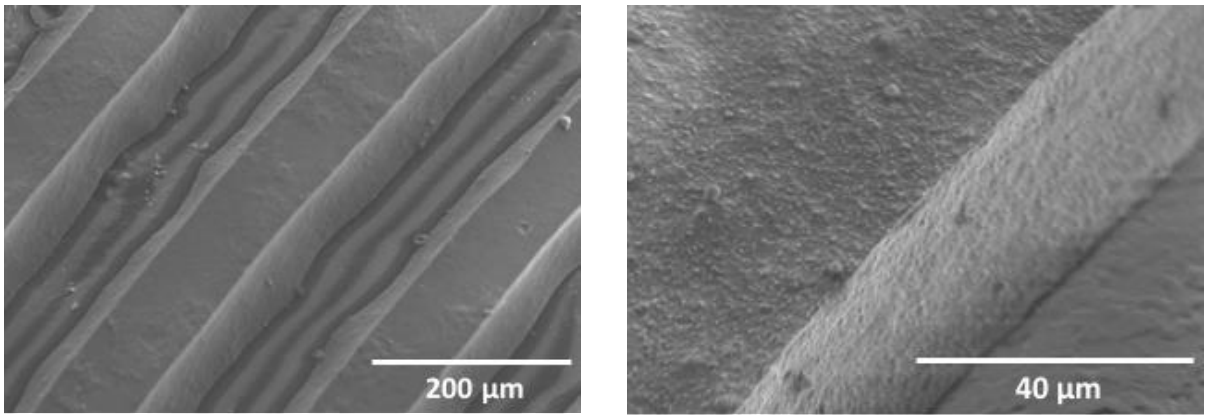

(a) (b)

Figure 10 Magnesium microstructures chemically-etched with 1:50 (v/v) hydrochloric acid. The difference in coil width between the bottom and top of the sample is attributed to the isotropy of the etchant.

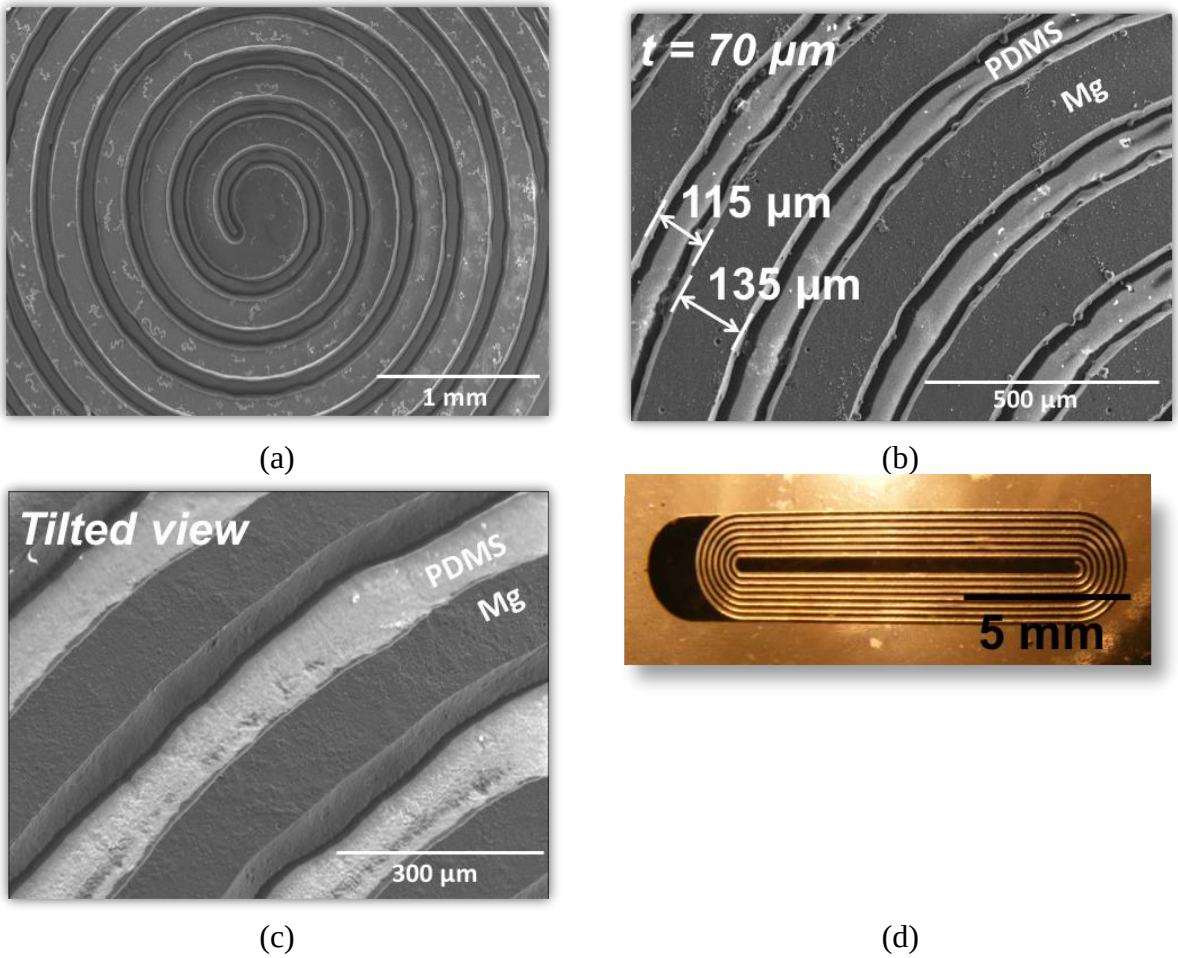

Figure 11 (a-c) SEM and (d) optical image of circular and ellipsoidal planar inductors mounted on PDMS.

2.1.4. Non-Aqueous Electrodeposition of Magnesium

The subsequent sections of this chapter present the development of a MEMS-compatible Mg electrodeposition process for the fabrication of biodegradable bio-MEMS. Specifically, the through-mold electrodeposition of Mg was investigated with an emphasis on (1) ease of integration with traditional MEMS processing and (2) use of biocompatible and non-permanent materials to enable the development of biodegradable MEMS. In contrast to the bulk micromachining of commercial Mg, electrodeposition is an additive approach that enables batch-scale micropatterning of Mg structures with specifically designed patterns. Potentially, the use of multiple electroplating steps enables the development of 3D

microstructures, which would be challenging to achieve using the above-mentioned subtractive Mg patterning technologies. Due to its high electronegativity, Mg is difficult to electroplate from an aqueous electrolyte solution. Instead, non-patterned Mg electrodeposition has been demonstrated in organic solutions and ionic liquids, most commonly with Grignard reagents solubilized in ether [7], [19-24]. For example, Mg electrodeposition has been used to generate porous deposits of Mg nanoparticles for hydrogen storage applications and non-patterned surface coatings for corrosion-resistance [117], [123]. However, challenges with Mg electrodeposition have hitherto limited its application to MEMS [115], [124]. While Mg electrodeposition takes place in a non-aqueous solution, the metal is reactive with protic solvents and water. Hence, pre-plating processing materials (e.g., the electroplating mold) must survive extended immersion in non-aqueous solutions and post-plating processes should avoid prolonged exposure to aqueous solutions. In addition, materials utilized in the fabrication process must either be biocompatible and biodegradable, or easily removable to eliminate the presence of permanent materials in a biodegradable device without exposure to harsh processing conditions that might initiate or significantly accelerate device degradation.

We have previously demonstrated the non-aqueous electrodeposition of aluminum microstructures from lithographically-defined photosensitive polyimide molds [125]. The removal of thick polyimide films required either extensive dry etching in oxygen-based plasmas or wet etching in commercial strippers. Based upon our work on Mg patterning [115] and non-aqueous electrodeposition of Al [125], the present study explores the development of through-mold Mg electroplating with water-soluble molds and on a flexible polyimide substrate to enable the development of completely biodegradable Mg microstructures.

2.1.5. MEMS-Compatible Process for Magnesium Electrodeposition

To achieve Mg microstructures, Mg was electrodeposited through a lithographically-defined SU-8 mold. Although SU-8 is not biodegradable, its chemical insolubility in solvents and amenability to lithographic patterning supported the use of SU-8 as the electroplating mold material for preliminary Mg electrodeposition and optimization studies. As shown in Figure 12, Ti/Cu/Ti (50 nm/ 500 nm/ 50 nm) was

sputter deposited onto a glass substrate and chemically-etched through a patterned photoresist mask to obtain a mesh seed layer. Next, photosensitive SU-8 epoxy (SU-8 2025, MicroChem) was used to lithographically define the electroplating mold due to its chemical insolubility in the solvent-based electroplating solution. Briefly, SU-8 was spin-coated to a thickness of 75 μm and soft baked to remove residual solvent. The sample was then physically inverted for backside exposure, where the metallic pattern of the mesh seed layer served as the bright-field mask. Samples were then cross-linked during a post-exposure bake and developed in PGMEA (Thinner Type P). In this manner, the electroplating mold occupied the negative space of the mesh seed layer. Alternatively, for deposition of Mg onto a silicon substrate, the SU-8 mold may be aligned to the underlying mesh seed layer through conventional top-side exposure using a lithographic mask. The uppermost Ti of the seed layer was chemically removed in dilute hydrofluoric acid.

The sample was then loaded into an oxygen- and moisture-free glovebox under nitrogen atmosphere and cleaned with salicylic acid solubilized in tetrahydrofuran (THF). The electrodeposition process was conducted in a glovebox because the electrolyte solution is anhydrous and contains strong reducing agents. The measured temperature and relative humidity were approximately 27°C and <5%, respectively. Commercial Mg foil (250-μm-thick) served as the anode and was mechanically polished with sand paper (2000 grit) and rinsed in THF prior to use. The electrolyte solution comprised 3 M methylmagnesium chloride (CH3MgCl) in THF. Magnesium was electrodeposited under direct and pulse current at peak current densities of 5, 10, 15, and 20 mA/cm2 and 20%, 50% and 100% duty cycles to determine optimal plating conditions After electrodeposition, samples were removed, rinsed in THF, and allowed to dry overnight prior to unloading from the glovebox. In subsequent experiments, aluminum chloride (AlCl3) was added to the electrolyte solution, resulting in a 6:1 molar ratio of CH3MgCl:AlCl3 in THF.

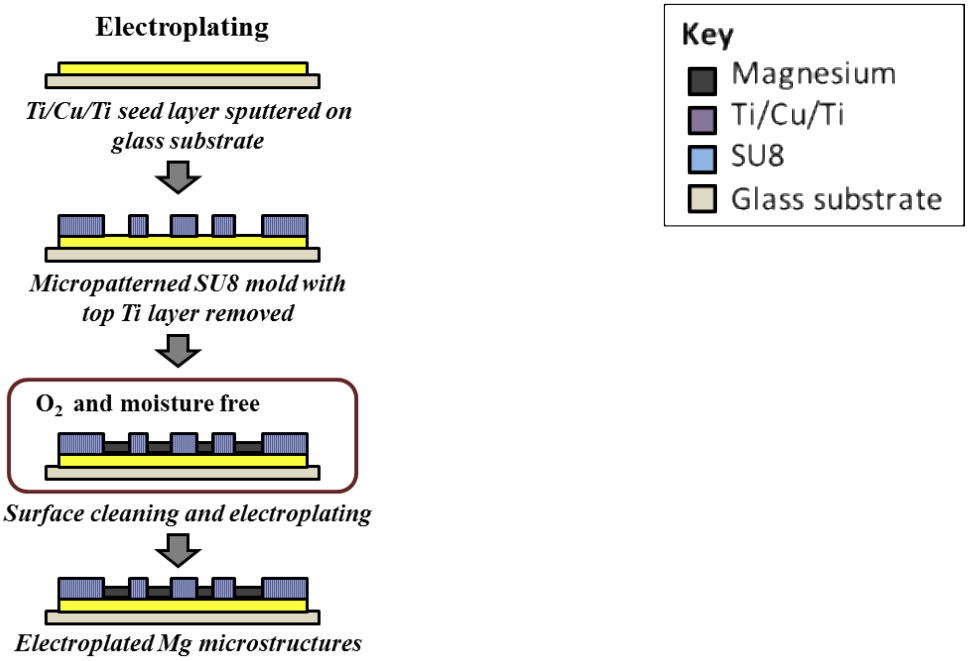

Figure 12 Fabrication scheme for the through-mold electrodeposition of magnesium from non-aqueous electrolyte. Magnesium is electrodeposited through lithographically-defined SU-8 under inert nitrogen atmosphere.

2.1.6. Characterization of Magnesium Electrodeposited from Non-Aqueous Electrolyte

Magnesium microstructures electrodeposited through lithographically-defined SU-8 molds are shown in Figure 13. Electroplated Mg coils were plated under pulse current conditions (i_{peak} = 15 mA/cm^2; t_{dep} = 2 h; t_{on} = 0.2 ms, t_{off} = 0.8 ms; 20% duty cycle) in 3 M CH_3MgCl and corresponded to a deposition rate of approximately 7 µm/h. It was observed that the pulse plating condition provided better electrodeposition into the micropatterned SU-8 trenches (i.e., <300 µm in width), whereas direct current was sufficient for electrodeposition into larger areas. The electroplated Mg microstructures exhibited a thickness of 15 $\pm$ 5 µm and a grain size of 10 µm. The measured surface roughness of electroplated Mg was approximately 6 µm, in comparison to the submicron roughness of commercial, cold-rolled Mg foil. The electroplated material demonstrated coherent and dense packing despite the surface grain size. EDX analysis determined that the elemental composition at the surface of the electroplated material was 89% Mg and 11% O, which compares favorably to commercial Mg foil (Table 2.I). Electrical resistivity of the

electroplated Mg was characterized by conventional four-point DC resistance measurement technique and determined to be 8.7 μΩ·cm. For comparison, commercial Mg foil was 5.3 μΩ·cm and the reported resistivity of bulk Mg is 4.4 μΩ·cm. Figure 14 shows planar circular inductors that were fabricated by Mg electrodeposition and embedded in PDMS. The achievable feature sizes were 250 μm and 50 μm in coil width and spacing, respectively.

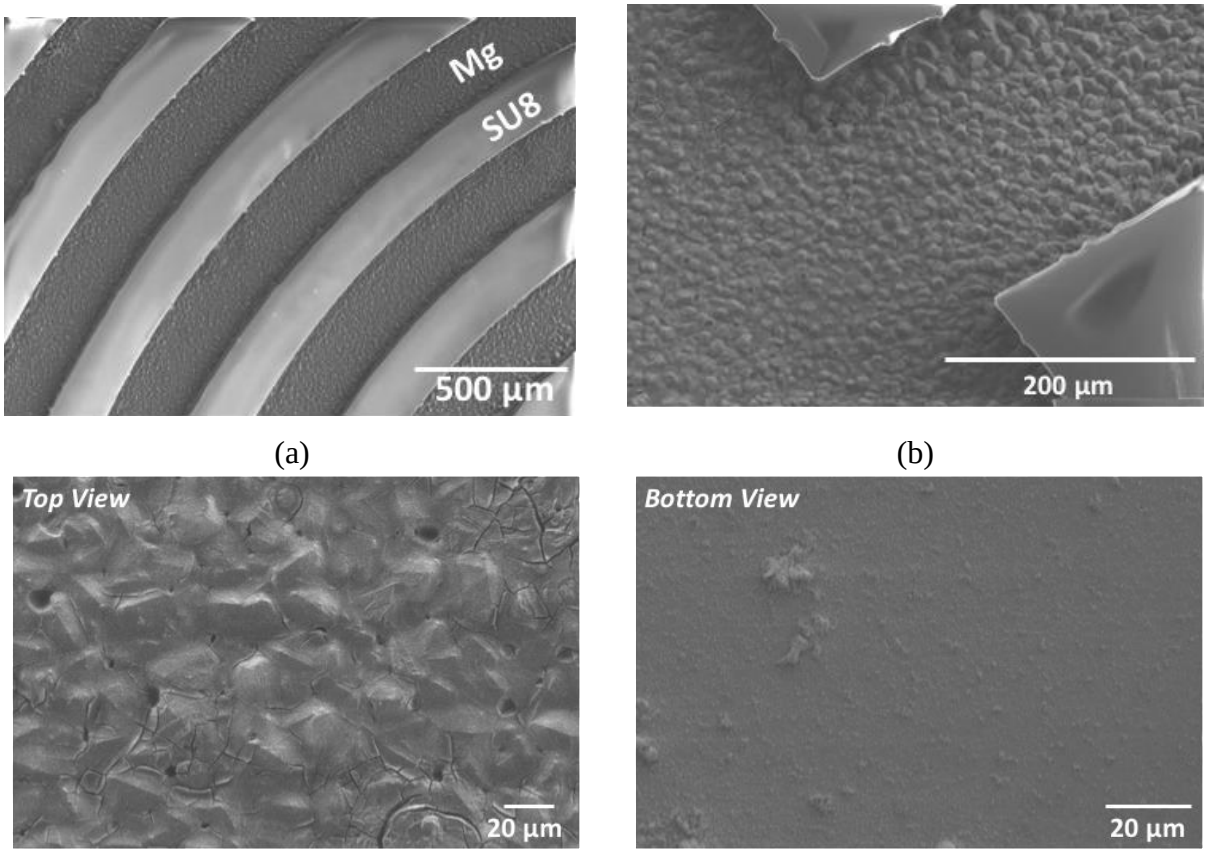

Figure 13 Electroplated magnesium through lithographically defined SU-8 molds: SEM images of surface morphology of (a) an electroplated Mg coil and (b) Mg electroplating adjacent to the SU-8 corner. SEM images of the (c) top and (d) bottom surface of electroplated Mg. Samples were plated under pulse current conditions with an average current density of 15 mA/cm^2 at 20% duty cycle to a thickness of 15 μm.

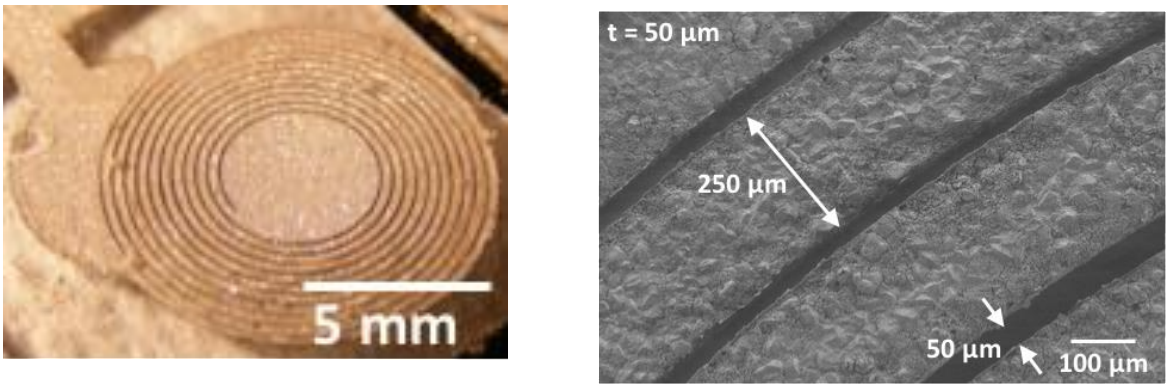

(a) (b)

Figure 14 (a) Optical and (b) SEM images of electroplated Mg coils embedded in PDMS.

The addition of $AlCl_3$ to the electroplating solution was explored to enhance the quality of the electroplated Mg, increase electroplating bath conductivity and hinder electrolyte decomposition (Figure 15). Studies have suggested that $AlCl_3$ enhances conductivity, voltage stability, and current efficiency of the electroplating bath by increasing ionization of Grignard reagent in ether (e.g., CH_3MgCl in THF). Further, $AlCl_3$ at concentrations below 10:1 molar ratio ($AlCl_3$:CH_3MgCl) has been shown to reduce grain size. Co-deposition of Al was not reported at molar ratios below 3:1 [19], [28]. Figure 15 shows the direct comparison of Mg microstructures electroplated in a Grignard reagent solution with and without the addition of $AlCl_3$. The samples were plated to a thickness of 50 µm under identical pulse plating conditions in both electrolyte solutions. For electroplated Mg thicker than 10 µm, the average grain size did not appreciably change along the center of the electroplated region with the addition of $AlCl_3$. However, Mg electroplated in pure CH_3MgCl solution showed preferential plating at the edges of the conductive region, adjacent to the SU-8 mold (Figure 15a). Surface morphology of Mg plating at the SU-8 border showed larger grains that deformed the SU-8 mold. In contrast, Mg microstructures electroplated in the presence of $AlCl_3$ demonstrated more uniform plating from the center to the edge without any deformation of the adjacent SU-8. Cross-sectional imaging of 50-µm-thick electroplated Mg confirmed the dense crystal packing of Mg microstructures electroplated with $AlCl_3$.

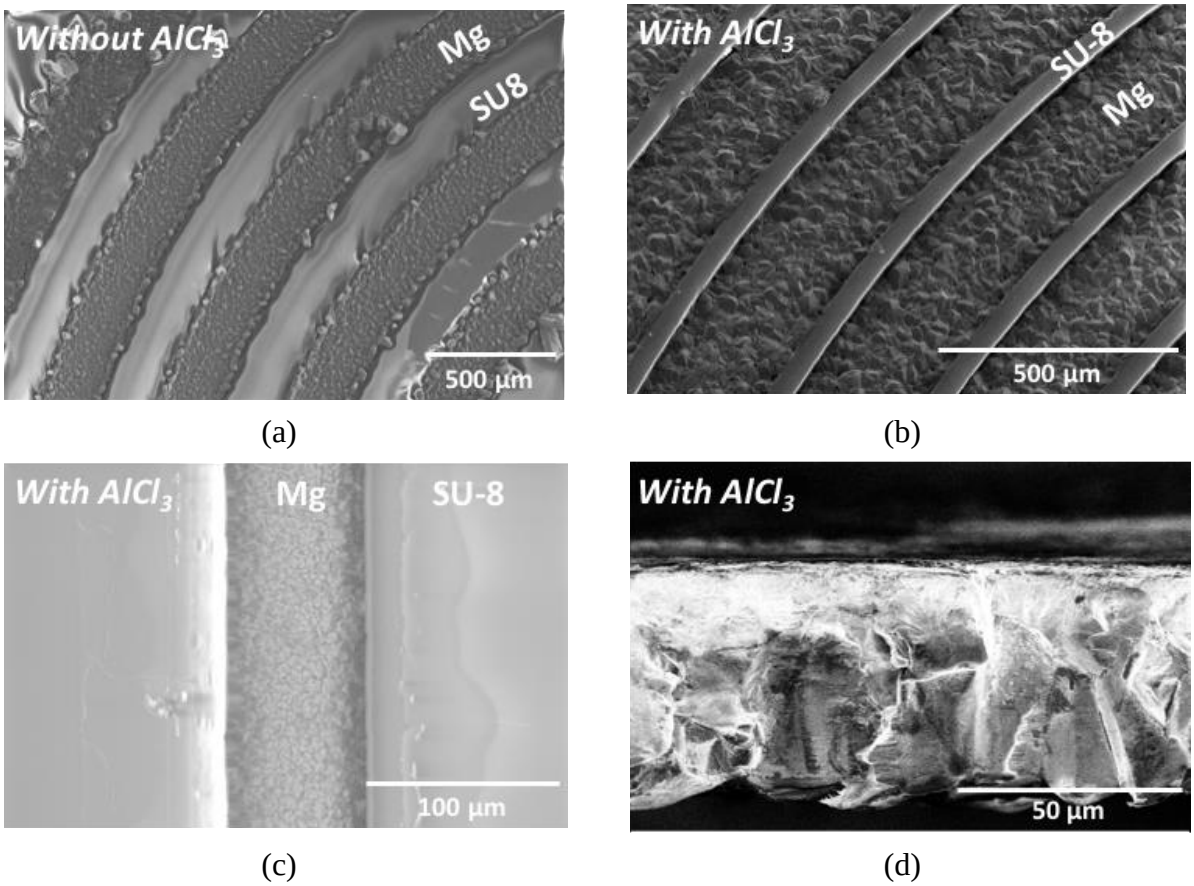

Figure 15 Comparison of magnesium electroplated (a) without and (b-c) with the addition of $AlCl_3$. Samples were plated under current-controlled conditions at 15 mA/cm^2 and 20% duty cycle in 250-µm-wide SU-8 trenches to a thickness of (a, b, d) 50 µm and (c) 10 µm.

Surface elemental composition of the electroplated material was 85% Mg, 15% O, and insignificant Al, confirming that the addition of $AlCl_3$ did not result in Al co-deposition (Table 2). Further, the percentage of Al detected is less than commercial Mg-Al alloys that have been considered for biodegradable, implantable applications. For example, AZ-31 and AZ-91 alloys have been explored for use as biodegradable bone screws and bone plates, and feature 3% and 9% Al, respectively [30-32]. The biocompatibility of the AZ-31 has been well demonstrated in vitro and *in vivo* [109], suggesting that Al composition equal to or less than that of the alloy may be physiologically tolerated. These findings suggested that the Al found in the electroplated Mg does not detract from its biocompatibility, though it remains to be validated experimentally. X-ray diffraction was performed on Mg electroplated with the

addition of AlCl3 to compare the crystal orientation of the plated material to commercial Mg foil (Figure 16). The top surface of the 50-µm-thick electroplated Mg showed a singular peak corresponding to the [002] orientation of the hexagonal close packed crystal structure of Mg. The bottom surface showed two strong peaks that corresponded to the [002] and [101] crystal orientation with a (002)/(101) peak intensity ratio of 2.2. This suggested that Mg grown by confined electrodeposition through a mold, under the studied electroplating conditions, shows preferential orientation along the [002] crystal axis. Commercial Mg foil was also analyzed by XRD and exhibited a singular peak between 30° to 40° in the 2θ region that aligned with the [002] peak observed with electroplated Mg samples.

Table 3 Comparison of the elemental composition of electroplated Mg and commercial Mg (CP-Mg), as determined by EDX analysis.

Elemental Composition by EDX			
	Electroplated Mg		CP-Mg
Element	Without $AlCl_3$	With $AlCl_3$	
Mg	89%	85%	90%
O	11%	15%	10%
Al	0%	<1%	0%

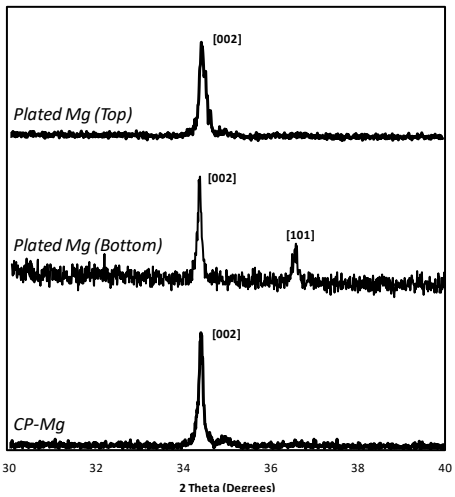

Figure 16 Comparison of crystal orientation of electroplated Mg and commercial Mg (CP-Mg) based on XRD analysis. Data of plated Mg corresponds to Mg electrodeposited from solution containing $AlCl_3$ as an additive.

Surface morphology, cross-sectional structure, elemental composition, and crystal orientation results supported that Mg electroplated from a mixture of CH_3MgCl and $AlCl_3$ is comparable to commercial Mg foil. In addition, it was experimentally confirmed that addition of $AlCl_3$ to the plating solution increased the conductivity of the bath and extended its lifetime by hindering electrolyte decomposition. The reduced concentration of CH_3MgCl in the electroplating mixture also rendered the plating solution more transparent, enabling visibility of the sample during the plating process. For these reasons, a 6:1 molar ratio of CH_3MgCl to $AlCl_3$ was exclusively used henceforth as the electrolyte solution for the presented Mg electroplating studies.

2.1.7. Fabrication of Magnesium Electrodeposited Through Water-Soluble Molds

In this section, polyvinyl alcohol (PVA, MW = 2000 Da) and commercial polyimide film (Kapton, 3-mil-thick) were used as the electroplating mold and substrate, respectively. These materials were selected to enable the use of electrodeposited Mg for biodegradable bio-MEMS applications. Specifically, the fabrication process was designed to eliminate the use of non-biodegradable and/ or not easily removable

materials. For example, the removal of SU-8 by reactive ion etching with O_2 gas can be rather time consuming at thicknesses greater than 10 µm. In contrast, PVA is a water-soluble polymer with poor solubility in non-aqueous solvents, suggesting that it can serve as a mold for non-aqueous electroplating processes and subsequently be removed by solubilizing in water [124]. Moreover, PVA is a FDA-approved, biocompatible polymer that is found in various consumer food products [129]. Kapton film was selected as the substrate to facilitate post-plating substrate removal and packaging with biodegradable material sets [130].

The fabrication process begins with sputter deposition of Ti/Cu/Ti (50 nm/ 500 nm/ 50 nm) onto a 3-mil-thick polyimide film mounted onto a carrier wafer using a thin layer of negative photoresist (Futurrex, NR9-1500PY) (Figure 17). This ensured that the bottom surface of the polyimide film was fixed to a rigid carrier during subsequent sonication. The polyimide films were cleaned and briefly treated with oxygen plasma prior to metal deposition. Next, PVA was micropatterned onto the polyimide via a lift-off process using negative-tone photoresist (Futurrex, NR21-20000). The negative image of the desired electroplating mold was lithographically patterned with 100-µm-thick NR-21 and briefly treated with oxygen plasma. PVA solutions were prepared with commercially purchased PVA under constant stirring at 90°C, which exceeds the glass transition temperature of PVA without exceeding the boiling point of water, until a homogenous solution was achieved. To improve surface wettability, samples were briefly treated with oxygen plasma and a dilute PVA solution (10 wt.%) was spin coated onto the samples. Next, two layers of PVA, at a concentration of 33 wt.%, were spin-coated onto the samples at 1000 rpm for 45 seconds. Samples were dried in an oven at 100°C for 10 min to remove residual water and cooled to room temperature. To facilitate removal of the NR-21 pattern, samples were treated with reactive ion etching in oxygen gas for five minutes to etch away PVA coating the edges of the NR-21 features. This was performed at 200 mTorr and 200 W with a 5:1 ratio of O_2 and CHF_3 gas. Samples were then sonicated in acetone to remove the negative photoresist, resulting in a micropatterned water-soluble mold. The topmost titanium of the seed layer was dry etched by reactive ion etching in SF_6 gas to prevent exposure of the sample to

aqueous etchants. Samples were loaded into the glovebox and electroplated in a 1:6 molar ratio of aluminum chloride and methylmagnesium chloride in a two-electrode-cell configuration. The pulse plating conditions were an average current density of 10 mA/cm2 and a duty cycle of 20% (t_{on} = 1 ms, t_{off} = 4 ms), which corresponded to a deposition rate of approximately 7 µm/h. After electroplating, samples were rinsed with THF, dried, and removed from the glove box. Magnesium samples were stored within the glovebox unless immediate use was desired to eliminate long-term exposure to ambient conditions.

The PVA mold was removed either by solubilizing in deionized (DI) water or by reactive ion etching with oxygen gas, if dry processing was desired. Magnesium samples were rinsed in isopropanol and thoroughly dried after aqueous removal of the PVA to eliminate residual moisture. In addition, samples were cleaned with 10 wt.% citric acid to remove surface oxidation when necessary. The dry etching of PVA was performed using the reactive ion etching parameters described earlier. Complete removal of the PVA mold was achieved with 25-30 minutes of etching. The Mg microstructures were laminated into prepared 200-µm-thick poly-L-lactic acid (PLLA) sheets with a nanoimprinter (Obducat NIL) in two steps; Mg was embossed into the PLLA at 10 bar and 140°C for four minutes and maintained at 10 bar and 70°C for one minute before cooling down to the demolding temperature (T_{demold} = 30°C). The polyimide film was peeled from the Mg/PLLA, with the Cu and Ti seed layers selectively adhering to the polyimide. The resulting construct is an example demonstrating the amenability of the PVA and Kapton-based process flow with fabricating biodegradable MEMS.

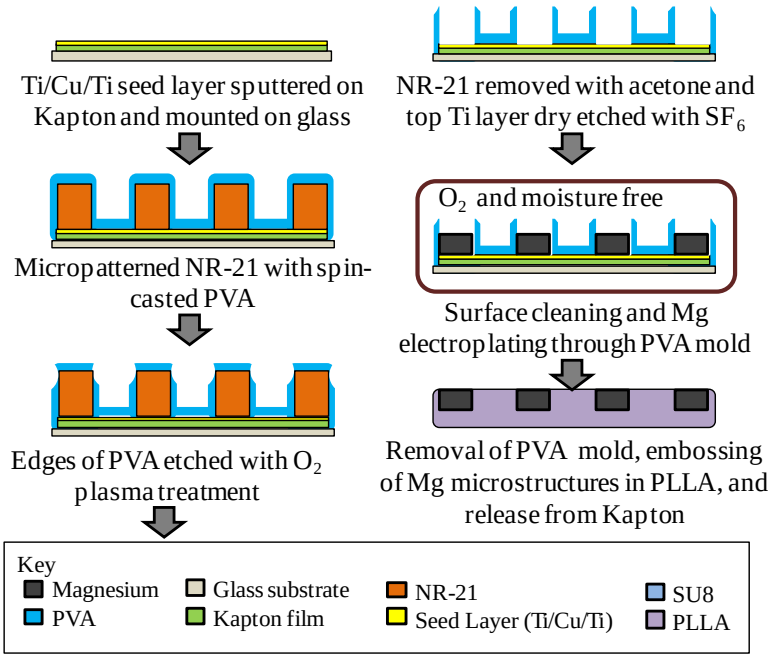

Figure 17 Fabrication scheme of Mg electroplating through water-soluble PVA molds. Microstructures electroplated through PVA are released from a polyimide (Kapton) substrate and transferred to a biodegradable polymer.

2.1.8. Characterization of Magnesium Electrodeposited Through Water Soluble Molds

Unlike traditional photoresists for electroplating, which are susceptible to swelling and dissolution in solvent, we selected a water-soluble material, PVA, for the micropatterning of solvent-resistant molds for Mg electroplating. Using embossing technologies, electroplated Mg microstructures were transfer molded into a biodegradable polymer. Magnesium microstructures electrodeposited through PVA molds and released and embedded into PLLA are shown in Figure 2.12. The presented PVA molds are 75 µm in height and 100 µm in width. Dimensions of the micropatterned PVA are determined by the corresponding NR-21 molds. Magnesium structures with thicknesses in the 10 to 100 µm range have been electroplated through micropatterned PVA molds. Thickness of the Mg microstructures was determined by PVA mold height, which was, in turn, limited by thickness of the corresponding NR-21 template. However, this issue may be resolved by replacing NR-21 with thicker negative tone resist (e.g., AZ 125 nXT), which can achieve thicknesses in the hundreds-of-microns range. Magnesium electrodeposited through the PVA molds

exhibited uniform thickness across the microstructure, with no dendritic plating observed at the PVA borders (Figure 18b). The presented Mg microstructures were electroplated through a water-soluble PVA mold and onto a flexible polyimide substrate, in comparison to chemically-resistant SU-8 mold and rigid glass or silicon substrate, to promote the use of Mg electroplating for biodegradable MEMS applications. SU-8, glass, and bulk silicon are not biodegradable materials and their post-plating removal requires either extensive dry etching with oxygen plasma or exposure to corrosive, wet chemicals [131]–[133]. While these processing techniques are common to the microfabrication of traditional MEMS, they are less suitable for the processing of biodegradable MEMS, which are susceptible to corrosion and highly sensitive to chemical and physical conditions. Moreover, prolonged exposure to the solvent electroplating solution (i.e., greater than 4 hours) causes micropatterned SU-8 molds to swell, crack, and delaminate. This often causes adjacent electroplated Mg to either crack or delaminate and places an upper limit on the electrodeposition time per sample. Polyvinyl alcohol overcomes the limitations observed with SU-8, as it is soluble in water and poorly soluble in solvents. It was experimentally verified that micropatterned PVA molds can withstand immersion in the electroplating solution for over 24 hours. Consequently, the PVA molds demonstrated greater chemical resistance to the electroplating solution than SU-8 and ease of removal after Mg electrodeposition by solubilizing in water. This can be shown by the integrity of the PVA mold and removal of the PVA post-plating in Figure 18b-c, respectively. Further, Mg electroplated through PVA molds did not exhibit any cracking.

An alternative approach to water-based PVA removal is by dry etching with oxygen plasma. The spin-casting conditions for the PVA were determined such that the PVA does not entirely fill the trenches created by the micropatterned NR-21. Instead, the PVA coated the bottom substrate and sidewalls of the NR to render a U-shaped horseshoe cross section (Figure 17). Hence, a larger surface area of the PVA mold is exposed and the etch depth for complete removal of the PVA is less than that of corresponding SU-8 molds, which feature filled rectangular cross sections. Due to differences in geometry and chemical composition,

complete removal of the PVA mold by reactive ion etching can be achieved in 20 minutes with a 5:1 ratio of O_2 and CHF_3 gases, whereas dry etching of corresponding SU-8 molds requires over 1 hour of processing.

The electrodeposition of Mg onto a flexible polyimide substrate facilitated metal-transfer-molding of the Mg microstructures to a biodegradable substrate. After removal of the PVA mold, the Mg microstructures were embossed into PLLA (Figure 18d). Constant pressure and temperature were applied to the embossed Mg/PLLA construct and after the embossing process, the Mg/PLLA was removed from the non-degradable polyimide by peeling off the flexible substrate. As the Cu and Ti seed layers selectively adhere to the polyimide film due to surface energy principles, no subsequent processing was required to remove these non-degradable metals from the Mg/PLLA construct. EDX analysis indicated that the PLLA embossing process increased oxidation on the electroplated Mg surface by 15%, but did not affect elemental composition of the bulk Mg film. Poly-L-lactic acid (PLLA) was selected as the encapsulation material for proof-of-concept because it is an FDA-approved, commercially-available, and well-studied biodegradable polymer. Microfabrication with PLLA has also garnered interest from the bioMEMS community in recent years [14], [18], [28]. It should be noted that alternative biodegradable polymers may be used for the embossing and encapsulation of Mg. Moreover, the electrodeposition of Mg microstructures through PVA molds and onto polyimide is a modular fabrication process that can be integrated with the prior or subsequent micropatterning of additional biodegradable elements (e.g., Zn, Fe). The PVA molds and flexible substrate provide a versatile approach for the fabrication and integration of electroplated Mg for biodegradable MEMS applications.

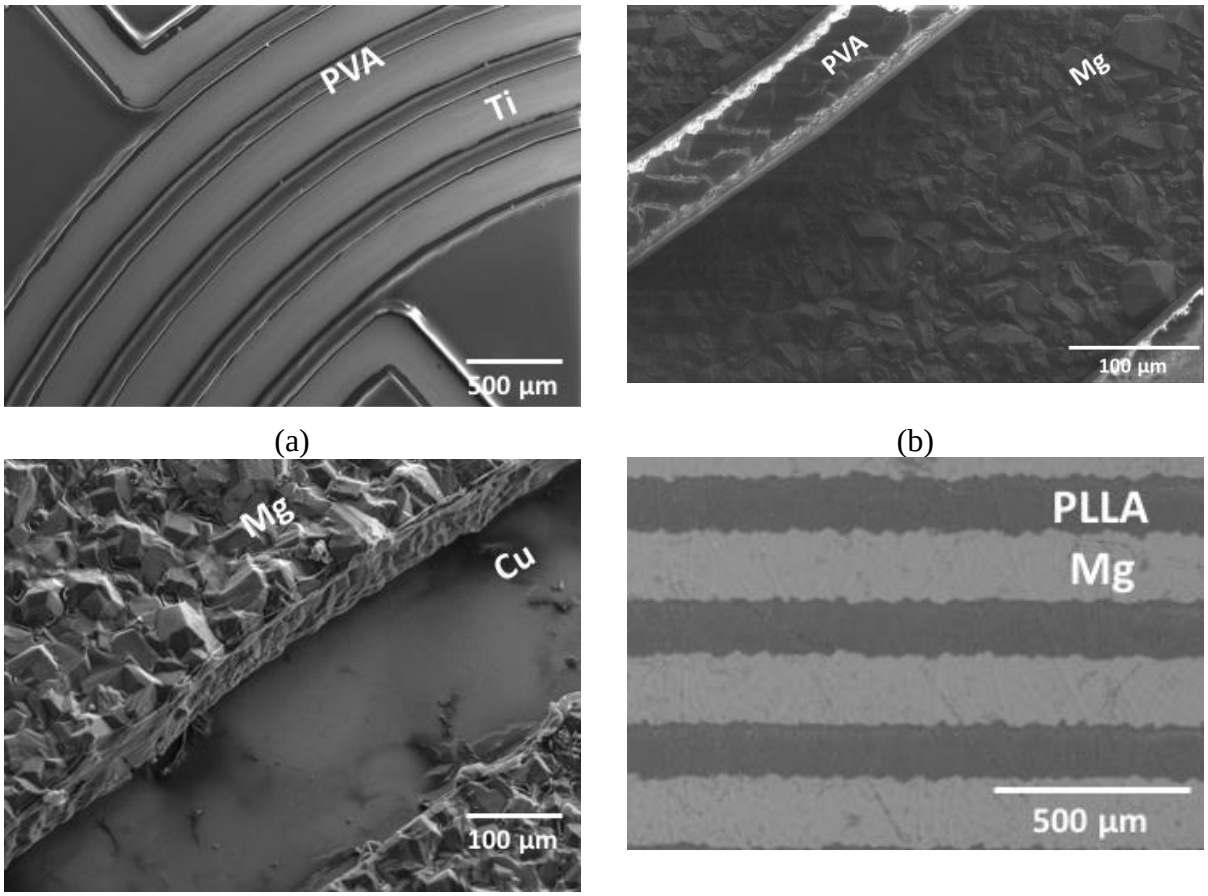

Figure 18 SEM images of (a) microfabricated water-soluble molds using PVA, (b) electroplated Mg through PVA molds, (c) electroplated Mg after mold removal, and (d) bottom of electroplated Mg after embossing into PLLA and removal from substrate. Image obtained using VP-mode at 30 Pa and backscatter electron detector.

2.1.9. Achieving Finer Feature Sizes with Electroplated Mg

While the PVA-based fabrication process supported the through-mold plating of Mg and subsequent mold removal, the processing capability limited the patterning resolution to the order of tens-of-microns (i.e., feature width and thickness). In order to achieve finer feature sizes, electroplating through a silicon dioxide mold, deposited by plasma-enhanced chemical vapor deposition (PECVD) and patterning by dry etching through a lithographically-define photomask, was implemented. The oxide mask was 500 nm in thickness and conventional CMOS processing supported patterning capability and subsequent Mg deposition down to 3 µm in resolution. Further, dry etching with a fluorine-based plasma

(e.g., sulfur hexafluoride (SF_6)) can also remove the oxide mold after Mg deposition without distorting the plated film.

Since Mg electrodeposition is isotropic and the plated film thickness exceeded that of the oxide mask, lateral film growth also occurred. For example, Figure 19b shows the SEM image of electroplated Mg in a chevron pattern, where the feature width of the oxide mask was 7 μm and the plated feature width was 13 μm. The film thickness was 2.5 ± 0.5 μm; the variability was due to surface roughness. The minimum line width achieved was 4 μm, which was 1 order of magnitude smaller than what had been demonstrated with PVA-molds. Elemental analysis (data not shown) confirmed that the plated film was 97% magnesium and 3% oxygen. The results not only support the use of oxide molds for electroplating finer Mg features, but also indicate that the PVA and oxide molds each harbor their respective advantages in through-mold Mg electrodeposition based on the intended feature dimensions and design.

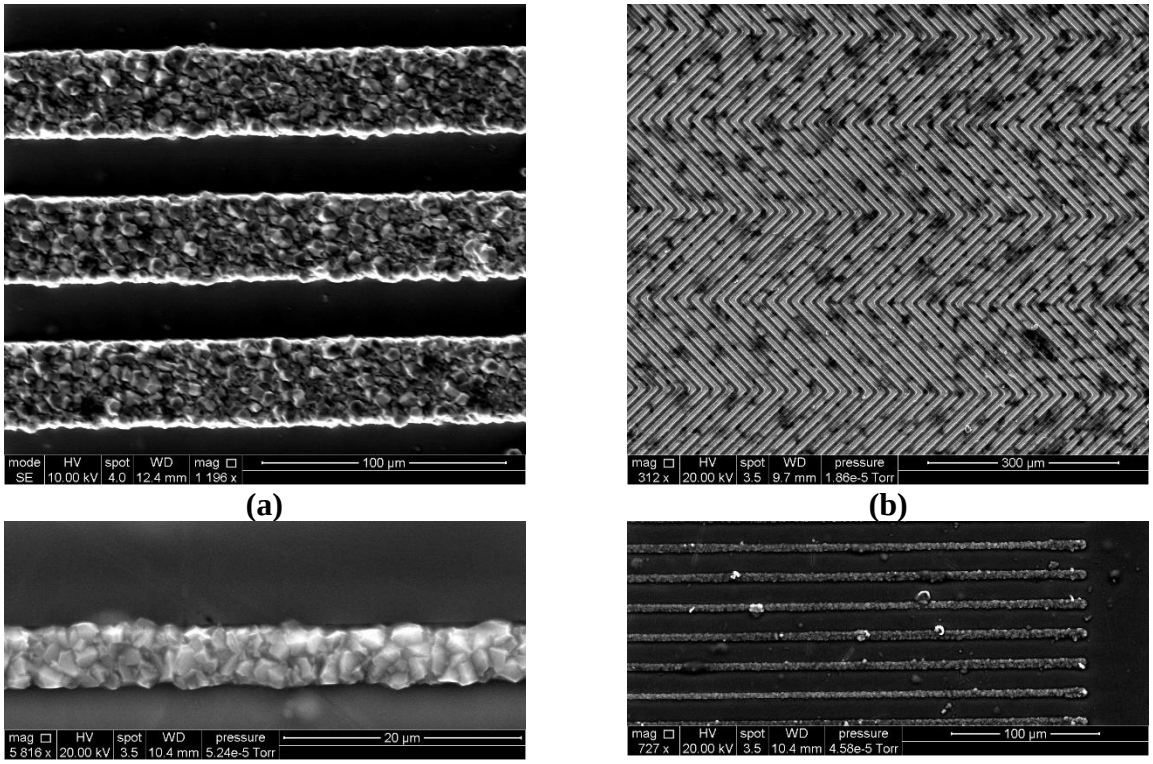

(a) **(b)**

(c) **(d)**

Figure 19 SEM images of Mg electroplated through a silicon dioxide mold, where lateral plating was permitted and finer feature sizes, compared to through-mold plating with SU-8 and PVA molds, were achieved.

2.1.10. Degradation Behavior of Electroplated Magnesium

The degradation characteristics of the electroplated Mg were evaluated electrochemically by potentiodynamic characterization. Tests were performed with a potentiostat (WaveDriver 10, Pine Instruments) in physiological saline, wherein samples were immersed in the solution for five minutes before testing to come to equilibrium. A three-electrode-cell configuration was implemented with Mg, platinum and silver/ silver chloride (Ag/AgCl) as the working, counter and reference electrodes, respectively. Open circuit potentials (OCP) were recorded and linear sweep voltammetry was performed for a 1 V range centered at the measured OCP at a scan rate of 5 mV/s. Tests were conducted in

phosphate-buffered saline (1x PBS) to emulate the physiological environment and to maintain the solution at the physiological pH (7.4).

Figure 20 shows the polarization curves of electroplated Mg compared against commercial Mg foil. Electroplated Mg demonstrated a corrosion potential of -1.55 V *vs.* SHE, whereas commercial Mg foil showed a corrosion potential of -1.31 V. The difference in corrosion potential suggested that the electroplated Mg has a greater tendency to corrode than commercial foil. This may be attributed to the larger grain size of electroplated Mg, as studies have found that increased surface roughness contributes to increased pitting corrosion in Mg and its alloys. Further, this may be attributed to the native passivation layer that forms on the Mg surface, which comprises magnesium hydroxide ($Mg(OH)_2$) in aqueous environments. The passivation film is more continuous on a smooth surface and, hence, provides greater protection against corrosion [90]. This agrees well with theory, where the differences between the standard electrode potential and corrosion potential are attributed to surface effects and oxide formation. Specifically, the corrosion potential depends not only on the tendency of the metal to dissolve in solution (i.e., standard electrode potential), but also the formation, solubility and stability of a passivating oxide film. Interestingly, electroplated Mg showed a lower corrosion rate than commercial Mg foil. Polarization curves indicated a corrosion current of 0.32 $\mu A/cm^2$ and 0.45 $\mu A/cm^2$ for electroplated Mg and commercial Mg foil, respectively, and was attributed to the differences in corrosion rates between nanocrystalline and polycrystalline materials. The fluctuations observed in the anodic curves were attributed to the pitting nature of Mg corrosion, which manifests in the repeated breakdown and formation of the passivation layer. These findings suggested that the corrosion properties of electroplated Mg slightly differ from that of commercial Mg foil. The corrosion resistance of the electroplated Mg may be enhanced by reducing surface roughness, such as by chemical-mechanical polishing or electrochemical polishing, or by surface passivation techniques [2], [36].

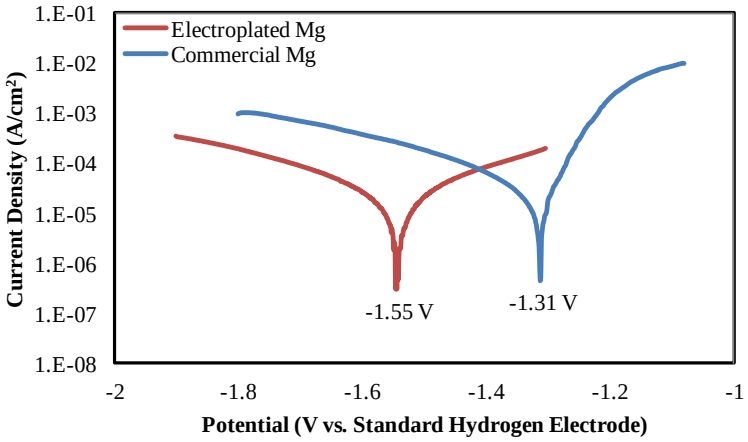

Figure 20 Corrosion evaluation of electroplated and commercial Mg based on potentiodynamic testing of samples in phosphate-buffered saline (1x PBS).

2.1.10. Comparison of Magnesium Fabrication Processes

Table 4 summarizes the advantages and limitations of the three investigated magnesium microfabrication technologies. Laser cutting and chemical etching represented subtractive approaches to the micropatterning of magnesium. Laser cutting demonstrated the smallest feature size and, in comparison to chemical etching, is amenable to sharp (i.e., non-rounded) features. However, the quality of the laser cut structures was limited by redeposition of oxidized debris on the sidewall. Chemical removal of the redeposition reduces the thickness of the structure and increases the roughness of exposed surfaces and sidewalls. Chemical etching provided a batch process for the micropatterning of magnesium with clean, sloped sidewalls. Results from etching were less uniform than that of laser cutting and electroplating, with the outermost regions and non-rounded features etching more quickly. Further, the quality of the starting magnesium material affected the results of chemical etching and the minimum feature size was also limited by the isotropy of the etchant.

Through-mold electroplating provided an additive approach for magnesium micropatterning at thicknesses that exceed what is achievable with sputtering and evaporation. In contrast to laser-cutting and chemical etching, through-mold electroplating provides magnesium microstructures with clean, vertical

side walls. Further, the additive approach of electroplating is more amenable to the microfabrication of non-planar microstructures. The minimum feature size is limited by the lithographic patterning of the electroplating mold and by the grain size of the plated material. However, grain size and surface morphology may be controlled by the electroplating parameters and electrolyte composition. This study reports preliminary results for the through-mold electroplating of magnesium. As the electrodeposition takes place in a non-aqueous solution, negative photoresists commonly used for electroplating molds were incompatible with this approach. The mold material must withstand long-term immersion in a solvent without solubilizing or substantial swelling. In addition, the electroplating process must take place in an oxygen- and moisture- free environment.

Further, the non-aqueous electrodeposition of Mg can be adapted for the development of biodegradable microstructures for MEMS devices. The fabrication process and materials were developed to overcome the chemical reactivity, susceptibility to corrosion, and aggressive electrodeposition conditions of Mg. Magnesium electroplated from $AlCl_3$-enhanced magnesium-based electrolyte solution showed negligible aluminum (i.e., <1%) and comparable elemental composition to that of commercial Mg foil. Further, through-mold electroplated Mg exhibited similar crystal orientation, electrical resistivity, and corrosion potential to that of commercial Mg, and supported direct MEMS integration and development of completely biodegradable constructs. The results, from material analyses, fabrication compatibility, and application to bio-MEMS, underscore the utility and advantages of magnesium and, in particular, the through-mold electrodeposition of Mg for the development of biodegradable MEMS.

Table 4 Summary of the three approaches for microfabrication with magnesium.

	Laser-cutting	**Chemical etching**	**Electroplating**
Type	Subtractive	Subtractive	Additive
Obtained feature size	width $w = 80 \pm 5$ μm gap $g = 20 \pm 5$ μm thickness $t = 70$ μm*	$w = 160 \pm 10$ μm $g = 140 \pm 10$ μm $t = 70$ μm*	$w = 4 \pm 0.5$ μm $g = 4 \pm 0.5$ μm $t = 3.0$ - 50 μm
Roughness	1.4 μm	0.2 μm	3.2 μm
Electrical resistivity**	5.3 μΩ·cm	5.3 μΩ·cm	8.7 μΩ·cm
Advantages	• Finer feature size • Amenable to designs with sharp (i.e., non-rounded) features	• Clean sidewalls (positive slope) • Batch process	• Control of material grain size based on plating conditions • Batch process • Broad range of feature sizes
Limitations	• Redeposition on sidewall; chemical removal is isotropic and reduces thickness of structure • Serial process	• Isotropic etching limits minimum achievable feature widths • Less uniform; etches outermost features (i.e., outer turns of a coil) and sharp features more quickly	• Requires deposition within an oxygen- and moisture- free environment • Mold material must withstand long-term immersion in solvent; prohibits use of many common photoresists

** On 70-μm-thick commercially available magnesium foil*

*** For reference, the electrical resistivity of bulk magnesium is 4.4 μΩ·cm [9]*

2.2. Passivation Schemes for the Corrosion Protection of Magnesium

2.2.1. Introduction

The micropatterning, integration and characterization of magnesium was established in the previous section to support the use of magnesium in implantable, biodegradable devices. Despite its desirable properties, Mg exhibits a fast degradation rate under physiological conditions [96], [109], [135], [136]. Traditional methods for hindering Mg corrosion, such as those employed in automotive

manufacturing, are largely incompatible with physiological applications. The surface modification of Mg, either by modifying or depositing a passivation coating, often incorporates chemical elements that are toxic and not biocompatible or require a thickness on the order of hundreds of microns, which detract from the passivation strategy's appeal for Mg structures that are only a few microns to tens-of-microns in thickness. Common protective approaches for magnesium include electrochemical plating, conversion coatings, anodizing, physical vapor deposition and organic coatings [89], [137].

Electrodeposited coatings of copper-nickel-chrome (Cu-Ni-Cr), electroless nickel (Ni) and nickel-gold (Ni-Au) have been explored in computer and consumer electronic applications. It should be noted that the ambient environment, to which consumer electronics are exposed, presents milder corrosion conditions than the *in vivo* physiology [89]. The improved wear resistance, solderability and stable electronic contacts afforded by Ni-based coatings has promoted their use for Mg corrosion protection. However, these coatings are neither biocompatible (e.g., Cu, Ni and Cr) nor biodegradable (e.g., Au). Further, a series of pre-treatment and activation steps must be performed prior to the electrodeposition of the aforementioned coatings because it is difficult to directly plate onto Mg due to its high reactivity. Magnesium may form a passivating hydroxide layer or undergo chemical dissolution in aqueous electrolytes [135]. This may result in poorly adhered coatings and precludes the use of most acidic electrolytes for the deposition process [138]. Lastly, the electrodeposited films must be pore-free in order to prevent galvanic coupling of the Mg with the coating metal, which is more noble than Mg and would, therefore, accelerate Mg corrosion. A minimum coating thickness of 50-100 μm has been recommended for Cu-Ni-Cr coatings.

Conversion coatings are formed by chemical or electrochemical treatment to produce a superficial layer that is chemically bonded to the substrate surface. Conversion coatings on Mg, which include metal oxides, chromates and phosphates, hinder Mg corrosion either by serving as a low solubility barrier or by containing corrosion inhibiting compounds [89], [138]–[140]. The toxicity of conversion solutions, however, detracts from their use in physiological applications. For example, conventional conversion

coatings feature chromium-based compounds, which can be toxic and carcinogenic.

Anodization has served as an alternative approach to conversion coatings for the corrosion protection of magnesium [141]–[143]. The anodization process produces a stable oxide film with a cellular structure at the metal-coating interface. The pore size and wall thickness are determined by the electrolyte composition, temperature, current density and applied voltage during anodization. The pores are subsequently sealed by precipitation of the hydrated metal species inside the pore (i.e., $Mg(OH)_2$) to achieve a corrosion resistant film [141]. As with most electrochemical processes, the quality of the film depends on the initial surface morphology of the Mg substrate, such as its surface defects, porosity and roughness, because these factors impact the throwing power and film adhesion. While thicker films may be desired for pore-free coverage of the Mg surface, increasing thickness can detract from the fatigue strength due to localized heating during the anodization process. Further, the brittle nature of the ceramic film often necessitates a top coat, such as paint, for mechanical robustness. There are several commercial processes for the anodization of Mg, such as the Dow 17 and Anomag processes, which form $NaMgF_3$ and MgO-$Mg(OH)_2$ films, respectively [89].

Thin film barriers, such as those deposited by physical vapor deposition techniques, and organic encapsulation will be discussed in the subsequent section because, unlike electrodeposition and anodization, these methods are largely substrate-independent. The deposition, morphology and quality of the deposited film does not significantly depend on the underlying substrate and, hence, are classified as encapsulation techniques rather than Mg passivation strategies in the context of this work.

While many of the industrial passivation strategies are ill-suited for biodegradable purposes, the general structure of electrodeposition techniques can still be applied [89], [96], [99], [100], [138], [144], [145]. A schematic of the electrodeposition process is presented in Figure 21. The process typically begins with degreasing Mg foil with organic solvents, followed by chemical-mechanical polishing of the Mg surface to remove any surface non-uniformities or defects. Next, acid pickling in a dilute enchant is performed to roughen the surface and remove any native oxide/hydroxide film that may have formed. The

Mg substrate is then activated in a chemical solution, commonly fluoride-based, to render the Mg surface less susceptible to re-oxidation [89], [146]. Finally, zinc is optionally electrodeposited onto the Mg surface prior to deposition of the target passivation material to render the exposed surface more chemically-resistant to acidic environments, as many electroplating solutions are [138], [147], [148]. The first 3 preparation steps (i.e., degreasing, polishing and chemical etching) were employed in the previous section for the micropatterning of commercial Mg foil [89]. Given that fluoride- and zinc-based chemistries are physiologically tolerated, the use of related passivation schemes are contemplated in this section for the biocompatible, biodegradable passivation of Mg.

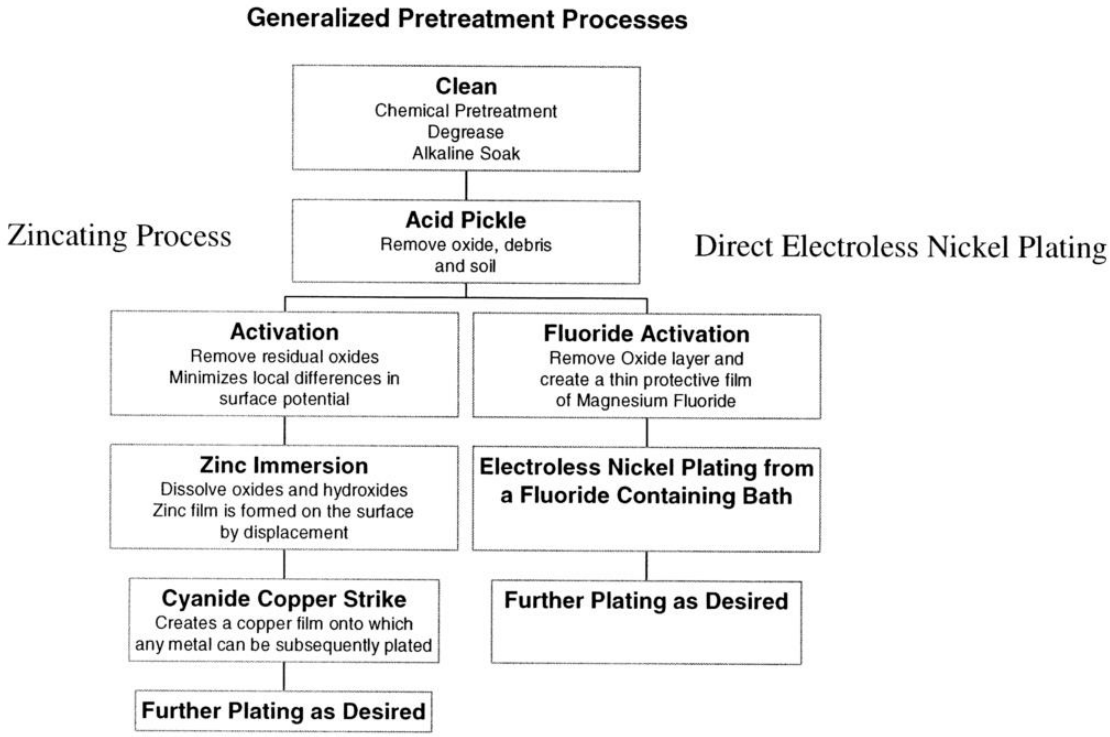

Figure 21 Schematic illustrating the conventional surface treatment process prior to electrodeposition on Mg [89].

Zinc is a biodegradable metal that exhibits slower degradation kinetics than magnesium [79], [96], [148], [149]. Biodegradable devices comprising laser micromachined and electroplated Zn have been demonstrated in literature [80], [96]. Hiebl *et al.* fabricated a biodegradable coronary stent by laser

micromachining commercial Zn foil. Biological testing revealed the complete degradation of the Zn-based stent after 100 days in blood serum [150]. Luo *et al.* demonstrated a biodegradable passive wireless pressure sensor featuring electroplated Zn as the sensor conductor material. A mesh layer of iron was evaporated onto the surface of the Zn conductor so that the galvanic coupling and, hence, degradation rate of the Zn can be controlled by the area ratio of the Zn and Fe bi-layer. In this manner, the degradation of Zn was reduced from the timescale of a couple of years to a few days. The Zn conductors were approximately 60 µm in thickness and electrodeposited in an acid chloride electrolyte bath [79], [80]. Although Zn electrodeposition is most commonly performed in an acid chloride bath, the electrolyte would react violently with Mg [138].

Studies have successfully electroplated Zn in ionic liquids and heated alkaline electrolytes [138], [151], [152]. These investigations were performed to obtain a viable deposition process on Mg. Ionic liquids are non-aqueous and, hence, do not corrode or react with Mg. Further, ionic liquids are stable in air and water, enabling their using under ambient conditions. An ionic liquid-based electrolyte typically contains an amine salt, a hydrogen bone donor or metal halide, and a Zn-based salt [148], [151]. For example, Bakkar *et al.* selected choline chloride, urea and zinc chloride as the electrolyte and investigated the effect of direct versus pulse current electrodeposition. Results indicated that direct current densities corresponded to porous, granular deposits, whereas pulse current densities produced finer microstructures and improved adherence. However, cross-sectional imaging revealed that pulse current deposited Zn contained micro-cracks that propagated perpendicular to the coating. The findings were similarly observed during electrochemical corrosion testing, where cracks manifested as negligible improvements to the corrosion rate [152].

Zhang *et al.* successfully electrodeposited Zn onto Mg substrates in a heated alkaline electrolyte after initial conversion and activation steps. Briefly, the process begins with a stannate conversion coating, which yields a porous $MgSnO_3 \cdot H_2O$ layer that is nanoscale in thickness, and activation in concentrated hydrofluoric acid buffered with ammonium fluoride. The conversion and activation steps improve the

quality of the subsequently deposited Zn film by providing a porous and electriferous surface [138]. The enhanced surface roughness improves film adhesion by increasing the interfacial surface area [153]. The pretreatment also enhances the surface wettability through the presence of hydrophilic polar groups. Scanning electron micrographs showed that the electrodeposited Zn was non-porous, compact and uniform with an average grain size of 1-2 μm. Despite the tin-based conversion layer, only Zn was detected by x-ray diffraction (XRD) when Zn coatings thicker than 10 μm were deposited. Linear sweep voltammetry confirmed the effectiveness of Zn as a corrosion protection layer because the potentiodynamic sweeps approximated that of pure commercial Zn rather than modular improvements to that of Mg. Specifically, the passive region characteristic of Zn was observed until the pitting potential was reached. Further, Zn coatings corresponded to lower corrosion rates and increased the corrosion potential by approximately 400 mV [138].

Electrochemical modeling of Zn-coated Mg was obtained by electrochemical impedance spectroscopy (EIS). The equivalent circuit model representing the electrochemical corrosion of Zn-coated Mg is shown in Figure 22 and agreed well with experimental results. The passive elements of the circuit can be correlated to the physical phenomenon of the electrochemical system. The solution resistance (R_s) reflects the electrolyte conductivity and electrode distance between the reference and working electrodes, whereas the charge transfer resistance (R_{CT}) corresponds to the Zn-coated Mg's susceptibility to corrosion; the higher the charge transfer resistance, the less susceptible. A constant phase element (CPE) is commonly used in place of a capacitor because the capacitive reactance of electrochemical systems does not always scale linearly with frequency. The inductor (L) and inductive resistance (R_L) correspond to the pitting phenomenon observed with Mg corrosion [138].

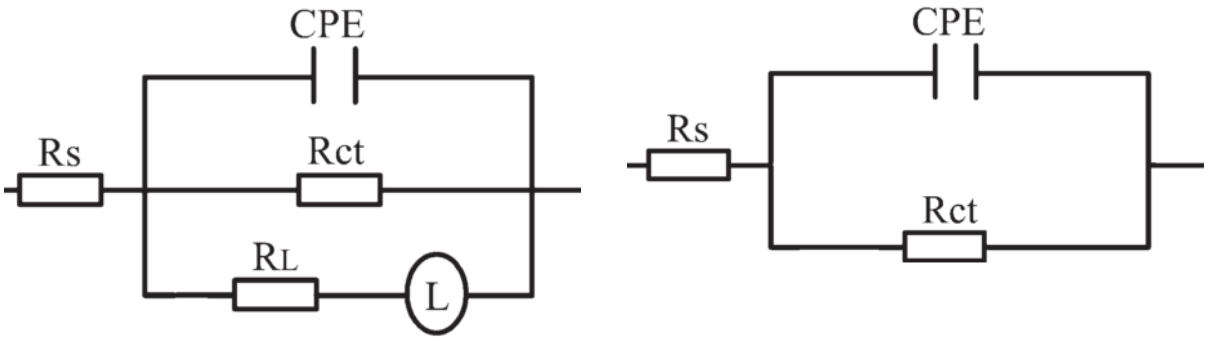

Figure 22 Equivalent circuit model capturing the electrochemical corrosion of (a) pure Mg and (b) Zn-coated Mg in 3.5 wt.% sodium chloride [138].

The electrodeposition parameters control the morphology and, in turn, the corrosion properties of the Zn film. It was previously speculated that nanocrystalline film would exhibit a higher corrosion rate than a corresponding polycrystalline layer due to the larger volume fraction of inter-crystalline defects (e.g., grain boundaries) [153]. However, it was experimentally observed that nanocrystalline Zn featured a slower corrosion rate than polycrystalline Zn. This was attributed to the improved homogeneity of the nanocrystalline Zn film. The polycrystalline and nanocrystalline Zn were both electrodeposited, but pulse current densities were implemented in the case of nanocrystalline Zn. Scanning electron images showed the stark contrast in surface morphology of the two Zn samples, suggesting that grain size alone did not account for the differences in corrosion behavior. In addition, the results highlight the design window for further improving the corrosion resistance of Zn coatings on Mg and the importance of optimizing the coating for a designated type of Mg substrate and corrosion medium [147], [153].

Towards a more biomimetic passivation scheme, hydroxyapatite (HAP) has been explored to hinder the degradation kinetics of Mg [144], [145], [154]–[160]. Hydroxyapatite is a ceramic material comprising calcium phosphate and is native to bone. Biological testing *in vitro* demonstrated that HAP is not only biocompatible, but also bioactive; HAP has been shown to promote osteogenesis and osseointegration [161], [162]. Given the proposed goal of demonstrating a biodegradable, implantable device for monitoring bone fracture healing, a bone-like material that offers both corrosion protection and

promotion of bone regeneration would be ideal. Hydroxyapatite can be deposited by sol-gel and electrophoretic processes, as well as by spray-coating and electrodeposition [144], [155], [160], [163]. Electrodeposition is typically preferred due to its ease of implementation, low cost and ability to coat irregular geometries. The resulting HAP film is typically tens-of-microns in thickness and sintered at elevated temperatures ($T > 1150^{\circ}C$) [144], [145], [157], [158], [164]. Unlike Mg and Zn, HAP is not electrically conductive and its electrodeposition proceeds by a series of chemical reactions. Depending on the electrolyte composition and deposition parameters, one of the 4 types of calcium phosphate can be formed. In order of increasing solubility, the calcium phosphate types are hydroxyapatite ($Ca_{10}(PO_4)_6(OH)_2$), TCP ($Ca_2(PO_4)_3 \cdot nH_2O$), OCP ($Ca_8H_2(PO_4)_6 \cdot 5H_2O$ and DCPD or brushite ($Ca(HPO_4) \cdot 5H_2O$). As can be seen, HAP is the most stable form of calcium phosphate, as it possesses the slowest dissolution rate in aqueous media. The net chemical reaction describing HAP formation is given by [144], [145]:

$$10\ Ca^{2+} + 6\ PO_4^{3-} + 2\ OH^- \rightarrow Ca_{10}(PO_4)_6(OH)_2$$

During the electrodeposition, hydroxyl ions formed at the cathode increases the local pH and induces the precipitation of phosphate ions due to acid-base reactions. The phosphate ions react with calcium ions to form DCPD on the cathode surface. Alkaline treatment subsequently converts the DCPD into HAP. During this treatment, HAP is converted from DCPD based on the following reaction [144]:

$$10\ CaHPO_4 \cdot 2H_2O + 12\ OH^- \rightarrow Ca_{10}(PO_4)_6(OH)_2 + 4\ PO_4^{3-} + 30\ H_2O$$

Pulse current densities are often preferred for HAP electrodeposition. In the case of constant current, polarizations in the concentration is formed due to the slow speed of ion diffusion from the bulk electrolyte to the substrate surface. Further, hydrogen evolution due the reduction of water occurs on the cathode surface and is exacerbated with direct current deposition [157], [164]. The effect of pulse current deposition is not unilaterally positive, however. Wang *et al.* obtained calcium-deficient HAP by electrodeposition under pulse current conditions, which corresponded to faster HAP dissolution and,

thereby, faster Mg degradation. The calcium-deficient HAP exhibited higher shear strength than traditional HAP (i.e., 41.8 MPa versus 14 MPa, respectively), which better approximated that of cortical bone (i.e., 35 MPa). The authors speculated the improved mechanical performance was due to the reverse pulse deposition and the Mg^{2+} substitution (for the Ca^{2+} deficiency) which might have dislodged loose HAP particles and improved HAP-Mg integration, respectively [157]. Wei *et al.* further examined the mechanical properties of HAP and experimentally determined that the linear coefficient of thermal expansion (CTE) is 13-15 με/K for HAP. For reference, the CTE of Mg and Zn are 25 and 30, respectively [155].

Fluorinated hydroxyapatite (FHA) has shown better corrosion protection and bioactivity than traditional HAP [144], [146], [162]–[167]. The former is attributed to the improved film coating on Mg because studies have found that Mg ions inhibit HAP crystallization and result in fragile flake-like morphology. For example, the calcium-deficient HAP obtained by Wang *et al.* exhibited two morphologies, one of which was irregular flakes that were approximately 100 nm in diameter. Some of the flakes had even grown perpendicular to the film surface. Adjacent flakes occasionally fused together, rendering macro-sized pores in the crevices. The second morphology was a fine acicular structure indicative of newly formed crystal nuclei [157]. Song *et al.* similarly observed the flake-like morphology in DCPD and HAP in a study comparing the degradation of DCPD, HAP and FHA. In contrast, SEM images of FHA showed two layers. The inner layer comprised closely packed, columnar structures with hexagonal cross-sections approximately 100-200 nm wide; the external layer was more irregular and larger in morphology. After 2 weeks of immersion in SBF, DCPD showed mainly $Mg(OH)_2$ peaks during XRD analysis, whereas HAP and FHA retained their characteristic peaks even after 1 month of immersion. However, HAP also exhibited $Mg(OH)_2$ peaks. Measurements of hydrogen gas evolution further supported that FHA possesses the slowest degradation [144].

The degradation of FHA- and HAP-coated Mg differs from the galvanic corrosion of Mg protected by metallic coatings. Briefly, additional apatite is formed after immersion in SBF that further decreases Mg

degradation. The negative surface charge presented by hydroxyl and phosphate groups interact with calcium ions in SBF to form calcium-rich amorphous calcium phosphate (ACP). The newly formed layers possess a positive surface charge that interacts with phosphate ions in SBF to form calcium-poor ACP. Crystallization results in bone-like apatite. The replacement of hydroxyl ions with fluoride ions in FHA increases the negative surface charge because fluoride ions are more electronegative and have smaller ion radii. The enhanced negative charge of FHA more strongly attracts calcium ions in solution and, ultimately, promotes the nucleation of bone-like apatite more so than traditional HAP [144], [168].

The slower degradation of FHA, in turn, provides a more favorable environment for osseointegration. Figure 23 shows a conceptual schematic of how FHA promotes osseointegration. Li *et al.* observed higher cell proliferation after 2-3 days of cell culturing compared to traditional HAP, as well as enhanced osteoblast differentiation in human bone marrow stromal cells (hBMSC). The bioactivity of FHA is particularly beneficial because implanted Mg, such as bone screws and bone plates, have shown hydrogen gas buildup and fibrous encapsulation in the implant area due to fast corrosion. The slower corrosion and osseointegration provided by FHA coatings can overcome these limitations that could otherwise result in loose connection of the implant to the tissue [162].

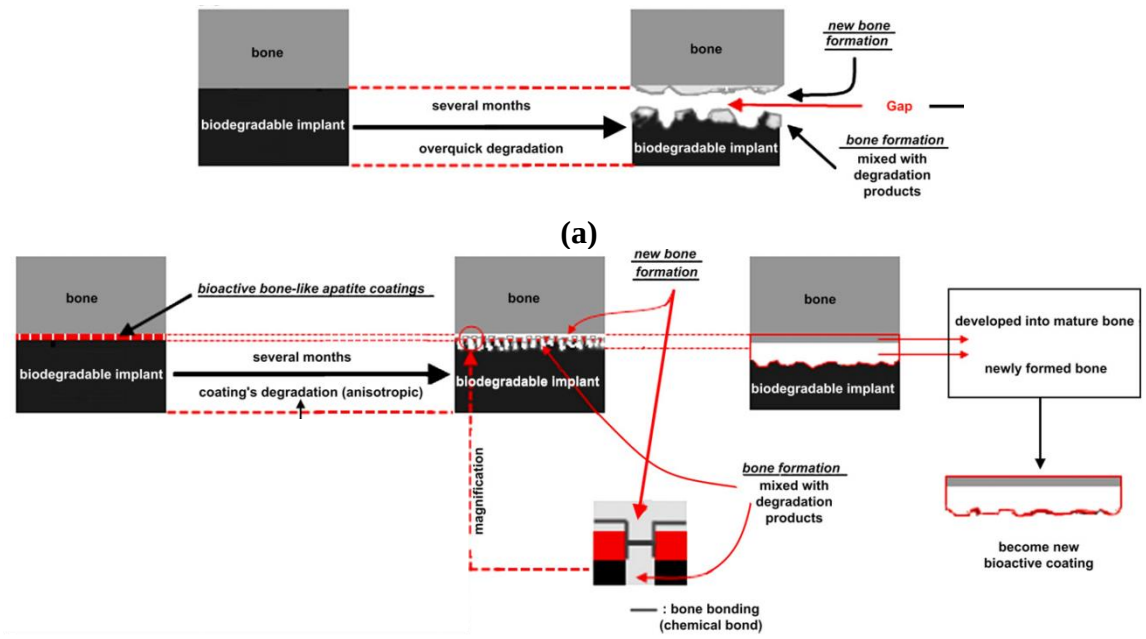

Figure 23 Schematic illustrating bone formation with (a) pure Mg and (b) apatite-coated Mg implants [162].

The primary difference between FHA and HAP electrodeposition is the addition of a fluoride-based salt to the electrolyte [144], [146], [164]. The most commonly used salt is sodium fluoride (NaF), an additive in commercial mouthwash that is also biocompatible. The chemical structure of electrodeposited FHA is $Ca_5(PO_4)_3(OH)_{2-x}F_x$, where x is determined by the concentration of sodium fluoride. Since fluoride ions are a good nucleation agent for hydroxyapatite, FHA deposition can be achieved in one single electrodeposition step, whereas HAP requires heated alkaline treatment [164]. The conversion reduces the weight and volume of the deposited film and increases the film stress. Fluorinated hydroxyapatite is formed by a series of reactions during electrodeposition. The net chemical reaction is shown below:

$$10\ (Ca^{2+}, Mg^{2+}) + 6\ PO_4^{3-} + x\ F^- + (2-x)\ OH^- \rightarrow (Ca, Mg)_{10}(PO_4)_6(OH, F)_2$$

Both calcium and magnesium ions are shown as reactants (in parentheses) because Mg can corrode in the electrolyte and become incorporated into the coating [146]. Another notable additive is hydrogen peroxide to reduce hydrogen gas formation and the corresponding gas pores and cracks in the deposited film. The

reduction of hydrogen peroxide competes with the reduction of water to form hydroxyl ions, but does not produce hydrogen gas as a product [144].

Electrochemical techniques offer a quantitative approach to characterizing Mg degradation under the context of metallic corrosion in an electrolyte. Linear sweep voltammetry (LSV) and electrochemical noise testing (ECN) provide different information about the corrosion process and will herein be explained [82], [90], [113], [169]–[171]. To understand the corrosion characterization afforded by these techniques, it is important to first introduce some fundamentals in electrochemistry. When an electrode is immersed into an electrolyte solution, an electrochemical double layer forms on the electrode surface that comprises inner and outer Helmholtz planes. Immediately beyond the double layer is the diffusion layer. A simplified schematic of this is shown in Figure 24. The Inner Helmholtz Plane (IHP) features the direct adsorption of ions or molecules to the electrode surface. Anions are more frequently found in the IHP because ions must shed their waters of hydration prior to adsorption to the electrode surface and negatively charged ions hydrate less strongly than positively charged ions. The Outer Helmholtz Plate (OHP) is the closest plane that solvated ions can approach to the electrode surface. The solution-side of the double layer is a region of non-uniform charge and forms a high electric field; the potential difference formed between the solution-side of the double layer and the metallic electrode contributes to what is known as the double layer capacitance. Under open-circuit conditions, the potential difference adjusts itself through the electron transfer (i.e., reactions) such that the rates of the forward and reverse reactions are equal. This potential difference serves as a reference point in the discussion of electrochemical kinetics [172], [173].

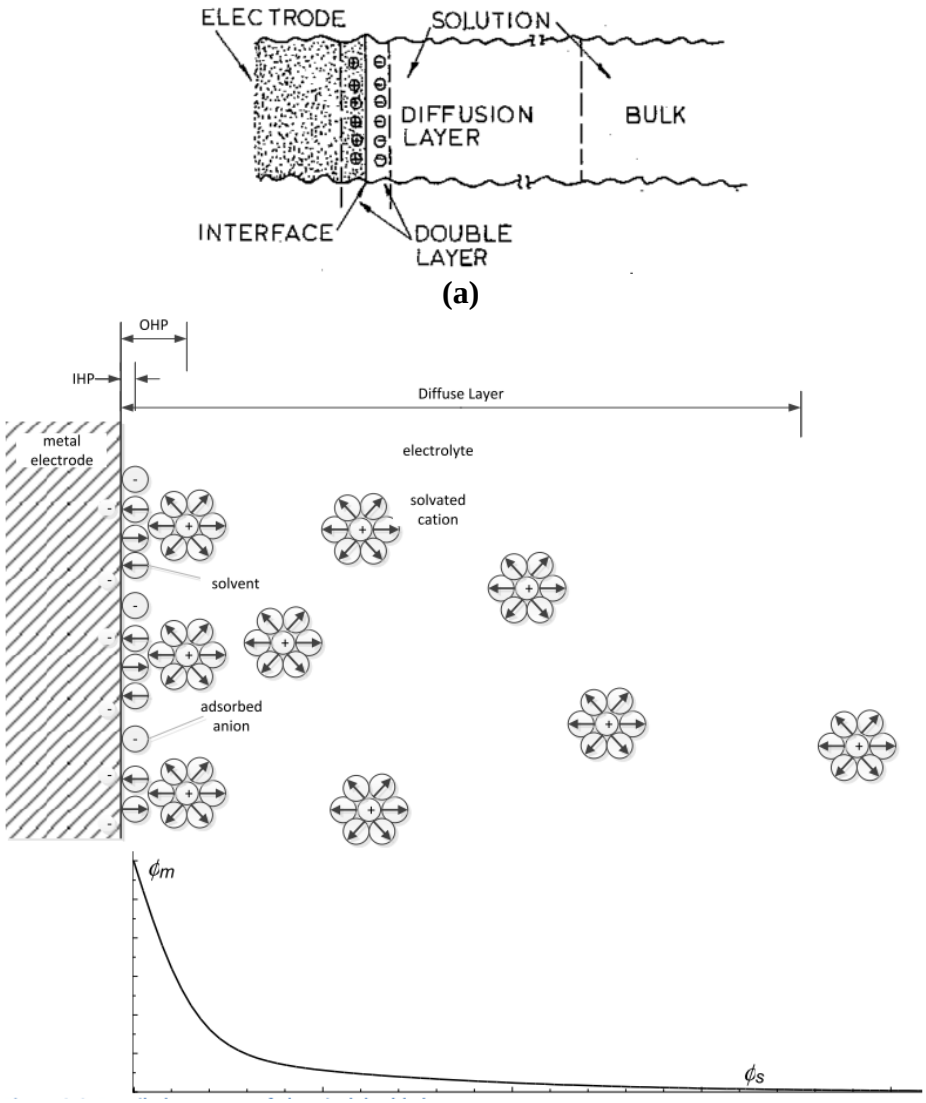

Figure 24 Schematic of the surface of an electrode immersed in an electrolyte [172].

The Butler-Volmer equations characterize the kinetics of electrochemical reactions [172], [173]. For reference, anodic currents are defined to be positive by convention. Given that the activation energy of a reaction depends on temperature and concentration, the reaction rate of a first-order elementary reaction is given by:

$$r = k_f c_0 = k_f^0 c_0 \exp\left(\frac{-\Delta G_f^{\ddagger}}{k_B T}\right) \tag{2.1}$$

where k_f, c_0, ΔG_f, k_B and T correspond to the rate constant, concentration of oxidized species, free energy difference between the initial reactants and the transition state, Boltzmann constant and temperature, respectively. A similar expression can be provided for the reverse reaction. A schematic of the energy change associated with a reaction on the electrode surface is provided in Figure 25. The activation energy of an electrochemical reaction can be changed based on the electrode potential. For example, the reduction reaction is favored at an electrode potential of E_1 because the energy of the reduced state is lower than that of the oxidized state. The converse is true at an electrode potential of E_2. The parameter β captures the fraction of the total energy change that impacts the cathodic activation energy and, consequently, (1-β) is the fraction that impacts the anodic activation energy. Hence, the free energy associated with the cathodic and anodic reactions can be expressed as:

$$\Delta G_c^{\ddagger}(E_2) = \Delta G_c^{\ddagger}(E_1) + \beta F \Delta E \tag{2.2}$$

$$\Delta G_a^{\ddagger}(E_2) = \Delta G_a^{\ddagger}(E_1) + (1-\beta) F \Delta E \tag{2.3}$$

The cathodic reaction rate can now be expressed as:

$$r_c(E) = k_c c_{ox} exp\left(-\frac{\beta F E}{k_B T}\right) \tag{2.4}$$

Where the activation energy at the reference potential ($\Delta G_c^{\ddagger}(E_1)$) is a constant that is incorporated into the rate constant. Applying Faraday's law gives the anodic and cathodic current densities as:

$$\frac{i_a}{F} = r_a(E) = k_a c_{red} exp\left(-\frac{(1-\beta) F E}{k_B T}\right) \tag{2.5}$$

$$\frac{i_c}{F} = -r_c(E) = k_c c_{ox} exp\left(-\frac{\beta F E}{k_B T}\right) \tag{2.6}$$

Evaluating the expression at the equilibrium potential, E_{eq}, gives the following expressions for the exchange current density:

$$\frac{i_0}{F} = k_a c_{red} exp\left(\frac{(1-\beta)FE_{eq}}{k_B T}\right) = k_c c_{ox} exp\left(-\frac{\beta F E_{eq}}{k_B T}\right) \quad (2.7)$$

where the net current is zero and the magnitudes of the anodic and cathodic currents are equal. A higher exchange current density indicates that a reaction will occur more readily for a given potential. Now the anodic and cathodic current densities can be re-expressed as:

$$i_a = i_0 \left[exp\left(-\frac{(1-\beta)F(E-E_{eq})}{k_B T}\right)\right] \quad (2.8)$$

$$i_c = i_0 \left[exp\left(-\frac{\beta F(E-E_{eq})}{k_B T}\right)\right] \quad (2.9)$$

The surface overpotential, η_s, provides the driving force for a reaction and is described by:

$$\eta_s = E - E_{eq} \quad (2.10)$$

Formally, the overpotential reflects the difference between the potential drop across the electrochemical double layer at the potential of interest and the voltage drop across the double layer at the equilibrium. Replacing β and (1-β) with α_c and α_a, respectively, extends the Butler-Volmer kinetics to include elementary and non-elementary reactions. The net current density given by Butler-Volmer (BV) kinetics is:

$$i = i_0 \left[exp\left(-\frac{\alpha_a F \eta_s}{k_B T}\right) - exp\left(-\frac{\alpha_c F \eta_s}{k_B T}\right)\right] \quad (2.11)$$

Hence, the BV equation establishes the relationship between current density and surface overpotential. The emphasis on current density implicates that BV kinetics are sensitive to the surface roughness of an electrode because surface roughness increases the effective surface area of an electrode beyond its geometric area [172].

The Tafel approximation simplifies the BV equation and facilitates data fitting by linear regression. Observe that the BV equation contains two exponential terms, which correspond to the anodic and cathodic currents. At large and positive overpotentials, the anodic term dominates and the cathodic exponential term can be eliminated. Under such conditions, the surface overpotential can be obtained by rearranging the terms and is given by:

$$\eta_s = \frac{k_B T}{\alpha_a F} ln(i) - \frac{k_B T}{\alpha_a F} \ln(i_0) \tag{2.12}$$

The equation shown above is the anodic Tafel equation, which features one less parameter than the Butler-Volmer equation. The utility of the Tafel equation lies in the ability to fit current-voltage data by linear regression on a semi-log graph. The corresponding slope and y-intercept can be used to obtain the anodic transfer coefficient and exchange current density. Similar simplifications can be made for large negative overpotentials, where the cathodic term dominates [172], [173].

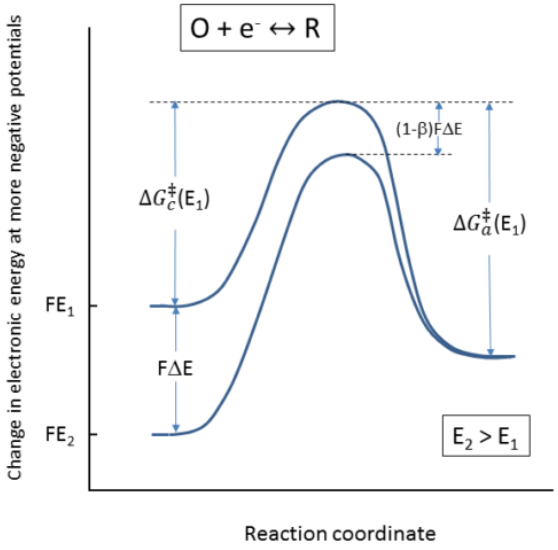

Figure 25 Energy diagram for a reaction that occurs on an electrode surface [172].

Linear sweep voltammetry is an electrochemical technique that gathers the current-voltage data for performing BV or Tafel analysis. The method is commonly performed to investigate irreversible reactions, such as the galvanic corrosion of Mg, because the potential is only swept in one direction [99], [123], [140], [157], [174]. A three-electrode configuration is commonly used for LSV; the working, counter and reference electrodes correspond to the electrode of interest (i.e., Mg when evaluating Mg corrosion), an electrochemically noble electrode that does not react in the electrolyte of interest (e.g., platinum) and an electrode with a stable internal potential (e.g., saturated silver/silver chloride (Ag/AgCl)), respectively. A potential range of 250-500 mV centered about the open circuit potential is applied between the working

and reference electrodes; the current is measured from the working electrode to the counter electrode. The potential corresponding to the inflection point in the current, when the direction of the current changes from positive to negative, is the corrosion potential. Given that the potential is thermodynamically driven, a more positive corrosion potential suggests a smaller driving force for galvanic corrosion; metals with more noble corrosion potentials are less likely to corrode. Whereas the standard electrode potential is a reversible potential that captures the tendency of a metal to form metal ions in solution, the corrosion potential is typically more positive than its corresponding standard electrode potential and is irreversible. The difference between the standard electrode potential and corrosion potential may be attributed to a number of factors, such as the formation of a protective oxide film, solubility of the oxide and stability of the oxide film in the electrolyte (e.g., aggressive passivation breakdown in a chloride environment).

In turn, current is kinetically-driven and the corrosion rate of a metal in a given electrolyte can be determined based on the corrosion current and Faraday's law. The corrosion current can be graphically or analytically obtained by linear extrapolation from the Tafel approximations of the anodic and cathodic portions of LSV data. Specifically, the corrosion current is the current at which the anodic and cathodic Tafel fits intersect [79]. An illustration of how the corrosion current and corrosion potential can be graphically obtained is presented in Figure 26. Observe that the corrosion rate determined by LSV assumes that the metal undergoes uniform corrosion, where the thickness of the sample corrodes at the same rate and in the same manner across the entire surface of the substrate. This, however, is not always the case; magnesium is particularly prone to pitting corrosion and stress corrosion cracking [90], [175]. The accelerated corrosion observed locally with pitting and stress corrosion cracking can jeopardize the functionality of a device long before the entire thickness has been consumed by corrosion. Linear sweep voltammetry analysis does not capture this phenomenon.

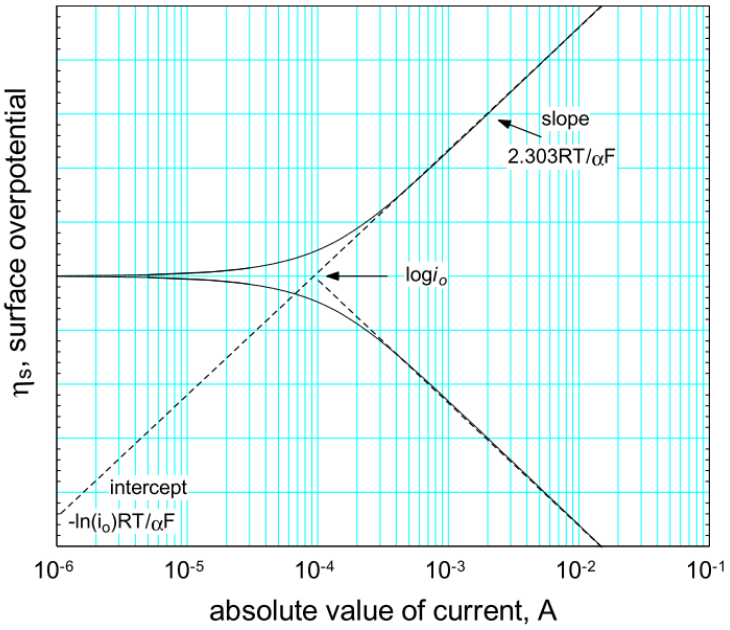

Figure 26 Schematic of how the corrosion potential and corrosion current can be graphically determined from Tafel approximations [172].

Electrochemical noise testing provides a quantitative approach to investigating localized corrosion [170], [176], [177]. Since pitting corrosion is stochastic, no two samples (even of the same material) corrode identically. This results in a net current between the two samples. Hence, ECN testing assumes that signal fluctuations are a product of spontaneous changes in corrosion rate [177]. A key advantage of ECN testing, in comparison with LSV, is the ability to continuously monitor a given sample without external perturbation (i.e., an applied voltage). ECN is a non-destructive test that permits continuous corrosion monitoring of the same sample. In contrast, the electrode is destroyed from LSV testing and, hence, the same sample cannot be used to monitor the change in corrosion behavior over time. Figure 27 shows a schematic of the 3-electrode-setup that can be used to perform ECN testing in the zero-resistance ammeter (ZRA) configuration. The ZRA configuration enables dual measurement of the noise current and noise voltage [170].

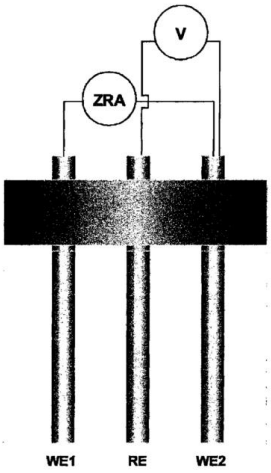

Figure 27 Three-electrode setup for ECN testing in the zero-resistance ammeter configuration [170].

The interpretation of electrochemical noise can be categorized into sequence-independent and sequence-dependent methods [169], [170], [176], [177]. Statistical analysis governs sequence-independent analysis, where key corrosion metrics are derived from the mean, root mean square (RMS), standard deviation, variance and skewness of the noise data. For example, the noise resistance (R_n), corrosion current (I_{corr}) and pitting index (PI) can be calculated by:

$$R_n = \frac{\Sigma_E}{\Sigma_I} \tag{2.13}$$

$$I_{corr} = \frac{B}{R_n} \tag{2.14}$$

$$PI = \frac{\Sigma_I}{I_{RMS}} \tag{2.15}$$

where Σ_E, Σ_I, B and I_{RMS} refer to the standard deviations of the noise voltage and current, Stern-Geary constant and RMS of the noise current, respectively. The Stern-Geary constant can be obtained by LSV and is given by:

$$B = \frac{\alpha_a \cdot \alpha_c}{2.3 \cdot (\alpha_a + \alpha_c)} \tag{2.16}$$

where α_a and α_c correspond to the anodic and cathodic transfer coefficients. The corrosion rate can be

determined from the corrosion current based on Faraday's law, similar to LSV. Consequently, this approach still assumes uniform corrosion. The pitting index characterizes how prone a metal is to pitting corrosion, where an index less than 0.01 corresponds to uniform corrosion and an index greater than 0.1 indicates pitting. Pitting index values between 0.01 and 0.1 suggests a mixture of uniform and pitting corrosion [177]–[179].

Sequence-dependent analysis considers the temporal component of the data and, as such, pre-processing of the data is important. This often includes linear trend removal to account for drift, windowing and averaging. Averaging may either be performed with multiple tests performed with the same type of samples and under the same conditions or with adjacent data points. For example, averaging a single data set by 4 would reduce a hypothetical data length from 2048 to 512 data points and increase the period between each data point four-fold. The noise impedance (Z_n) and thermal noise ($\sigma_{E,\ thermal}$) of the electrochemical data is given by:

$$Z_n = \frac{\varphi_E}{\varphi_I} \tag{2.17}$$

$$\sigma_{E,thermal} = \sqrt{4k_B T R_n BW} \tag{2.18}$$

where φ_E, φ_I, k_B, T, R_n and BW denote the power spectral density of the voltage noise and current noise, Boltzmann's constant, temperature, noise resistance and bandwidth, respectively. The power spectral density (PSD) can be obtained by the Fourier transform of the autocorrelation of a data series, though maximum entropy methods (MEM) have also been used to fit the autocorrelation data instead. Lower order fits with MEM provides a smoother power spectral density; as the order approaches the length of the data series, the results resemble the PSD obtained by Fourier transform. A rule of thumb is for the MEM order to be 10% of the data length [177], [179].

Although electrochemical noise can be distinguished from thermal, Johnson and shot noise, electrochemical noise shows characteristics similar to traditional shot noise [180]. Briefly, the electrochemical noise attributed to pitting and uniform corrosion exhibit different temporal signatures and

sequence-dependent (e.g., frequency) analysis can be implemented to identify the various corrosion behaviors present. In traditional electrical engineering, shot noise is a consequence of the quantization of charge; the number of charges passing at a given point is, thereby, a random variable. In turn, electrochemical noise resembling shot noise is produced during the breakdown of a passive film, pit initiation and hydrogen evolution. Relating electronic shot noise and electrochemical Stern-Geary relations provides the following expression:

$$\varphi_I = 2q\bar{I} = 2f_n q^2 \tag{2.19}$$

where q, $\bar{I}$ and f_n correspond to the charge, mean current and mean frequency of charge emission, respectively. The above relation builds upon a premise of assumptions: corrosion is anodic and manifest as current transients in the data, both working electrodes have nominally the same corrosion rate, all current pulses are unrelated to each other, the solution resistance is zero (or orders of magnitude smaller than the noise resistance) and the double layer capacitance is negligible. Under these conditions, the noise resistance is also comparable to the polarization resistance obtained either by LSV or EIS. The corrosion current and charge can be re-expressed:

$$I_{corr} = \frac{B}{R_n} = B\sqrt{\frac{\varphi_I}{\varphi_E}} \tag{2.20}$$

$$q = \frac{\sqrt{\varphi_E \varphi_I}}{B} \tag{2.21}$$

Charge in the present electrochemical context does not equal the elementary charge of an electron, but rather the charge of elementary electrochemical reactions. Metastable pitting, however, may involve much larger charge quantities. The mean frequency of charge emission can be determined by substituting the corrosion current and charge into the previous relation:

$$f_n = \frac{I_{corr}}{q} = \frac{B^2}{\varphi_E} \tag{2.22}$$

Large values, such as frequencies higher than 1 kHz/cm^2, suggest uniform corrosion. The PSD of the

voltage (φ_E) is typically evaluated at the lowest possible frequency (e.g., 1-10 mHz) given the test conditions. Hence, meaningful electrochemical noise data presupposes a low-noise test setup, particularly at low frequencies (i.e., <1 Hz) [169], [176], [177], [180]. Electrochemical noise testing is traditionally conducted in a Faraday cage to reduce ambient noise. The maximum and minimum frequencies of interest determine the largest permitted hole and thickness of the Faraday cage, respectively. Even when ambient noise is entirely eliminated, however, instrument noise of the potentiostat presents a lower limit to the noise floor.

Localized corrosion proceeds in two steps: pit initiation and pit growth [180]–[183]. Pit initiation refers to the formation of new pits on the metallic substrate, whereas pit growth refers to already formed pits [183]. The mean frequency of charge emission typically follows a Weibull distribution and provides information about the pit initiation of a sample. For reference, the Weibull distribution is a continuous statistical distribution with two characteristic parameters: scale (λ) and shape (k). Both parameters can range from zero to positive infinity. The cumulative distribution function (CDF) of a Weibull distribution is:

$$F(x) = \begin{cases} 1 - e^{-\left(\frac{x}{\lambda}\right)^k}, x \geq 0 \\ 0 \qquad\qquad\quad , x < 0 \end{cases} \tag{2.23}$$

Observe that a Weibull distribution is an interpolation between an exponential distribution (k=1) and a Rayleigh distribution (k=2, $\lambda=\sqrt{2}\sigma$). If X is a random variable representing the time to failure, then a shape parameter less than 1 suggests a decrease in failure rate over time. In turn, shape parameter greater than 1 indicates an increasing failure rate with time and is commonly observed with aging. Shape parameters equal to 1 and 3 correspond to a constant failure rate (i.e., due to random events) and approximate a normal distribution, respectively. The Weibull parameters can be obtained by linearly fitting experimental data based on the mathematically manipulated expression below:

$$ln\{-ln[1 - \hat{F}(x)]\} = ln(x) \tag{2.24}$$

where $\hat{F}(x)$ denotes the CDF data of interest. The shape (λ) and scale (k) parameters can be determined

from the slope (m) and y-intercept (b), respectively, as follows:

$$m = \text{ƙ} \tag{2.25}$$

$$b = -\text{ƙ} \cdot ln(\lambda) \tag{2.26}$$

The empirical CDF ($\hat{F}(x)$) is estimated from cumulative frequency analysis. Briefly, the cumulative probability can be empirically approximated by:

$$F(x) = \frac{M}{N+1} \tag{2.27}$$

where M and N refer to the rank of the data point in ascending order and length of data, respectively. The denominator is N+1 rather than N in the case where x may exceed the observed x_{max}. From conditional probability, the pit initiation rate (σ) is given by:

$$\sigma(t) = \frac{\text{ƙ}}{\lambda} t^{\text{ƙ}-1} \tag{2.28}$$

The above expression corresponds to the failure rate in Weibull analysis for reliability engineering and provides a predictive measure of localized pitting during galvanic corrosion [180], [184].

Pit growth can be evaluated by applying the Gumbel distribution and extreme value statistics to electrochemical noise [180], [184]. Based on Faraday's law, the volume (V) and radius (r_{pit}) of a pit can be calculated based on charge. Integration of the noise current data over time yields experimental values for the charge passed during corrosion events.

$$V[cm^3] = \frac{qMW}{Fz\delta} \tag{2.29}$$

$$r_{pit} = \sqrt[3]{\frac{3V}{2\pi}} \tag{2.30}$$

where q, MW, F, z and δ denote the charge, molecular weight, Faraday's constant, charge equivalence and density of the sample, respectively. Obtaining charge from the integration of current transients assumes that the charge is due to the formation of metastable pits. Moreover, the calculation assumes that the charge is

not due to hydrogen reduction within a pit. The above expression for pit radius further assumes that every pit exhibits a hemispherical geometry. Representing the pit radius as a random variable, its CDF can, again, be determined by cumulative frequency analysis [180]. The reduced variant of the random variable provides a useful measure for linearizing the data to experimentally determine relevant parameters. The reduced variant is given by:

$$Y = -ln\{-ln[F(Y)]\} \tag{2.31}$$

The Gumbel parameters can be graphically or analytically determined. Specifically, the scale and shape parameters correspond to the slope (α) and x-intercept (μ), respectively. From the Gumbel distribution, the predicted maximum pit radius (Pit_{max}) and probability of a pit growing to a given radial size are as follows:

$$Pit_{max} = \mu + \alpha \cdot \ln(\frac{A_i}{A_{total}}) \tag{2.32}$$

$$\mathbb{P}(r_{pit}) = 1 - exp\left\{-exp\left[\frac{-(r_{pit} - Pit_{\max})}{\alpha}\right]\right\} \tag{2.33}$$

where A_i and A_{total} are the area of interest and total surface area, respectively. Gumbel analysis is valid for extrapolating from a small sample area to a larger area of interest due to its derivation from extreme value statistics. Whereas many pit growth models capture the behavior of one single pit, Gumbel analysis extrapolates the behavior of a series of pits, providing a more practical model for understanding pitting corrosion [184].

The present study details the corrosion protection of electroplated Mg with Zn, HAP and FHA coatings. Optimization of the passivation coatings prioritizes efforts that align with MEMS-relevant dimensions and fabrication processes. The ability of the passivation coatings to hinder physiological degradation is examined using electrochemical techniques because not only is the corrosion rate of interest to device design, but the mechanism by which a coating fails is also helpful in understanding the optimal application and use for a particular coating.

2.2.2. Electrodeposited Zinc for the Corrosion Passivation of Magnesium

The electrodeposition of zinc was investigated as a corrosion passivation coating onto magnesium. This section details the optimization and characterization of Zn electrodeposited by direct current methods. The current density and deposition technique were varied to determine their effect on electroplated Zn morphology and corrosion protection properties. Subsequently, the optimal thickness was explored. All processes were conducted in an aqueous electrolyte comprising 30 g/L $ZnSO_4 \cdot 7H_2O$, 120 g/L $Na_2P_2O_7$, 5 g/L Na_2CO_3 and 5 g/L NaF at 60˚C. Figure 28 shows the scanning electron micrographs of Zn electroplated onto Mg under direct current that ranged from 5 mA/cm^2 to 80 mA/cm^2. Although studies have previously demonstrated the electrodeposition of Zn onto Mg, the plated film strongly depends on the deposition parameters. As can be observed in the SEM images, the surface morphology drastically differs based on current density. The Zn coatings were more uniform in surface morphology across the extent of the sample area, but the grains appeared disarrayed; at 5-10 mA/cm^2, some of the grains protruded out of plane, perpendicular to the film surface, and exhibited jagged edges akin to bark chips (Figure 28a-b). In contrast, Zn films on Mg were non-uniform when deposited at high current densities (e.g., 40-80 mA/cm^2). Two distinct surface morphologies were observed: (1) a thicker, brush-like growth and (2) a thinner, granular deposit. The morphologies are indicated by yellow and blue arrows in Figure 28c, respectively. Moreover, high current density corresponded to the appreciable presence of pinholes in the deposited Zn coating, as identified by the red arrow in Figure 28f. The SEM analysis suggested that, despite the irregular arrangement of grains, Zn coatings electrodeposited at lower current densities might provide more uniform and pinhole-free protection of Mg.

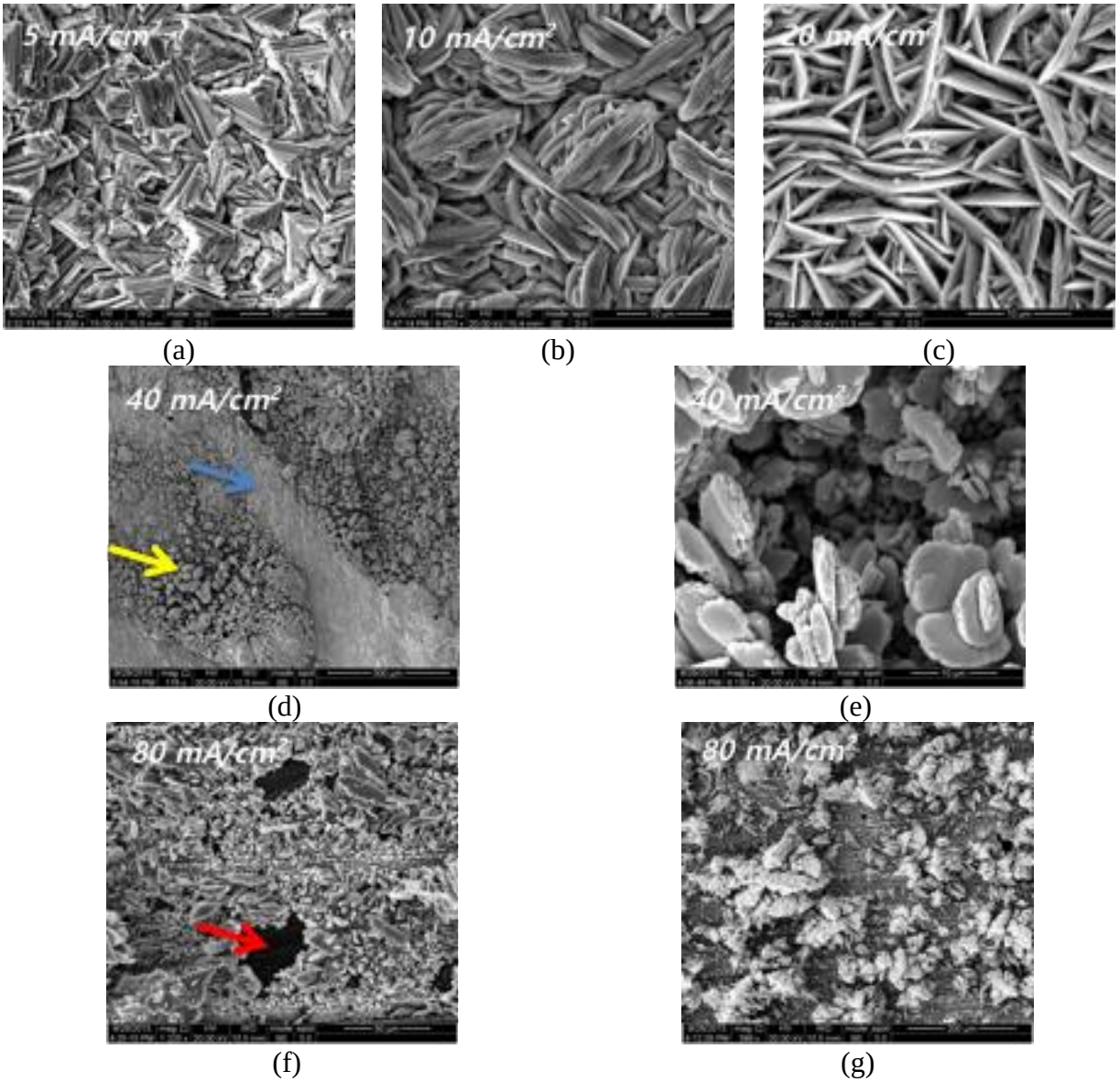

Figure 28 Scanning electron micrographs of Zn coatings on Mg electrodeposited under varying direct current densities. Several images are shown for samples deposited at higher current densities because the surface morphology was not homogenous.

Elemental analysis further supports the use of low current densities for electroplating Zn onto Mg. Table 5 provides the atomic composition of the Zn coatings determined by elemental analysis. The zinc-to-oxygen ratio decreased with increasing direct current density. Films deposited at 5 mA/cm^2 exhibited 95% Zn and 4.5% O, whereas films deposited at 80 mA/cm^2 featured only 85% Zn and 8.6% O. It is speculated that the higher oxygen content is due to the preferred formation of zinc oxide when

depositing at high current density or the higher surface area associated with the dendritic morphology; the oxidation of Zn occurs readily under atmospheric conditions. The atomic composition of Mg also increased from trace levels (<1%) to 5.9%, aligning with SEM observations of pinholes in the coating that exposed the underlying Mg substrate. In addition to confirming that high current density Zn films are less suitable for corrosion protection, EDX analysis indicated that the loosely arranged grain structures associated with low current density deposition does not correspond to a porous film—the Mg coverage is complete.

Table 5 Atomic elemental composition of Zn coatings electrodeposited onto Mg in heated alkaline electrolyte at varying DC current densities.

	Deposition Current Density (mA/cm^2)				
Element	**5**	**10**	**20**	**40**	**80**
Zn	95	90	93	86	85
O	4.5	9.0	6.5	13	8.6
Mg	0.3	0.5	0.3	0.4	5.9
P	0.2	0.5	0.2	0.6	0.5

The surface morphology of direct current electrodeposited Zn was further investigated by x-ray diffraction. A sample XRD scan and a summary of the results are shown in Figure 29a and Figure 29b, respectively. Although Mg and ZnO peaks were identified, the dominant peaks corresponded to different crystallographic orientations of Zn. The [101] orientation was preferentially electroplated for all current densities. Based on XRD analysis, the [101] peak was three- and two-fold higher [100] and [002] peaks, respectively, and all ratios were greater than unity.

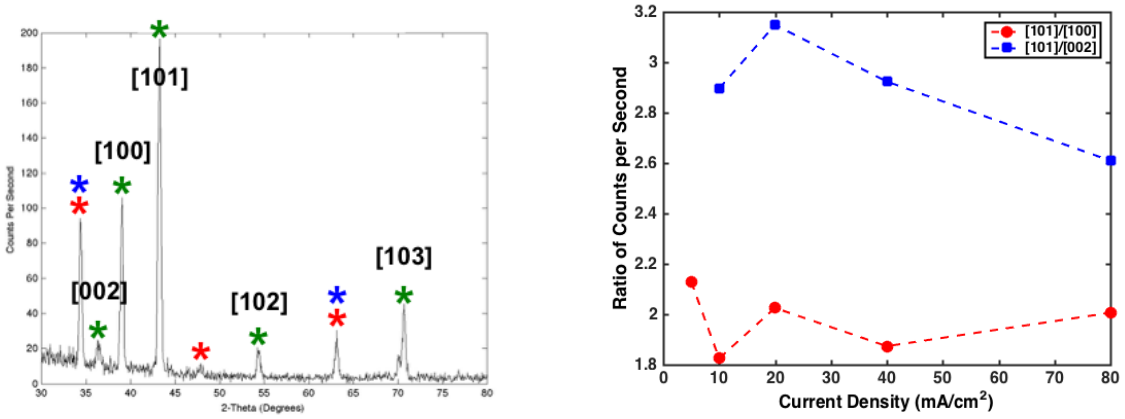

(a) (b)

Figure 29 X-ray diffraction results revealing negligible differences in crystallographic orientation of Zn electrodeposited on Mg under varying direct current densities. The green, blue and red asterisks in (a) correspond to Zn, ZnO and Mg peaks, respectively.

The corrosion protection of Mg with electrodeposited Zn was characterized electrochemically by linear sweep voltammetry. The potentiodynamic polarization curves and summary of results are shown in Figure 30 and Table 6, respectively. The polarization curves of pure Zn and pure Mg were included for comparison, as they present the upper and lower limits in corrosion behavior. A distinct passivation region can be observed with pure Zn that spanned approximately 100 mV and terminated at a pitting potential of -1 V vs. Ag/AgCl. None of the Zn-coated Mg samples exhibited this phenomenon. Overall, electrodeposited Zn films exhibited a corrosion potential between that of pure Zn and pure Mg; the mixed potential suggested electrolyte exposure to both Zn and Mg surfaces, though does not capture the extent of Mg exposed. The coatings marked a 500-mV improvement in corrosion potential compared to pure Mg. Films deposited at lower current densities exhibited more noble corrosion potentials and a 150-mV increase in corrosion potential was observed between 80 mA/cm^2 and 10 mA/cm^2, suggesting that an additional 30% improvement in Mg corrosion protection can be achieved with well-optimized deposition parameters.

Electrodeposited Zn coatings reduced the corrosion rate of Mg in simulated body fluid. For reference, the corrosion rate of pure Zn was 1 µm/day, which is nearly 4 orders of magnitude lower than that of pure, uncoated Mg. The rapid corrosion of Mg further promotes non-uniform degradation and stress

corrosion cracking. Direct current electrodeposited Zn coatings hindered Mg corrosion by approximately 1 order of magnitude at low current densities, but only reduced the corrosion rate by half at the highest current density. The threshold in current density was 20 mA/cm^2, below which the best corrosion protection was obtained. Specifically, the corrosion rates were 0.47 mm/day and 4.7 mm/day for Zn-coated Mg deposited at 10 mA/cm^2 and 80 mA/cm^2, respectively. Hence, a 20x reduction in corrosion rate can be achieved with electrodeposited Zn coatings. Given the ease of integrating electrodeposition with microfabrication techniques, the findings present a promising approach to hindering the degradation of magnesium-based implantable MEMS devices.

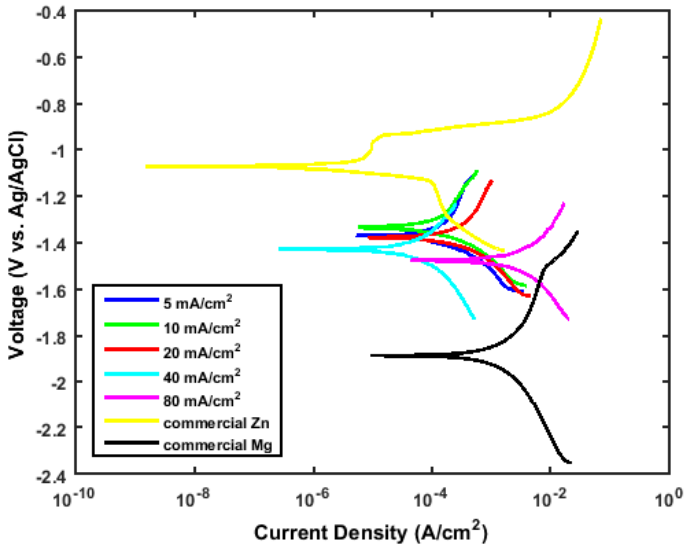

Figure 30 Potentiodynamic polarization curves of electrodeposited Zn coatings on Mg compared to commercial Mg and Zn foil. Tests were conducted in SBF.

Table 6 Summary of LSV results for Zn coatings electrodeposited onto Mg under direct current at varying current densities.

Current Density (mA/cm^2)	**5**	**10**	**20**	**40**	**80**		
Deposition time (min)	**240**	**120**	**60**	**30**	**15**	**Pure Zn**	**Pure Mg**
E_{corr} (V vs. Ag/AgCl)	-1.37	-1.33	-1.38	-1.43	-1.48	-1.07	-1.83
i_{corr} ($\mu A/cm^2$)	121	95.1	197	358	932	0.255	1867
C.R. (mm/day)	0.60	0.47	0.97	1.8	4.6	0.001	9.13

2.2.3. Improved Corrosion Protection with Pulse Electroplated Zinc

The electrodeposition of Zn by pulse plating (PP) methods was further explored for the corrosion protection of magnesium. Based on the findings with direct current deposition, it was hypothesized that the corrosion properties of Zn can be tuned based on the peak current density used during PP. The forward on and off times were 0.1 ms and 1.0 ms, respectively, which correspond to a duty cycle of 33%. Scanning electron micrographs, shown in Figure 31, indicated that the surface morphology of electrodeposited Zn varies based on the peak forward current density. Further, the morphology differed from Zn coatings electrodeposited by direct current methods. Films deposited at peak current densities of 80 mA/cm^2 and 320 mA/cm^2 appeared granular and fibrous, respectively; 160 mA/cm^2 corresponded to a hybrid of the two morphologies. None of the PP Zn coatings exhibited noticeable pinholes or the surface non-uniformities observed with DC electrodeposition at high current densities.

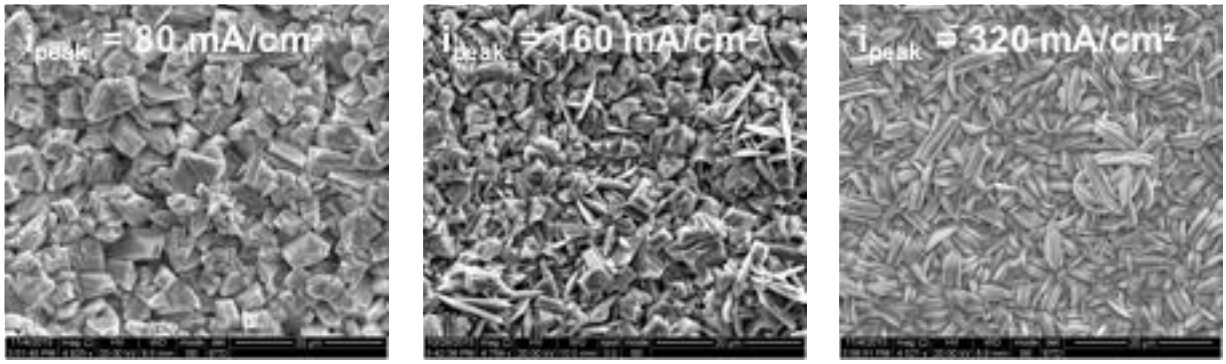

(a) (b) (c)

Figure 31 Scanning electron micrographs of Zn coatings on Mg electrodeposited under varying pulse current densities.

Elemental analysis was performed on PP Zn coatings of varying peak current densities, where the deposition time was adjusted to ensure a constant charge for all the samples. The Zn content was similar for all PP Zn samples (i.e., 95-98%) and higher than films obtained by DC plating. In turn, the oxygen content ($\leq$2%) was lower than DC plated Zn films. Not only was the oxygen content lower than that of Zn films deposited at high DC current densities, where it was speculated that the increased surface area due to the dendritic and brush-like growth may have promoted atmospheric oxidation after electrodeposition, but the atomic percent of oxygen was also lower than that of Zn films plated at low DC current densities. This suggested that direct current electrodeposition may promote the formation of zinc oxide onto the substrate surface, whereas this effect is suppressed by pulse plating techniques. The improved surface morphology and atomic composition of the PP Zn films suggested that they might provide better protection against Mg corrosion.

Table 7 Elemental composition of Zn coatings electrodeposited onto Mg by pulse plating.

	Peak Current Density (mA/cm^2)		
Element	**80**	**160**	**320**
Zn	95	96	98
O	2	<1	1
Mg	2	3	<1
P	1	1	1

X-ray diffraction analysis reveals a stark difference in crystal orientation amongst the PP Zn coatings. The results, which are presented in Figure 32 and Figure 33, suggest that [101] is the preferred orientation of PP Zn. In fact, the ratio of [101] to [100] is 2-4 times higher than that of DC plated Zn coatings, though the effect does not scale linearly with peak current density, as was the case with DC current densities. The [101] orientation was expressed most strongly in PP films deposited at a peak current density of 160 mA/cm^2. It is unclear whether the crystal orientation of Zn films affects their packing density and corrosion behavior, since corrosion can proceed anisotropically due to exposed crystal orientations.

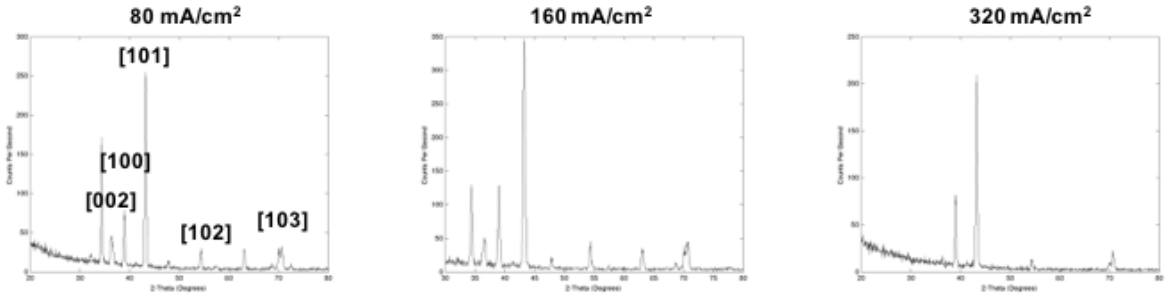

(a) (b) (c)

Figure 32 Surface morphology of pulse electroplated Zn on Mg, characterized by XRD.

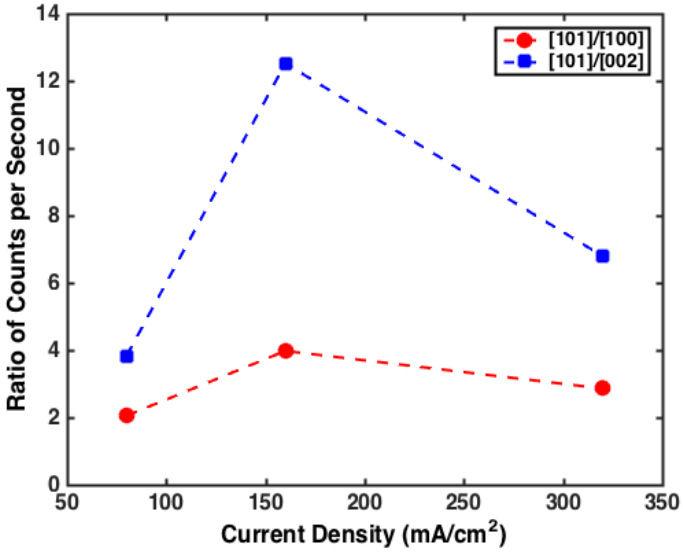

Figure 33 Preferential crystallographic orientation of Zn coatings electrodeposited onto Mg under varying pulse current densities.

Interestingly, the corrosion potential of PP Zn coatings was higher than that of pure Zn (Figure 34 and Table 8). Films deposited at a peak current density of 80 mA/cm^{2}exhibited a passivation region similar to the corrosion behavior of pure Zn. This suggested that the surface morphology and composition of PP Zn corresponded to a reduced tendency to corrode compared to commercial rolled Zn foil. Since the corrosion potential deviates from the standard electrode potential due to surface effects (e.g., oxide formation, solubility and stability), the more noble corrosion potential observed with PP Zn was attributed to the preferential crystal orientation, reduced surface defects and high film purity achieved by pulse plating. In addition, the corrosion rate improved by 2-3 orders of magnitude with pulse plating, as compared to direct current methods. The lowest corrosion rate achieved with DC plated Zn was 0.47 mm/day, whereas the lowest obtained by PP was 0.2 µm/day. These results resemble the corrosion rate of pure Zn, suggesting that the coating quality of PP Zn is superior to that of DC plated Zn. Taken together, the results suggest that PP significantly reduces the susceptibility to corrosion the corrosion kinetics compared to DC deposition. Further, the PP Zn coatings were 4.8-5.5 µm in thickness, in comparison to the tens-to-hundreds of microns thick coatings suggested by literature. The deposited thicknesses are within reason for use in MEMS applications and particularly for the corrosion protection of Mg that is in the ones-to-tens of microns thickness range. Further, since Zn is conductive and can be soldered onto, Zn coatings may be most advantageous in the corrosion protection of connection lines and contact pads, where low resistances (relative to the device) are desirable. Given that Zn is more electrochemically noble than Mg, Zn-coated samples are highly susceptible to galvanic coupling and, hence, accelerated corrosion if both Mg and Zn are exposed. This suggests that the partial coverage of a Mg-based device with Zn may be unwise unless the outer encapsulation layer offers a strong line of defense against water ingress and galvanic coupling. A second application of Zn coatings for Mg is in electrochemical devices, such as galvanic batteries, where the output potential can be geometrically controlled based on the selective exposure of Mg and Zn against a biodegradable cathode. These ideas will be further explored in the subsequent chapter, which details the development of biodegradable devices based on the materials and characterization of the present chapter.

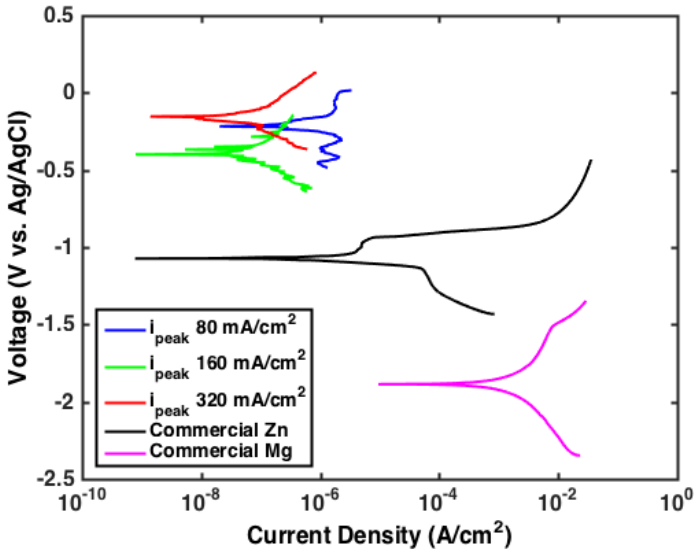

Figure 34 Potentiodynamic polarization curves of pulse electroplated Zn coatings on Mg compared to commercial Mg and Zn foil. Tests were conducted in SBF at 37℃.

Table 8 LSV results for pulse electroplated Zn coatings electrodeposited onto Mg.

Pulse Current Density (mA/cm^2)	**80**	**160**	**320**	**Pure Zn**	**Pure Mg**
E_{corr} (V vs. Ag/AgCl)	-0.22	-0.40	-0.16	-1.07	-1.83
i_{corr} (µA/cm^2)	0.24	0.04	0.06	0.255	1867
C.R. (µm/day)	1.2	0.2	0.3	1.0	9,130
Coating Thickness (µm)	4.8	5.5	5.0	n/a	n/a

The corrosion protection afforded by electrodeposited Zn coatings was further optimized based on coating thickness. It was hypothesized that a critical thickness would be observed, below which the corrosion rate is high due to incomplete coverage. In turn, above the critical thickness, the corrosion rate would decrease appreciably because all exposed surfaces of Mg have been replaced with Zn. However, it was hypothesized that increasing the film thickness beyond the critical thickness would increase the corrosion rate if the mechanical properties of the coating differ significantly from that of the underlying Mg substrate or if the film is not mechanically robust. These hypotheses were examined by evaluating the electrochemical corrosion of PP Zn films of varying thicknesses. In addition, it was previously assumed

that electrochemical reactions, such as corrosion, follows the Arrhenius relation with respect to temperature. To validate this assumption, LSV was performed to evaluate the corrosion rate of PP Zn coatings at room temperature and at 37˚C. The results are summarized in Figure 35.

The non-linear decrease in corrosion rate with thickness was observed only with PP coatings deposited at a peak current density of 80 mA/cm^2. Specifically, the corrosion rate decreased by 3-4 orders of magnitude (to approximately 0.001-0.01 mm/day) beyond a critical thickness of 1.9 µm when evaluated at room temperature (22˚C). However, the hypothesized trend was not observed when the same type of coatings was characterized at 37˚C. The corrosion rate fluctuated between 0.01 mm/day to 20 mm/day within a 2 µm range of thickness, suggesting that the elevated temperatures accelerated corrosion kinetics and resulted in unpredictable, sample-to-sample behavior. Interestingly, this unstable corrosion is commonly observed with Mg due to its fast corrosion kinetics. Further, the maximum corrosion rate recorded at 37˚C is higher than that of pure Mg, suggesting that the underlying Mg had become exposed and galvanically coupled to the Zn coating. Stress corrosion cracking and pitting corrosion may further contribute to the higher observed corrosion rate.

The corrosion rate of PP Zn deposited at a peak current density of 320 mA/cm^2 increased by 1-2 orders of magnitude at 37˚C. Zinc coatings electrodeposited at a peak current density of 320 mA/cm^2 were characterized at thicknesses up to 15 µm by LSV. The resulting corrosion rates hovered in the 0.001-0.1 mm/day range when evaluated at 37˚C. In turn, a corresponding 5-µm-thick PP Zn film exhibited a corrosion rate of 0.0002 mm/day at room temperature. Even though the corrosion reaction of Zn-coatings advanced aggressively with temperature, the kinetics were consistent across samples and remained 3 orders of magnitude lower than the behavior observed with 80 mA/cm^2 films at 37˚C. Hence, PP Zn coatings at a peak current density of 320 mA/cm^2 are favorable for physiological device applications. Interestingly, a parabolic relationship was observed at this higher current density, where Zn coatings too thin or too thick exhibited higher corrosion rates. The lowest corrosion rate was observed at 3-5 µm thickness. The lowest corrosion rate at 37˚C was 4 µm/day and corresponded to a film thickness of 3.4 µm. The results provided

preliminary support of the proposed hypothesis of a non-linear relationship between corrosion rate and coating thickness. Overall, it can be concluded that electrodeposited Zn successfully reduces Mg corrosion and its benefits are most pronounced with films deposited by pulse plating methods. Even at physiological temperatures, the surface morphology, film quality and corresponding corrosion properties of PP Zn better approximate that of pure Zn than pure Mg, providing an order-of-magnitude reduction in corrosion.

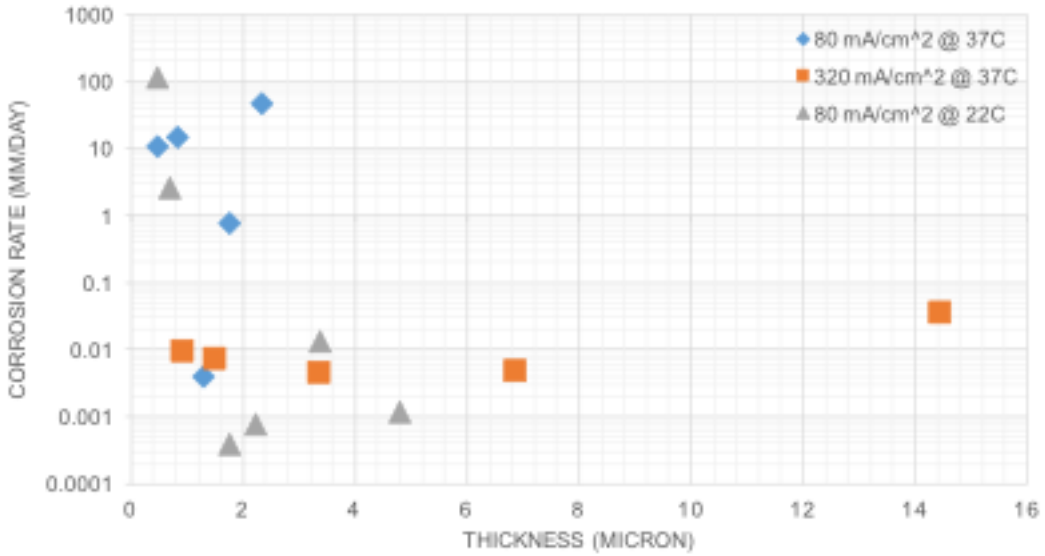

Figure 35 Effect of the peak current density of PP Zn coatings on corrosion rate.

2.2.4. Hydroxyapatite as a Biodegradable and Biocompatible Passivation Material

Hydroxyapatite was examined as a corrosion protection coating for Mg in biodegradable MEMS devices. As discussed previously, HAP is a calcium phosphate material that is naturally found in bone. In addition, HAP is a non-conductive ceramic material that can passivate Mg without contributing to the device resistance (as opposed to Zn coatings). The electrodeposition of HAP on Mg was conducted at a constant voltage of 3 V in an electrolyte containing 0.1 M $Ca(NO_3)_2$, 0.06 M $(NH_4)_3PO_4$ and 10 mL/L 30wt.% H_2O_2 (pH 4). Figure 36 shows the SEM image of HAP deposited to varying deposition times. The surface morphology was not appreciably different with deposition time and was homogenous

across the sample surface. A combination of flake and spindle type morphologies covered the Mg substrate surface, as indicated by green and blue arrows in the micrographs, respectively. However, the thickness was not uniform across the sample, as some areas featured thicker growth. Further, pinholes were observed in the HAP coating even after 3 hours of deposition under constant voltage conditions, which typically offers more uniform coverage since all surfaces of the sample are held at the same potential. Pinholes in the HAP film are highlighted with red arrows in the SEM images. Elemental analysis and XRD will be important in validating whether the pinholes correspond to sites of exposed Mg, as this would detract of the use of HAP as a corrosion protection coating for Mg.

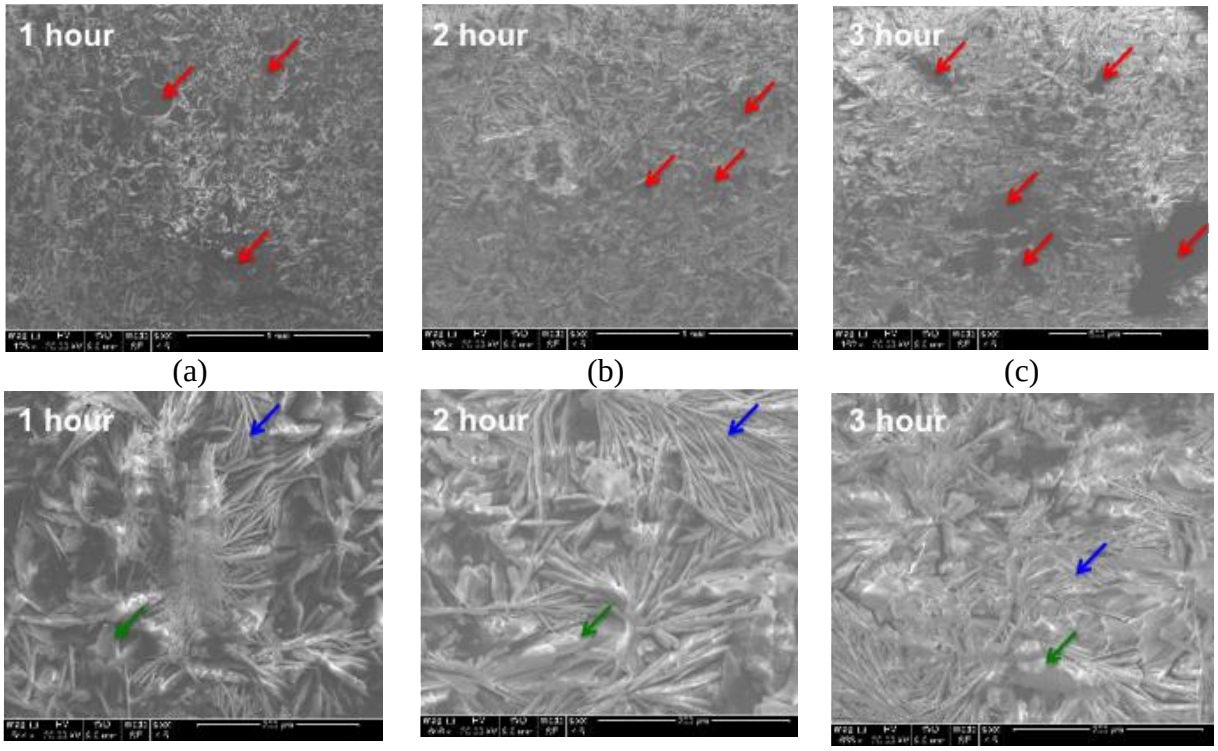

Figure 36 Scanning electron micrographs of HAP coatings on Mg electrodeposited under constant voltage for varying deposition times.

The elemental composition of HAP after 3 hours of electrodeposition was analyzed by EDX. The results are summarized in Table 9 for the spindle- and flake-like growths, as well as pinholes in the coating. The results confirmed that the pinholes visually observed in the SEM images are, in fact, sites of exposed

Mg; EDX detected 85% Mg in the pinholes. This agreed well with literature, which found that HAP nucleates poorly on Mg surfaces. Only trace levels of Mg were detected from the HAP coatings independent of morphology. The experimental calcium to phosphate ratio was 2.9, as opposed to the theoretical value of 1.67. Hence, the electrodeposited HAP was calcium-rich. X-ray diffraction further confirmed the presence of Mg in spite of the electrodeposited HAP coating (Figure 37). The findings suggest that, based on traditional metallic corrosion, HAP is insufficient in passivating Mg to hinder its degradation kinetics.

Table 9 Atomic elemental composition of HAP-coated Mg after 3 hours of electrodeposited under constant voltage. The corresponding regions where the EDX was performed is shown in the red, blue and green arrows in the SEM images of Figure 36.

Element	**Exposed Mg (Red)**	**Spindles (Blue)**	**Flakes (Green)**
Mg	84.4	0.9	0.6
Ca	0.2	24	29
O	9.8	58	54
P	0	9.4	10
Na	0	3.3	3.0
C	5.6	4.2	3.5

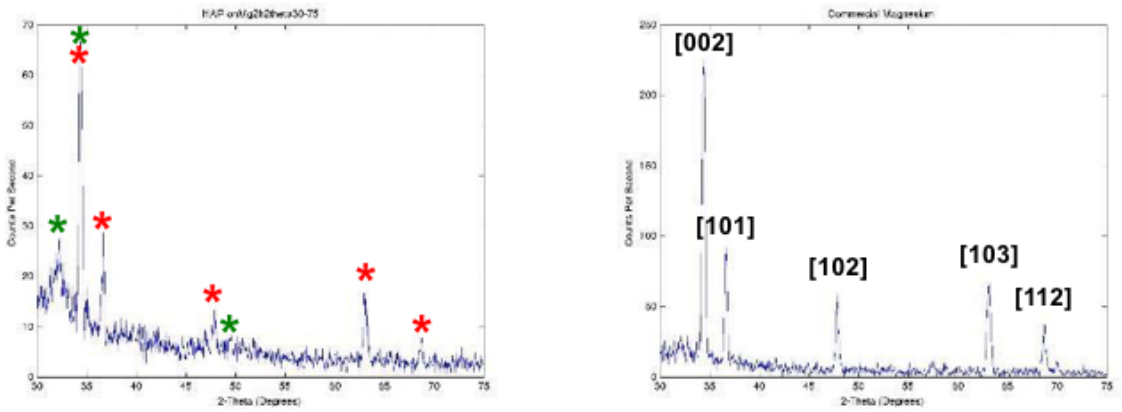

(a) (b)

Figure 37 Surface morphology of (a) HAP-coated Mg and (b) pure Mg, as characterized by XRD. For reference, the red and green asterisks refer to peaks that correspond to Mg and HAP, respectively. The crystal orientation that correspond to each Mg peak are shown in (b).

Despite the poor film quality, HAP coatings improved the corrosion properties of Mg comparable to that of DC plated Zn coatings (Figure 38). The corrosion potential of HAP-coated samples was approximately 240 mV more noble than that of pure Mg. Longer deposition times corresponded to more positive corrosion potentials, but the improvements after 2 hours of deposition were negligible since variations of 10 mV are commonly observed even for samples with the same type of coating. In contrast, the corrosion rate increased with deposition time, possibly due to poor adhesion and mechanical robustness of the electroplated inorganic coating. As summarized in Table 10, HAP coatings reduced Mg corrosion by up to 32-fold, even though pinholes and sites of exposed Mg were observed on the sample surface. Recall that studies have found that additional HAP forms when immersed in physiological solution. The formation of additional calcium phosphate coatings onto the sample surface likely competed with corrosion reactions, thereby reducing the corrosion rate.

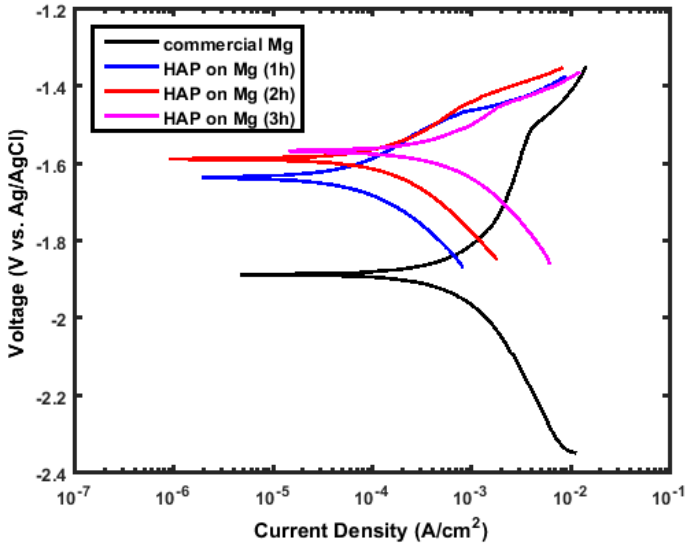

Figure 38 Potentiodynamic polarization curves of HAP-coated Mg compared to commercial Mg. Tests were conducted in SBF.

Table 10 Summary of LSV results for HAP-coated Mg.

Deposition Time (h)	**1**	**2**	**3**	**Pure Mg**
E_{corr} (V vs. Ag/AgCl)	-1.64	-1.59	-1.57	-1.83
i_{corr} (μA/cm^2)	57	52	318	1867
C.R. (mm/day)	0.28	0.26	1.57	9.13

Given the increase in corrosion rate observed with thicker HAP coatings, it was imperative to understand whether the mechanical robustness and adhesion of HAP films undermine their use in the corrosion protection of Mg under mechanical loading environments. Figure 39 shows the SEM images of HAP-coated Mg before and after cyclic tensile strain. The corresponding elemental analysis is summarized in Figure 40. Consistent with earlier findings, cracks and pinholes were observed in the HAP coating even prior to mechanical conditioning. Extensive crack propagation and coating delamination can be seen on samples after cyclic straining, however. This may be attributed to the more brittle properties of calcium phosphate, as well as poor adhesion between the HAP coating and Mg substrate. Interestingly, EDX revealed that areas where HAP had delaminated (blue) showed only 23% Mg content. Further, the presence of HAP was still detected, suggesting that traces and debris may remain on the surface. Since the samples

were not immersed in SBF, the HAP content was not due to the formation of new apatite on the exposed surface.

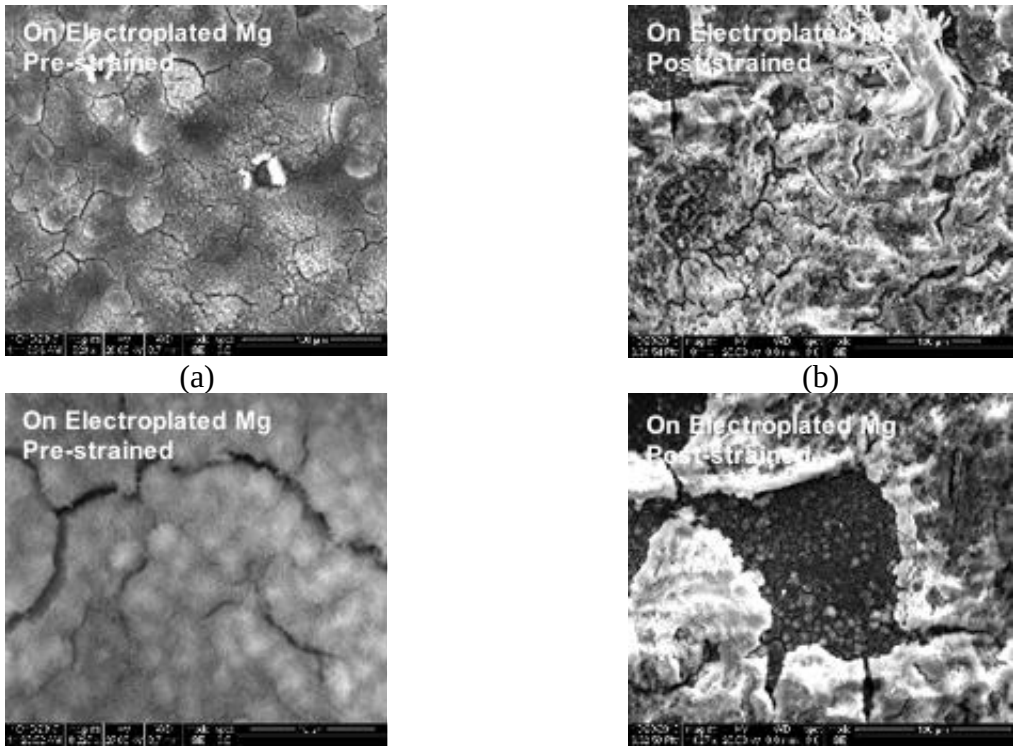

Figure 39 Scanning electron micrographs of HAP-coated Mg (a, c) before and (b, d) after mechanical conditioning. Strained samples were subject to 1% tensile strain at 1 Hz for 1000 cycles.

Figure 40 Elemental composition of HAP-coated electroplated Mg after mechanical conditioning. An accompanying SEM image is provided to highlight where the EDX analysis was performed.

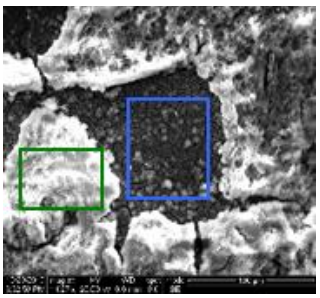

Element	Pre-strain	Post-Strain	
		Green	Blue
Mg	7	<1	23
Ca	18	28	15
O	59	55	49
P	11	13	10
Na	6	4	3

Cross-sectional imaging confirmed the poor film quality and adhesion on Mg. The scanning electron micrographs presented in Figure 41 were obtained by focused ion beam (FIB) etching of the HAP-coated Mg. The layer on top of the HAP coating in Figure 41b is a platinum blanket that was deposited to protect the HAP during FIB etching. The cross-sectional micrographs show fissures and cracks running through the entire thickness of the HAP coating. Moreover, gaps can be observed between the HAP and Mg, particularly adjacent to cracks in the coating, confirming the results obtained from mechanical conditioning and corrosion testing; poor adhesion and film quality detract from the mechanical robustness and, thereby, corrosion protection properties of electrodeposited HAP.

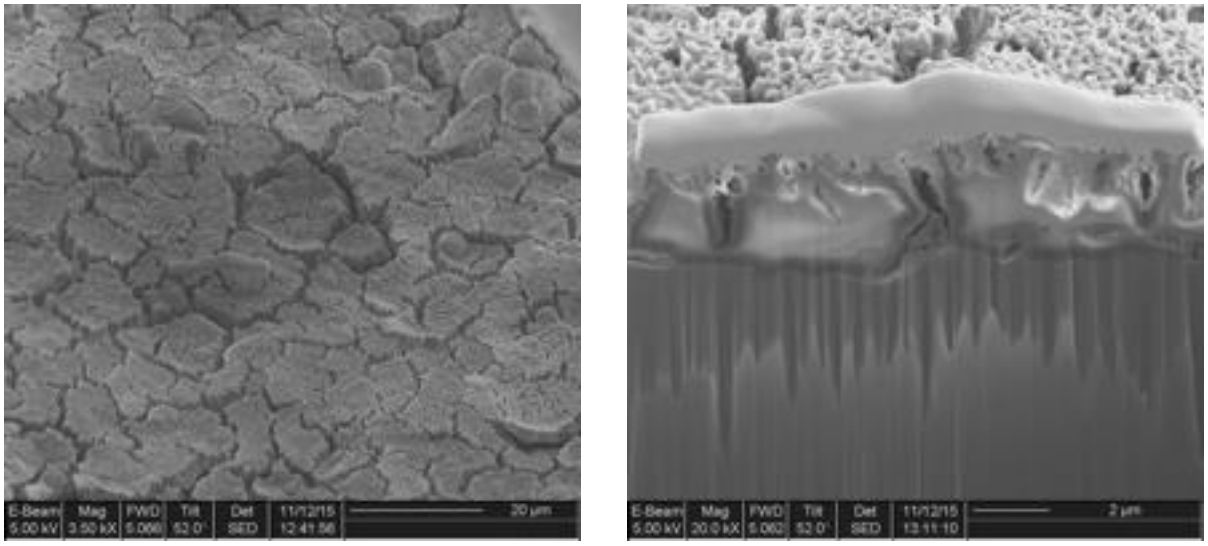

(a) (b)

Figure 41 Cross-sectional SEM images of HAP electrodeposited onto Mg obtained by FIB.

2.2.5. Improved Corrosion Protection with Fluorinated Hydroxyapatite

Fluorinated hydroxyapatite was investigated as an alternative to HAP for a bioactive, non-conductive corrosion protective coating. Electrodeposition of FHA was conducted under direct current conditions in an electrolyte similar to what was used for HAP deposition. Sodium fluoride and hydrogen peroxide were added to the electroplating solution to support the deposition of FHA and minimize hydrogen evolution on the sample surface, which would result in porous deposits. Elemental analysis, summarized in

Table 11, identified only trace levels of Mg, suggesting good film coverage of the Mg substrate. The calcium to phosphate and oxygen to fluoride ratios were 1.73 and 13.75, respectively. The theoretical ratio of calcium to phosphate is 1.67, but the experimental value for HAP and FHA have routinely been calcium-rich. Given a 2 mM addition of sodium fluoride to the electrolyte, it was expected that the oxygen to fluoride ratio would be 12, which corresponds to a fluorinated apatite of $Ca_5(PO_4)_3(OH)_{2-x}F_x$ where x is equal to 2. However, a ratio of 13.75 suggests that x is equal to 1.76 for the electroplated FHA. Hence, the chemical structure of the electrodeposited FHA was $Ca_5(PO_4)_3(OH)_{0.24}F_{1.76}$. It is speculated that the fluoride content will promote nucleation of FHA on Mg surfaces, as compared to HAP.

Table 11 Elemental composition of FHA coatings electrodeposited onto Mg. The atomic ratios of calcium to phosphate (Ca:P) and calcium to fluorine (Ca:F) are indicative of the FHA composition.

Element	Mg	Ca	O	P	Na	F
Atomic %	<1	26	55	15	1	4

Cross-sectional imaging shows a densely-packed coating with no islands or fissures extending through the film. Figure 42 further shows an intimate adhesion between the deposited FHA and underlying Mg. Occasional cracks are seen near the FHA-Mg interface, but are subsequently covered by additional plating. The film thickness was approximately 3 μm with submicron variability across the sample surface. The SEM, EDX and FIB images confirmed that FHA features better film quality and adhesion to Mg than electrodeposited HAP. X-ray diffraction identified peaks characteristic of calcium phosphate, as well as Mg (Figure 43).

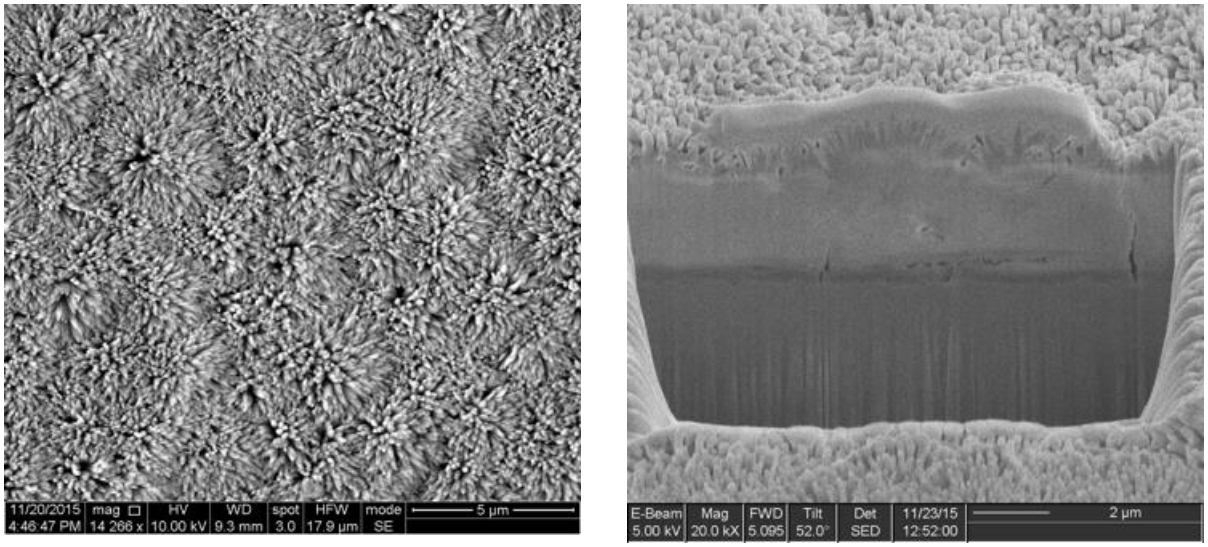

(a) (b)

Figure 42 Comparison of the cross-sectional images of FHA coatings Mg obtained by FIB-SEM.

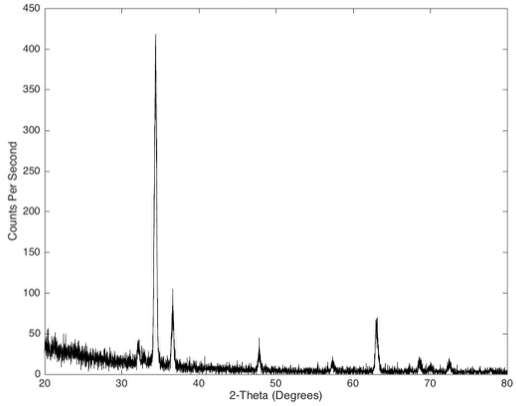

Figure 43 Surface morphology of FHA-coated Mg, as characterized by XRD.

The corrosion of FHA-coated Mg was evaluated by LSV in simulated body fluid at 37˚C. The potentiodynamic polarization curves are presented in Figure 44 along with results for HAP and pure Mg for reference. The corrosion characteristics are summarized in Table 12. All FHA-coated samples exhibited a more noble corrosion potential than HAP and Mg. Lower current density depositions corresponded to more positive corrosion potentials. The lowest corrosion potential was -1.16 V vs. Ag/AgCl, which marked a 670 mV and 390 mV improvement compared to pure Mg and HAP coating, respectively. The corrosion

rate of FHA coatings was similar to HAP deposits. Films deposited at current densities greater than or equal to 1 mA/cm^2 demonstrated a corrosion rate of approximately 0.4 mm/day, whereas current densities less than 1 mA/cm^2 corresponded to a corrosion rate of approximately 0.17 mm/day. Hence, FHA deposited at lower current densities offers better corrosion protection and shows corrosion kinetics similar to that of HAP. The LSV analysis indicated that FHA-coated Mg is less likely to corrode, but the corrode kinetics resemble that of HAP and DC plated Zn. Overall, the results indicate that FHA is more favorable than HAP for the corrosion protection of Mg because FHA offers better film quality, adhesion and surface uniformity. The selective use of FHA and PP Zn for corrosion protection will depend on the application. As mentioned previously, Zn is a conductive material and, thereby, can impact device resistances. Calcium phosphate is non-conductive, inorganic and bioactive, which may be advantageous in orthopedic settings or applications where brittle materials are desired. More importantly, from a corrosion perspective, the use of FHA and calcium phosphate films supports longer term protection because once pinholes and cracks form on a Zn coating, subsequent corrosion will proceed rapidly due to galvanic coupling between the Mg and Zn. This does not apply to calcium phosphate coatings. In fact, HAP coatings offered corrosion protection even though noticeable pinholes and fissures were observed on the film because the principle by which it hinders Mg corrosion differs; surface reactions for apatite formation compete with Mg corrosion. Hence, catastrophic failure would occur once a Zn coating has been jeopardized, whereas the decay of an FHA coating would be gradual. The difference in failure mode might govern which coating is preferable for corrosion protection.

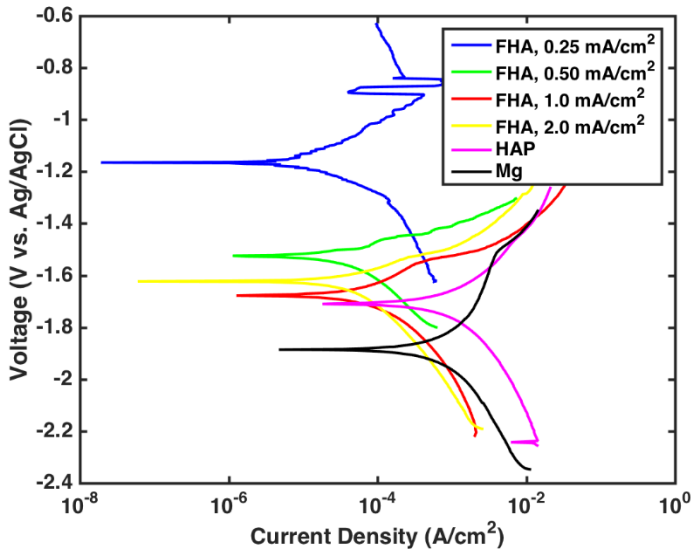

Figure 44 Potentiodynamic polarization curves of FHA-coated Mg compared to commercial Mg. Tests were conducted in SBF at 37℃.

Table 12 Summary of LSV results for FHA-coated Mg.

Current Density (mA/cm^2)	**0.25**	**0.50**	**1.0**	**2.0**
Deposition Time (min)	**120**	**60**	**30**	**15**
E_{corr} (V vs. Ag/AgCl)	-1.16	-1.52	-1.68	-1.62
i_{corr} (µA/cm^2)	32	37	91	81
C.R. (mm/day)	0.16	0.18	0.44	0.39

Since hydroxyapatite-based materials are bioactive, the long-term corrosion behavior of FHA-coated Mg was examined. The coating was deposited at 0.5 mA/cm^2 because further reducing the current density would significantly lengthen the deposition time, but provide negligible improvements in corrosion rate (Table 12).

Figure 45 shows the polarization curves, corrosion potential and corrosion rate of FHA-coated samples immersed in SBF at 37°C for 2 weeks. At indicated time points, samples were retrieved for characterization by LSV. Since LSV is a destructive test, samples were sacrificed at each time point. The data shown represent the mean (n = 3) for each time point examined. The corrosion potential gradually increased to a more noble potential during the first 3 days of physiological conditioning, after which the

corrosion potential stabilized at approximately -1.5 V vs. Ag/AgCl for the remainder of the 14-day study. The corrosion rate fluctuated during the initial 24 hours, but monotonically decreased thereafter. The evolution in corrosion behavior supported literature reports that FHA is a bioactive material. As the results (i.e., more noble corrosion potential and decrease in corrosion rate) indicated that the corrosion protection of FHA can improve over time and further supported its use in Mg passivation.

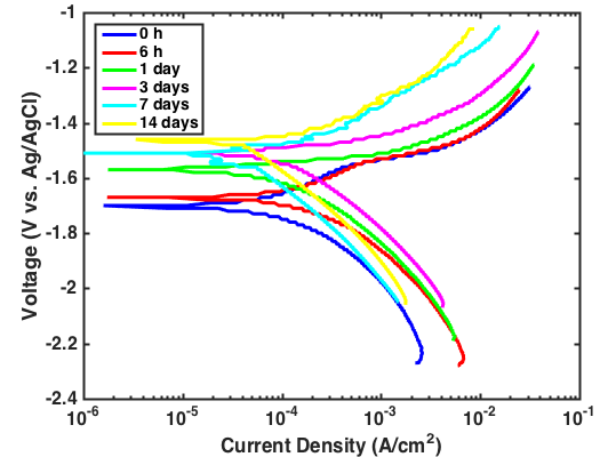

(a)

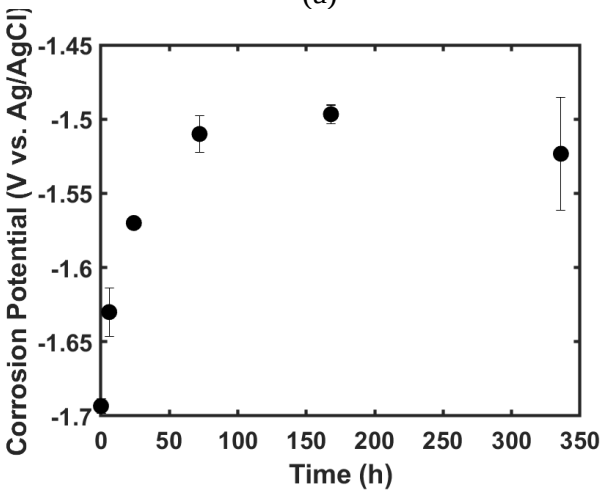

(b)

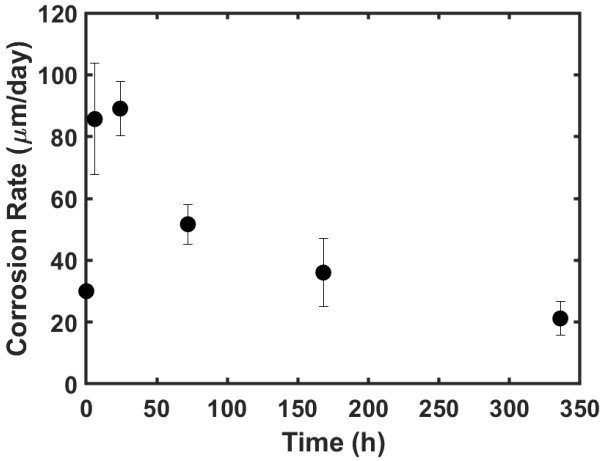

(c)

Figure 45 Potentiodynamic testing of FHA-coated Mg after long-term immersion in SBF: (a) representative potentiodynamic data over 14 days of physiological conditioning, (b) corrosion potential and (c) corrosion rate, as determined by Faraday's law and corrosion current density, of FHA-coated Mg samples. Data represents mean ± SEM (n=3).

2.2.6. Electrochemical Noise Analysis of Magnesium Passivation

Electrochemical noise analysis was performed on PP Zn and FHA coatings, as well as pure Zn and pure Mg for reference. The objective of the study was to understand the mechanism by which corrosion proceeds with the different material coatings. Corrosion, thus far, has been characterized by LSV, which assumes uniform corrosion across the sample surface in order to determine corrosion rate based on Faraday's Law. However, pitting corrosion, stress corrosion cracking and galvanic couples introduce non-linear elements to electrochemical corrosion that demand additional characterization. Statistical analysis of ECN data can provide information on localized corrosion, such as with pit initiation and pit growth. Further, the testing provides lateral on the evolution of corrosion with respect to time. The tests are performed under zero-resistance ammeter (ZRA) configuration using two identical samples as the working electrodes and saturated Ag/AgCl as the reference electrode. Raw voltage and current data are shown in Figure 46 for pure Mg initially after immersion in SBF (t = 0 h) and after 45 hours. The fluctuations in the waveform correspond to transient corrosion events. A change in the direction of current suggests that the net corrosion taking place on one working electrode has exceeded that of the other. Although both working electrodes are theoretically equally susceptible to corrosion, sometimes one of the working electrodes becomes the net anode because the corrosion reaction renders the pH local to the electrode surface more acidic. The second working electrode becomes the net cathode and, in this manner, the net anode becomes more prone to corrosion, thus steering the direction of the electrochemical current towards one direction. This effect, which would accelerate corrosion, is not observed with the data presented in Figure 46, as the ECN current crosses the 0-mA axis several times throughout the measurement period.

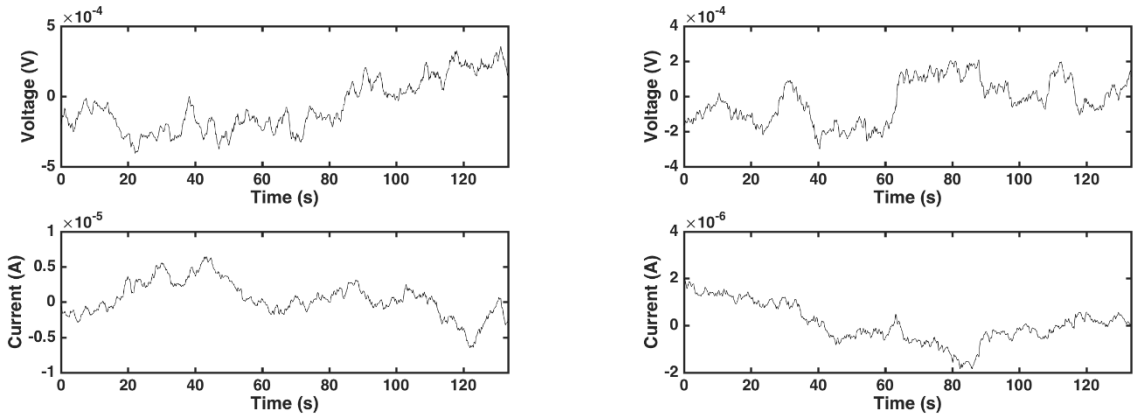

(a) (b)

Figure 46 Raw voltage and current noise data obtained from ECN testing of pure Mg after (a) 0 and (b) 45 hours.

The sequence-independent analysis of ECN data is summarized in Figure 47 for PP Zn and FHA coatings on Mg. The noise resistance is similar to the polarization resistance, where lower resistances suggest increased susceptibility to corrosion. The noise resistance of pure Zn and pure Mg are shown for reference. As expected, the noise resistances are highest and lowest for pure Zn and pure Mg, respectively. Zinc-coated Mg demonstrated a noise resistance similar to that of pure Zn during the initial time frame, but plummeted and approached that of Mg after 300 min of testing. This suggested that corrosion of the PP Zn coating had progressed to expose a sufficient area of the underlying Mg such that the dominating electrochemical reaction is Mg corrosion. After 800 min, the noise resistance of PP Zn-coated Mg falls below that of pure Mg, suggesting the increased susceptibility of corrosion due to the galvanic coupling between the Zn coating and underlying Zn. The change in corrosion behavior, from the initially low corrosion rate to the final elevated galvanic corrosion, of PP Zn coatings would not have been captured with LSV, since the test is instantaneous and assumes uniform corrosion.

Consistent with speculations based on SEM and LSV results, ECN data shows different corrosion mechanisms between the ceramic FHA and metallic PP Zn. Fluorinated hydroxyapatite exhibited an increasing noise resistance over time. The noise resistance of FHA becomes higher than that of PP Zn coating and pure Zn after 300 min and 2200 min, respectively. The increased corrosion resistance supports

theory that additional apatite forms when FHA is immersed in physiological solution to not only provide increased corrosion protection over time, but also to compete with corrosion reactions. Whereas LSV testing favored PP Zn due to its lower corrosion rate, ECN testing supports the longevity of FHA coatings.

Figure 47b shows the time-varying corrosion rate of PP Zn and FHA coatings. Pure Zn demonstrated the lowest corrosion rate, while Mg and FHA coatings exhibited the highest and similar corrosion profiles. This revealed that the source of corrosion for FHA coatings is still Mg, rather than dissolution of the apatite coating. The corrosion rate of PP Zn coatings approached the steady state value of Mg corrosion after 1700 min. Even though noise resistance data showed that Zn-coated Mg was more likely to corrode than pure Mg after 800 min, the corrosion rate of the Zn coating remains similar to that of pure Mg. The pitting index for all samples across the entire testing time frame points towards pitting, further emphasizing the utility of ECN testing for understanding localized corrosion. Pitting index values greater than 0.1 indicates that pitting and localized corrosion is the dominant mechanism of corrosion. The shot noise charge emission presented in Figure 47d will be used for statistical fitting by Weibull distributions to understand the pit initiation rate of the samples.

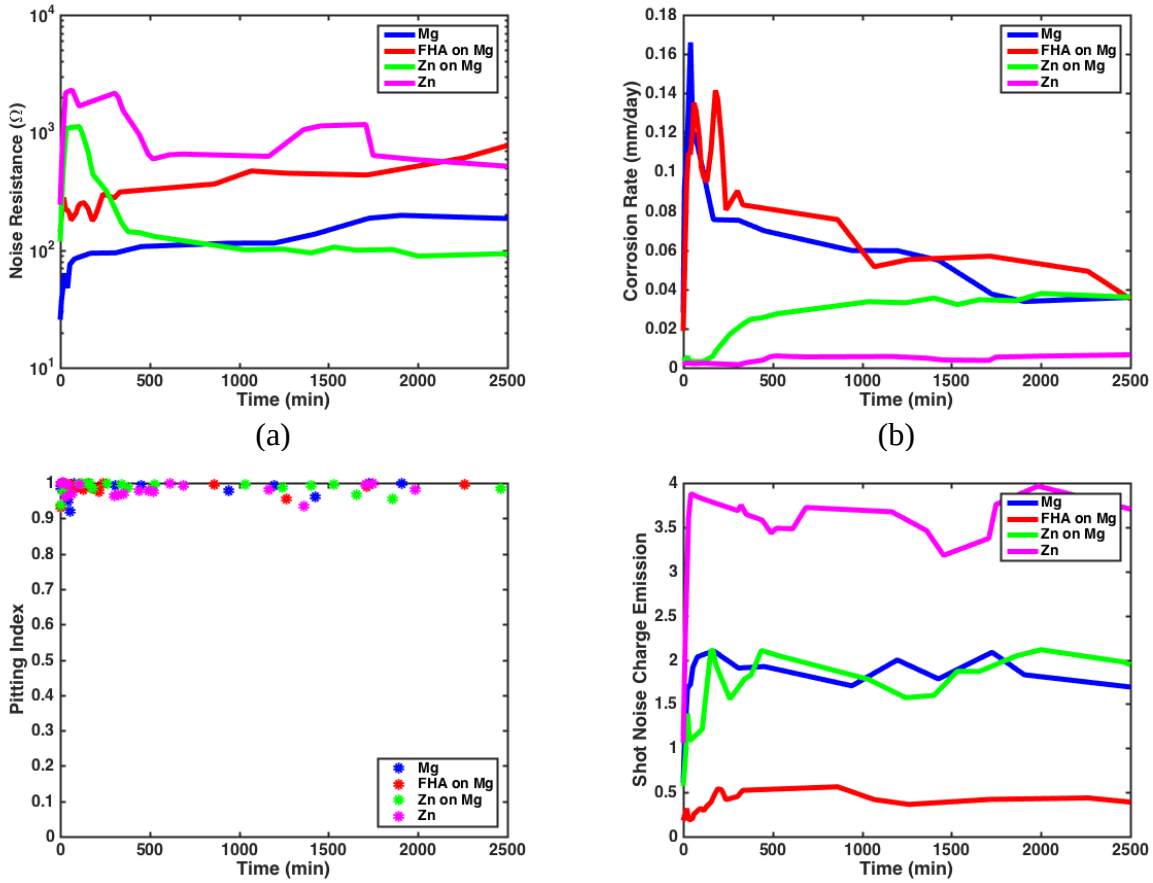

Figure 47 Comparison of the (a) noise resistance, (b) uniform corrosion rate, (c) pitting index and (d) shot noise charge emission, as determined from ECN analysis of Zn-coated Mg, FHA-coated Mg, pure Mg and pure Zn.

Linearized fitting of the ECN data with the Weibull cumulative distribution function are shown in Figure 48. Multiple linear fits indicate multiple phenomenon taking place. The single linear trend shown in Figure 48a revealed that the primary mechanism of Mg corrosion in SBF is pitting. Pure Zn and Zn-coated Mg exhibit two linear trends that correspond to uniform and localized corrosion, such as pitting and stress corrosion cracking. Localized corrosion exhibits lower frequency charge emissions, which are depicted further right on the x-axis. For clarity, the linear data corresponding to localized corrosion is depicted in blue. Interestingly, FHA-coated Mg showed 3 linear trends. In addition to uniform and localized corrosion,

the highest frequency trend might indicate apatite formation or adsorption/desorption reactions on the FHA surface.

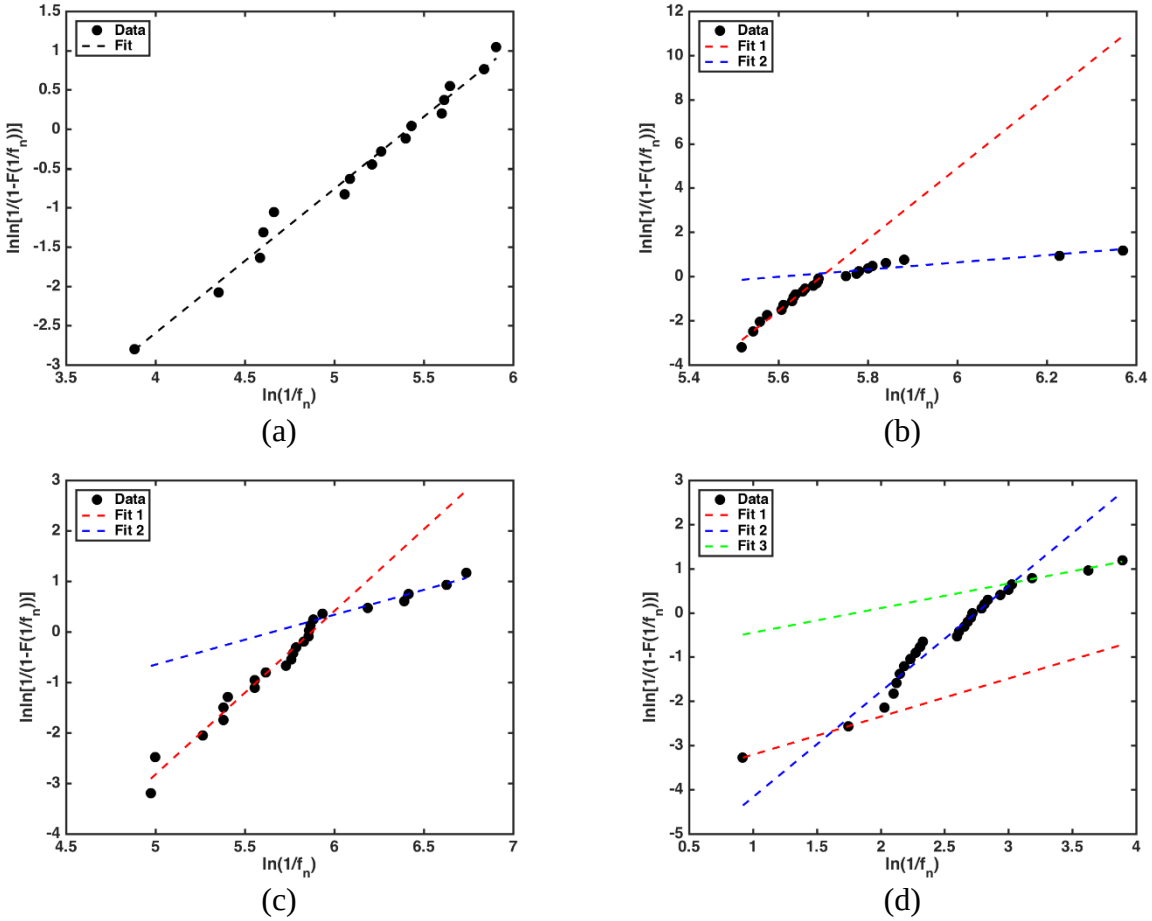

Figure 48 Sequence-dependent analysis of pitting initiation based on ECN data of (a) pure Mg, (b) pure Zn, (c) Zn-coated Mg and (d) FHA-coated Mg. Data shows the linearized Weibull fit of the mean frequency of charge emission.

Interestingly, the pit initiation rates only increased for pure Zn and pure Mg (Figure 49). Fluorinated hydroxyapatite and PP Zn demonstrated decreasing and constant pit initiation rates, respectively. For clarification, the data indicates that the formation of new pits have decreased over time and not that the growth of existing pits has decreased. Scanning electron images, shown in Figure 50, confirmed the findings from sequence-independent and sequence-dependent analysis of ECN data. Specifically, the noise resistance of Zn-coated Mg likely decreased rapidly because a pit formed in the Zn

coating exposed the underlying Mg. In Figure 50a, a hollow Zn shell can be seen, as well as a large opening in the Zn coating. The latter could have formed from the rapid growth of one pit, coalescence of multiple pits and/or the stress-induced breakdown of an opening in the Zn coating (due to rapid corrosion of the underlying Mg). It is speculated that residual Mg remained within the hollow Zn coating because the noise resistance did not return to the expected level for pure Zn. What remained of the Zn coating showed extensive cracking and corrosion within the cracked network, indicating that the integrity of the Zn coating has been jeopardized from the galvanic corrosion. The FHA coating, on the other hand, remained intact with only pinholes distributed across the surface (Figure 51). Further, cracks were only observed propagating from the pinholes. Elemental analysis (not shown) confirmed that bulk presence of Mg within the FHA pits, similar to what was suggested with earlier LSV data—that calcium phosphate coatings protect against Mg corrosion even when cracks and pinholes are present.

In closing, the extensive deposition optimization and corrosion characterization studies have presented two viable corrosion protection coatings for MEMS-scale Mg structures. The orders of magnitude lower corrosion rate, but rapid failure of Zn-based coatings promotes its use in acute biodegradable applications or in settings where the consumption of Zn is desirable. The moderate corrosion rate, which remains 3 orders of magnitude less than that of pure Mg, but longevity of FHA coatings support its use in cases where sustained functionality is desired. Both coatings can be electrodeposited at the micron-scale thickness and are compatible with microfabrication processes. The application of FHA and PP Zn coatings will be explored in the subsequent chapter for biodegradable strain sensors and energy sources.

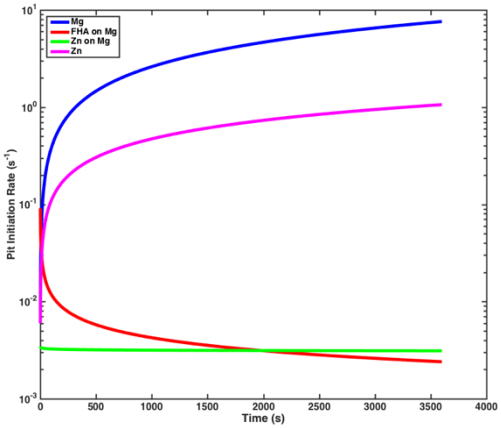

Figure 49 Comparison of the pit initiation rate, as determined by conditional probability and Weibull approximations, of Zn-coated Mg, FHA-coated Mg, pure Mg and pure Zn.

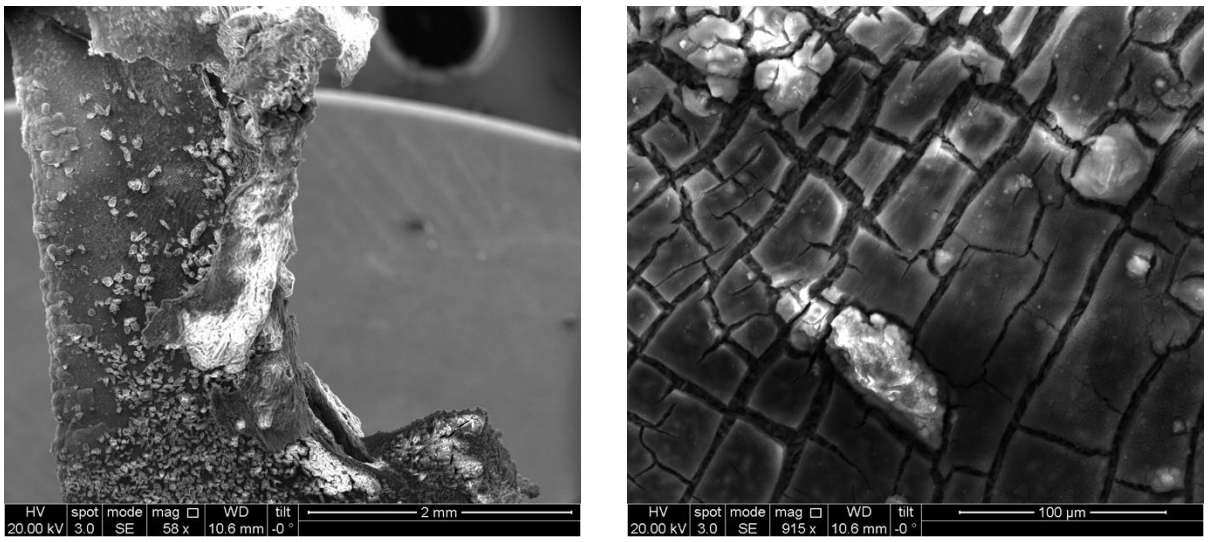

(a) (b)

Figure 50 Non-sequence-dependent analysis of ECN data for Zn-coated Mg, which shows the (a) noise resistance, (b) uniform corrosion rate, (c) pitting index, (d) shot noise charge emission and (e-f) SEM image of sample after testing.

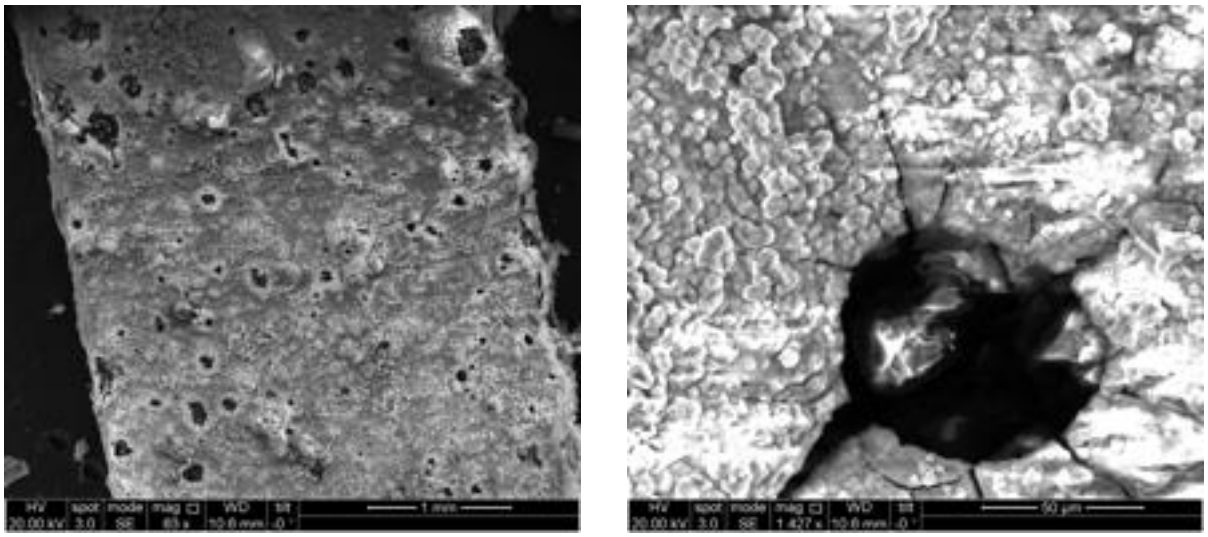

(a) (b)

Figure 51 Sequence-dependent analysis of ECN data for FHA-coated Mg after 48 hours of testing in SBF.

2.3. Polymeric Coatings and Barrier Thin Films for Biodegradable Device Encapsulation

`2.3.1. Introduction

In the previous section, passivation schemes with zinc and hydroxyapatite were explored to hinder the degradation kinetics of magnesium. These coatings were electroplated onto the Mg structures and, hence, the morphology and corrosion behavior of these materials strongly depended on the underlying Mg. Device encapsulation, however, can provide a second line of defense against water and electrolyte ingress and, in this manner, retard corrosion of the device layer. Specifically, thin-film barrier technology has previously been implemented in food and pharmaceutical packaging, as well as in the development of organic electronics. The thin films are typically vacuum deposited to provide a submicron-thick and highly conformal coating [108], [185]–[189]. One of the key distinctions between such barrier encapsulation methods and the Zn, HAP and FHA coatings presented in the previous section is that the barrier thin films

can be deposited onto a broad variety of materials without gross differences in encapsulation performance [108], [190]–[192].

The advent of organic electronics, such as organic light emitting diodes (OLED) and organic photovoltaic transistors (OPVT), has catalyzed advances in the development of barrier film technology. To achieve low cost and mechanical flexibility, organic electronics replace traditional CMOS-based substrates and packaging with polymeric materials [186], [187], [189], [193]. Ultrathin glass has also been explored for its flexibility, transparency and water impermeability. However, material sourcing and processing of ultrathin glass are cost-prohibitive [108]. In contrast, polymeric processing is simple and inexpensive, but polymers exhibit comparatively higher permeation rates to moisture and oxygen [80], [194], [195]. Barrier film technology has been a pivotal strategy in the packaging schemes of organic electronics to retard moisture and oxygen ingress. While barrier films remain widely used in food and pharmaceutical packaging today, the sensitivity of electronics to moisture and oxygen demand more stringent design constraints for OLED devices. To achieve a device lifetime greater than 10,000 hours, the water vapor transmission rate (WVTR) and oxygen transmission rate (OTR) of OLED devices must not exceed 10^{-6} g/m^2/day and 10^{-3} cm^3/m^2/day, respectively. The calculations were estimated based on the amount of water and oxygen needed to degrade the reactive metals used in OLED cathodes and have been experimentally confirmed. In addition, the barrier film must be mechanically robust and stable (i.e., good adhesion, corrosion resistant) during device flexure and throughout the device lifetime. The barrier films must also be compatible with OLED materials and processing, taking into consideration the elastic modulus, thermal stability, UV stability and dimensional stability of the polymer substrates [108], [188], [189].

Given the strong parallels between the design constraints of a biodegradable strain sensor and the packaging requirements of organic electronics, biodegradable device encapsulation can be enhanced by adapting the advance passivation strategies of organic electronics. The ensuing introduction will provide a quantitative explanation of water permeation through barrier films, followed by a review of barrier film materials and deposition techniques.

The principles of water vapor permeation through a barrier film are adsorption, diffusion and desorption [189], [196], [197]. Adsorption is the bonding of a gas to a surface, where the permeate (i.e., water vapor) adsorbs to the barrier surface and dissolves in it. Desorption is the release of a gas from a surface. Both adsorption and desorption can be classified based on the type of bond formed between the gas molecule and the solid surface. Physisorption, such as by Van der Waals forces and dipole-dipole bonds, is a weak interaction with bond strengths less than 0.5 eV/molecule. Chemisorption, such as by covalent bonding, offers stronger bond strengths. Under equilibrium conditions, the permeate concentration at the solid surface is given by:

$$c = S \cdot p \tag{2.34}$$

where c, S and p correspond to the permeate concentration, sorption coefficient and partial pressure of the adsorbed gas over the surface, respectively. According to Henry's law, the sorption coefficient is constant for a given gas-solid combination. The Langmuir model, however, states that the space available on a solid surface is limited to one monolayer of permeate. Consequently, the sorption coefficient is a function of permeate concentration; a monolayer is reached asymptotically with increasing pressure, as shown below.

$$S = \frac{c_m}{a \cdot exp\left[\frac{-H_a}{UT}\right] + p} \tag{2.35}$$

where c_m, a, H_a, U, T and p denote the concentration for a full adsorbate monolayer on the solid surface, an adsorbate-surface system parameter, heat of adsorption, universal gas constant, temperature and partial pressure of the adsorbed gas, respectively. The Brunauer-Emmett-Teller sorption model considers the condensation of gas on the surface, which allows a multitude of monolayers on the solid surface and is given by:

$$S = \frac{g}{(p_{cond} - p) \cdot \left(1 + (g' - 1) \cdot \frac{p}{p_{cond}}\right)} \tag{2.36}$$

where g and g', p_{cond} and p are adsorbate-surface system parameters, saturation pressure of the gas and partial pressure of the adsorbed gas over the surface, respectively. The saturation pressure can be

approximated by Magnus' formula, which relates the saturation vapor pressure of a gas to the temperature under typical atmospheric conditions [189], [196]. Note that in the case of device immersion in a liquid, such as with a biodegradable device under physiological conditions, the adsorption and desorption principles may not apply.

Diffusion of the permeate through a solid barrier layer may proceed through the bulk film or through defects present in the barrier film [188], [194], [197], [198]. The former, termed intrinsic diffusion, is generally neglected in diffusion models of barrier film technology because the WVTR of metallic and inorganic materials is orders of magnitude lower than the WVTR through defects and polymers (Table 13) [108], [199]. Thus, the intrinsic WVTR represents a lower bound for barrier passivation schemes and the ratio of the intrinsic to effective WVTR of a barrier film provides an indication of the defect density of the film. Diffusion in a polymer can be visualized as unit diffusion steps, during which a particle passes over a potential barrier to advance to the next position. The positions can either be holes initially present in the polymer matrix or result from the rearrangement of polymer chains. As polymer chains interact by Van der Waals forces, the activation energy required for rearrangement is low even at room temperature [189].

Table 13 Water vapor transport rate of commercial polymers commonly used in OLED devices. Reported values were experimentally determined for 100-µm-thick polymer films at 37-40˚C [108].

Polymer	**WVTR ($g/m^2/day$)**
Polyethylene (PE)	1.2 – 5.9
Polypropylene (PP)	1.5 – 5.9
Polystyrene (PS)	7.9 – 40
Polyethylene terephthalate (PET)	3.9 – 17
Polyethersulfone (PES)	14
Polyimide	0.4 – 21
OLED requirement	10^{-6}

The diffusion of water through a barrier film can be represented by Fickian diffusion [188], [196], [198]. Fick's first of diffusion states that the diffusion of a permeate is driven by a concentration gradient.

Fick's second law can be derived by coupling Fick's first law with the continuity equation and relates the concentration of a permeate species with time. The first and second laws are:

$$J_z = -D\frac{\partial c}{\partial z} \tag{2.37}$$

$$\frac{\partial c}{\partial t} = D\frac{\partial^2 c}{\partial z^2} \tag{2.38}$$

where J, D, c and t denote the flux of the permeate, diffusion coefficient, permeate concentration and time, respectively [185], [189], [200]. For the initial and boundary conditions that: (1) the initial permeate concentration is zero on the device side of the barrier layer, (2) the permeate concentration outside the barrier layer is constant, and (3) the permeate concentration on the device side of the barrier is always zero (i.e., sink conditions because the diffused water molecule reacts with the device layer immediately), the total amount of water that permeates the barrier layer is characterized by:

$$Q(t) = \frac{D \cdot t \cdot c_1}{\Gamma} - \frac{\Gamma \cdot c_1}{6} - \frac{2 \cdot \Gamma \cdot c_1}{\pi^2} \cdot \sum_{n=1}^{\infty} \frac{(-1)^n}{n^2} \cdot exp\left[-\frac{D \cdot \pi^2 \cdot n^2 \cdot t}{\Gamma^2}\right] \tag{2.39}$$

$$Q(t \to \infty) = \frac{D \cdot c_1}{\Gamma} \cdot \left(t - \frac{\Gamma^2}{6 \cdot D}\right) = J_\infty \cdot (t - t_1) \tag{2.40}$$

where Q, t, D, c_1, Γ and t_1 correspond to the total mass of transmitted permeate, time, diffusion coefficient, ambient concentration, thickness of the barrier film and lag time, respectively [185], [189]. The initial lag time depends on the history of the barrier passivation scheme. If the encapsulant is initially free of permeate, the initial permeate flux reaching the device may be slower than steady state behavior, as shown in Figure 52 [196].

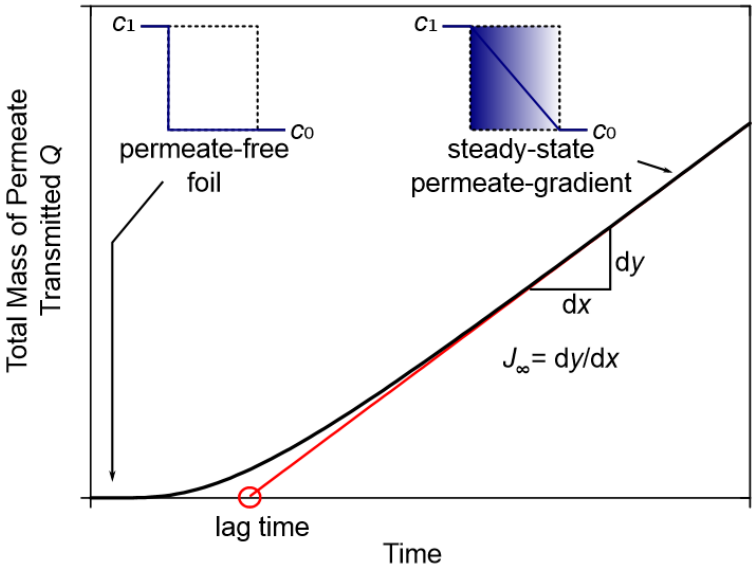

Figure 52 Conceptual schematic illustrating the amount of permeate, Q, transmitted through a barrier film over time [196].

Water permeation through an inorganic barrier primarily proceeds through defects in the film. The defects can form due to the surface roughness of the underlying substrate, dust, as well as particles introduced during the deposition process. For example, irregularity on the substrate surface may shadow adjacent areas, creating nodules in the thin film that propagate with increasing film thickness. At a critical thickness, typically 10-40 nm depending on the material and deposition method, full coverage of the nodules and, hence, substrate surface is achieved. The WVTR typically decreases exponentially with increasing film thickness until the critical thickness, at which the WVTR will drop by several orders of magnitude, but any further increases in thickness will yield sub-exponential improvements in WVTR [108], [185], [200]. Klumbies *et al.* experimentally demonstrated this behavior with atomic layer deposited (ALD) aluminum oxide (Figure 53); the critical thickness was in the 30-40 nm range. In fact, films much thicker than the critical thickness may yield detrimental effects in barrier passivation due to film delamination and mechanical stress, such as with intrinsic film stress and film cracking due to differences in the coefficients of thermal expansion between the inorganic barrier film and the underlying polymer substrate. As nodules can arise from surface irregularities that shadow a surface larger than the diffusion range and the diffusion

range increases exponentially with time, the defect density of a barrier thin film typically decreases with increasing deposition temperature [185], [189]. However, elevated processing temperatures are incompatible with most polymers and, hence, limits the utility of phenomenon for OLED and biodegradable device encapsulation.

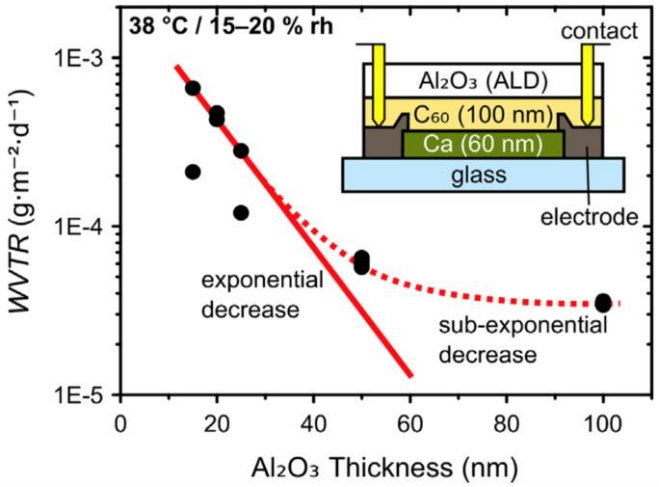

Figure 53 WVTR versus thickness of atomic layer deposited alumina, illustrating the exponential reduction in WVTR below the critical thickness and the sub-exponential improvements observed above the critical thickness [185].

Defects in an inorganic barrier film can be classified into three categories, as illustrated in Figure 54. Macro-defects are characterized by defect diameters greater than 1 nm. Permeate flux through a macro-defect does not interact with the barrier material, resulting in an activation energy similar to that of the bare polymer substrate. Nano-defects are 0.3-1.0 nm in diameter and permeate flux through nano-defects depends on interaction with the barrier film. Consequently, the activation energy associated with nano-defects is typically greater than that of the bulk polymer substrate. Oxygen transport typically proceeds via macro-defects, but water can also permeate nano-defects, since water can condensate in small pores and even corrode the barrier layer. Lattice interstices are the smallest of the defect categories, with defect diameters in the 0.1-0.3 nm range. Although the density of lattice interstices may be large, lattice interstices do not appreciably contribute to water vapor or oxygen transport through barrier films because

water and oxygen molecules are too large; the activation energies for transport are, thus, very high at temperatures relevant to organic and implantable electronics [185], [189], [193].

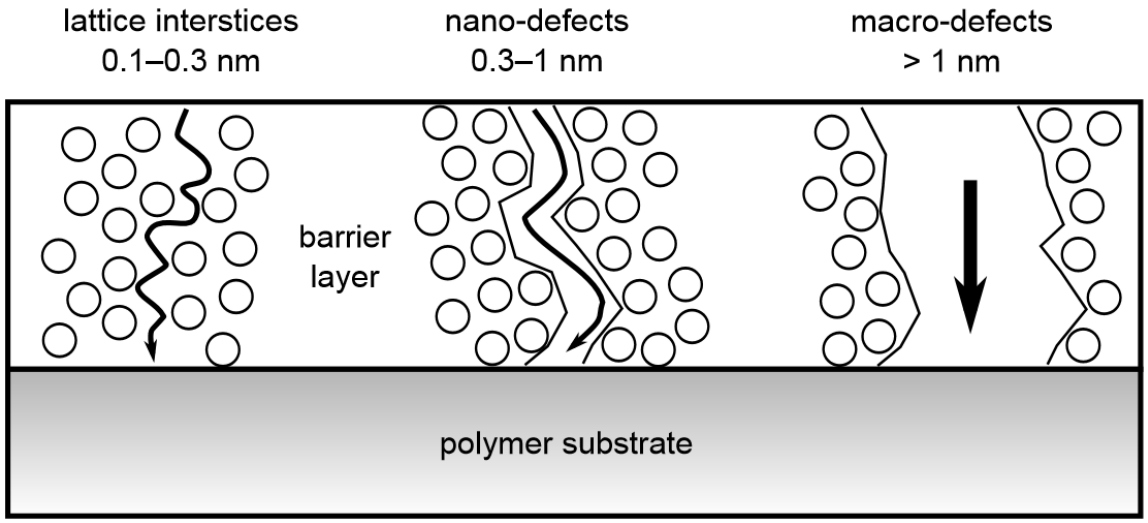

Figure 54 Classification of barrier film defects based on size [189].

Several models aim to capture the defect-assisted permeation of water through barrier films, as outlined in Figure 55. The ideal-laminate model assumed homogenous diffusion across the film surface and a constant permeation coefficient at each position of the barrier layer, as given by:

$$\frac{\Gamma_{stack}}{P_{stack}} = \sum_{i=1}^{n} \frac{\Gamma_i}{P_i} \tag{2.41}$$

where n, Γ and P correspond to the number of laminated layers, thickness and permeation coefficient, respectively. The coverage model limits barrier permeation to occurring only through areas exposed by film defects. However, the coverage model does not address the observed phenomenon that permeation through large defects is smaller than through many small defects, which occurs because radial diffusion in the polymer substrate occurs at the defect edges and, hence, scales with defect perimeter [189]. The pinhole model accounts for this behavior and assumes a low adsorbate concentration on the surface, so that Henry's law applies. The steady state flux is:

$$J_\infty = P \cdot \frac{\Delta p}{\Gamma} \cdot \frac{A_d}{A_{tot}} \cdot \left(1 + 1.18 \cdot \frac{\Gamma}{d_0}\right) \tag{2.42}$$

where J_∞, P, Δp, Γ, A_d, A_{tot} and d_0 refer to the steady state flux, permeation coefficient, partial pressure difference, barrier film thickness, total area of the defects, surface area of the barrier film and nominal diameter of the defect, respectively. The pinhole model is valid for defect distances greater than triple the film thickness [108], [189], [196], [197], [199]. However, pinhole interactions reduce the overall permeation rate for smaller defect distances, as addressed by the pinhole-interaction model.

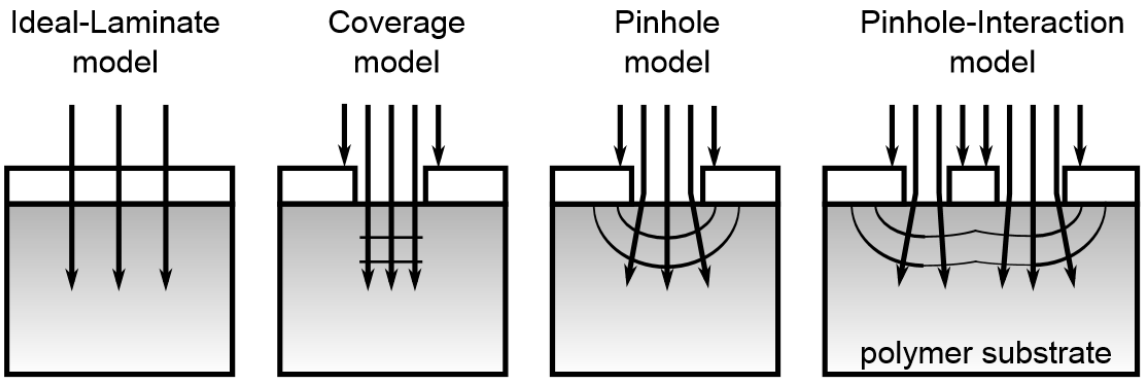

Figure 55 Defect permeation models. All assume negligible interaction with the barrier material and, hence, apply only to macro-defects [189].

An alternative approach is to simplify defect-assisted water permeation to a one-dimensional radial diffusion problem. In this case, Fick's second law is given by:

$$\frac{\partial c}{\partial t} - D \cdot \frac{1}{r} \cdot \frac{\partial}{\partial r}\left(r \frac{\partial c}{\partial r}\right) \tag{2.43}$$

where D, c, and r correspond to the diffusion coefficient, permeate concentration and radial distance from the center of a given pinhole, respectively [199]. While this system models a radial diffusion in a single pinhole and ignores pinhole-pinhole interactions, the model predictions were experimentally validated by Kim *et al.* and provide insight that can guide subsequent data analysis in this section. Applying a semi-infinite boundary condition, the concentration is zero as the radial distance approaches infinite (i.e., $c = 0$ as $r \rightarrow \infty$); sink conditions are assumed based on the fast reaction kinetics of water with the

device layer. The boundary condition at the center of a pinhole (i.e., r = 0) is unclear. Two cases were examined for the boundary condition at r = 0: (1) constant concentration (i.e., $c = c_0$) and (2) constant total flux (i.e., $Q = Q_0$). An analytical solution for the first case can be obtained by the method of separation of variables and is provided below:

$$c = \sum_{n=1}^{\infty} exp(-\lambda_n^2 Dt) \cdot \left[c_{1,n} J_0(\lambda_n r) + c_{e,n} Y_0(\lambda_n r)\right] \tag{2.44}$$

where the solutions are expressed by Bessel functions of the first (J_0) and second (Y_0) order. The second case can be solved with a similarity function; the solution and similarity function, respectively, are given by:

$$c = c_0 \int_{\eta}^{\infty} \frac{1}{\eta'} exp(-\eta'^2) \partial\eta' \tag{2.45}$$

$$\eta = {}^{r}/_{\sqrt{4Dt}} \tag{2.46}$$

The effect of the different boundary condition can be compared in the contour profiles shown in Figure 56. The diffusion rate decreases more rapidly with the constant concentration boundary condition. Experimental results for water permeation through individual pinholes are presented in Figure 56c-d [199]. The data was obtained by optical measurements of WVTR through a barrier comprising 100 nm of silicon nitride and 200 nm of polymer (CYTOP, AGC Chemicals). The radial growth of pinholes over time resembles the contour plot shown in Figure 56b, where the diffusion rate decreases more gradually, suggesting that local degradation at a pinhole proceeds by radial diffusion with a constant total flux. The corresponding growth in pinhole area is plotted in Figure 56d and confirms that the permeation rate in a pinhole is constant over time for barrier films deposited directly on top of the active material [199].

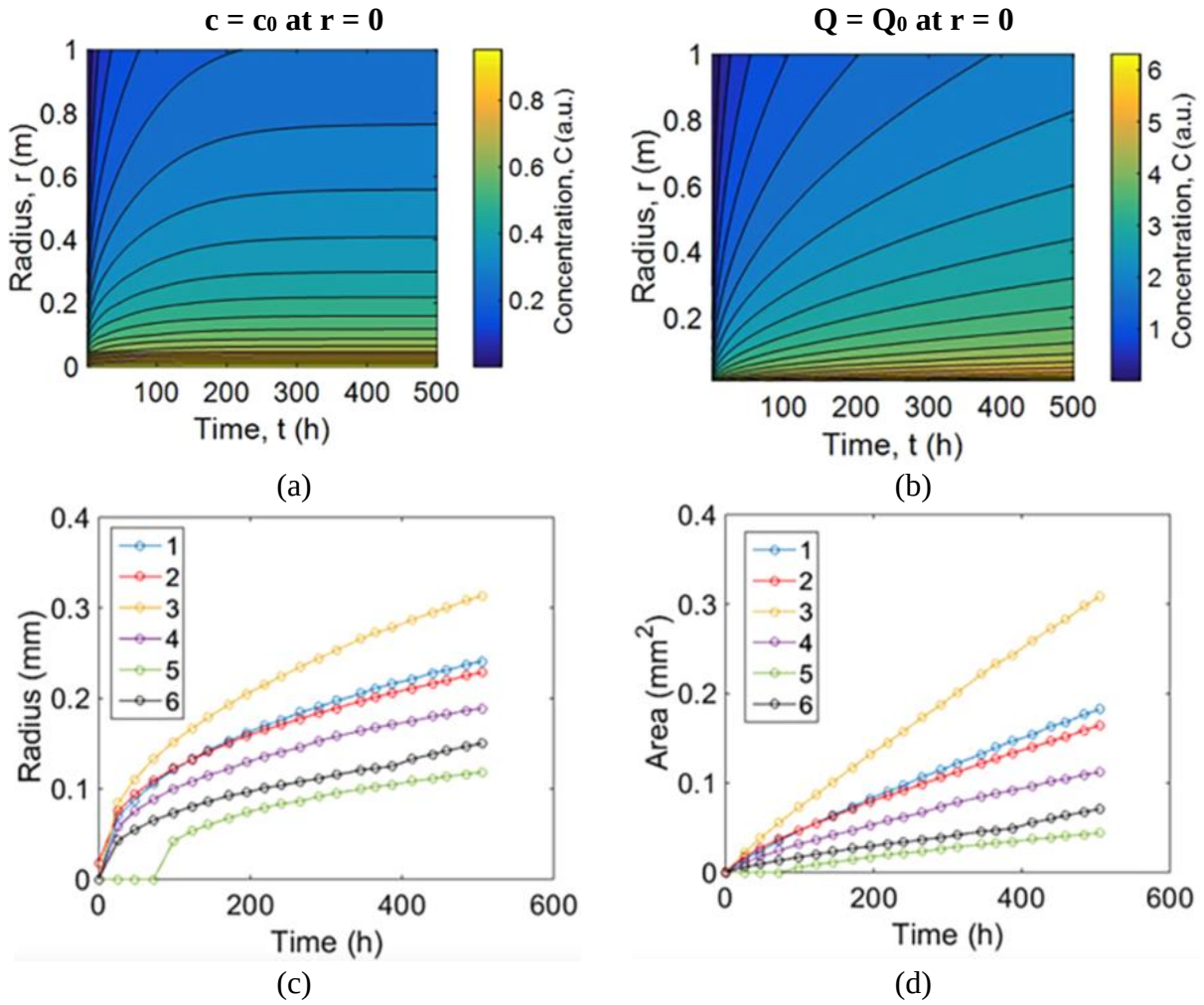

Figure 56 (a-b) Computational and (c-d) experimental results for one-dimensional radial diffusion of water through a pinhole. Contour plot of concentration on a radius versus time plane for the boundary condition of (a) constant concentration and (b) constant total flux at the center of the pinhole and sink conditions as the radial distance from the pinhole center approaches infinite. Experimental results were determined from optical measurements of WVTR through 100 nm of silicon nitride and 200 nm of polymer (CYTOP) [199].

While the WVTR of inorganic barriers is orders of magnitude lower than that of polymers, water permeation through single barrier films remains orders of magnitude larger than OLED requirements. The WVTR of single films is approximately 10^{-3} g/m^2/day, excluding atomic layer deposited materials [108]. To overcome this limitation, multi-layers comprising alternating layers of inorganic and organic thin films are deposited to create a tortuous path for water transport, as depicted in Figure 57 [186]–[188], [191]. A polymer and inorganic barrier pair is termed a dyad. The polymer layers smooth the surface, fill defects in

the underlying inorganic layer and decouple defects between successive inorganic layers. For these reasons, direct paths for water permeation from the outer environment through the entire encapsulation become rare and even single dyads exhibit improved barrier performance compared to an inorganic barrier alone [187], [200]. While increasing the number of dyads can drive down the WVTR, minimizing the dyads necessary to satisfy the water permeation design constraint is desirable due to the cost, time and throughput associated with multi-layer passivation processing. Further, the reduction in WVTR associated with each dyad is typically non-linear, where diminishing returns are observed with WVTR for each successive layer deposited. However, additional dyads can prolong the initial lag time to reaching steady state conditions and, in this manner, extend the device lifetime without further reductions in WVTR (Figure 58). Studies have shown that the advantages of multi-layer barrier schemes still limit the WVTR to 10^{-4} g/m^2/day if the inorganic films feature a defect density greater than 500 defects/mm^2 for defects smaller than 1 µm in diameter. Delamination is another challenge with implementing multi-layer barriers and may arise due to thermal-mechanical stress and low adhesion between organic and inorganic layers [189], [192], [196].

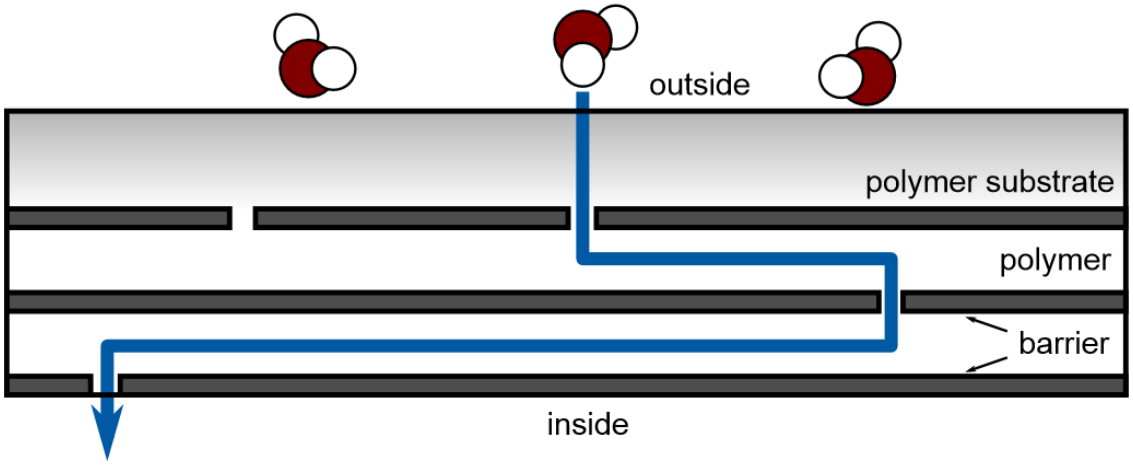

Figure 57 Illustration of water permeation through a multi-layer passivation scheme, which requires diffusion through a tortuous path [189].

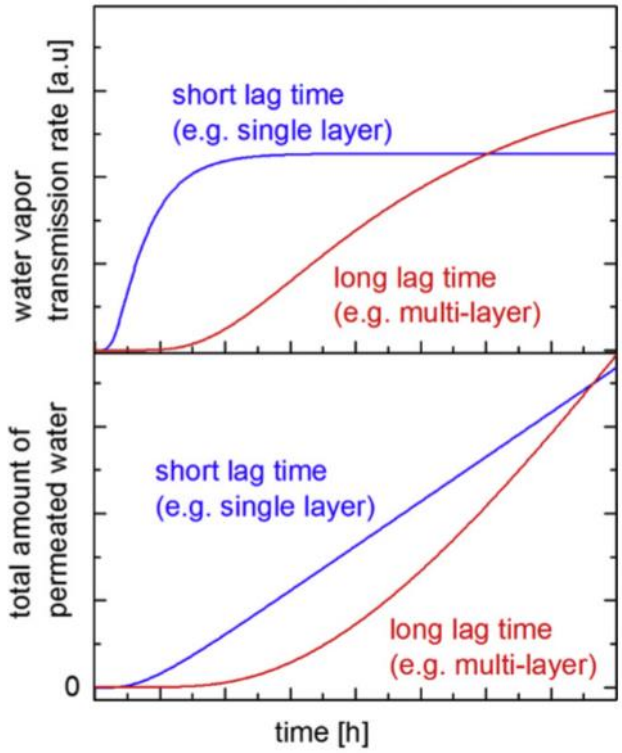

Figure 58 Schematic illustrating the initial transient effects of water permeation through single- versus multi-layers [196].

Greener *et al.* examined the organic polymer layer in optimizing WVTR through multi-layers. The authors modeled the multi-layer barriers with a defect-assisted diffusion model, where the inorganic layers are impermeable except through pinholes and the diffusion through organic layers is Fickian. As expected, decreasing the nominal defect size, increasing the average distance between pinholes and/or decreasing the diffusion coefficient of water through the polymer reduces the WVTR. Interestingly, two regimes in water transport were observed. For polymer film thicknesses less than the nominal defect size, increasing the polymer thickness corresponded to a linear increase in WVTR in logarithmic-space. This suggested that within this regime, diffusion through the polymer dominates water permeation. For polymer films thicker than the nominal defect size, increasing the polymer thickness did not significantly increase the WVTR, suggesting that water permeation is dominated by diffusion through the pinholes. The authors presented the

barrier improvement factor (BIF) as a metric for evaluating the effectiveness of multi-dyad barriers as compared to single inorganic films. The BIF may be calculated as follows [197], [201]:

$$BIF = \frac{WVTR_{single}}{WVTR_{multi}} \tag{2.47}$$

The key findings are summarized in Figure 59, which indicate that the tortuous path of multi-layers applies only for polymer films less thick than the nominal defect size. Figure 59 shows that the rate of barrier improvement with each additional dyad (i.e., slope) is significantly greater with polymer films thinner than the nominal defect size [201].

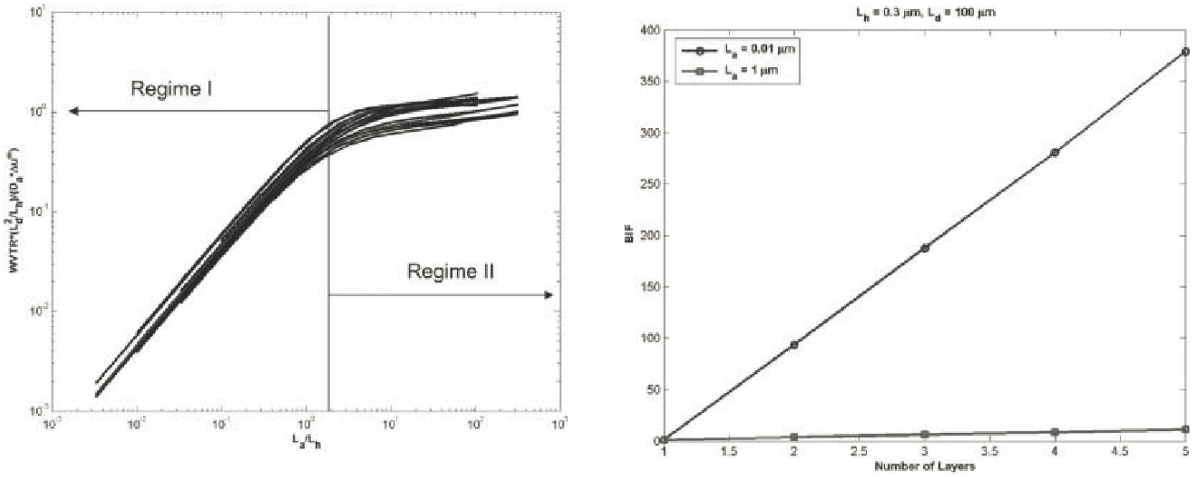

(a) (b)

Figure 59 Computational modeling results illustrating the effect of polymer film thickness, relative to nominal defect size, on WVTR through multi-layer barriers. L_a and L_h refer to the polymer film thickness and nominal defect size (i.e., diameter), respectively.

The importance of the polymer film thickness for each dyad within a multi-layer structure places an emphasis on the polymer selection and processing capability. Ultraviolet-curable acrylates have most commonly been used as the organic layer [200], [201]. For example, BARIX is a commercial acrylate-based polymer produced by Vitex. The BARIX precursor is flash evaporated onto the substrate surface and then UV-cured. The vacuum deposition process in a cleanroom facility is desirable for minimizing dust particles, as well [186], [200]–[202]. ORMOCER is a water-based polymer introduced by Fraunhofer that has gained

popularity due to its surface-smoothing capability. However, the aqueous precursor might introduce water into the multi-layer system and detract from the water permeation lag time. The deposition process, whether evaporation, spin casting or spray coating, must offer good control of film thickness in order to ensure consistent barrier performance [108], [196].

The material and deposition techniques for inorganic barriers have largely extended from traditional CMOS processing. Silicon dioxide, silicon nitride and silicon oxynitride have been explored for barrier passivation of OLED devices [196], [197], [200]. While bulk silicon dioxide is effectively impermeable to moisture and oxygen, barriers deposited by thin film deposition methods contain defects and water can permeate the films by defect-assisted diffusion, as discussed previously. The oxides of cerium, sodium, magnesium, aluminum, zirconium, titanium and tantalum have also been investigated for barrier protection. It has been found that materials that do not react (i.e., corrode or dissolve) to moisture or oxygen show similar barrier performance [108]. The deposition technique plays a greater role in determining the WVTR and OTR of inorganic thin films. Thin film deposition methods bifurcate into two general categories: physical vapor deposition (PVD) and chemical vapor deposition (CVD). Evaporation and sputtering are commonly used PVD techniques (Figure 60a-b), with equipment available in most commercial and academic fabrication facilities. As the name implies, films deposited by evaporation undergo a phase change from a solid (i.e., the source material) to a vapor. The source may be heated thermally or with an electron-beam and the vaporized material collects on the substrate surface, where it condenses and returns to a solid state. Evaporation is a “line-of-sight” deposition technique and does not conformally coat the topography on a substrate surface, as depicted in Figure 60c. Sputter deposition proceeds by applying a voltage across two electrodes in the presence of a gas species (e.g., nitrogen or oxygen) to achieve a plasma. The gas species accelerate towards a target, or source material, and knocks off some of the target material. These target particles collide with each other, as well as with the gas species, in a cascade until it arrives on the substrate surface. Due to the ion bombardment and avalanche process, sputter deposited films can cover step heights and non-planar substrates (Figure 60c). The deposition power,

process pressure and gas species control the sputtered film morphology [203], [204]. Evaporation is more commonly used in food packaging due to its lower cost and higher throughput, but sputter deposition offers denser and higher quality films [108]. The WVTR of evaporated and sputtered films are approximately 10^{-1}-10^{1} g/m^2/day and 10^{-2} g/m^2/day, respectively.

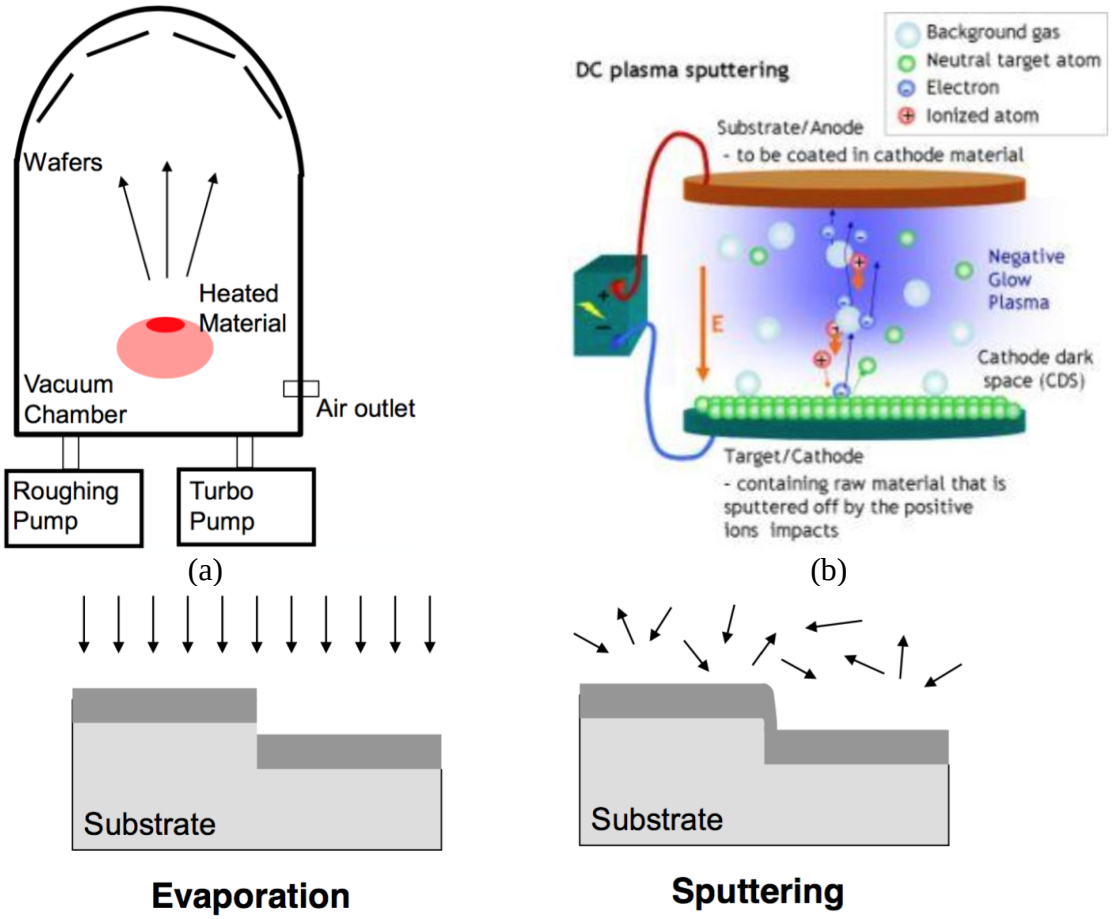

Figure 60 Schematics illustrating the principles of operation for (a) evaporation and (b) sputter deposition, as well as (c) a comparison of the surface coverage of the deposited film [203], [204].

Plasma-enhanced chemical vapor deposition (PECVD) and atomic layer deposition (ALD) are chemical vapor deposition techniques for inorganic thin films (Figure 61). The presence of a plasma in PECVD processes drives chemical reactions that would not otherwise be possible at low temperatures. This is favorable for processing with polymeric substrates, whose glass transition and melting temperatures often

prohibit processing at elevated temperatures. Atomic layer deposition was first developed in the 1970s by the semiconductor industry for use as ultrathin, highly conformal dielectrics [194]. The ALD process is based on surface-limited reactions that result the deposition of one monolayer per ALD cycle. Two reactant gases are sequentially pulsed into a reaction chamber, each separated by a period of purging with inert gas (i.e., nitrogen). The exothermic nature of the reaction supports the operation of most ALD processes at lower, polymer-compatible temperatures. However, decreasing the process temperature corresponds to an increase in the defect density of the film and typically require longer pulse and purge times [185], [189]. The defect density also depends on the surface roughness of the substrate, again highlighting the importance of a smooth polymer layer in multi-layer processing. The WVTR of PECVD and ALD films are typically in the 10^{-2} g/m^2/day and 10^{-4}-10^{-5} g/m^2/day ranges, respectively [108], [185], [187], [189], [193], [194], [196]. Table 14 summarizes the water permeation properties of inorganic thin films deposited by the various PVD and CVD methods discussed. As shown, ALD films offer the best barrier performance, with water permeation rates that are orders of magnitude lower than other methods.

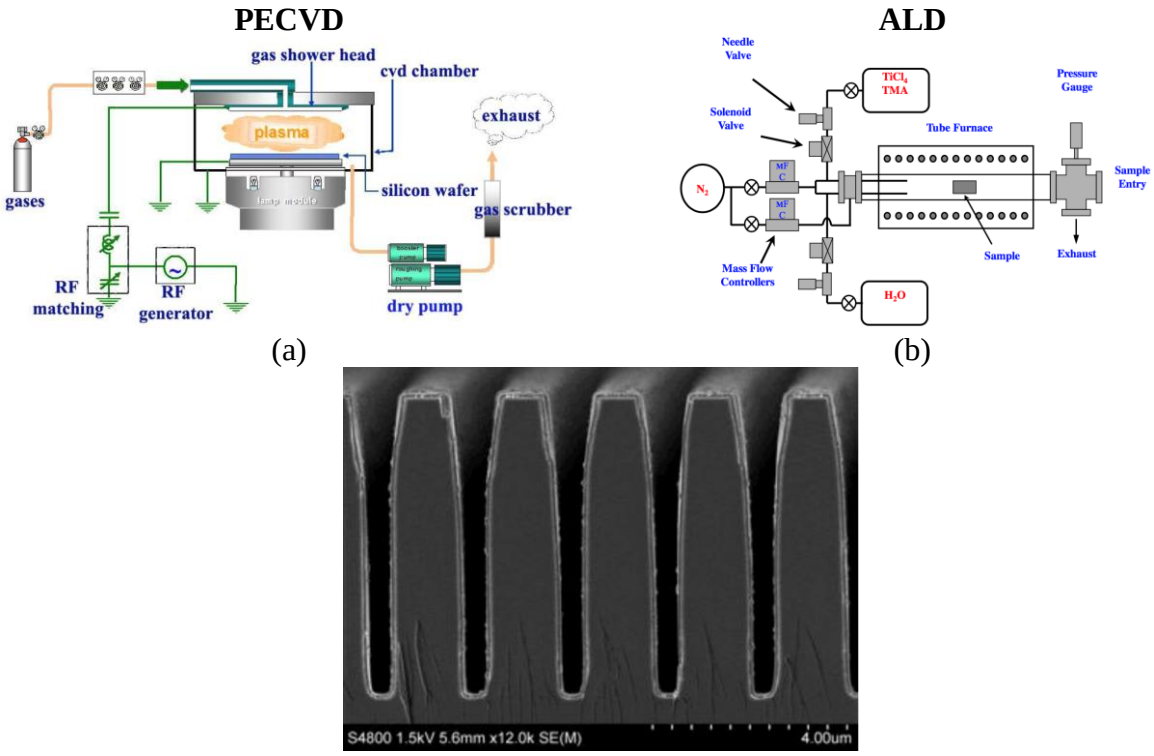

Figure 61 Conceptual illustration of the (a) PECVD and (b) ALD deposition processes. Both are chemical vapor deposition techniques that yield conformal coatings. (c) Scanning electron micrograph of germanium antimony telluride deposited on high aspect ratio trenches by ALD [203], [204].

Table 14 Summary of lower limits in WVTR achieved with various PVD and CVD processes [108], [185], [187], [189].

Deposition Method	**WVTR ($g/m^2/day$)**
Evaporation	10^{1}-10^{-1}
Sputtering	10^{-2}
Plasma-enhanced chemical vapor deposition	10^{-2}
Atomic layer deposition	10^{-4}-10^{-5}

Material diversification is more limited with ALD and PECVD systems, since both are chemical processes that require specific precursor gases for deposition and there are a limited number of gas lines supplied to a given piece of equipment. Hence, it may be difficult to deposit a particular material by CVD in communal fabrication facilities or in highly specialized cleanrooms. For example, whereas silicon

dioxide and aluminum dioxide, or alumina, are materials commonly available on ALD systems in academic research, magnesium fluoride (MgF2) and magnesium oxide (MgO) are not. This presents a limitation in the investigation of ALD-deposited biodegradable barrier films for use in transient implantable devices. As the barrier performance of an inorganic material is determined primarily by the deposition technique, however, an ALD-deposited non-degradable material may serve as a surrogate in the investigation of biodegradable barrier technology. Such an approach is pursued in this study, where ALD-deposited alumina is examined as a surrogate for ALD-deposited MgF_2. The results are compared to sputter deposited MgO and MgF_2 both as single and multi-layers for barrier protection against water permeation.

The atomic layer deposition of alumina and magnesium fluoride have been experimentally demonstrated in literature [185], [189], [205], [206]. Trimethylaluminum (TMA) and water are precursors for the atomic layer deposition of alumina. As shown in Figure 62, the surface is initially hydrated to promote the adhesion of TMA and the deposition proceeds by two chemical reactions that are repeated iteratively until the desired film thickness is achieved [185], [189]:

$$AlOH + Al(CH_3)_3 \rightarrow AlOAl(CH_3)_2 + CH_4$$

$$AlCH_3 + H_2O \rightarrow AlOH + CH_4$$

Given the ultrathin and conformal property of ALD films, alumina layers as thin as 10 μm have been implemented to coat MEMS-based micro-engines and as transparent dielectrics in optical applications [189].

Magnesium fluoride can also be deposited by ALD. Since most metal oxides intrinsically absorb energy in the deep and vacuum ultraviolet wavelengths, MgF_2 is an appealing alternative for low-loss optical components in excimer lasers. Magnesium fluoride is a dielectric with a wide band gap and low refractive index [205], [206]. Atomic layer deposition of MgF_2 has been demonstrated with magnesium β-diketonate ($Mg(thd)_2$) and tantalum pentafluoride (TaF_5) as the precursors. Pilvi *et al.* achieved conformal film growth and the correct stoichiometry within the temperature range of 250-400°C. However,

deposition at lower temperatures resulted in poor film adhesion and increased thickness variations. The surface roughness was approximately 7 nm [206]. Hennessy *et al.* later showed that MgF_2 can be also deposited by ALD with bis(ethylcyclopentadienyl)magnesium ($Mg(CpEt)_2$) and anhydrous hydrogen fluoride (HF) as the precursor materials. The latter approach supported deposition at lower temperatures through the use of anhydrous HF; reactions with metal-fluoride precursors do not proceed at temperatures below 200-250°C. The high volatility and reactivity of $Mg(CpEt)_2$ further supported operation at lower processing temperatures. Results showed self-limiting and highly uniform film growth. The surface roughness was approximately 0.5 nm for films deposited at 100°C [205].

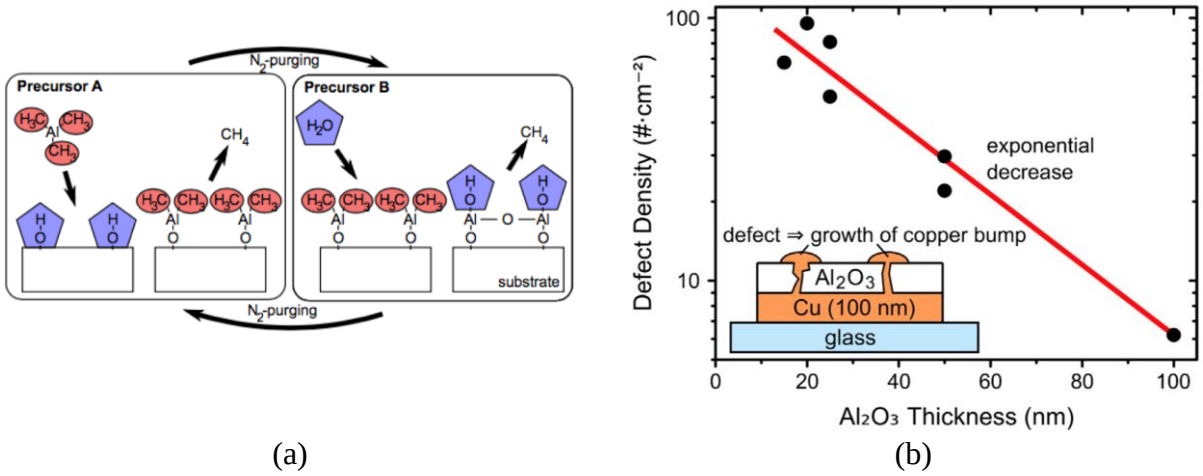

(a) (b)

Figure 62 (a) Schematic of the chemical reaction that occurs during the ALD-deposition of alumina and (b) a semi-logarithmic plot of defect density versus film thickness for alumina deposited at 80℃ [185], [189].

While OLED devices require barrier protection from moisture and oxygen, the encapsulation of biodegradable devices featuring magnesium as the active material should primarily protect against water ingress. Further, biodegradable devices operating on the principle of piezoresistivity do not require optical transparency in the encapsulation layers. This relieves some of the design constraints associated with OLED encapsulation. This section explores barrier film technology using biodegradable materials with the aim of hindering water permeation and, thereby, corrosion of the active device layer. Specifically, magnesium oxide and magnesium fluoride will be evaluated as inorganic barriers. As MgO and MgF_2 can only be sputter deposited in the available fabrication facility, ALD-deposited Al_2O_3 will serve as a surrogate in

exploring biodegradable barriers deposited by atomic layer deposition. Polycaprolactone (PCL), polyglycerol sebacate (PGS) and poly-L-lactide (PLLA) will be evaluated as organic barriers. Single layer and multi-layer passivation schemes will be explored to, ultimately, determine whether barrier technology comprising biodegradable materials can effectively hinder moisture ingress into transient implantable devices.

2.3.2. Water Permeation of Biodegradable Polymers

In order to adapt barrier film technology to biodegradable materials, three questions must be addressed. First, will the degradation behavior of the biodegradable materials interfere with their ability to hinder water permeation? The degradation kinetics of the biodegradable materials selected for barrier passivation should be sufficiently slow, so that within the intended time frame of study, the biodegradable material has undergone negligible film breakdown. Otherwise, the structural and dimensional changes of the degrading film will provide a more direct route for water transport and possibly even rupture passivation schemes above and below the film (i.e., in multi-layers). Second, does water permeation differ appreciably between biodegradable and non-degradable materials? Table 13 and Table 14 presented the WVTR of commercial non-degradable polymers and inorganic films based on different thin film deposition techniques, respectively. Given the susceptibility of biodegradable materials to film breakdown in an aqueous environment, the WVTR of biodegradable polymers might be higher than that of non-degradable polymers. Further, the assumption that the intrinsic WVTR of inorganic thin films is orders of magnitude lower than defect-assisted WVTR might be invalid for biodegradable inorganic materials. Last, do the processing limitations of biodegradable materials restrict their integration as multi-layer barriers and with the fabrication of biodegradable devices?

To assess these questions, this section will begin by examining the WVTR of select biodegradable polymers and their performance will be compared to that of non-degradable organic materials. Polycaprolactone and poly-L-lactide are commercially-available and FDA-approved polymers, whereas polyglycerol sebacate must be synthesized in-house for use. The molecular structure of PCL, PGS and

PLLA are presented in Figure 63a-c. All three polymers degrade by hydrolytic cleavage to the polymer backbone, an example of which is shown in Figure 63d [78], [80], [104], [168], [207]–[218]. Polycaprolactone breaks down into 6-hydroxylcaproic acid and acetyl-coenzyme A by hydrolysis. The products are subsequently eliminated from the body via the citric acid cycle [168]. The specific degradation time of the polymers vary based on the molecular weight of the formulation used, but the degradation time of bulk PCL and PLLA typically exceeds 24 months [80], [168], [195]. The degradation lifetime of PGS is on the order of a few months. Whereas PCL and PLLA are thermoplastics, PGS is a thermoset that is cured under vacuum at 130˚C for 48 hours. Further, PGS is an elastomeric material that can withstand more than 30% tensile strain prior to break [211], [212], [214].

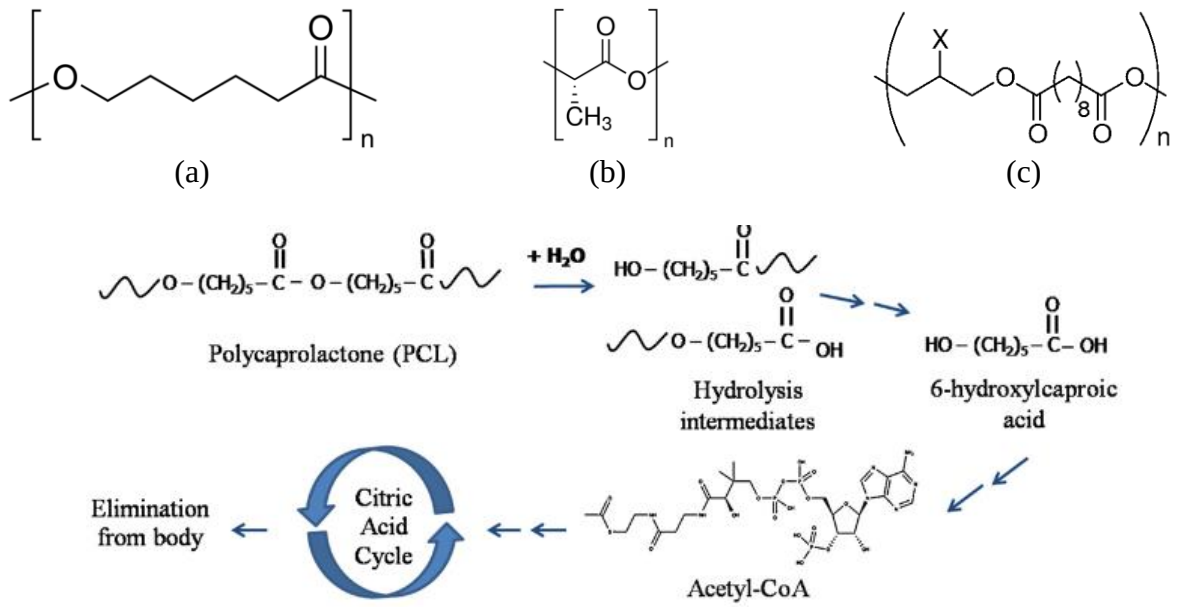

Figure 63 Molecular structure of (a) PCL, (b) PGS and (c) PLLA and (d) the biodegradation cycle of PCL via hydrolysis [80], [168], [195].

The ideal WVTR measurement technique depends on the barrier design. As observed in Figure 64 and Table 15, the WVTR of various organic and inorganic materials vary across 6-8 orders of magnitude. Testing guidelines for high WVTR materials (i.e., 10^0-10^2 g/m^2/day), such as polymers, are presented in

ASTM E96 and F1249 [80], [189], [195], [196]. Testing setups can easily be configured with standard laboratory equipment, but commercial systems are also available for more standardized testing. The WVTR characterization of PCL, PGS and PLLA was performed in accordance with ASTM guidelines. Briefly, the barrier layer of interest serves as a permeable membrane separating two chambers. The first chamber introduces water vapor at a set point temperature and relative humidity. Sink conditions are assumed in the second chamber, where desiccant is placed to absorb water that has permeated the barrier membrane. The desiccant is weighed at regular time intervals throughout the testing period. The WVTR can be determined by the rate of mass change over time, normalized by the area of the barrier membrane. The resolution of the technique depends on the testing parameters, such as the dimensions of the barrier membrane, the amount of desiccant used and the resolution of the mass balance used for measurement. In this study, 400-µm-thick PCL and PGS membranes, as well as PLLA membranes ranging from 250-350 µm in thickness, were characterized for water permeation room temperature and 100% relative humidity [80].

The WVTR of select biodegradable polymers are presented in Figure 64; the results are summarized in Table 15. All samples exhibited a constant flux, as indicated by the linear trend observed with the mass of permeated water over time. Overall, the WVTRs of PCL, PGS and PLLA were in the 10^1 $g/m^2/day$ range. While the observed WVTRs were higher than those of most non-degradable polymers used in barrier applications by approximately 1 order of magnitude, the water permeation performance remained within the expected range for organic materials. This suggested that on the timescale of days, the degradation kinetics of the selected biodegradable polymers do not appreciably impact their barrier performance. Interestingly, PGS, which features the shortest degradation time, exhibited the highest WVTR; its WVTR was more than 250% larger than that of PCL for the same film thickness. It was previously hypothesized that the WVTR of PCL would be the lowest due to its hydrophobicity, which hinders water absorption, as indicated by swelling ratio data reported in literature. However, the WVTR of 400-µm-thick PCL was 19.2 $g/m^2/day$, which is 43% higher than the WVTR of 350-µm-thick PLLA. This may be attributed other factors that impact water diffusion, such as molecular chain length and the activation

energy required for polymer chain rearrangement. In the context of bulk device encapsulation, the results show that PLLA is the best candidate on the basis of water permeation. Additional properties, such as physical and mechanical, must also be considered when ultimately deciding on the polymer for bulk encapsulation. In the context of multi-layer barriers, the WVTR of the organic layer is less important since the alternating layers are intended to present a tortuous path for water transport, rather that bulk transport across the thickness of the film. Hence, both PCL and PLLA should be considered for biodegradable barrier films

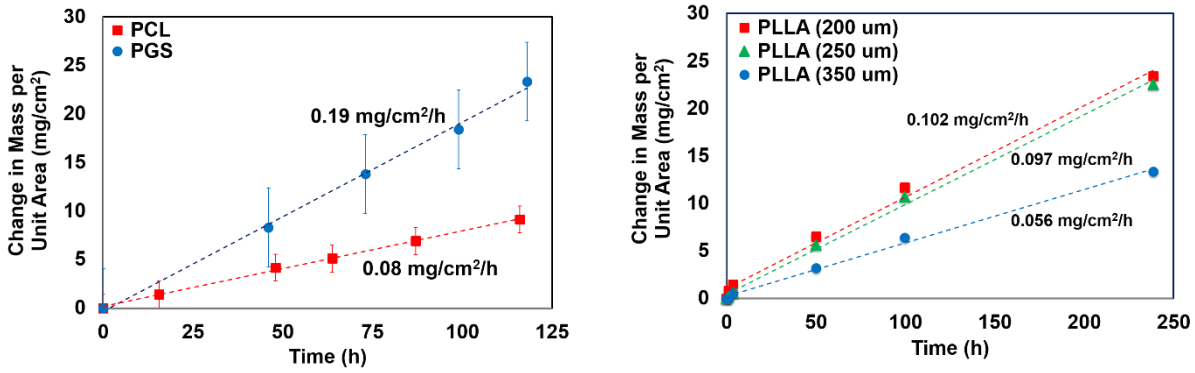

(a) (b)

Figure 64 Water vapor transport rate of (a) 400-µm-thick PCL and PGS membranes (data are mean ± SEM for n = 3) and (b) PLLA membranes of varying thicknesses [79], [124].

Table 15 Summary of the WVTR across PCL, PGS and PLLA membranes of various thicknesses.

Polymer	**Thickness (µm)**	**WVTR (g/m²/day)**
PCL	400	19.2
PGS	400	45.6
PLLA	200	24.5
	250	23.3
	350	13.4

2.3.3. Fabrication and Characterization of Thin Film Barrier Passivation

Magnesium oxide and magnesium fluoride were evaluated as biodegradable thin film barriers. Although both materials have previously been considered as thin film barriers, they were examined under different conditions. It was imperative to ensure that the dissolution rate of MgO and MgF_2 do not prevent their application in barrier technology when the samples are entirely immersed water rather than exposed to water vapor at 85% relative humidity (a commonly selected testing condition).

The fragility and the significantly lower permeation rate of inorganic thin films precludes their characterization using the ASTM testing methods for polymers. The most common technique for measuring WVTR through inorganic thin films is the optical calcium (Ca) test. There are two versions of this test, intended to measure either the intrinsic or defect-assisted water permeation through the barrier. Both cases harness the principle that calcium corrodes in water to form calcium oxide (CaO) [185], [189], [196]. Magnesium can be used to substitute calcium, since Mg reacts readily with water, as well. The optical tests assume that fast kinetics (i.e., instantaneous consumption of all ingressing water by Ca or Mg) and selectivity to the reactive species (i.e., H_2O). The Ca and Mg corrosion reactions are presented below:

$$Ca + 2H_2O \rightarrow Ca(OH)_2 + H_2$$

$$Mg + 2H_2O \rightarrow Mg(OH)_2 + H_2$$

When dried under ambient conditions, calcium hydroxide ($Ca(OH)_2$) and magnesium hydroxide ($Mg(OH)_2$) become calcium oxide and magnesium oxide, respectively. Calcium and magnesium are reflective, whereas calcium oxide and magnesium oxide are transparent. Therefore, when barrier films are deposited onto a thin film of either Ca or Mg on a glass substrate, optical imaging in transmission mode (i.e., light source from below the sample) can identify regions where water has permeated. If measuring the intrinsic WVTR, the Ca or Mg layer should be sufficiently thick so that permeated water cannot instantaneously react with the entire thickness of the film. The sample should be exposed to water under the desired test conditions (i.e., temperature, relative humidity). At periodic time points, the sample is

retrieved from the testing condition for optical imaging. As water permeates the barrier over time, the thickness of Ca or Mg will decrease as it progressively reacts into CaO or MgO. The corresponding intensity of the transmitted light should progress from 0% to 100% once the entire Ca or Mg film is consumed:

$$L(t) = \frac{I(t)}{I_0} \cdot L_0 \tag{2.48}$$

where L(t), I(t), I_0 and L_0 refer to the time-dependent thickness of Mg, time-dependent intensity of transmitted light through the barrier sample, initial intensity of the transmitted light through the sample and initial thickness of the Mg film, respectively, for a Mg-based intrinsic WVTR test. The optical test for intrinsic WVTR is premised on the assumption the barrier sample exhibits macroscopic homogeneity. Time-lapsed images can then be processed to determine the amount of Ca or Mg consumed at each time point. The amount of permeated water can, then, be calculated based on stoichiometry:

$$m_{intrinsic} = [L_0 - L(t)] \cdot A \cdot \rho_{Mg} \cdot \left(\frac{2MW_{H_2O}}{MW_{Mg}}\right) \tag{2.49}$$

where m, A, ρ_{Mg}, MW_{H2O} and MW_{Mg} denote the mass of water that has permeated the barrier sample, sample area of Mg, density of Mg, molecular weight of water and molecular weight of Mg, respectively, when Mg is used in the optical test. Assuming constant flux, the intrinsic WVTR can be obtained by linear regression of the amount of water permeated with respect to time, normalized by the sample area, as shown by:

$$WVTR_{intrinsic} = \frac{1}{A_{barrier}} \cdot \frac{dm_{intrinsic}}{dt} \tag{2.50}$$

where $A_{barrier}$ is the area of the optically imaged sample and, in the case of intrinsic permeation, equal to the sample area of Mg [196]. If measuring the defect-assisted WVTR, the Ca or Mg film should be sufficiently thin so that water permeating the barrier reacts with the entire thickness of the film. Samples should similarly be retrieved at periodic time points throughout environmental conditioning for optical imaging under transmission mode. Defects where water has permeated should transmit light and appear bright, whereas areas where water has not reached should reflect light and appear dark. In this manner, the optical images provide a binary indicator of where water has permeated with a resolution based on the pixel

resolution of the imaging system. The amount of water that has permeated by defect-assisted diffusion can be calculated from the percentage of white pixels:

$$m_{defect} = A(t) \cdot L \cdot \rho_{Mg} \cdot \left(\frac{2MW_{H_2O}}{MW_{Mg}} \right) \tag{2.51}$$

where A(t) denotes the time-dependent area of MgO. Assuming constant flux and steady-state conditions, the corresponding defect-assisted WVTR is given by:

$$WVTR_{defect} = \frac{1}{A_{barrier}} \cdot \frac{dm_{defect}}{dt} \tag{2.52}$$

The accuracy of the optical test for measuring defect-assisted WVTR depends on the pixel resolution of the imaging system implemented. The optical test is generally favored in academia, as it does not require any specialized equipment and boasts relatively high accuracy.

In this study, the intrinsic and defect-assisted WVTR of inorganic single and multi-layer barriers were characterized by optical testing (Figure 65). Three-inch-diameter fused silica wafers (500 µm thickness) served as the sample substrate, as it supported higher quality imaging than traditional 1-mm-thick microscope slides. The fused silica was diced into quarter-wafer pieces and cleaned in piranha etchant (i.e., 3:1 v/v ratio of sulfuric acid and hydrogen peroxide). The silica samples were rinsed in DI water and dried with inert nitrogen before the sputter deposition of 30 nm of Mg (PVD Magnetron Sputterer, Kurt J. Lesker). The deposition was performed under DC mode at 150 W, 5 mTorr of nitrogen and 5 minutes of pre-sputtering, which yields a deposition rate of 14.3 nm/min. The desired inorganic barrier thin film was, subsequently, deposited onto the surface. Magnesium oxide and magnesium fluoride were deposited by RF sputtering at 200 W and 5 mTorr of nitrogen, which corresponded to deposition rates of 0.50 nm/min and 0.43 nm/min, respectively. Samples were allowed to cool down for at least 30 minutes prior to venting the system to avoid premature Mg oxidation and thermo-mechanical stressing. Alumina was deposited by ALD at a process temperature of 80˚C to maintain processing compatibility with polymeric materials. The precursor gases were TMA and water; the pulse and purge times for both reactants

were 0.015 seconds and 30 seconds, respectively. The deposition rate was slightly lower than ALD performed at higher temperatures (i.e., 250˚C) and was 0.08 nm/cycle.

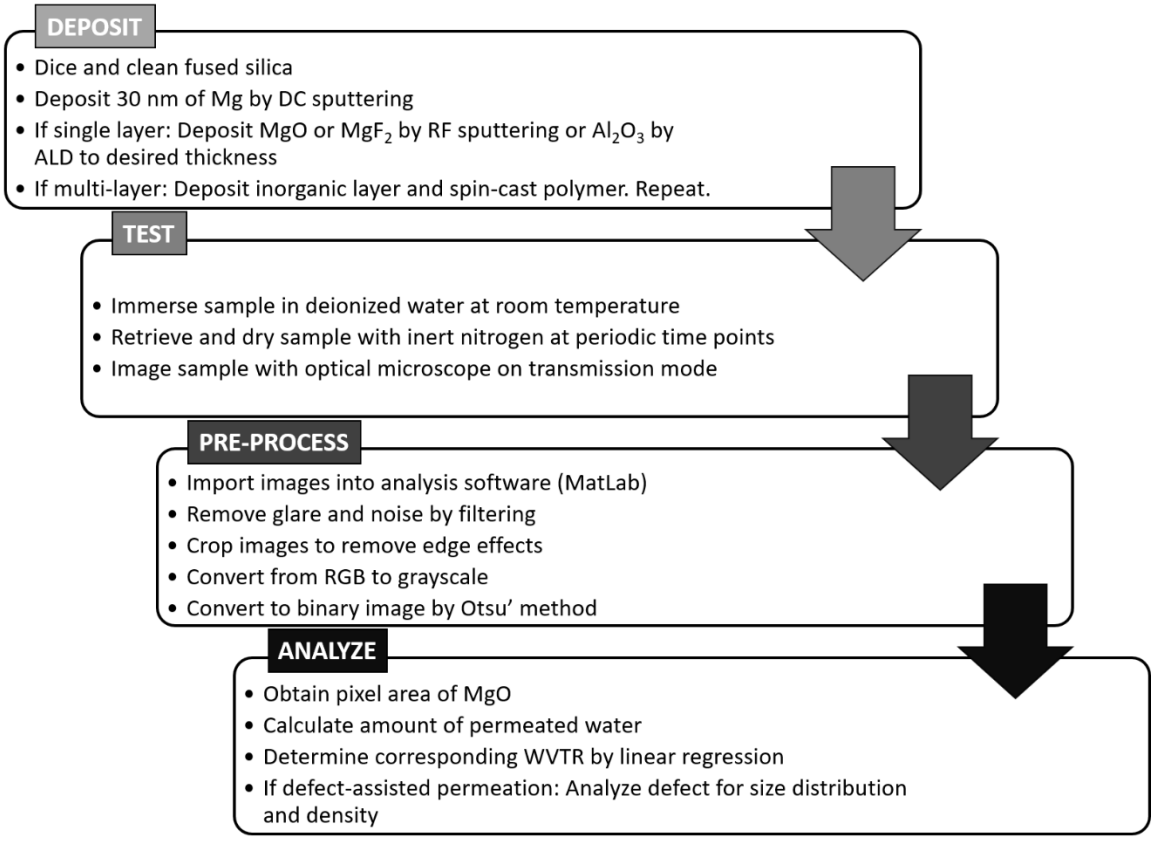

Figure 65 Schematic illustrating the fabrication of the barrier thin films and subsequent characterization of water permeation.

In multi-layer characterization, PCL (M_n = 80 kDa, Sigma Aldrich) and PLA (M_n = 17 kDa, Purac) were selected as the organic barrier material. The PCL and PLA were suspended in 1,4-dioxane and dichloromethane to a concentration of 33 mg/mL and 50 mg/mL, respectively. The polymer solutions were spin-casted onto the barrier samples at a spin speed of 2000 rpm for 60 seconds, after a pre-spin at 500 rpm for 5 seconds to distribute the solution across the sample surface. Spin-cast PCL and PLA were dried on a hot plate at 90˚C and 50˚C, respectively, and stored under vacuum to remove any residual solvent.

An optical microscope was used for WTR measurements in transmission mode. Seven-by-seven frame stitching was applied to image a large sample area while maintaining high pixel resolution. This

corresponded to a sample area of 1.15 cm^2 (1.2 cm by 0.96 cm), in contrast to the 0.25-0.40 mm^2 area typically reported in literature. The acquired images were 8171 by 6497 pixels in size, providing a pixel resolution of 1.5 μm/pixel. Acquired images were imported into MATLAB for pre-processing and analysis. Specifically, glare and noise removal were performed, followed by image cropping to eliminate edge effects and conversion from RGB to grayscale. The 8-bit grayscale images were converted to binary (i.e., black and white) by Otsu's method, which determines the conversion threshold by finding the minimum intra-variance and maximizing inter-variance. The intrinsic or defect-assisted WVTR are then determined based on the equations described earlier. Object detection algorithms were implemented to identify defects to understand the size distribution and density of defects throughout the time course of water permeation. The results for single layer barriers of MgO, MgF_2 and Al_2O_3, as well as multi-layers of MgF_2 and Al_2O_3, are presented in the following discussion.

2.3.4. Barrier Passivation of Sputter Deposited Magnesium Oxide

The intrinsic and defect-assisted WVTRs of magnesium oxide were examined. However, the intrinsic WVTR of MgO was significantly higher than the defect-assisted WVTR, as observed in the optical images presented in Figure 66. A 150-nm-thick Mg film passivated with a 15-nm-thick MgO film completely dissolved in 60 minutes, corresponding to a WVTR of 7.2 g/m^2/day (Figure 67). Increasing the barrier film thickness by five-fold only reduced the WVTR by 36%. These results are 3 orders of magnitude higher than the reported WVTR of sputter deposited barrier films and only 2-3 times lower than the WVTR of biodegradable polymers. The results are summarized in Table 16. It is speculated that the high permeation rate is attributed to the fast dissolution rate of MgO in water. Specifically, MgO becomes $Mg(OH)_2$ when hydrated and magnesium hydroxide dissolves in water over time; this phenomenon also explains why the native hydroxide film on a Mg surface is unable to protect against Mg corrosion. Further, the slow deposition rate of MgO by sputtering, corresponding to 150 minutes for a 75-nm-thick films, together suggested that MgO is not a suitable candidate for biodegradable barrier film technology. While elevating

the sputter deposition temperature can improve the film quality and deposition rate, this is not compatible with the integration of MgO with PCL or PLLA.

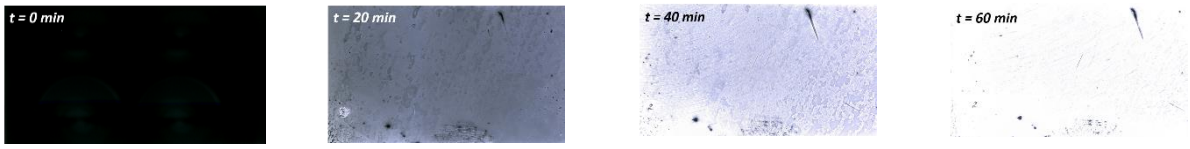

(a) (b) (c) (d)

Figure 66 Optical images of intrinsic water permeation across 15-nm-thick MgO over time.

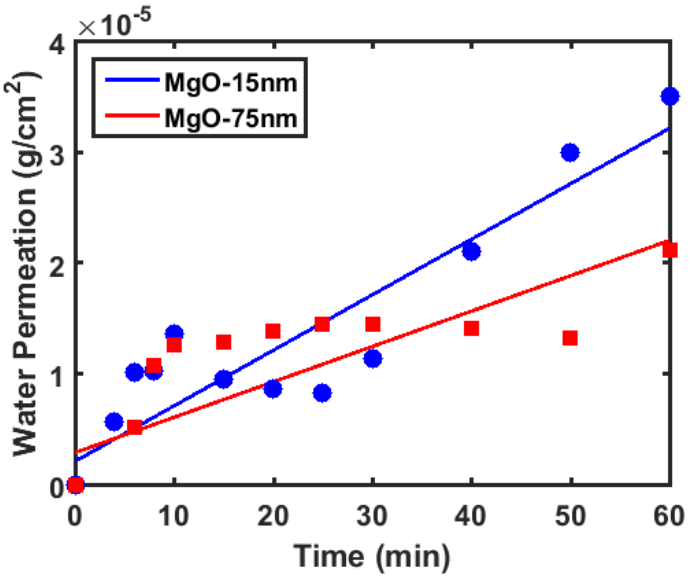

Figure 67 Intrinsic water permeation of sputter deposited MgO films.

Table 16 Intrinsic WTR of sputter deposited MgO

Thickness (nm)	Deposition Time (min)	Water Transport Rate (g/m^2/day)
15	30	7.2
75	150	4.6

2.3.5. Barrier Passivation of Sputter Deposited Magnesium Fluoride

The defect-assisted water permeation through sputter deposited MgF_2 thin films was examined. Figure 68 shows the time-lapsed images of Mg corrosion where water had permeated a defect in a 75-nm-thick MgF_2 film (i.e., depicted as white in the binary images). Consumption of the underlying Mg can proceed either by increasing defect density or by increasing radial diffusion in a pinhole over time. The former effect appeared to dominate during the initial testing period, but the radial diffusion of water within a pinhole becomes more apparent in later time points. Interestingly, defects tended to form near other defects and with region of MgO growing radial over time, thereby reducing the distance between two given defects, some defects coalesced into a single larger defect. This can be observed in the upper-left quadrant of the optical images during 60-120 minutes of immersion.

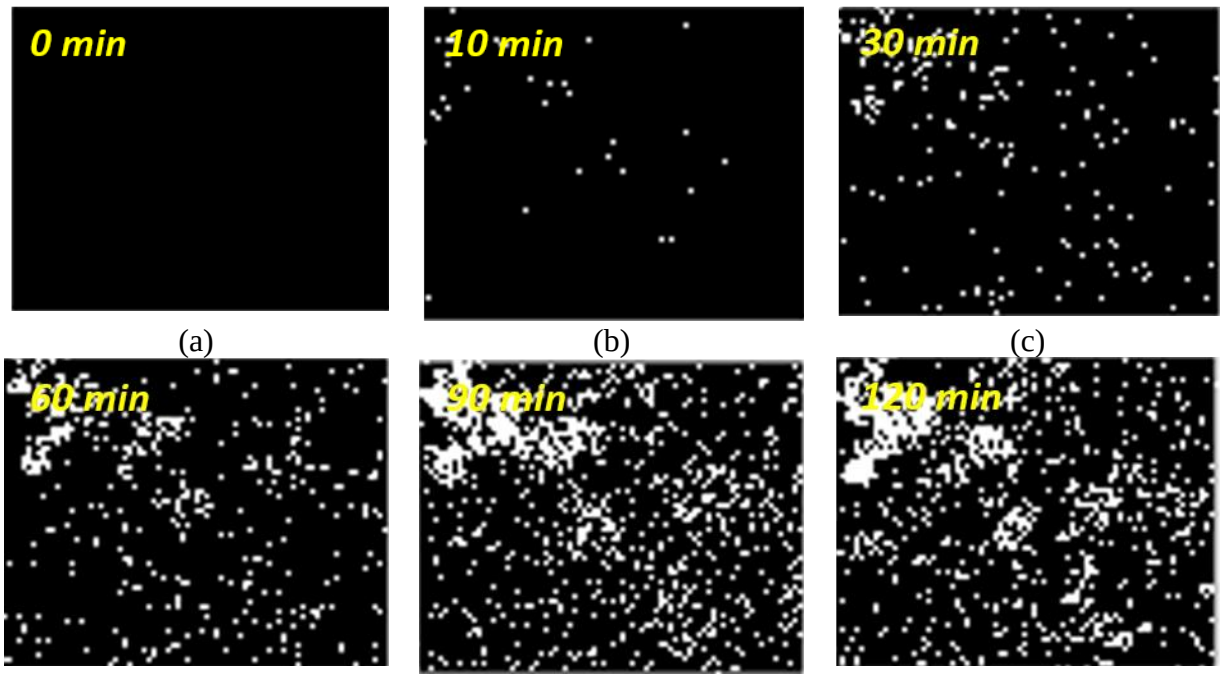

Figure 68 Time-lapsed optical images of defect-driven water permeation of sputter deposited 75-nm-thick MgF_2 films

The distribution of pinhole size is shown in Figure 69. Recall that the resolution of the measurement system is 1.5 μm and pinholes smaller than the resolution limit cannot initially be detected. The pinholes observed prior to sample conditioning in water (i.e., at t = 0 min) corresponded to pinholes in the Mg layer, which may have formed during the Mg deposition process or due to water permeation from the ambient environment. Since the total number of pinholes across a large sample area was fairly low, they are likely intrinsic defects of the sputter deposition process. The initial distribution of pinholes in the Mg layer resembles a normal distribution centered at a radius of 3.5 μm. During the initial 10 minutes of water immersion, the number of pinholes rapidly increases, as observed in the increasing y-axis limits of the histograms, and the spread no longer resembled a normal distribution. The defect number grew by several orders of magnitude to approximately 15,000 across the sample surface. This rapid increase is a characteristic effect of the initial transient period, when water permeates a film that was initially water-free. The pinholes were predominantly 2.5-7.5 μm in radius, but outliers were also observed in the tens-of-microns range. As immersion time further increased, the defect radius grew, as expected from the radial diffusion of water inside a pinhole. At 30 minutes, the maximum radius was in the hundreds-of-microns range, whereas the majority of defects hovered in the 10-100 μm range. It can be observed from subsequent time points that the skewness of the radii distribution increases over time. In addition to the coalescing of adjacent pinholes, surface scratches (i.e., sample imperfections) and mechanical rupturing of the inorganic thin film may contribute to the outliers in the pinhole radius distribution.

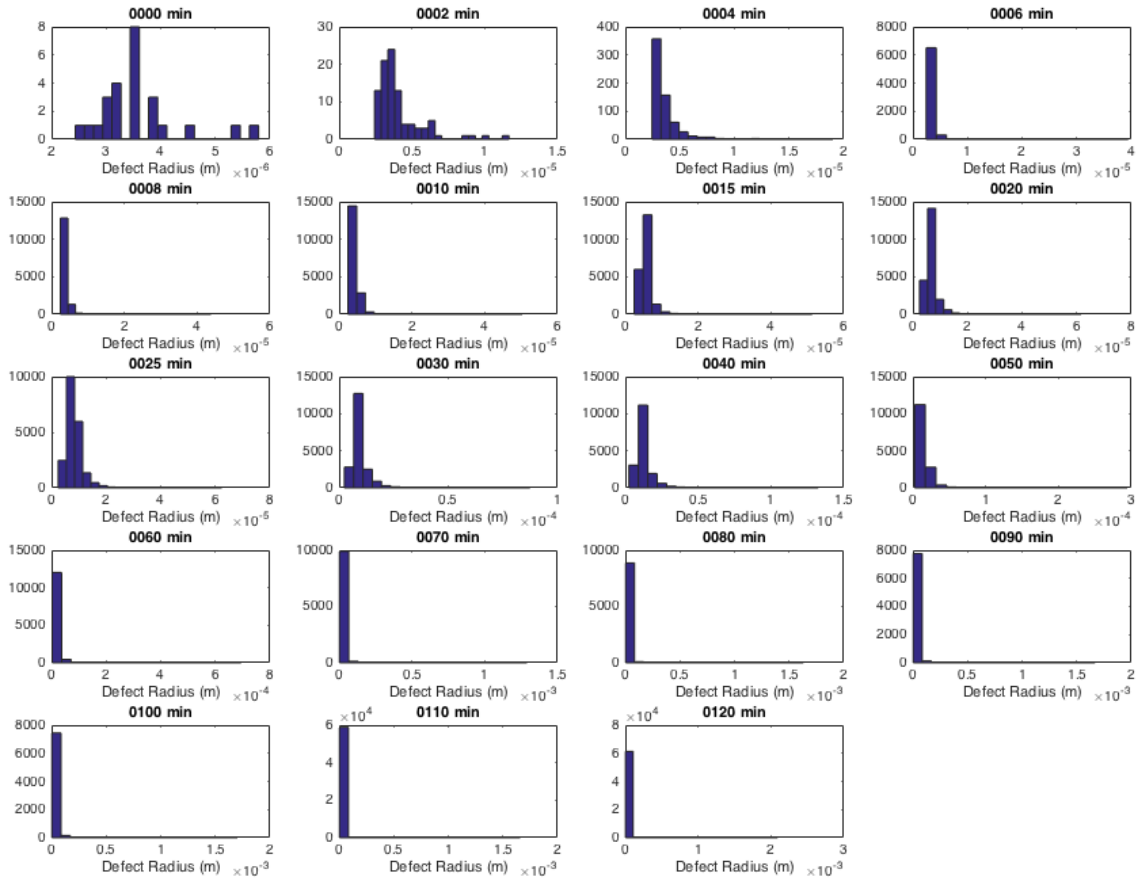

Figure 69 Distribution of defect radii for 75-nm-thick MgF_2 films due to water permeation over time.

To better understand the water permeation phenomenon of MgF_2 barriers, Figure 70 shows the maximum defect radius and defect density of MgF_2 thin films over time. The maximum defect radius was selected because the distribution of defect radii did not resemble a normal distribution after exposure to water and, therefore, the average defect radius does not sufficiently capture the defect growth phenomenon. Further, the most frequently occurring defect radius (i.e., mode) was nearly constant throughout the testing period; the mode was approximately 1.5-2.5 µm for all samples, capturing the formation of new defects more so than the growth of existing defects. Comparing the maximum defect radius results shown in Figure 70a to the computational modeling results presented by Kim *et al.* suggested that the growth of a pinhole proceeds by a constant flux boundary condition at the center point of a pinhole (and sink conditions far away from the radial center of a pinhole). The maximum defect radius did not grow rapidly initially,

followed by a period of nearly constant defect size, as would be the case with a constant concentration boundary condition. Rather, the maximum defect radius exhibited modest growth over time proportional to the square root of time. Further, the water permeation profile shown in Figure 71a is based on image analysis of the areal consumption of Mg. The linearity observed in water permeation over time agrees with the area versus time behavior shown in Figure 56d, where pinhole growth by radial diffusion with constant flux at the pinhole center corresponded to linear areal growth. It should be noted that the timescale of pinhole growth experimentally observed with sputtered MgF_2 was shorter than the computational results based on ALD-deposited films, which is consistent with the higher WTR associated with sputtered materials. The radial growth of the pinholes did not vary appreciably amongst the three different film thicknesses that were analyzed (i.e., 25-75 nm in thickness). This was expected because the radial diffusion of water that has already permeated a barrier defect should not depend on the barrier film thickness.

The defect density of sputtered MgF_2 barriers showed a similar trend among all the thicknesses examined. During the initial 15 minutes of testing, water permeating new (i.e., previously water-free) defects dominated and corresponded to a rapid rise in defect density. After the initial period, the coalescing of adjacent defects countered the formation of new defects and resulted in a net decrease in defect density. The ensuing reduction in defect density was non-linear and the rate of reduction decreased over time because water permeation in a few large defects (e.g., coalesced defects) is slower than water permeation through a large number of smaller defects. Interestingly, the defect density of sputtered MgF_2 films (25-75 nm thickness) converged to a similar value over time; the final defect density of sputtered MgF_2 films was approximately 4000 per cm^2.

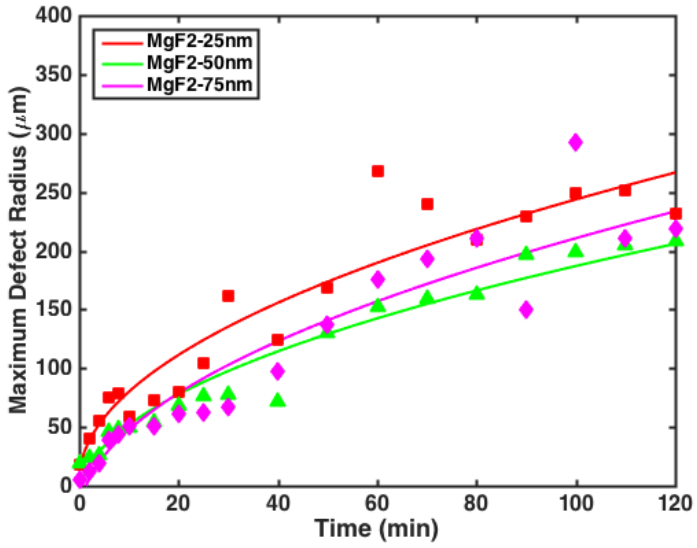

(a)

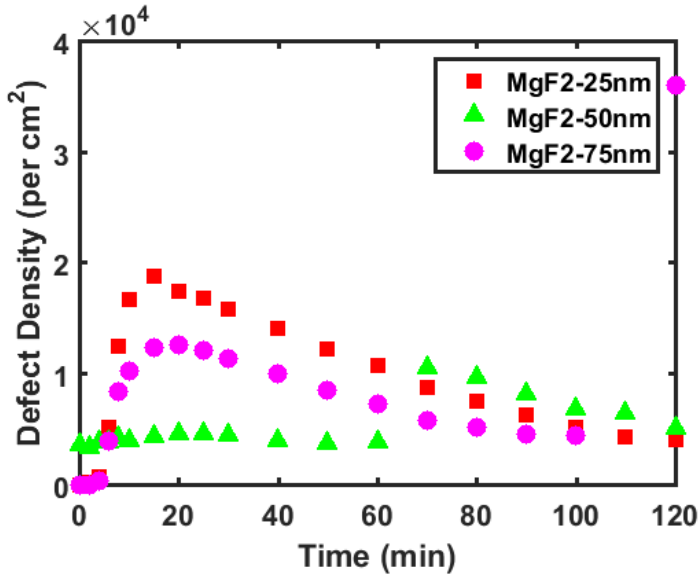

(b)

Figure 70 Average (a) defect radius and (b) defect density versus time of sputter deposited MgF_2 films parametrized by film thickness.

Figure 71a-b show the water permeation behavior and corresponding WTR of sputter deposited MgF_2 films, respectively. Both figures demarcate the critical thickness of sputtered MgF_2 films, above which the WTR does not improve significantly with increased film thickness. Experimental data indicates that the critical thickness is approximately 20-25 nm. The WTR of the sputtered MgF_2 films are displayed in Table 17. The WTR of MgF_2 films decreased by 1-2 orders of magnitude above the critical thickness.

The lowest WTR was 6.0 x 10^{-2} g/m^2/day and corresponded to 50-nm-thick MgF_2. This marked a 3-4 orders of magnitude improvement over sputtered MgO films and biodegradable polymers, respectively. Further, the observed WTR agreed with the WVTR of sputtered, non-degradable materials reported in literature (Table 17), suggesting that the timescale of MgF_2 dissolution kinetics does not significantly detract from barrier applications.

The non-monotonic behavior of WTR with respect to film thickness (i.e., the higher WTR observed with 75-nm-thick MgF_2 compared to that of 50-nm-thick films) aligned with literature, which indicated that films excessively thicker than the critical thickness can yield detrimental effects; the mechanical robustness and thermo-mechanical stress of films increases with thickness. The higher WTR of 75-nm-thick films was not attributed to variations in the initial film quality (e.g., surface scratches and residue), as the WTR of two identical films does not vary by more than 50-100% in WTR. This margin of error would not entirely account for the higher WTR. Further, all samples were fabricated in a class 100 cleanroom and stored under vacuum to minimize process variability from sample-to-sample and environmental exposure, respectively. Together, the findings suggested that sputtered MgF_2 is a viable material for biodegradable barrier technology and that films in the 25-50 nm thickness range are ideal.

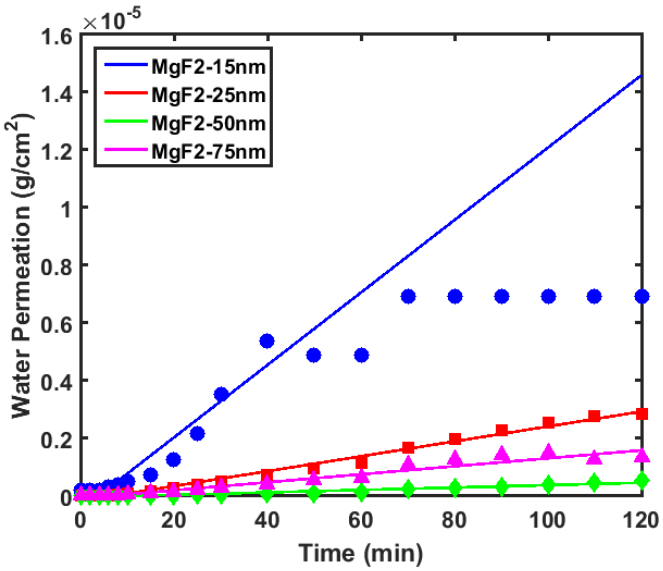

(a)

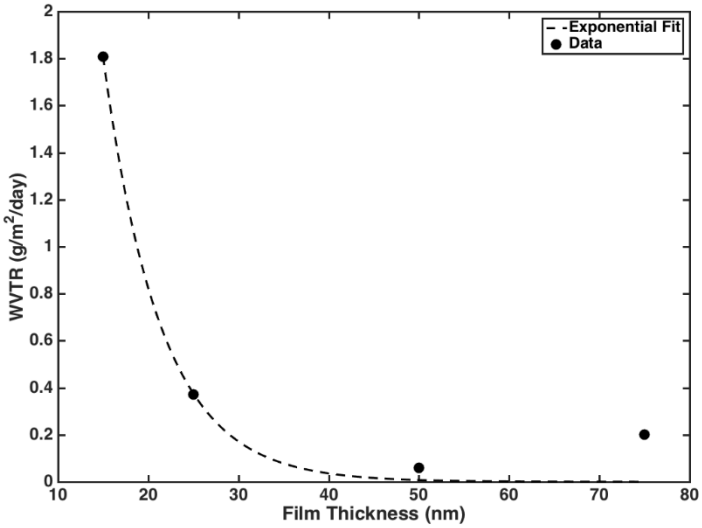

(b)

Figure 71 (a) Water permeation over time and (b) WTR based on linear regression of sputtered MgF_2 films of varying thicknesses.

Table 17 Intrinsic WTR of sputter deposited MgF_2.

Thickness (nm)	Deposition Time (min)	Water Transport Rate (g/m^2/day)
15	33	1.81×10^{0}
25	56	3.72×10^{-1}
50	112	6.03×10^{-2}
75	168	2.00×10^{-1}

2.3.6. Barrier Passivation of Atomic Layer Deposited Aluminum Oxide

Atomic layer deposited alumina was investigated as a surrogate for ALD-deposited MgF_2 in the following WTR studies. The objective of the study was to understand how to further improve biodegradable barrier technology and, as discussed previously, water permeation rates through ALD-deposited thin films is typically orders of magnitude slower than through the sputter-deposited films of the same chemistry. However, ALD requires specialized pre-cursor gases and, as such, material diversification on a given ALD system is limited. Since magnesium fluoride could not be deposited by ALD at the nanofabrication facility where this study was conducted, ALD-deposited alumina was selected as a surrogate because water permeation through barrier thin films is a defect-driven phenomenon; water permeation depends more on the deposition type than on the material selection. In addition, it was experimentally confirmed in the previous section that the biodegradable nature of MgF_2 does not interfere with its barrier performance at relevant time scales. Hence, a non-degradable material can appropriately serve as the surrogate for MgF_2.

Time-lapsed images illustrates the defect-assisted water permeation through ALD-deposited alumina (Figure 72). Comparing the 75-nm-thick alumina to sputter-deposited MgF_2 of the same thickness, the timescale at which water appreciable penetrates the underlying Mg layer is 2 orders of magnitude larger with atomic layer deposition. Further, the defect density is sparser and the defect growth, slower, with ALD barrier films. Literature reports that WVTR through ALD-deposited films can be as low as 10^{-5} g/m^2/day, or 3 orders of magnitude lower than with sputter deposition. Consequently, the testing duration must be appropriately extended to capture the defect-driven phenomenon. The distribution in pinhole size, as shown in Figure 73, resembles the histograms for sputtered MgF_2. Specifically, the defect size exhibited a non-normal distribution and was skewed towards lower radii. Unlike the sputtered barrier films, however, ALD alumina did not exhibit a sharp increase in the number of defects during the initial testing period. Recall that the number of defects observed in sputtered MgF_2 was approximately 15,000 after 10 minutes of water exposure. Here, the transient effects manifested over the timescale of 200 minutes and the number of defects was in approximately 200. The size and number of defects remained fairly consistent until

approximately 14,000 minutes of testing, after which the defect number sharply rose and indicated barrier failure.

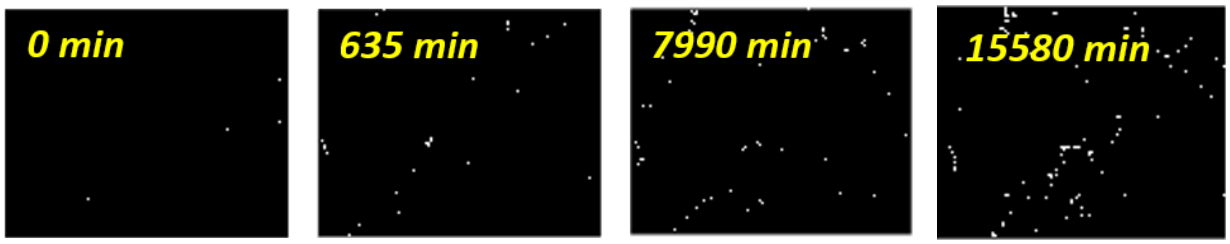

(a) (b) (c) (d)

Figure 72 Time-lapsed optical images of defect-assisted water permeation of atomic layer deposited 75-nm-thick Al_2O_3 films

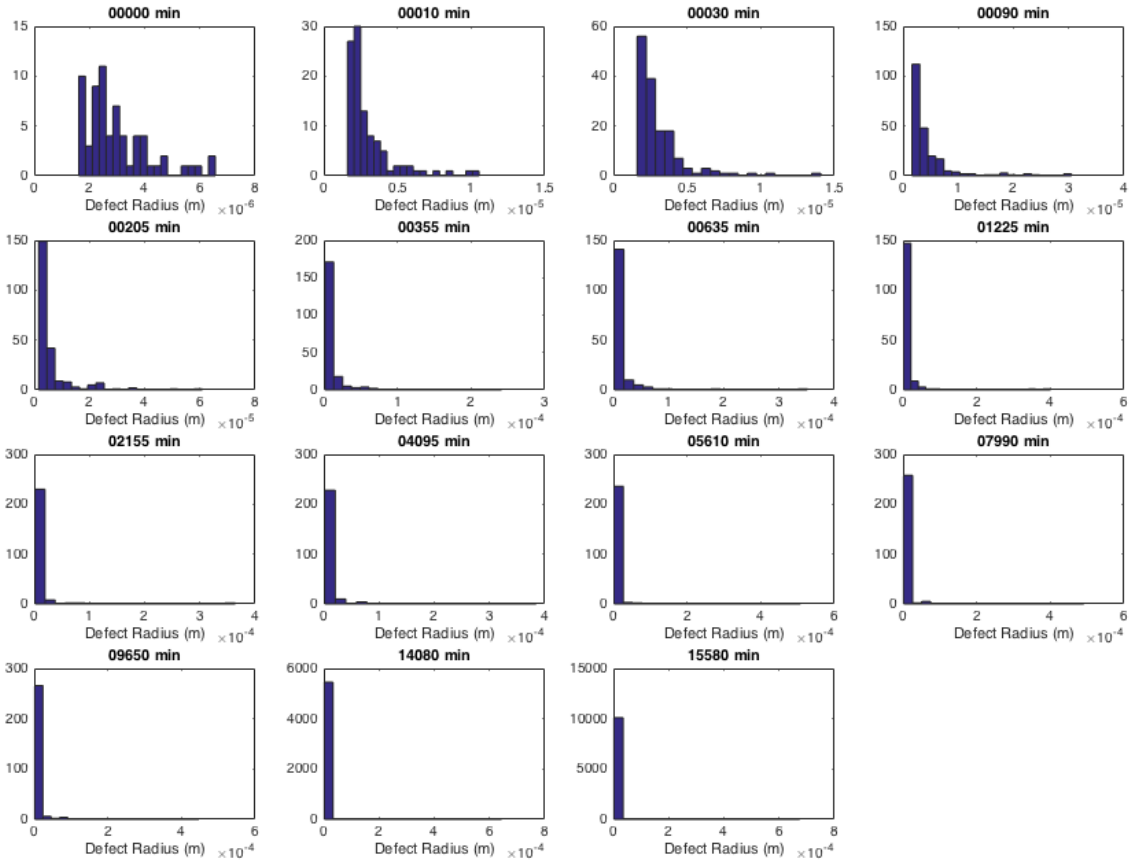

Figure 73 Distribution of defect radii for 25-nm-thick Al_2O_3 films due to water permeation over time.

The maximum defect radius and defect density are reported in Figure 74 for 25-75 nm thicknesses. Unlike sputter deposited films, ALD-deposited alumina exhibited a steady increase in defect radius and defect density until a critical lifetime, beyond which the maximum defect radius and defect density increased more dramatically. The log-scale plot depicting defect density over time highlights this behavior, where the defect density for 25-nm-thick and 50-nm-thick films increased by 1-2 orders of magnitude after 10,000 minutes of water exposure. In turn, 75-nm-thick films did not exhibit this demarcation indicative of barrier failure. The critical lifetime may be a consequence of local delamination or stress cracking after prolonged exposure to water. The slower radial growth and sparser defect density prior to the critical lifetime are inter-dependent, since fewer defects reduces the likelihood of adjacent defects coalescing and, in turn, hastens the growth in maximum defect radius.

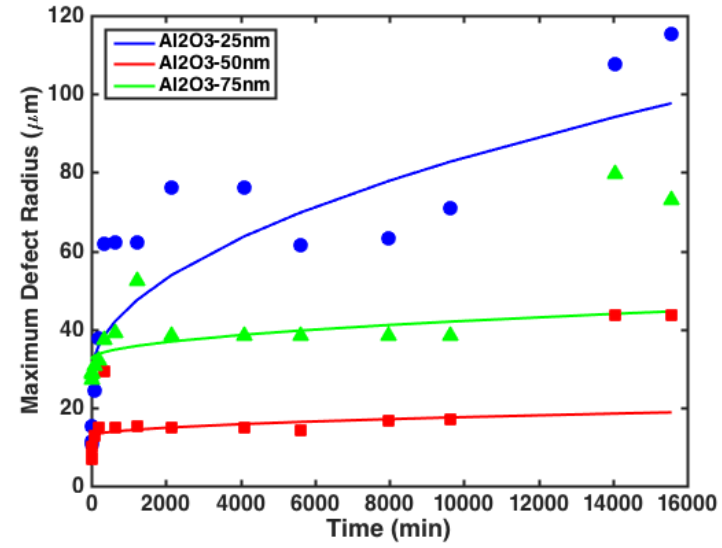

(a)

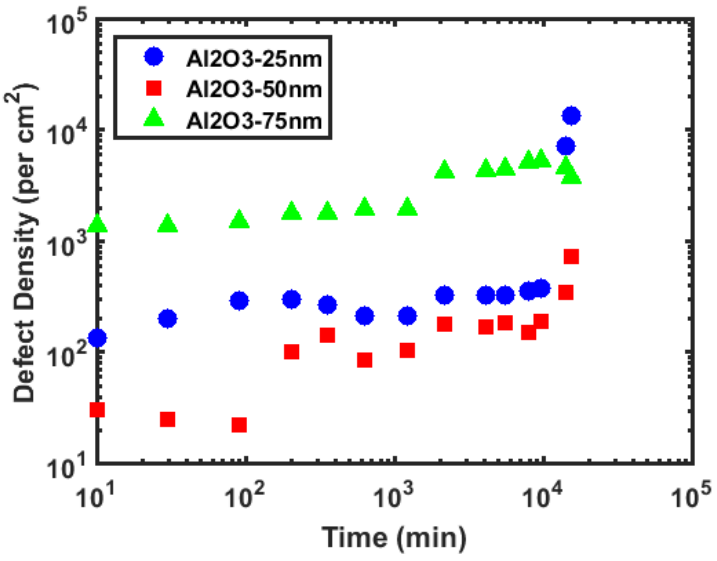

(b)

Figure 74 Average (a) defect radius and (b) defect density versus time of atomic layer deposited Al_2O_3 films parametrized by film thickness.

The water permeation analysis from time-lapsed optical testing revealed that the WTR of ALD alumina deposited at 80°C can be as low as 2.87 x 10^{-5} g/m^2/day (Figure 75 and Table 17). The results were obtained from evaluating films spanning from 3 nm to 75 nm in thickness. Defect analysis was performed only films 25 nm or thicker because the critical thickness of ALD alumina was found to be approximately 25 nm. Films thinner than 25 nm exhibited orders of magnitude faster water permeation and were not of

interest to this study. Alumina films thinner than the critical thickness featured an exponential reduction in WTR, whereas films thicker than the critical thickness showed a slower, sub-exponential reduction in WTR. These trends and the critical thickness were similarly observed by Klumbies *et al.* using an optical calcium test [185].

This study confirmed that atomic layer deposited barrier films can better hinder water permeation than sputter deposited films. Assuming that the WTR of barrier films is largely independent of the film material as long as the material does not react to water, the findings of this study suggested that ALD-deposited MgF_2 would be the optimum material in biodegradable barrier technology.

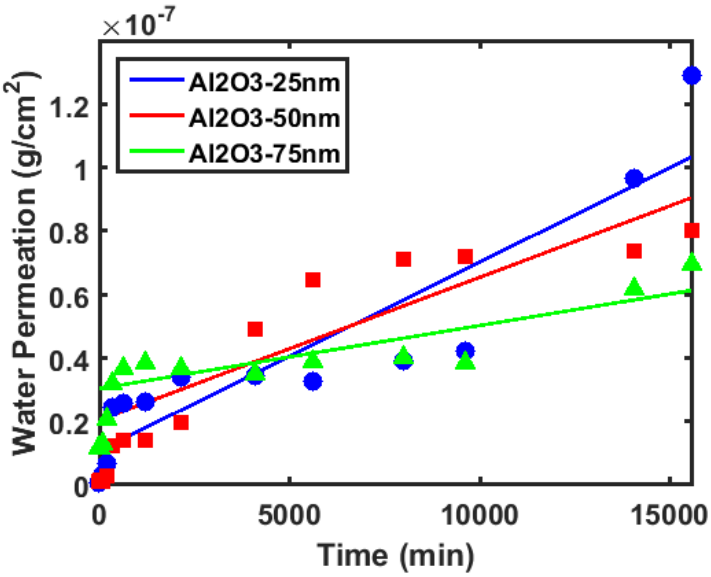

(a)

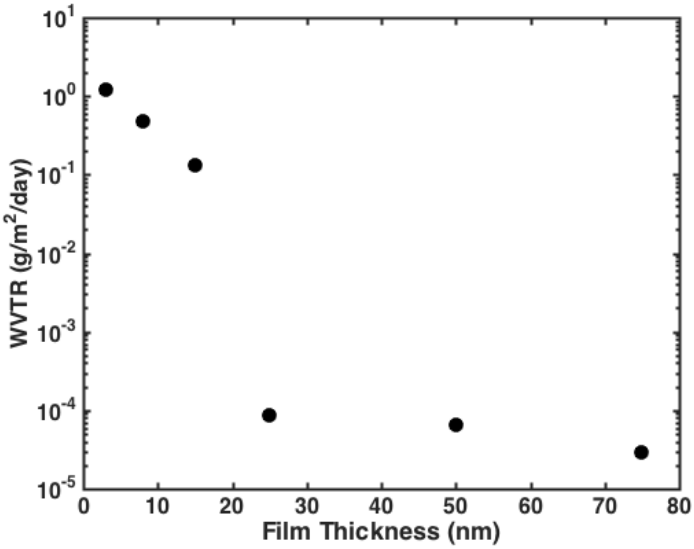

(b)

Figure 75 (a) Water permeation over time and (b) effective WTR, determined by linear regression for time points after the initial lag time, of atomic layer deposited Al_2O_3 films of varying thicknesses.

Table 18 Effective WTR of sputter deposited Al_2O_3.

Thickness (nm)	Deposition Time (min)	Water Transport Rate ($g/m^2/day$)
3	38	1.21×10^{0}
8	100	4.75×10^{-1}
15	188	1.33×10^{-1}
25	313	8.57×10^{-5}
50	626	2.87×10^{-5}
75	939	3.13×10^{-5}

2.3.7. Multi-Layer Passivation with Sputtered Magnesium Fluoride and Polycaprolactone

This section explores biodegradable multi-layer technology for improving barrier performance against water permeation. It was previously shown that MgF_2 is a biodegradable inorganic material that, when sputter deposited, provides barrier protection comparable to non-degradable sputtered thin films. To enhance the barrier protection, multi-layers comprising alternating layers of MgF_2 and spin-cast PCL was explored. Polycaprolactone was selected as the biodegradable polymer because it is less expensive that PLLA and demonstrated comparable water permeation rates. Further, the solubility of PCL in 1,4-dioxane (DOX) facilitated the spin-casting of PCL because the boiling point of dioxane is 101°C and, thus, the polymeric solution does not dry too quickly during the spinning process (unlike dichloromethane, the solvent for solubilizing PLLA). The spin casting was performed with a 25 mg/mL solution of PCL-DOX at 2000 rpm for 60 seconds. The sample was subsequently heated to evaporate residual solvent and stored under vacuum prior to use. Magnesium fluoride was sputter deposited to a thickness of 40 nm, which is slightly above the critical thickness, for optimum barrier performance.

Magnesium fluoride and PCL multi-layers of up to 3 dyads were investigated. The time-lapsed images of 3 dyads of MgF_2 and PCL are shown in Figure 76. In contrast to MgF_2 alone, the multi-layers demonstrated fewer defects and a slower rate of defect growth due to the tortuous path presented. Optical images after 1200 minutes of testing resembled the results of 75-nm-thick MgF_2 alone after less than 30 minutes of exposure. In addition, defect coalescence was not appreciably observed with MgF_2 multi-layers and can be noted by the absence of macro-defects in the optical images. Histograms of defect

radius over time (Figure 77) highlighted the extended initial transient period with MgF_2-PCL multi-layers, where water permeating an initially water-free barrier manifested as a lag time in the formation of defects. The majority of defects remained less than 10 μm throughout the entire testing period.

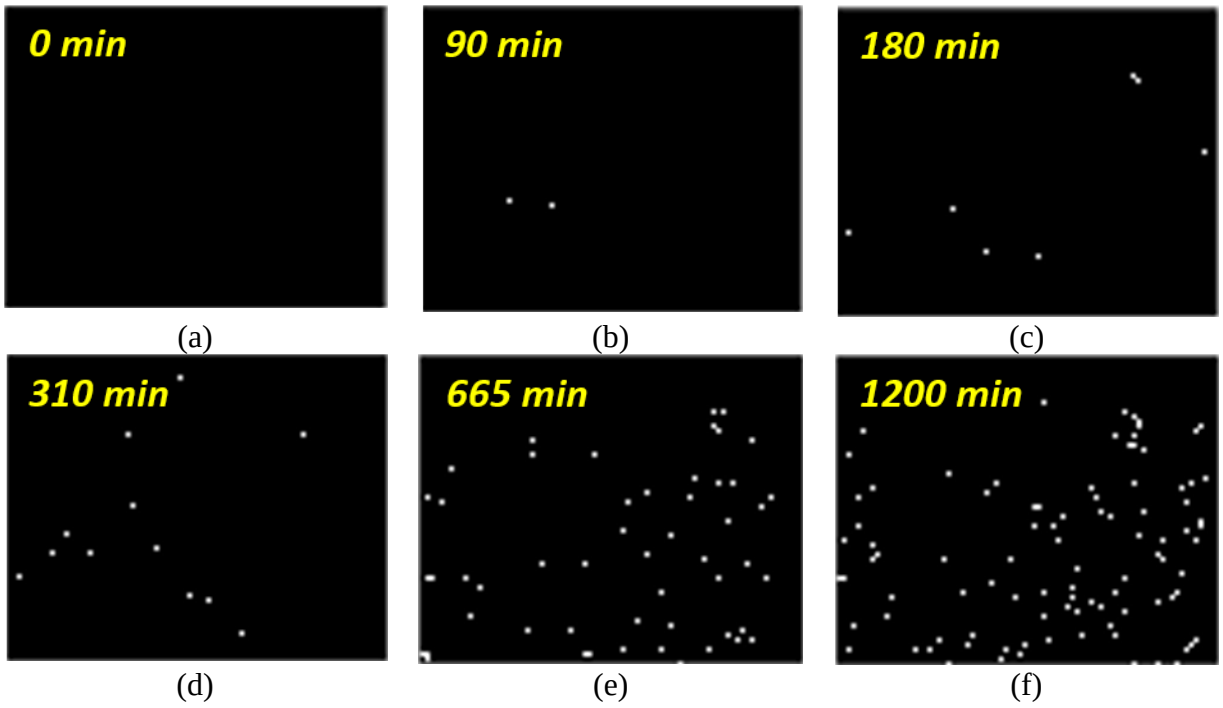

Figure 76 Time-lapsed optical images of defect-assisted water permeation 3 multi-layers of sputter deposited MgF_2 and spin cast PCL.

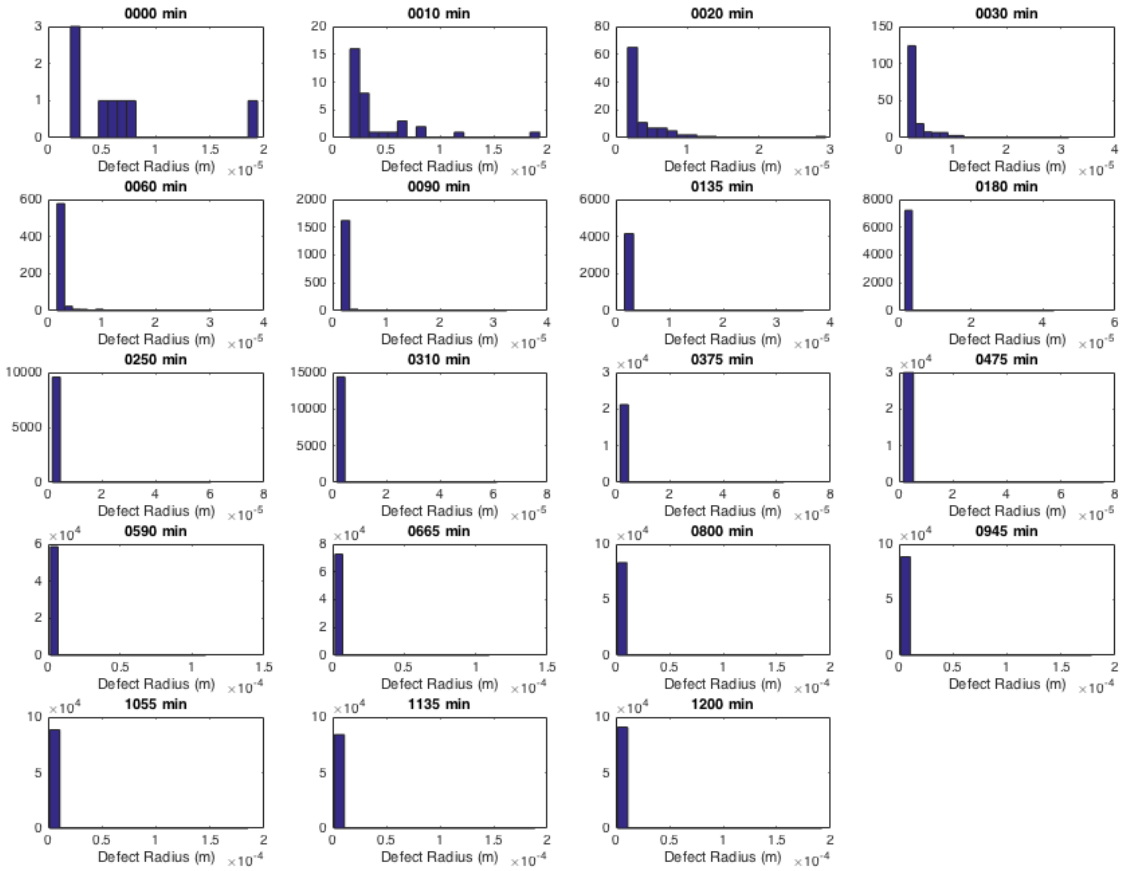

Figure 77 Distribution of defect radii for 3 multi-layers of sputter deposited MgF_2 and spin cast PCL due to water permeation over time.

Defect analysis revealed that MgF_2-PCL dyads hindered defect-assisted water permeation in comparison to MgF_2 alone. Even single dyads (i.e., 1 layer of MgF_2 and PCL) achieved slower radial growth and exhibited smaller maximum defect radii than MgF_2 barriers alone. For example, after 1200 minutes of testing, the maximum defect radius was approximately 50 μm for a single MgF_2-PCL dyad, whereas the maximum defect radius was 200-250 μm for 25-75 nm thick MgF_2 films. The five-fold reduction demonstrated by introducing a polymeric top-coat indicates the fragility of inorganic thin films, where abrasion and local film stress can undermine the integrity of the barrier protection. Similar to MgF_2 alone, the radial growth profile resembles the pinhole growth model presented by Kim *et al.*, where constant flux conditions persist the radial center of a pinhole. Since the tortuous path introduced by multi-layers introduces a lag time and hastens water ingress, the results also conceptually agreed with the more gradual

reduction in diffusion rate observed with constant flux conditions. The sharp increase in maximum defect radius observed in 2x multi-layers after 300 minutes of testing might correspond to local film delamination and the rapid ingress of water in one of the polymeric layers. This has frequently been observed in literature due to the poor adhesion between organic polymers and inorganic thin films. Polymeric swelling from water absorption may further exacerbate this concern. It is not believed that the rapid increase in maximum defect radius is attributed to the initial lag time associated with multi-layer barrier technology because a similar trend was not observed with 3x multi-layers.

However, the initial transience can be clearly observed in the defect density versus time plot presented in Figure 78. The characteristic time required to achieve a steady defect density increased with each additional MgF_2-PCL dyad. Specifically, the time lag imposed by 1 dyad, which does not present a tortuous path, is approximately 30 minutes. This time delay may be attributed to the hydration of the PCL top-coat that precedes defect-assisted permeation through the underlying inorganic barrier. In turn, the time lag exhibited by 2 and 3 dyads are 475 minutes and 665 minutes, respectively. Further, the steady state defect density decreased with the number of dyads in the barrier. The transient effects of the multi-layer samples confirmed that a tortuous path was effectively engineered to hinder water permeation. Based on the computational models presented by Greener *et al.*, this further suggested that the spin-cast PCL was sufficiently thin to limit water transport. Unlike MgF_2 alone, gross pinhole coalescence was not observed with MgF_2-PCL multi-layers at the timescales examined, which would have corresponded to a sharp decline in defect density over time. This further confirmed the improved barrier passivation established by the biodegradable multi-layers.

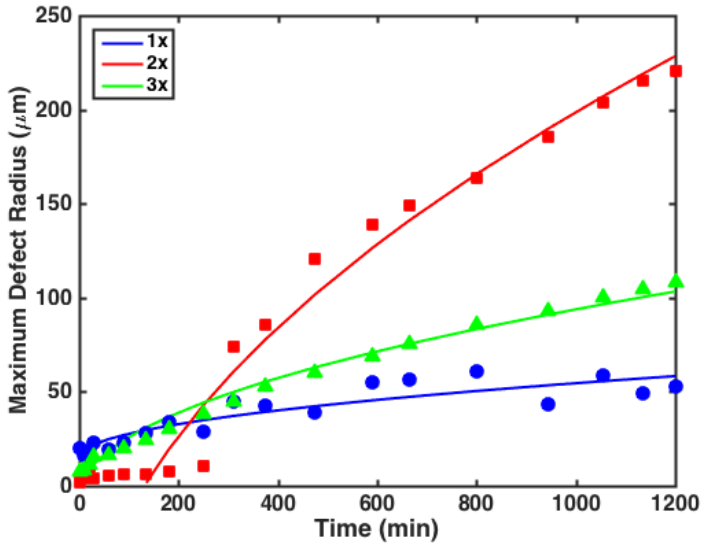

(a)

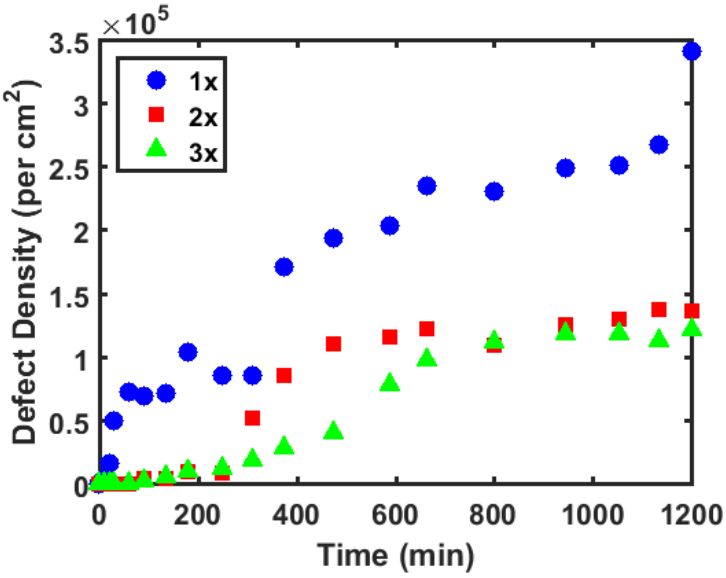

(b)

Figure 78 Average (a) defect radius and (b) defect density versus time of MgF_2-PCL multi-layers.

The water permeation through MgF_2-PCL multi-layers was determined by optical testing using Mg corrosion to identify water ingress. The results are depicted in Figure 79 and summarized in Table 19. The multi-layers exhibited a non-linear behavior characterized by an initial transient period and a subsequent steady state period. During the initial transient period, the rate of water permeation (i.e., flux) is not constant due to the tortuous path for water diffusion and the water-free history of the sample. The time delays

coincide with what was observed in Figure 78b, which depicted the defect density over time. The steady state behavior can be distinguished by a constant flux behavior. The WTR was determined by linear regression of steady state data only.

Additional dyads decreased the WTR, but with diminishing returns. The WTR of MgF_2-PCL multi-layers decreased by 72% when proceeding from 1 dyad to 2 dyads, but decreased by only 20% when proceeding from 2 dyads to 3 dyads. The lowest WTR achieved with MgF_2-PCL multi-layers was 1.95×10^{-3} g/m^2/day, which marked a 31-fold improvement (i.e., BIF) over a single MgF_2 barrier film. It should be emphasized that the WTR reduction is not the singular advantage of multi-layer barriers, but an extended transient period (i.e., the initial time lag) also deters water permeation. The effect of multi-layers on lag time becomes more pronounced with additional dyads, as illustrated in Figure 58 and as confirmed in Table 19. Literature indicates that for a dyad combination, a point of diminishing returns can be observed where increasing the number of multi-layers does not appreciably decrease the WTR. However, the initial time delay continues to grow with additional multi-layers and this extended transience has been equally valuable in enabling researchers to achieve an OLED device lifetime of 10,000 hours. The effect of additional dyads is similarly beneficial for biodegradable devices, where the desired functional lifetime is on the order of days to a few weeks. Overall, the results confirmed that biodegradable multi-layers are effective barriers to water transport and may serve as a first line-of-defense against corrosion of an active biodegradable device.

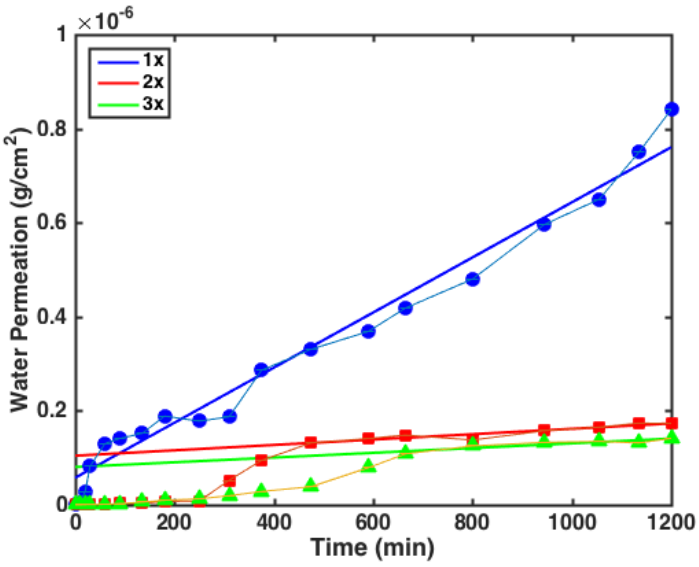

(a)

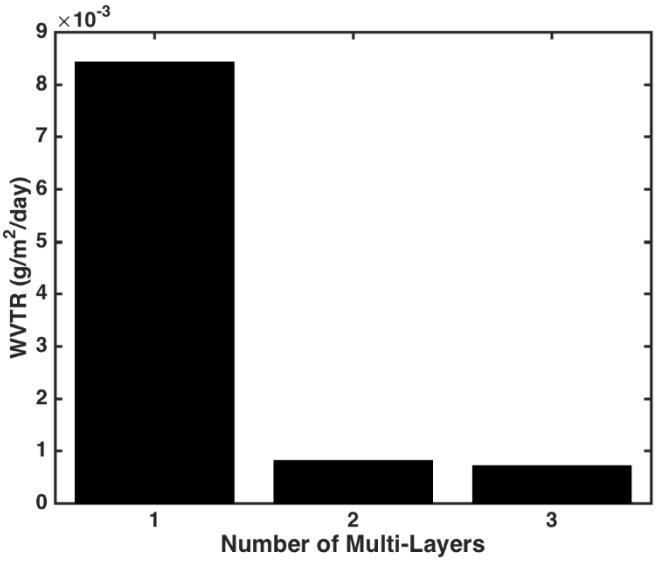

(b)

Figure 79 (a) Water permeation over time and (b) effective WTR based on linear regression of MgF_2-PCL multi-layers.

Table 19 Initial lag time to water permeation and effective WTR for multi-layers of sputter deposited MgF_2 and spin cast PCL.

Number of Multi-Layers	Initial Lag Time (min)	Water Transport Rate ($g/m^2/day$)	BIF
1	30	8.74×10^{-3}	6.9
2	475	2.44×10^{-3}	25
3	665	1.95×10^{-3}	31

2.4. Biodegradable Conductive Composites for Electrical Interconnects

2.4.1. Introduction

In order to achieve an active biodegradable device, research must not only pursue biodegradable sensors and energy sources, but also biodegradable circuitry and packaging. Towards these goals, biodegradable conductive polymer composites (CPC), which feature metallic fillers dispersed in an insulating polymer matrix, have been explored for their applications in biodegradable electrical interconnects, as well as in strain sensing.

While many advances have been made in semiconductor electronics, technological developments focused at the materials and/or device level often overlook packaging compatibility [5], [75], [81], [124], [219]. However, packaging and integration, such as with electrical interconnects, are important for supplying power, connecting to ground and signal transmission. The de facto material used for electrical interconnects has been eutectic tin-lead (Sn/Pb) solder, which has been adapted to pin through holes (PTH), surface mount technology (SMT), ball grid arrays (BGA), chip-scale packages (CSP) and flip chip technology [220]–[225]. Health and environmental concerns over the extensive use of lead has promoted research in lead-free alternatives in interconnect technology. While lead-free solders, primarily with tin-based alloys, have reached the commercial market, they typically feature higher processing temperatures than traditional lead-based solder. For example, tin-lead, tin-silver and tin-silver-copper solders exhibit melting points of 183˚C, 217˚C and 221˚C, respectively. The 30-40˚C increase in processing temperature

associated with lead-free solder may result in increased failed parts due to increased temperature exposure and limits their application in organic circuit boards and low-cost polymer-based packaging [226].

Electrically conductive adhesives (ECA) are a competitive alternative to traditional solder for electrical interconnects and where conductive polymer composites have found widespread application [220], [221], [227]. Electrically conductive adhesives can be divided into two major categories: isotropically-conductive adhesives (ICA) and anisotropically-conductive adhesives (ACA). The former typically features conductive fillers on the order of 1-10 µm in diameter and high conductor loading, resulting in direct particle-particle contact and conductivity in the x-, y- and z-directions. In contrast, the latter typically comprises conductive particles that are 3-5 µm in diameter and exhibit low conductor loading. Consequently, ACA are only conductive in the z-direction when pressure and/or heat is applied. Both ICA and ACA are advantageous over solder, as they commonly require lower processing temperatures, exhibit greater mechanical flexibility and support finer pitch [220]–[222], [227]–[232]. Table 20 compares the physical, mechanical, electrical and environmental properties of solder to ECA. The improved processing conditions and environmental impact of ECA comes with the tradeoff of higher electrical resistivity and lower thermal conductivity. However, many design strategies have been investigated in ECA research to overcome these limitations.

Table 20 A comparison between traditional Sn-Pb solder and electrically conductive adhesives [221], [223], [225], [233], [234].

Property	**Sn-Pb Solder**	**ECA**
Resistivity (Ω·cm)	1.5×10^{-5}	3.5×10^{-4}
Thermal Conductivity (W/m·K)	30	3.5
Shear Strength (psi)	2200	2000
Finest Pitch (mil)	12	<6-8
Minimum Processing Temperature (˚C)	215	150-170
Environmental impact	Poor	Mild
Thermal Fatigue	High	Minimal
Mechanical Flexibility	Low	High

Research on optimizing conductive polymer composites for ECA applications sometimes follows the "divide and conquer" strategy, where the electrical properties are tuned based on conductive filler design and the physical and mechanical properties are tailored based on the insulating matrix design. Materials that have been implemented as conductive fillers in ECA are silver (Ag), gold (Au), nickel (Ni), copper (Cu) and carbon (e.g., carbon black (CB) and carbon nanotubes (CNT)) [221], [228], [234]–[237]. Metallic fillers offer higher conductivity, but are susceptible to environmental degradation. In particular, Cu and Ni are prone to oxidation and corrosion, resulting in poor electrical stability at elevated temperature and/or relative humidity. Silver has been extensively used in ECA due to its high conductivity, low chemical reactivity, moderate cost and a unique attribute—a conductive oxide; silver oxide is conductive, in contrast to most metal oxides [228], [234], [235]. The size and shape (e.g., spheres, flakes) of conductive fillers are selected to favor higher surface area and, thereby, increased probability of particle-particle contact. Researchers have investigated silver-coated carbon particles, such as electroless-deposited Ag on graphite powders and graphite nanosheets, to achieve higher surface area geometry while reducing the amount of silver used and, hence, cost (Figure 80) [228], [234]. Liang *et al.* showed that at high loadings of the conductive filler, Ag-coated graphite reduced the resistivity by one order of magnitude compared to pure graphite, but remained more resistive than CPC comprising pure Ag fillers [228].

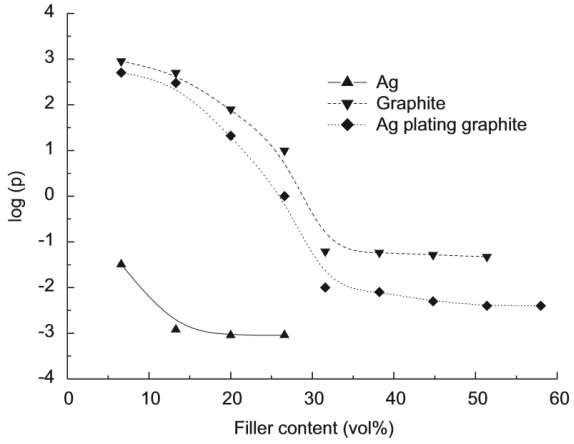

Figure 80 Electrical percolation of varying volume fractions of Ag-coated graphite powder dispersed in epoxy, compared to pure graphite and pure Ag particles [228].

The choice of polymer for use as the insulating matrix can either be a thermoset or a thermoplastic. A thermoset is a polymer that forms irreversible crosslinks after thermal and/or ultraviolet curing. Once cured, thermosets are typically more resistant to chemicals and heat. For this reason, thermoset-based ECA are more prevalent commercially. Epoxy, cyanate ester, silicone and polyurethane are commonly used as thermosets in ECA [228], [234], [238], [239]. Although silicone and polyurethane are elastomeric, researchers have reduced the tensile modulus and increased the elongation at break of epoxy-based ECA by varying the polymer chain lengths. One concern with thermosets is the internal stress introduced during curing and lower temperature cures are often investigated. In turn, thermoplastics are primarily processed by solvent evaporation, rendering thermoplastics easier to process and reworkable. However, the solvent evaporation process may result in voids that may result in poor electrical contact between a die and substrate. If more than 15% of the die surface area comprises voids, then the component is discarded as a failed part [220]. Li *et al.* compared the thermal coefficient of resistance (TCR) of thermoset- and thermoplastic-based conductive polymer composites. The thermoplastic-based CPC exhibited hysteresis, where the monotonic linear relationship between electrical resistivity and temperature differed depending on whether the temperature was ramping up or ramping down (Figure 81) [230]. In addition, thermoplastics are susceptible to thermal degradation at high temperatures. However, neither the TCR hysteresis nor thermal degradation are strong concerns when contemplating implantable applications because implantable ECA must exhibit electrical stability at a constant temperature of 37˚C. This supports the use of biodegradable polymers for the development of CPC-based biodegradable electrical interconnects, as most commercially-available biodegradable polymers are thermoplastics (e.g., polycaprolactone and polylactic acid).

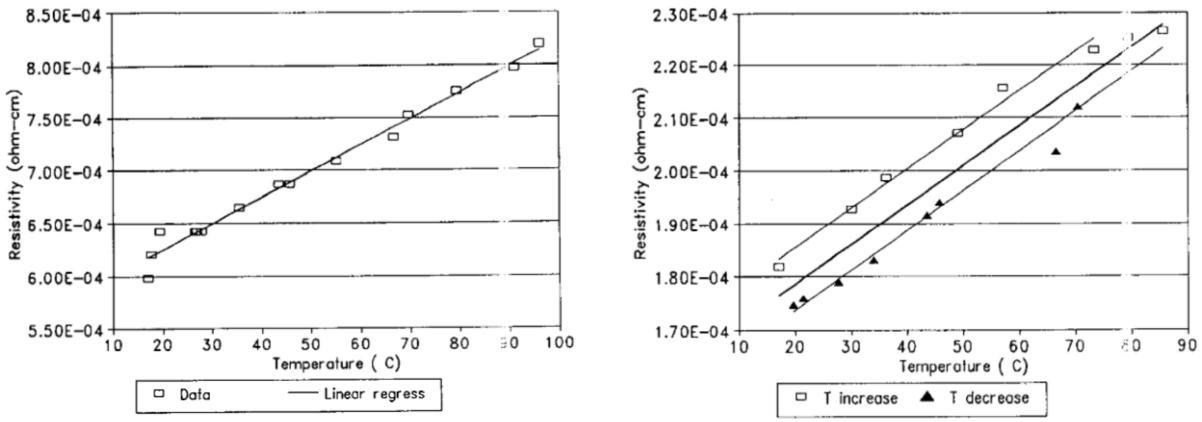

(a) (b)

Figure 81 Electrical resistivity versus temperature for CPC comprising (a) a thermoset and (b) a thermoplastic as the insulating matrix. The slope of the linear regression fit corresponds to the thermal coefficient of resistance [230].

The electrical behavior of conductive polymer composite can be described with percolation theory. Based on percolation theory, the electrical conductivity of a conductive polymer film can be represented by a set of lattice sites that are randomly or regularly positioned in space [240], [241]. At a critical probability, known as the percolation threshold, a connected network of sites forms and spans the length of the sample. The resistivity of conductive polymer composites (CPC) based on percolation theory is given by:

$$\rho_C = \rho_O(\psi_c - \psi_{crit})^{-\tau} \quad \psi_{crit} < \psi_c \tag{2.53}$$

$$\rho_C = \rho_I(\psi_{crit} - \psi_c)^{s} \quad \psi_{crit} > \psi_c \tag{2.54}$$

where ρ_c, ρ_O, ρ_I, ψ_C, ψ_{crit}, s and τ denote the resistivity of the composite, resistivity of the conductive filler, resistivity of the insulating polymer, volume fraction of the conductive filler, percolation threshold, and critical exponents, respectively [242], [243]. This suggests that the resistivity of a conductive polymer composite (CPC) can vary exponentially based on the conductive filler composition [236], [238], [242]–[245]. Thommerel *et al.* demonstrated over ten orders of magnitude increase in the conductance of conductive composite films comprising metallic microparticles (e.g., Al, Fe, and Zn) dispersed in poly-phenylsulfone (PPS) within a range of 10 vol.% centered about the percolation threshold. The study further

investigated the corrosion behavior of Zn-based conductive composites and observed that at volume fractions that approximated the percolation threshold ($\phi_f \approx \phi_{crit}$), conductance of the film stabilized after a transient decrease. This behavior was attributed to the compensation between solution infiltration and surface oxide formation on the Zn microparticles [243]. These findings indicated that the corrosion behavior of a composite film may be controlled by the material and volume fraction of the conductive filler, and permeation and corrosion protection properties of the insulator.

In addition, the electrical resistance of CPC films may be correlated to applied mechanical strain [236], [245]–[248]. Two factors contribute to the piezoresistive response: (1) changes in the inter-particle distance of the conductive filler due to elongation or compression; and (2) rotation or translation of asymmetrical particles due to the strain-induced deformation. The latter alters the number of conductive pathways in the strain direction [245]. These effects are captured by percolation phenomena and tunneling effect theory; the latter effect dominates when the volume fraction approximates the percolation point. Hence, it is advantageous for a biodegradable strain-sensitive composite to comprise a volume fracture centered at the percolation point. For applications where strain sensitivity is undesirable, however, operation above the percolation threshold is preferred. The mathematical description of tunneling facilitates the characterization of resistance with respect to applied strain and corrosion. Specifically, Simmons first characterized the electrical tunnel effect between similar electrodes separated by a thin insulating film, where the tunneling resistivity at low voltages ($e\Delta E << \lambda$) is given by [249]:

$$\rho_{tunnel} = \frac{h^2}{e^2\sqrt{2m\xi}} \cdot \exp\left(\frac{4\pi\zeta}{h}\sqrt{2m\xi}\right) \tag{2.55}$$

where m, e, h, ξ, ζ, and ΔE correspond to mass of an electron, charge of an electron, Planck's constant, height of tunnel potential barrier, potential barrier width (i.e., distance between CB particles), and voltage applied across the barrier. Li *et al.* demonstrated the logarithmic relation between compressive strain and resistivity for carbon black-filled (CB) cement composites. At small CB volume fractions ($\phi_f < \phi_{crit}$), the interparticle distance was too large for electron transit by tunneling and there were too few particles to form

a conductive network. At large volume fractions ($\phi_f > \phi_{crit}$), percolation theory dominated where compression increased physical contact between adjacent conductive particles and increased the number of conductive pathways. The loading also reduced contact resistance and, ultimately, corresponded to a decrease in resistivity. However, when the CB volume fraction approximated percolation threshold ($\phi_f \approx \phi_{crit}$), tunneling effect dominated, where compressive strain reduced interparticle distance and decreased film resistivity. Specifically, compressive strain sensitivity was 55.28 near the percolation threshold [245]. As seen, CPC films can achieve higher piezoresistive gauge factors than metallic films. Knite *et al.* expanded on the CPC piezoresistivity under elastic deformation:

$$R = \frac{\ell}{na^2}\left(\frac{\Delta E}{J}\right) = \frac{\ell}{Na^2} \cdot \frac{8\pi hs}{2\gamma e^2} \cdot exp(\gamma s) \tag{2.56}$$

$$s = s_0(1 + \varepsilon) \tag{2.57}$$

$$\text{and } \gamma = \frac{4\pi\sqrt{2m\xi}}{h} \tag{2.58}$$

where ℓ, N, a^2, s_0, R_0, s, and R denote the number of particles forming a conducting path, number of conductive paths, effective cross-sectional area where tunneling occurs, initial inter-particle distance, initial resistance, inter-particle distance under applied strain, and resistance under applied strain. Experimental data of a CB-polyisoprene composite under tensile strain was in good agreement with tunneling effect theory [236]. While operation at the percolation threshold may be desirable for strain-sensing applications, it should be noted the higher gauge factor is also accompanied by higher environmental sensitivity, such as from thermal effects and corrosion. Although operation in a physiological and, hence, temperature-regulated environment might eliminate concerns with thermal sensitivity, but the effect of corrosion on electrical conductivity and piezoresistivity remains.

This section examines the use of magnesium, zinc and iron microparticles for use in conductive polymer composites. Iron microparticles were ultimately selected for use in the development of biodegradable electrical interconnects due to their superior percolation properties throughout the examined degradation time period. Specifically, biodegradable conductive polymer composites featuring iron

microparticles and polycaprolactone as the metallic filler and insulating matrix, respectively, were fabricated by screen printing onto surrogate biodegradable circuit boards to demonstrate. The electrical, mechanical and degradation properties of the Fe/PCL interconnects were characterized, affirming the feasibility of biodegradable electrical interconnects and the compatibility of Fe/PCL conductive composites with MEMS processing. The Fe/PCL conductive composites were further explored for strain sensing applications due to the prospect of a high piezoresistive gauge factor and large strain range with conductive polymer composites.

2.4.2. Preparation of Biodegradable Conductive Composites

Biodegradable conductive polymer composites were developed using magnesium, zinc or iron microparticles as the conductive filler and polycaprolactone as the insulating matrix. Figure 82 shows scanning electron micrographs of the metallic microparticles. The Zn and Fe microparticles were spherical and approximately 3-20 μm and 10-35 μm in diameter, respectively. The Mg microparticles were flat and oblong in shape, approximately 10-100 mm in length. The microparticles were serially washed with dichloromethane (≥99.8%, Sigma Aldrich) and 1,4-dioxane (99.5%, Acros Organics) in triplicate. Polycaprolactone (average M_n 80,000, Sigma Aldrich) was selected as the insulating matrix because it is commercially available, easy to process and exhibits a lower elastic modulus and longer elongation at break than polylactic acid, rendering it more favorable for flexible interconnects (Table 21). For reference, the mechanical properties of PCL may be attributed to its low glass transition temperature (-60 ˚C), permitting polymer chains to move more easily under deformation than PLA (T_g = 50-55˚C). Commercial PCL pellets were solubilized in 1,4-dioxane to a concentration of 200 mg/mL. Oleic acid (90%, Sigma Aldrich) was then added to the serially-washed Fe. Oleic acid was selected as a surfactant to facilitate the homogenous suspension of microparticles in the CPC solution and to prevent sedimentations. Oleic acid is a monounsaturated fat naturally found in animal fats and vegetable oil. Its molecular structure comprises a hydrocarbon chain that terminates on one end in a carboxylic acid group. Consequently, one end of the

structure is hydrophobic and the other is hydrophilic, rendering it a useful surfactant. Finally, the PCL solution was added to the Fe and oleic acid mixture to reach the desired volume fractions.

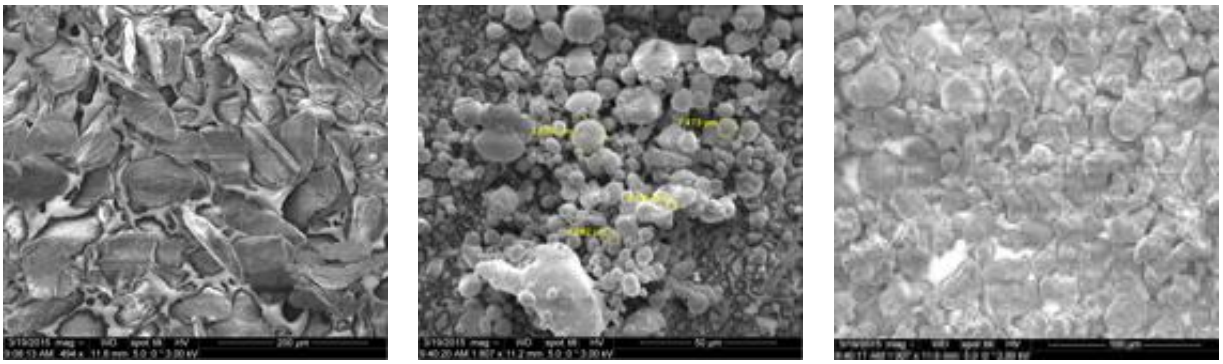

(a) (b) (c)

Figure 82 SEM images of the (a) Mg, (b) Zn and (c) Fe microparticles used for investigating biodegradable conductive polymer composites.

Table 21 Physical and mechanical properties of polycaprolactone and polylactic acid.

Polymer	**Polycaprolactone**	**Polylactic acid**
Glass Transition Temperature (˚C)	-60	50-55
Tensile Modulus (GPa)	0.2-0.3	3.1-3.7
Tensile Strength (MPa)	25-35	60-70
Elongation at Break (%)	>300	2-6

2.4.3. Electrical Percolation of Mg-, Zn- and Fe-based Conductive Polymer Composites

As electrical conductivity and mechanical robustness are key design requirements for interconnects, the effect of physiological degradation on the electrical resistivity and elastic modulus of Fe-PCL composites was investigated. Composite films with different volume fractions of Fe were prepared and immersed in simulated body fluid (SBF) at 37ºC in an incubator to simulate physiological degradation. At intermittent time points, the resistivity of the films was measured using electrical probe testing.

Figure 83 shows the electrical resistivity of Mg-, Zn- and Fe-based conductive polymer composites as a function of volume fraction and parameterized by the duration of physiological degradation. No

percolation was observed with Mg-PCL CPC films measured in air (t = 0 h) or after conditioning in SBF. Although the electrical resistivity decreased by 4 orders of magnitude after immersion in SBF, the lowest resistivity recorded was approximately 4.7 x 103 Ω·cm and more than 8 orders of magnitude larger than that of Ag-based CPC materials (Table 2.$). Further, the initial decrease in resistivity after SBF immersion was attributed to electrolyte permeation into the PCL matrix. As shown in Figure 83, the electrical resistivity of PCL decreased by 3 orders of magnitude after immersion in SBF. The high resistivity was attributed to magnesium hydroxide passivation on the surface of the Mg microparticles, either native and/or formed due to corrosion in SBF. Figure 84 shows the SEM image of a 40%vf Mg-PCL composite after 20 hours in SBF. Holes can be observed across the surface of the composite. As the holes were not present prior to exposure to SBF, it is speculated that they are the result of the hydrogen evolution and buildup of gas within the CPC film during Mg corrosion.

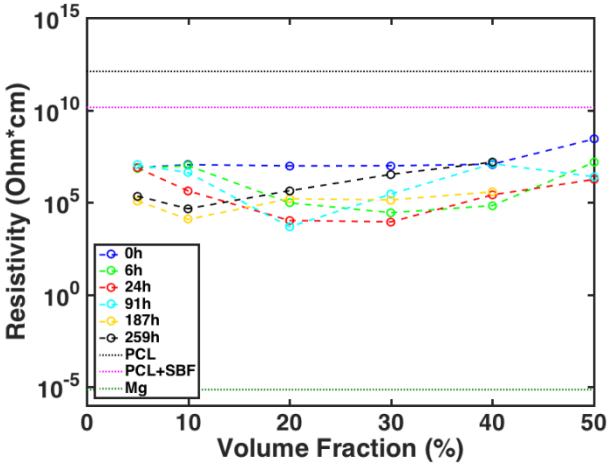

(a)

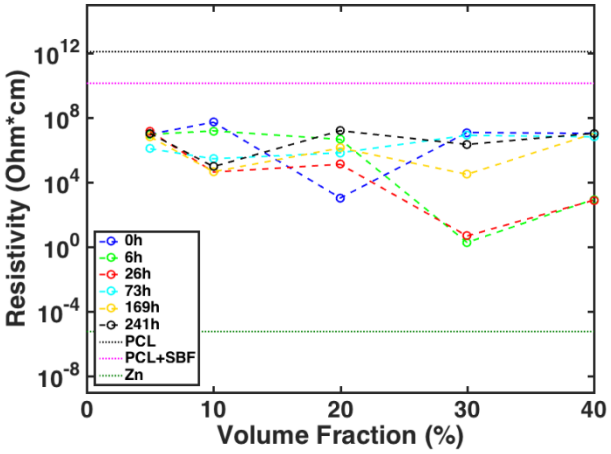

(b)

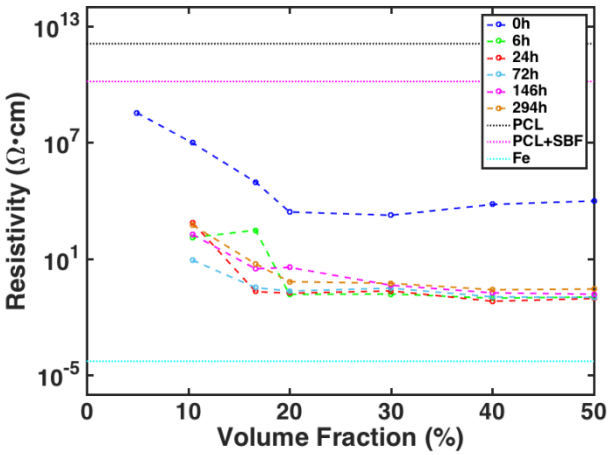

(c)

Figure 83 Electrical resistivity of biodegradable CPC films at varying volume fractions of (a) Mg, (b) Zn and (c) Fe, parameterized by degradation time.

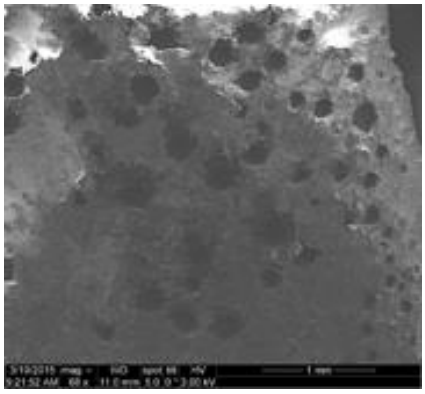

Figure 84 SEM image of 40%vf Mg-PCL composites after 20 hours of immersion in SBF. The holes observed in the film were not present prior to degradation conditioning. It is speculated that the holes are the result of hydrogen evolution during magnesium corrosion.

In contrast to Mg composites, Zn- and Fe-based CPC films exhibited electrical percolation at 25% and 17% volume fractions, respectively. The Zn-PCL composites did not show percolation until after 6 hours of immersion in SBF and sustained until 73 hours in SBF, after which the resistivity returned to the initial values recorded in air (t = 0 h) and percolation was no longer observed (i.e., t >= 73 h). Thus, Zn-PCL films exhibited a functional lifetime of 1-2 days on the basis of electrical resistivity. During this time period, the resistivity of Zn-PCL films at 30% volume fraction (vf) was 4.9 Ω·cm.

Iron-based CPC films demonstrated the largest reduction in resistivity at percolation. Measurements in air indicated that Fe-PCL composites were 9.4×10^{6} Ω·cm and 1.8×10^{3} Ω·cm for 10%vf and 30%vf, respectively. The 3-order-of-magnitude decrease was maintained after immersion in SBF, but the electrical percolation curve shifted downwards towards lower resistivity. Specifically, the resistivity of 10%vf and 30%vf Fe-PCL composites were 3.3×10^{1} Ω·cm and 8.4×10^{-2} Ω·cm, respectively. The Fe-PCL composites maintained electrical percolation at volume fractions greater than 17% for more than 500 hours. Overall, Fe-PCL composites exhibited the lowest resistivity amongst the CPC types examined at volume fractions above the percolation threshold and best approximated the expected resistivity of non-degradable, commercial ECA materials (e.g., Ag-epoxy composites).

Iron-polycaprolactone films exhibited superior electrical performance to Mg-PCL and Zn-PCL films as conductive polymer composites. For this reason, the remainder of this section will examine Fe-PCL composites exclusively for biodegradable interconnect and strain sensing applications.

2.4.4. Fabrication of Biodegradable Electrical Interconnects

Surrogate biodegradable circuit boards were constructed to evaluate the feasibility of micropatterning biodegradable electrical interconnects on similarly biodegradable circuitry, as shown in Figure 85. Briefly, surrogate biodegradable circuit boards were screen printed using 10-mil-thick polyester shim as the stencils. First, the polyester shim was micromachined with a CO_2 laser. The patterned shim was then laminated onto PLA substrates using polyvinyl alcohol (PVA) as the adhesive. The PLA substrates had been previously metallized with Fe traces 100 nm in thickness by sputter deposition through a shadow mask and laser micromachined (532 nm wavelength, 100 µJ pulse energy, 1 ns pulse width, and 10 W maximum power) to pattern the Fe traces. Specifically, 25% of the Fe surface area of each pad was ablated to expose the underlying PLA to promote adhesion of the composites. Finally, the Fe-PCL composite was applied and screen printed onto the pre-patterned Fe-PLA substrate. In this manner, electrically-continuous daisy chain structures were micropatterned on the PLA.

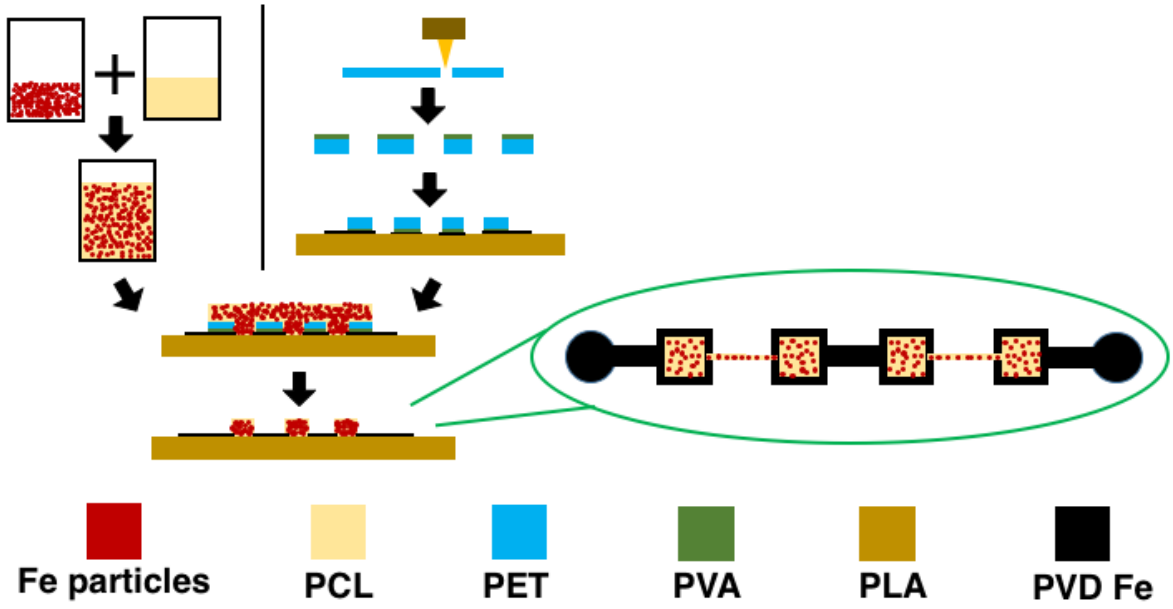

Figure 85 Fabrication scheme and daisy chain structures of Fe-PCL biodegradable electrical interconnects.

Figure 86 shows the micropatterned biodegradable daisy chain structures comprising Fe-PCL composites interconnects bridging sputter-deposited Fe traces. The interconnect width and thickness were 350 µm and 250 µm, respectively, which agree with the microscale dimensions of MEMS devices. Together, the micropatterned daisy chain structures demonstrate the compatibility of Fe-PCL composite interconnects with standard MEMS processing techniques. Fig. 2B shows the backside view of a daisy chain structure to visualize the laser machined Fe traces featuring 25% areal exposure of the underlying PLA substrate. The ablated regions with PLA exposure are in direct contact with the overlying screen-printed Fe-PCL composite to promote adhesion.

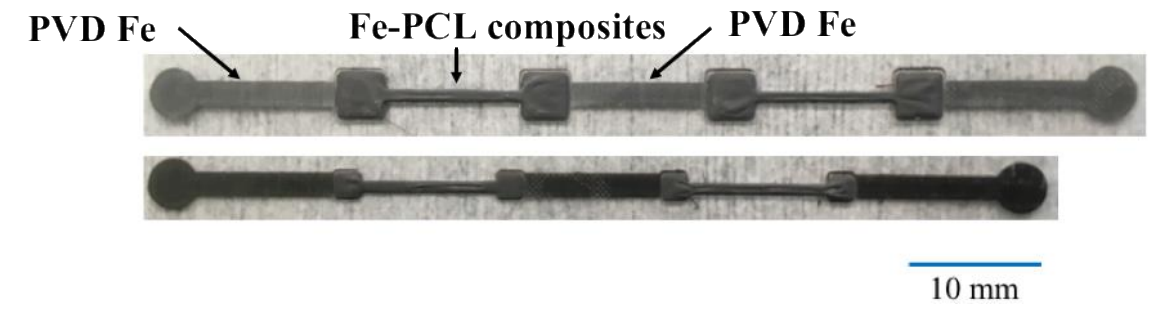

(a)

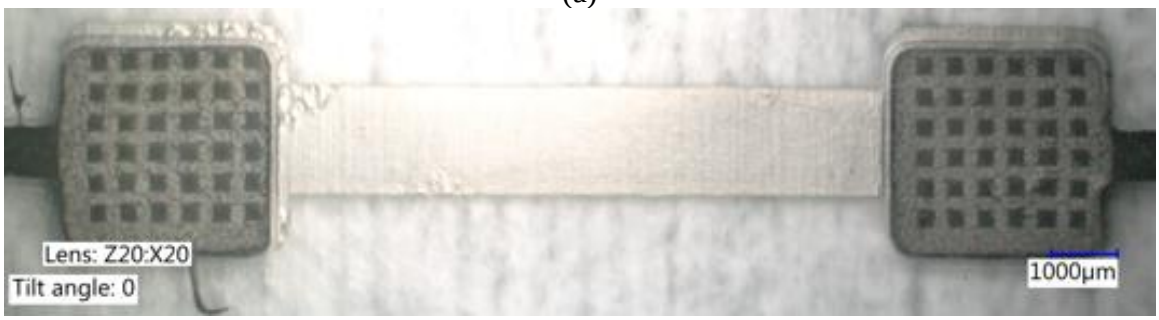

(b)

Figure 86 Optical images of micropatterned biodegradable daisy chain structures comprising Fe-PCL conductive polymer composites as interconnects bridging sputter-deposited Fe traces: (a) Zoomed out. (b) Backside view of bridged pad structures in a daisy chain. The surrogate biodegradable circuit board features mesh iron contact pads, where the underlying PLA is exposed in 25% of the surface area. This promoted adhesion of the composite-based interconnect to the surrogate board.

2.4.5. Electrical Stability of Fe-PCL Composites with Degradation and Mechanical Loading

The electrical resistivity of Fe-PCL composites were measured by electrical probe testing throughout the examined time course of biodegradation in SBF. In addition, physiologically conditioned Fe-PCL composite films were mechanically strained to 1% tensile strain at 1 Hz for 100 cycles in a uniaxial mechanical testing system (Bose Electroforce 3200) to monitor the elastic modulus of the composite with respect to degradation time. As biodegradable electrical interconnects may also be exposed to occasional mechanical strain due to physiological loading and local micromotion, the electrical resistivity of mechanically and physiologically conditioned Fe-PCL films was also monitored.

Figure 87 shows the electrical resistivity of composites with varying volume fractions of Fe throughout the time course of degradation. Although the resistivity is higher than traditional

interconnect materials, the Fe-PCL composites above the percolation threshold are still candidate materials for use in low current interconnects. In addition, the electrical resistivity of composite films with volume fractions of Fe above 17%vf remained stable within 500 hours of immersion in SBF and, thus, demonstrated a lifetime of over 20 days. The National Center of Manufacturing and Science (NCMS) issued a criterion for solder replacements on the basis of electrical stability. Specifically, the change in contact resistance of an interconnect must not exceed 20% after accelerated aging at 85°C and 85% relative humidity for 500 hours. This has been a difficult criterion for traditional, non-degradable ECA materials. In particular, non-noble metal surfaces (e.g., Sn/Pb, Sn, Cu, Ni) are susceptible to galvanic corrosion. Here, Fe-PCL composites are presented that satisfy the 500-hour requirement for electrical stability under a more corrosion testing environment.

After 500 hours, the resistivity of all films started to increase as corrosion proceeded**.** However, with physiological degradation, the resistivity of the composites at higher volume fraction of Fe (i.e., >40%) exhibited enhanced stability, potentially attributable to the smaller percentage of iron being lost at higher volume fractions as degradation proceeds (since the initial amount of iron at higher volume fractions is higher). Another potential explanation is that Fe corrosion products, such as oxides formed during degradation, present an electrical barrier to conduction. Unlike non-degradable ECA materials, the “divide and conquer” approach does not apply to biodegradable conductive polymer composites. The electrical properties are not merely determined by conductive filler, as the insulating matrix may hinder the corrosion process and extend the functional lifetime of the composite. In addition, the corrosion products are non-conductive and contribute to the insulating matrix of the composite system, possibly altering the mechanical properties of the film over time. The mechanical properties of Fe-PCL composites

are subsequently examined. As the electrical stability is an important parameter during the functional lifetime of an electrical interconnect, composites with 40%vf of Fe were selected for use in subsequent testing.

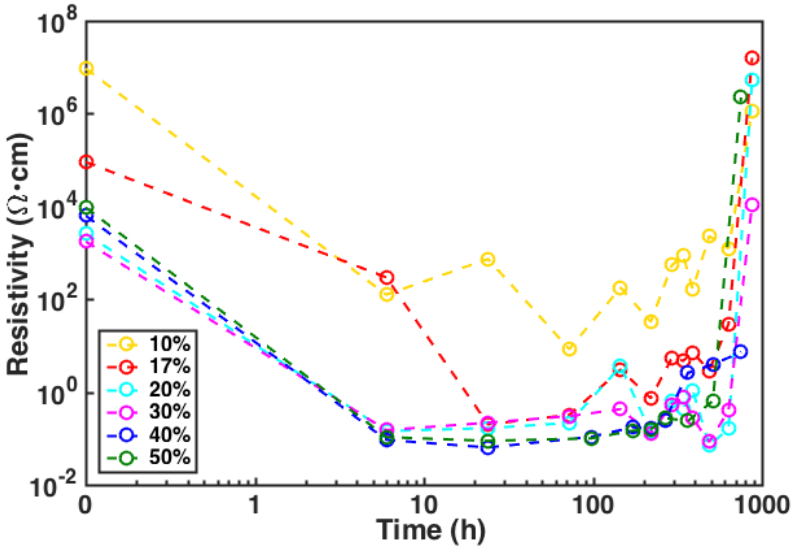

Figure 87 Electrical resistivity of Fe-PCL biodegradable conductive polymer composite films at varying volume fractions of Fe, parameterized by degradation time.

To assess the effects of intermittent strain on the interconnect conductivity, the electrical resistivity of 40%vf Fe-PCL composite films as a function of degradation time with and without intermittent cyclic tensile strain is compared (Figure 88). The mechanical conditioning simulated the strains that an implanted chip may experience in the body. Each strained sample was subjected to 100 cycles of a 1% strain at a frequency of 1 Hz. The resistivity of the intermittently strained films decreased and stabilized to approximately 0.3 Ω·cm within 6 hours in SBF, similar to the electrical resistivity of films that had not undergone mechanical strain. In addition, the resistivity fluctuations of both films were commensurate, which indicates that the stability in resistivity of composites with 40%vf of Fe was not significantly affected by intermittent strain under physiological degradation.

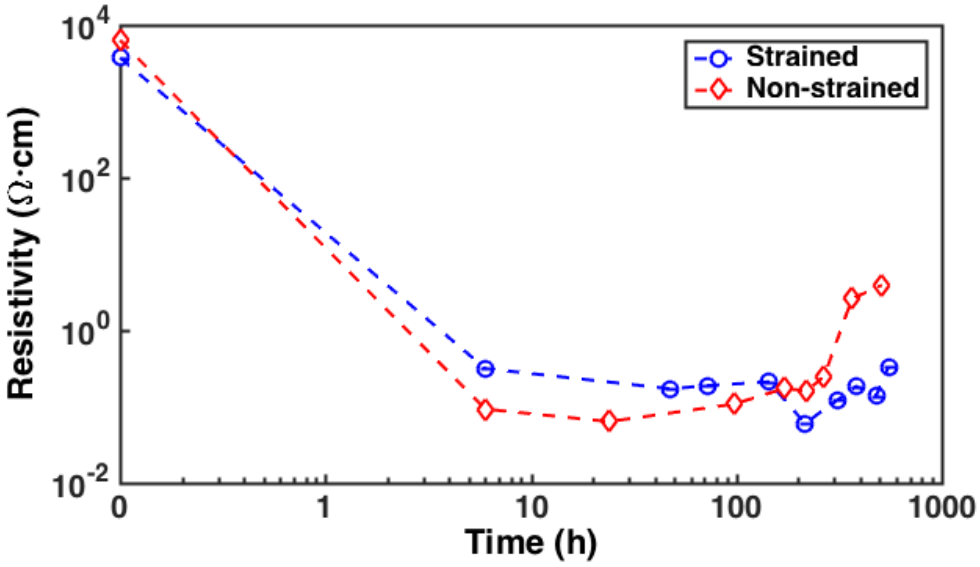

Figure 88 Electrical resistivity of Fe-PCL biodegradable conductive polymer composite films (40%vf of Fe) as a function of degradation time with and without intermittent strain.

2.4.6. Tensile Modulus and Adhesion Strength of Fe/PCL Interconnects

The functional lifetime of electrical interconnects may also be limited by its adhesion strength. While this is not desirable, physiological degradation may further exacerbate the effect. In order to overcome this design challenge, it was important to enhance the adhesion strength of Fe-PCL composites on biodegradable substrates and to ensure that the adhesion persists throughout physiological degradation. Towards these goals, as well as to demonstrate the processing compatibility of biodegradable Fe-PCL interconnects on similarly biodegradable substrates, Fe-PCL electrical interconnects were screen printed onto micropatterned Fe-PLA substrates. Specifically, iron traces were micropatterned onto a 250-µm-thick PLA substrate by sputter deposition through a shadow mask to form a grid of 10mm x 10mm squares of 100 nm thickness. Next, the sputtered Fe was ablated with an array of 250-µm-wide square holes to expose 25% of the underlying PLA and Fe-PCL composite (40%vf of Fe) was screen printed onto the micropatterned Fe using the fabrication procedure described earlier. Samples was then diced into individual coupons comprising three test samples per coupon and immersed in SBF at 37ºC for physiological conditioning.

At periodic time points, samples were retrieved for optical microscopy and adhesion testing in accordance with ASTM D3359-09 guidelines [8]. Briefly, two intersecting cuts were made through the Fe-PCL composite in each sample using a razor blade; the intersection point was aligned with the center of each square pattern and the intersection angle ranged between 30º and 45º. For each test, 75-mm-long strip of Scotch permanent tape was adhered onto the cut Fe-PCL composite with the tape running in the same direction as the smaller intersecting angle. Good contact was ensured before proceeding. Within 90 ± 30 s of application, the tape was pulled off rapidly at a peel angle as close to 180º as possible. Finally, the cut area was inspected for removal of composites from the substrate and adhesion was rated based on the ASTM scale. The scale ranges from 0 to 5, which correspond to complete removal of the adhesive material (i.e., poorest adhesion) and negligible loss of adhesive material, respectively.

During the intermittent strain process described above, it was possible to assess the elastic modulus of the 40%vf composite material as a function of degradation time (Figure 89). The elastic modulus of the composite was 200 MPa prior to immersion in SBF. The modulus of the Fe-PCL composite was larger than that of bulk PCL (0.8 ± 0.1 MPa) due to the Fe microparticle fillers dispersed throughout the PCL matrix. The elastic modulus stabilized at approximately 400 MPa after an initial increase upon immersion in SBF. The transient increase upon exposure to SBF may be attributed to the formation of surface oxides, which also shifts the effective volume fraction of PCL within the composite. However, the elastic modulus is still lower than that of metal and semiconductor interconnects (≈ 100 GPa), which suggests that the composites are more compliant and could provide more flexibility in interconnection. The elastic modulus fluctuated within 25% over 500 hours, indicating a relatively good stability in degradation.

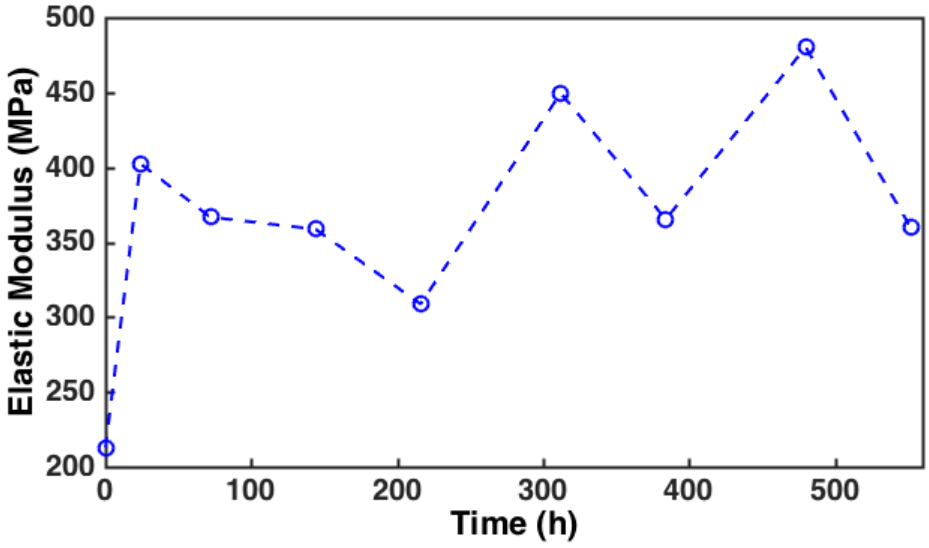

Figure 89 Elastic modulus of Fe-PCL biodegradable conductive polymer composite films (40%vf of Fe) as a function of degradation time under intermittent strain.

As biodegradable electrical interconnects must maintain adhesion onto similarly biodegradable substrates, the adhesion of Fe-PCL composites on Fe-PLA substrates was investigated with respect to degradation time (Figure 90). From previous experiments, it was found that the composites showed poor adhesion on stainless steel substrates, where composites could be peeled off without effort (i.e., rating of 0 in adhesion tests). Further, it was hypothesized that the corrosion products formed during degradation could embrittle the Fe-PCL composite and deteriorate its adhesion. However, the design of the Fe traces presented in this study, which featured 25% areal exposure of the underlying PLA substrate, significantly improved its adhesion with Fe-PCL composites. Specifically, the composites scored the maximum adhesion rating (i.e., 5) and retained their adhesion strength throughout the time course of degradation (Figure 91). The results not only confirmed that the design of the micropatterned Fe traces and Fe-PCL composites can successfully resolve previous adhesion challenges, but also support their use for biodegradable electrical interconnects in transient implantable applications.

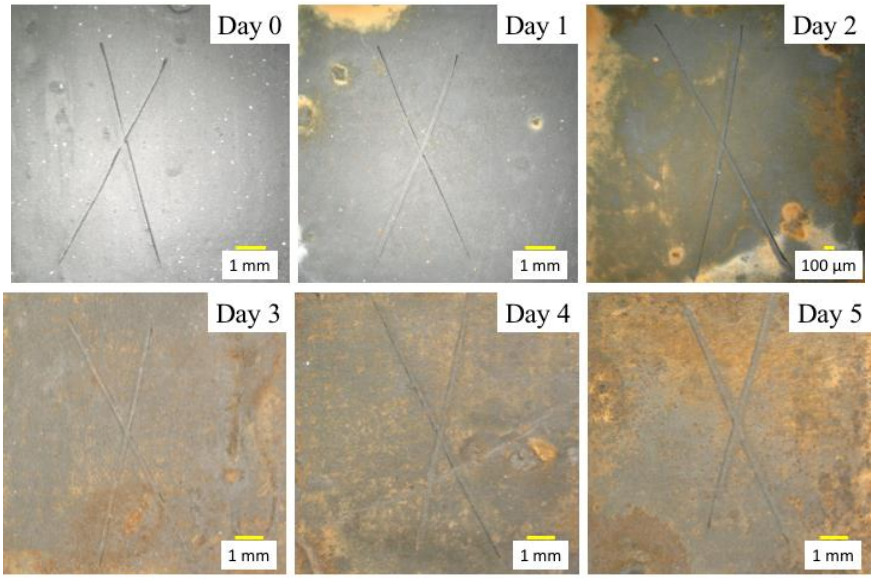

Figure 90 Optical images of physiologically conditioned Fe-PCL composites (40%vf of Fe) after adhesion tests were performed on PLA substrates with micropatterned Fe traces.

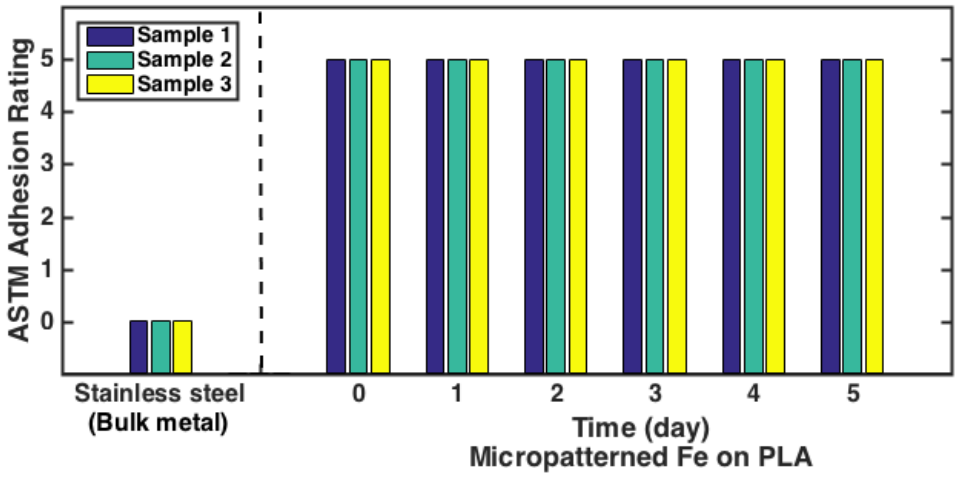

Figure 91 Adhesion test ratings of Fe-PCL composites on micropatterned Fe-PLA compared against stainless steel (i.e., bulk metal) control samples. Tests were performed on Fe-PCL composites after varying immersion times in SBF to simulate degradation conditions. Adhesion is rated between 0 to 5; higher ratings correspond to better adhesion.

2.4.7. Degradation Behavior of Fe/PCL Composites

The degradation behavior of Fe-PCL composite films (40%vf Fe) were evaluated by linear sweep voltammetry (LSV) (Gamry Reference 600). The test was performed at 37ºC in SBF using a three-electrode

configuration, where the working, counter and reference electrodes were the Fe-PCL composite, a platinum mesh, and a saturated silver/silver chloride electrode, respectively. The measurement scanned a 500-mV window centered about the open circuit potential at a scan rate of 2.5 mV/s after open circuit potential stabilization. The corrosion potential and corrosion rate were determined by linear fitting the results based on Tafel equations [9].

Figure 92 shows the polarization curves of Fe-PCL biodegradable conductive polymer composite films with 40%vf of Fe throughout degradation. The corrosion potential of the composite films was -0.537 V vs. Ag/AgCl prior to degradation conditioning in SBF, which approximates the corrosion potential of bulk Fe. The corrosion potential decreased when the degradation time increased, indicating the increasing corrosion tendency of the films. Moreover, the corrosion current density increased as a function of time, implying an increased corrosion rate as degradation continued.

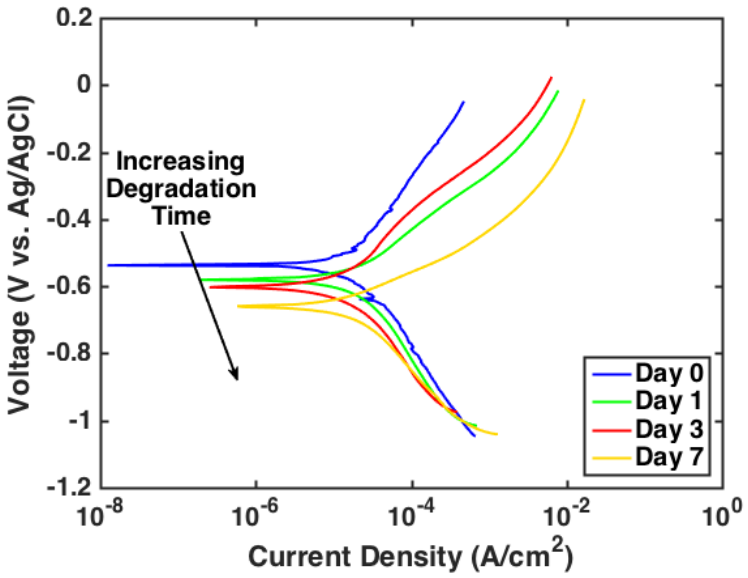

Figure 92 Polarization curves of Fe-PCL biodegradable conductive polymer composite films (40%vf of Fe) after physiological degradation.

2.4.8. Piezoresistivity of Fe-PCL Composites for Strain Sensing

The utility of conductive polymer composites is not only limited to packaging and circuitry, but have also been explored for strain sensing applications. As discussed earlier, conductive polymer

composites can be piezoresistive depending on the material composition. Figure 93 shows the strain sensitivity of Fe-PCL composites evaluated under cyclic tensile strain for 1-10 μm and 10-30 μm sized Fe particles over the time course of 22 days. Overall, the results confirmed that conductive polymer composites exhibit a higher strain sensitivity than solid Mg films or other metals that exhibit a geometry-based piezoresistivity; as discussed earlier, the higher strain sensitivity is attributed to a change in electrical resistivity with applied strain, rather than merely a change in geometry. However, the strain sensitivity of Fe-PCL films fluctuated over the time course examined. Specifically, Fe-PCL films comprising 10-30 μm particles demonstrated fluctuations in strain sensitivity of $\pm$88% within the initial 21 days (i.e., <550 hours). With smaller-sized particles (i.e., 1-10 μm), improved stability in strain sensitivity was observed, where during the initial 17 days (i.e., 400 hours), strain sensitivity $\pm$33%. Both formulations of Fe-PCL composites exhibited larger fluctuations than desired for the proposed strain sensors for monitoring bone fracture healing, however, and were not further explored for strain sensing applications in this study.

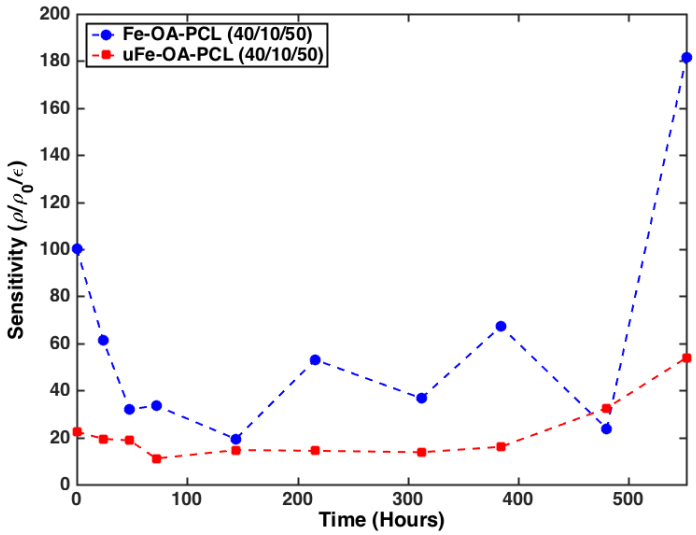

Figure 93 Strain sensitivity of Fe-PCL composites featuring two different particle sizes for the Fe conductive filler: 1-10 μm (μFe-OA-PCL) and 10-30 μm (Fe-OA-PCL). Sensitivity was determined based on electromechanical testing of CPC films under 1% cyclic tensile strain, where the gauge factor corresponds to the unit change in normalized resistivity with respect to applied strain.

In this section, the suitability of Fe-PCL composites as potential candidates for biodegradable electrical interconnects and piezoresistive strain sensors were investigated. The electrical percolation threshold of Fe-PCL composites was found at 17%vf of Fe. Stability of resistivity over a reasonable functional lifetime was achieved by utilizing composites with 40%vf Fe, in excess of the percolation threshold; stability was maintained even under intermittent tensile strain. Short term adhesion testing indicated reasonable adhesive stability of these interconnect materials. While the electromechanical properties were not conducive to strain sensing applications, these properties, together with the relatively low composite elastic modulus, supported their potential application as interconnects. The biodegradable electrical interconnects were shown to be compatible with standard processing techniques through the formation of micropatterned daisy-chain structures.

2.5. Conclusions on Biodegradable Materials

This chapter examined the fabrication and characterization of biodegradable materials for applications in MEMS-based devices. As discussed in the introduction of this thesis, the repertoire of biodegradable materials and fabrication schemes has been a rate-limiting step in development of and further improvements in biodegradable devices. Biodegradable conductors, passivation schemes and encapsulation strategies were explored in the forms of electroplated films, conductive polymer composites, multi-layer thin films, as well as bulk laminated layers with the purpose of expanding the current selection and processing of biodegradable materials for MEMS. The electrochemical and relevant electrical and mechanical properties of the materials were subsequently examined to understand the degradation and/or corrosion protection under physiological conditions. Electroplated magnesium, zinc and fluorinated hydroxyapatite, as well as thin film barriers, demonstrated favorable properties for use in biodegradable strain sensors for orthopedic applications. The subsequent chapter will explore the microfabrication and integration of these material sets for biodegradable devices.

CHAPTER 3

BIODEGRADABLE STRAIN SENSORS AND ENERGY SOURCES

3.1. Implantable Non-Degradable Strain Sensors for Understanding the Bone Healing

3.1.1. Introduction

With increasing interest in implantable and wearable technology, biomedical MEMS increasingly focuses on the clinical market [5], [27], [33], [73], [77], [80], [86], [87], [223], [250]. FDA-approved commercial products include sub-dermal glucose sensors, microneedle patches for insulin and vaccine delivery, and wireless pressure sensors for monitoring intra-aortic pressure in patients with congestive heart failure [36], [40], [52], [78], [251]. The size scale of MEMS corresponds well with the size scales of many biological systems, rendering MEMS as an attractive option for biomedical sensors. However, MEMS technology can also expand the quantitative tools currently available to biomedical researchers, where *in vivo* studies are heralded in fundamental science, as well as in tissue engineering and regenerative medicine (TE/RM). The size dimensions attainable with MEMS accommodate the physical constraints of rodents, the most commonly used animal model in academia [77], [252]. Further, the ability to investigate mechanical, electrical and biochemical cues continuously and in tandem (i.e., multi-modal) within an animal might reduce the number of animals required in a given study, promoting animal welfare, conserving research costs and supporting higher throughput studies. Hence, the impact and utility of bioMEMS lies not only in the clinical market, but also in the fundamental science arena [5].

In particular, MEMS technology offers three exciting opportunities: (1) longitudinal measurements of mechanical and biochemical cues in animal models, (2) *in vivo* monitoring of regenerative medicine therapies, and (3) close-loop feedback to guide therapeutic action (e.g., drug and growth factor delivery). For example, understanding the mechanistic reasons governing the success or failure of a given therapy is technically limited by the ability to monitor relevant environmental cues continuously and locally.

Quantitative techniques in animal models often rely on indirect measurements through imaging or endpoint studies, where the animal is sacrificed for *ex vivo* testing. MEMS can address this limitation and provide local, longitudinal monitoring of environmental cues while satisfying the size constraints of small animals. In this manner, MEMS technology can potentially enable researchers to better understand the spatiotemporal complexity of the physiological system.

Orthopedic research presents a facile path to adapting MEMS technology for use in animal studies [27], [58], [97], [219]. Researchers have been interested in the mechanical and biochemical cues regulating bone healing, where implantable strain and oxygen sensors would enable *in situ* measurements throughout the various stages of bone regeneration and remodeling [3], [5], [15], [29], [59], [60]. Current methods for assessing the mechanical properties of a bone defect either require sacrificing the animal to perform *ex vivo* mechanical characterization or employ radiographic imaging to indirectly determine bone density. Neither techniques enable longitudinal studies and direct assessment of the mechanical environment *in vivo* [7], [15], [29]. Computational modeling, such as finite element models and computational fluid dynamics, provide spatial information and the ability to perform parametric analysis to evaluate the importance of model variables [15], [29], [253]. However, the results of a computational model heavily depend on the input boundary conditions. As the boundary conditions are oftentimes approximated and premised on simplifying assumptions, this can significantly limit the accuracy of the model [7], [57].

Bone regeneration is a dynamic process. The loading distribution across the healing bone, implanted structural devices, and adjacent tissue may evolve throughout the time course of bone healing [5], [15], [29]. Bone regeneration features the organized formation and remodeling of multiple tissue phenotypes. The timescale of the various phases of bone healing varies from hours and days to months and years. The four phases of bone regeneration are: (1) acute inflammation and hematoma (hours to days), (2) callus formation (days to weeks), (3) woven bone (weeks to months) and (4) lamellar bone (months to years). A callus is a soft tissue matrix that primarily comprises collagen, whereas mineralization then leads to woven and lamellar bone with increasing mechanical stiffness. Woven bone features an unorganized

matrix of collagen and hydroxyapatite, as well as a disorganized vascular network [5], [6], [8], [9], [56], [59]. Bone remodeling gradually restores the vascular and skeletal structure to its full functionality. As can be seen, the mechanical strain applied across a bone defect and its adjacent fixation plate during physiological loading spans a large dynamic range throughout the full time course of bone healing [15], [57]. The ability to quantitatively monitor mechanical loading continuously *in situ* would promote current understanding of the mechanical basis of bone regeneration, as well as inform the development of regenerative medicine therapies for bone-loading tissues.

This study presents the development of a MEMS-based strain sensor for the *in vivo* monitoring of mechanical cues regulating bone healing. Specifically, the device will support the *in situ*, real time monitoring of mechanical loading across critically sized femoral defects in rodents, an animal model developed by collaborators for understanding bone healing.

3.1.2. Design Rationale for *In Vivo* Monitoring in Rodents

Figure 94 shows a schematic of the critically-sized femoral defect featured in the rodent model of this study. A critically-sized defect is defined as a non-union where direct bone regeneration is not possible. Instead, healing proceeds via the secondary pathway, where a collagen matrix first forms across the bone defect and is, subsequently, replaced by bone matrix [3], [15]. Fixation plates are installed to bridge the femoral bone defect and to limit mechanical loading across a 10 mm femoral defect, permitting only uniaxial loading parallel to the femur. Custom strain sensors were microfabricated to address the physical and mechanical design constraints of the rodent bone defect model. The strain sensor, designed to accommodate the physical constraints and loading regime of the rodent, is installed onto the distal surface of the fixation plate with accompanying circuitry packaged and routed to a subcutaneous pocket in the abdomen. Real time strain data recorded during ambulation enabled gait analysis during the acute phase of bone healing, which was not possible with previously employed techniques.

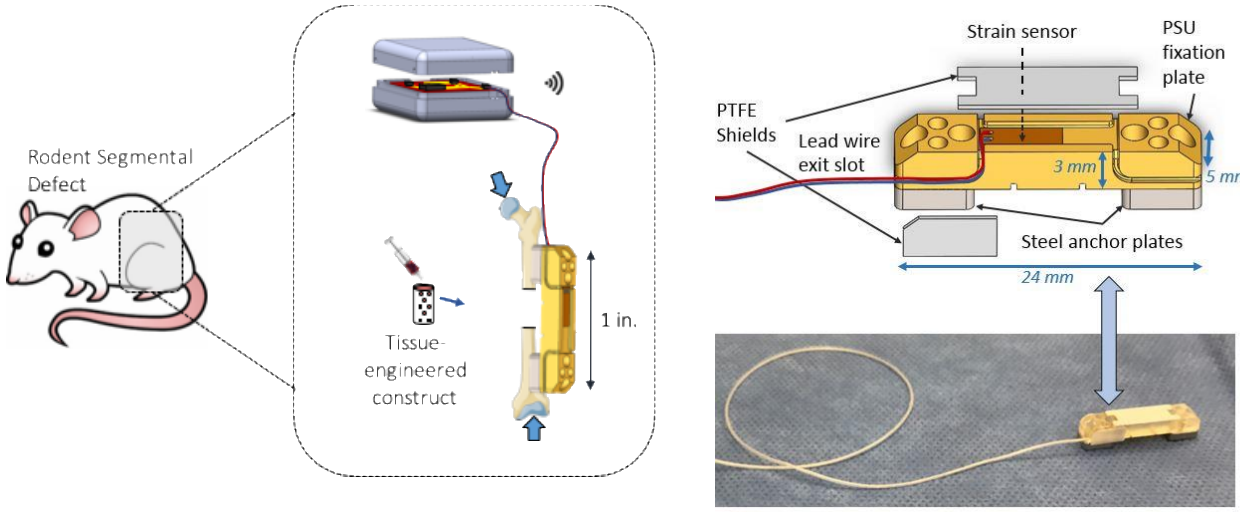

(a) **(b)**

Figure 94 (a) Schematic of rodent with a critically-sized femoral defect. (b) Graphic rendering of custom designed fixation plate that permits only uniaxial loading across a bone defect. The inset on the distal surface of the fixation plate accommodates the installation and encapsulation of the strain sensor.

The strain sensor presented in this study is a MEMS-based piezoresistive strain sensor featuring a full Wheatstone bridge design (i.e., piezoresistive gauges comprising all four elements of the bridge). The transduction mechanism often implemented by these strain sensors is piezoresistivity, wherein an applied mechanical strain elicits a change in the electrical resistivity of the sensing material and, in this manner, transduces a mechanical stimulus into an electrical response [204]

$$GF = \frac{\Delta R/R_0}{\Delta \mathrm{l}/l_0} = (1 + 2\nu) + \frac{\partial \rho/\rho_0}{\partial l/l_0} \tag{3.59}$$

where GF, R, l, ν, ρ, and the subscript "0" correspond to the piezoresistive gauge factor, electrical resistance, length, Poisson's ratio, electrical resistivity and initial value of the property without applied strain. As shown, piezoresistance is determined by both a geometric and materials response to applied strain. Piezoresistive strain sensors comprising semiconductor materials have been demonstrated using nano-crystalline silicon and doped silicon, which feature high and, in some cases, directional piezoresistive

coefficients [98], [254], [255]. For example, a flexible, n-type nanocrystalline strain gauge has been demonstrated for the monitoring of mechanical loading on stainless steel hip prostheses with an axial gauge factor of -23.5 [98]. Metallic strain gauges, which rely on a geometric effect to transduce mechanical strain into changes in electrical resistance, have also been demonstrated for orthopedic applications [97], [219]. Minimal film thickness and high resistivity metals, such as platinum (10.6 μΩ·cm) and nickel-chromium alloy (130 μΩ·cm), are desired with metal gauges [256]. However, gold (2.3 μΩ·cm) has also been considered due to its chemical inertness [219].

Although strain gauges are commercially available, few options satisfied the size and material constraints for use in rodent models. While low resistance (i.e., 350 Ω) single element resistors manufactured by Omega did satisfy this design constraint, the low resistance corresponded to higher current consumption, reducing the much-coveted battery lifetime *in vivo*. Further, single element strain gauges are susceptible to environmental and thermal drift, as well as alignment errors. In addition, they require bridge completion circuits to obtain differential voltage outputs in order to reduce the error associated with absolute voltage readouts. This arrangement was selected to improve accuracy of small strain measurements, cancel thermal and off-axis errors, eliminate alignment concerns with implementing a series of individual strain gauges, and eliminate the need for resistance matching and additional wiring steps for external Wheatstone bridge configurations. The Wheatstone bridge improves sensor accuracy by measuring changes in electrical potential with applied strain, which reduces noise contributions [257]–[260]. The Wheatstone bridge configuration will be implemented with a pair of sensors oriented axially and a pair oriented transverse to the direction of applied strain. For a balanced bridge with identical nominal resistances in each resistive element, the differential voltage output is given by:

$$\Delta E_G = \frac{1}{2} E_S \cdot GF \cdot \varepsilon \cdot (1+\nu)(1+\varkappa) \tag{3.60}$$

where ΔE_g, Es, GF, ε, ν, and $\varkappa$ correspond to the differential voltage output, source voltage, gauge factor of sensor, applied mechanical strain, Poisson's ratio, and a non-linearity factor, respectively. As thermal

effects are biaxial, thermal output would equally affect axially- and transversely-oriented sensors. In this manner, the differential output of the Wheatstone bridge is insensitive to thermal fluctuations [204], [219], [257], [258]. However, Johnson noise is temperature-dependent, as shown previously.

Material compatibility is critical to the design of implantable devices. The use of materials with poor biocompatibility may elicit strong inflammatory responses that jeopardizes the health of the host, as well as the integrity of the device. The inflammatory response to the implantable device may also modify the sensing environment and, thus, the sensor no longer captures the native biological response it was intended to monitor. In this study, titanium and gold are used to develop piezoresistive strain gauges on polyimide. Titanium and gold metallic films were selected for the conductive bridge elements due the high electrical resistivity of titanium and the chemical inertness of gold. Hence, they were selected over conventional MEMS materials with higher piezoresistive gauge factors (e.g., nano-crystalline and doped silicon with high directional piezoresistive coefficients and whose resistivity changes with strain) and higher resistivities (e.g., nichrome (130 μΩ·cm) and constantan (49 μΩ·cm)). For reference, the electrical resistivity of titanium and gold are 43 μΩ·cm and 2.3 μΩ·cm, respectively [256], [261]. This rendered the metals appropriate as piezoresistive sensors and connection lines, respectively. Given the *in vivo* application of the strain sensor, it was also important that the device is sufficiently encapsulated to prevent leaching at the time scales of interest. The strain sensor featured commercial polyimide (Dupont Kapton) as the substrate and a combination of parylene-C and aluminum oxide as the encapsulation layers; the biocompatibility and application of these materials for bioMEMS have been previously demonstrated in literature [50], [219], [250], [252].

To serve the proposed application, the device must detect mechanical strain during the acute phase of fracture healing, wherein the mechanical properties of the fracture site evolves as bone heals. Specifically, as bone regenerates and remodels across a critically-sized defect, progressing from endochondral

ossification to woven bone to calcified bone, the load distribution increasingly transfers from the fixation plate onto the healing bone [21], [262]. Table 22 shows the stiffness of the polysulfone fixation plate compared to that of cortical bone. As bone healing proceeds, stiffness of the defect begins to approach that of cortical bone and incurs more of the load sharing. Literature reports that physiological loading of a female Sprague Dawley rat at 13 to 26 weeks is 2.6 to 3.4 N and the hind leg bears one- to seven-fold that of physiological loading during physical activity [3], [15], [19], [29]. This corresponds to a maximal load of 24 N. Taken together, the proposed strain sensor should demonstrate a detection range of 500 to 5000 με. The frequency of physiological loading ranges from 0 to 5 Hz from standing to running [19], [263].

Table 22 Axial stiffness of fixation plate and strain sensor compared to cortical bone [29].

Substrate	**Axial Stiffness (N/mm)**
Fixation Plate	214
Strain Sensor	116
Cortical Bone	Inquire (E = 20 GPa)

3.1.3. Materials and Fabrication

Figure 95 shows the fabrication scheme for the strain sensor. Briefly, atomic layer deposition (ALD) of aluminum oxide, followed by e-beam evaporation of titanium and gold, were performed on commercial polyimide sheets. Shipley 1813 photoresist was then spin coated onto the substrate and lithographically micropatterned as a masking layer for metal etching. Evaporated gold and titanium films were wet etched in diluted potassium iodide solution and dry etched by reactive ion etching (RIE) with sulfur hexafluoride gas, respectively. Photolithography was performed again with AZ4620 after removal of the S1813 etch mask with acetone and sonication to define the contact pads. Through-mold electrodeposition of copper was performed using a commercial copper plating solution (Grobet) under direct current at 20 mA/cm^2, which corresponded to a deposition rate of approximately 0.5 um/min. Samples were rinsed in DI water and immersed into acetone to remove the AZ4620 mold after electrodeposition. Alumina was next deposited by ALD to serve as a barrier thin film against moisture

permeation prior to the chemical vapor deposition of parylene-C to provide bulk encapsulation. Contact pads were exposed by excimer laser machining (IPG Microsystems IX-255, which selectively ablated the parylene and alumina on top of the copper contact pads. Individual sensors were singulated by ablation with a green laser (IPG Microsystems IX-200-F) after mounting the polyimide sheet onto a glass substrate with NR9 photoresist. Sensors were rinsed with acetone, isopropanol and DI water to remove residual contaminants prior to use.

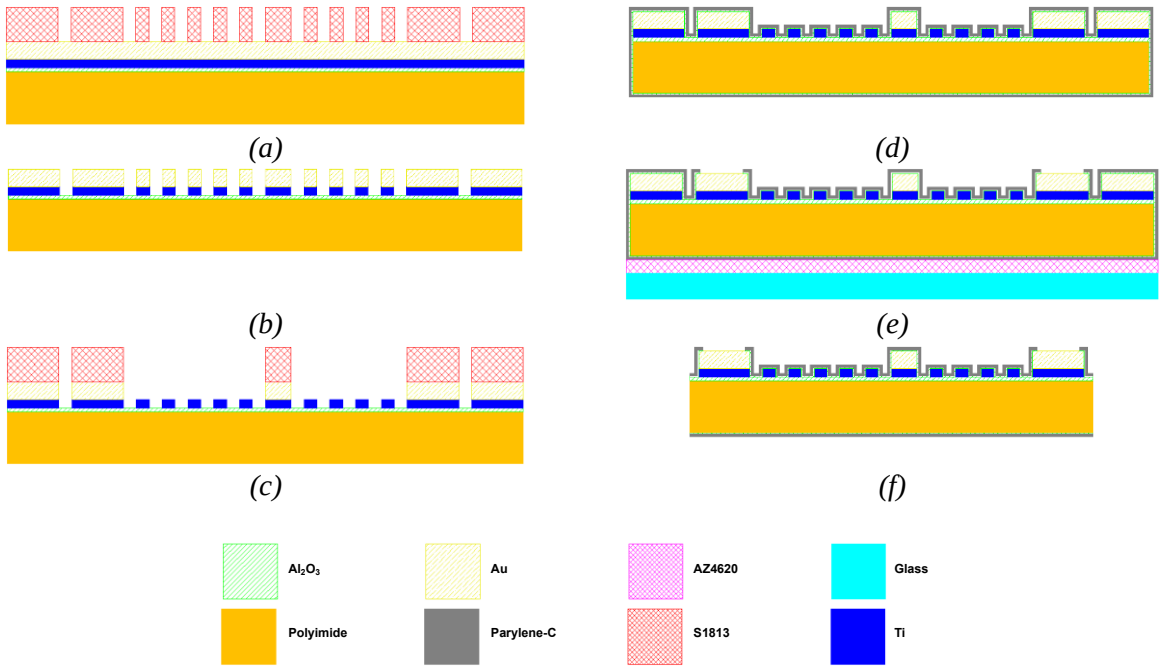

Figure 95 Fabrication scheme of the thin film piezoresistive strain sensor.

The devices were mounted onto polysulfone fixation plates for testing. Figure 94B shows an optical image of the fabricated sensor after packaging within the fixation plate. The sensors were mounted using low-temperature-curing epoxy (VPG Micro Measurements, AE-10), which can be cured at 60-70C. Four 40-AWG wires were tinned with solder and packaged with miniature polyolefin heat-shrink tubing. The proximal end of the packaged wires was soldered to the contact pads of the sensor. The polyolefin tubing was routed and inserted into the side of the fixation plate. Both the solder joints and routed polyolefin tubing were encapsulated with UV-curable, medical-grade encapsulant (Dymax 3041) to provide strain relief and

to prevent liquid ingress. Additional encapsulant (Dymax 1072-M) was applied to cover the sensor and the inset cavity was finally covered with a teflon plate.

Bench top electromechanical testing was performed with a Bose Electroforce 3200 mechanical testing system. The sensors were supplied with a constant 3V excitation source. The voltage output of the sensors was acquired through the Bose software. Electromechanical response of sensors was evaluated under direct loading from 0-100 N, which corresponded to physiological strain ranges, and at varying physiologically-relevant loading frequencies (50 mHz to 1 Hz). Tests were performed in triplicate and fixation plates were reinstalled into the testing system in between tests to eliminate setup variability. The sensor output, applied mechanical load and cross head displacement of the Bose were simultaneously recorded at a sampling rate of 100 Hz. Homogenous strain distributions across the fixation plate were assumed, such that cross head displacement of the mechanical testing uniform was used to determine applied strain. In addition, devices were tested in a three-point bending configuration under cyclic compression over the time course of 7 weeks to evaluate the effect of physiological conditioning, which were implemented *in* vitro at 37^{o}C in simulated body fluid (SBF). Strain amplitudes spanned a range from 75 με to 8000με to encompass the dynamic range of strain experienced during bone regeneration with a fixation plate. Data was digitally filtered with a low pass FIR filter with a cut-off frequency of 10 Hz. Long-term drift was similarly acquired with a commercial data acquisition module (NI RIO), which continuously measured the sensor output response to a 3V excitation source. Sensors packaged in fixation plates were immersed in simulated body fluid and stored at 37C to emulate physiological conditions throughout drift testing and in between electromechanical testing.

3.1.4. Electromechanical Sensor Characterization

The bone healing environment is a spatiotemporally heterogenous environment, with changing mechanical and biochemical properties, morphogenesis of multiple tissue types and evolving vascular networks and bone structures. Given the dynamic environment in which the strain sensor must operate, it

was important to perform thorough device characterization under representative physiological conditions, as well as to understand long-term drift and fatigue. To begin, electromechanical characterization of the strain sensors was performed on polysulfone blocks with and without medical-grade encapsulant to evaluate device performance independent of the packaging protocol required for the proposed rodent model. Under direct loading (i.e., two-point bending), strain sensitivities of 0.67 μV/V/με and 0.19 μV/V/με were observed in the nominal and encapsulated configurations, respectively (Figure 96a). This suggested that device packaging attenuates sensor performance. The theoretical gauge factor, as determined from Equation 3.59, is 1.64 for titanium-based strain gauges because the piezoresistivity of titanium stems solely from the geometric effect. Hence, attenuation in device sensitivity was observed in two stages; strain sensitivity under direct loading with the sensor mounted on the fixation plate was approximately 41% of its theoretical limit and further reduced by 29% after encapsulation and packaging within the fixation plate. The theoretical gauge factor is typically not observed due to attenuation across interfaces, such as from the substrate to the sensing elements of the sensor, but, more importantly, from the test specimen to the adhesive and adhesive to the sensor substrate. Medical grade epoxy was utilized for device mounting. Curing was performed with a custom fixture to maintain pressure across the strain sensor surface to ensure contact to the test specimen. However, air pockets within the adhesive, non-uniform pressure during the bonding process and non-uniform thickness of the adhesive can further exacerbate strain attenuation effects from the adhesive. In addition, the attenuation observed from device encapsulation indicates that strain distribution across the fixation plate is not uniform and, hence, cross head displacement of the mechanical testing system might not capture the local strain applied to the packaged strain sensor. Overall, packaged sensors demonstrated linear strain response from 300 με to 6500 με (Figure 96a-c), which encompasses the anticipated strains experienced during physiological loading across a healing bone defect. Linearity and strain sensitivity were maintained at loading frequencies from 50 mHz to 1.0 Hz, suggesting that the sensor can monitor the various forms of physiological loading and ambulation.

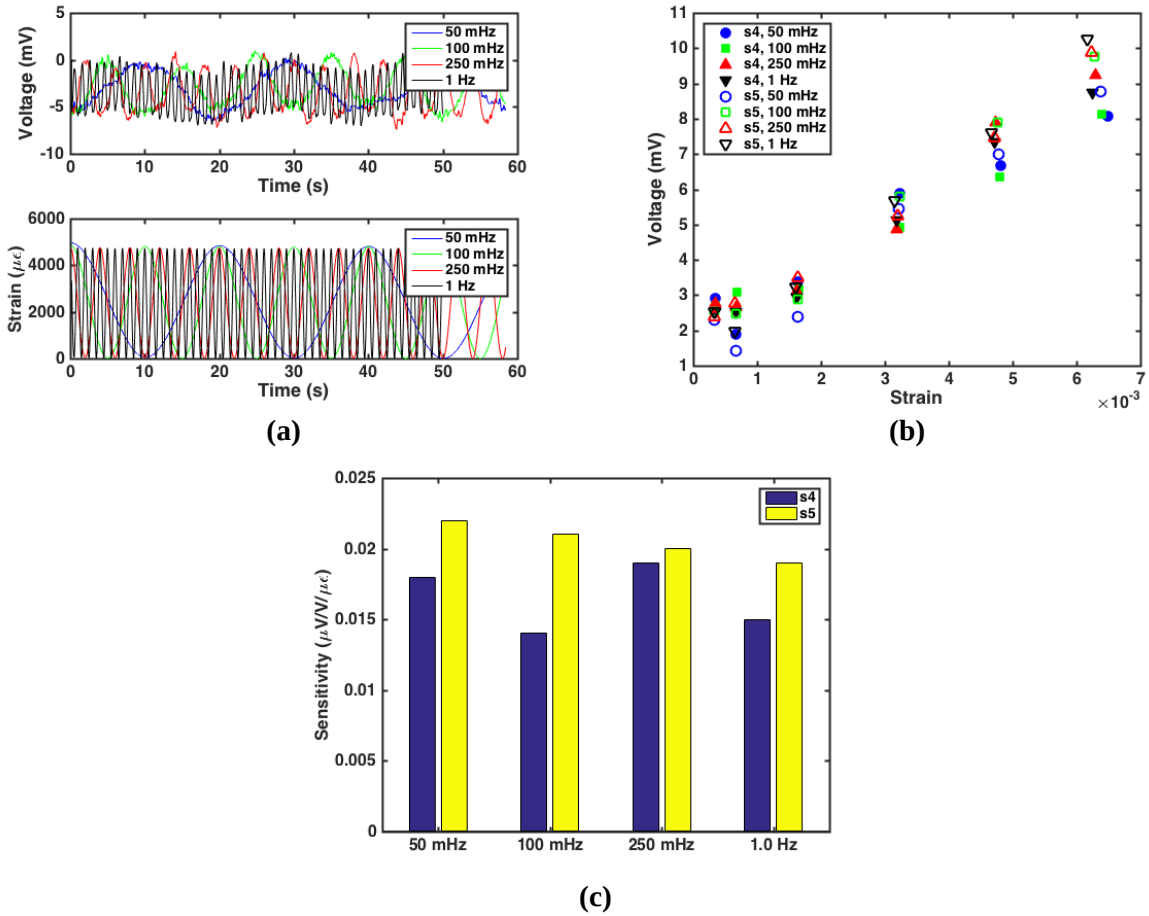

Figure 96 ***(a)*** *Strain sensor performance under cyclic compressive strain at varying physiologically-relevant frequencies.* ***(b)*** *Sensor response to cyclic loading at various frequencies.* ***(c)*** *Strain sensitivity with respect to loading frequency.*

3.1.5. Long-Term Performance Under Physiological Conditions

To emulate the *in vivo* testing environment, packaged sensors were immersed in physiological solution at 37˚C and retrieved periodically for electromechanical testing. The objective was to evaluate device sensitivity and stability under physiological conditions because electrolyte ingress would likely cause an electrical short, as well as corrode the contact pads. As testing was conducted in the three-point bending configuration, lower amplitude strains were successfully assessed and a strain amplitude range of 75 με to 8000 με, which spans the physiological range of strain experienced during bone regeneration with a fixation plate, was examined. A strain sensitivity of 0.15 μV/V/με was observed at day 0 (i.e., under ambient

conditions prior to any device exposure to physiological conditions). Device performance retained linearity over a large dynamic range of strain. Lower limits in strain amplitude were limited by testing capability. This was evidenced in Figure 97a, where fluctuations in voltage output of the sensor reflected fluctuations in applied strain. Device sensitivity remained within $\pm$5% of initial sensitivity until week 7, when strain sensitivity deviated by +10% from day 0 measurements. The increased deviation was attributed to electrolyte ingress and sensor degradation, as device functionality ceased after 7 weeks of physiological conditioning. Hence, the functional lifetime observed *in vitro* was 7 weeks. It is speculated that *in vivo* lifetime might exceed benchtop results because SBF is more corrosive than blood and interstitial fluid. Overall, the observed sensor stability suggested that the sensor passivation schemes and device packaging sufficiently prevented liquid ingress into the sensor and the packaging supports short-term *in vivo* applications.

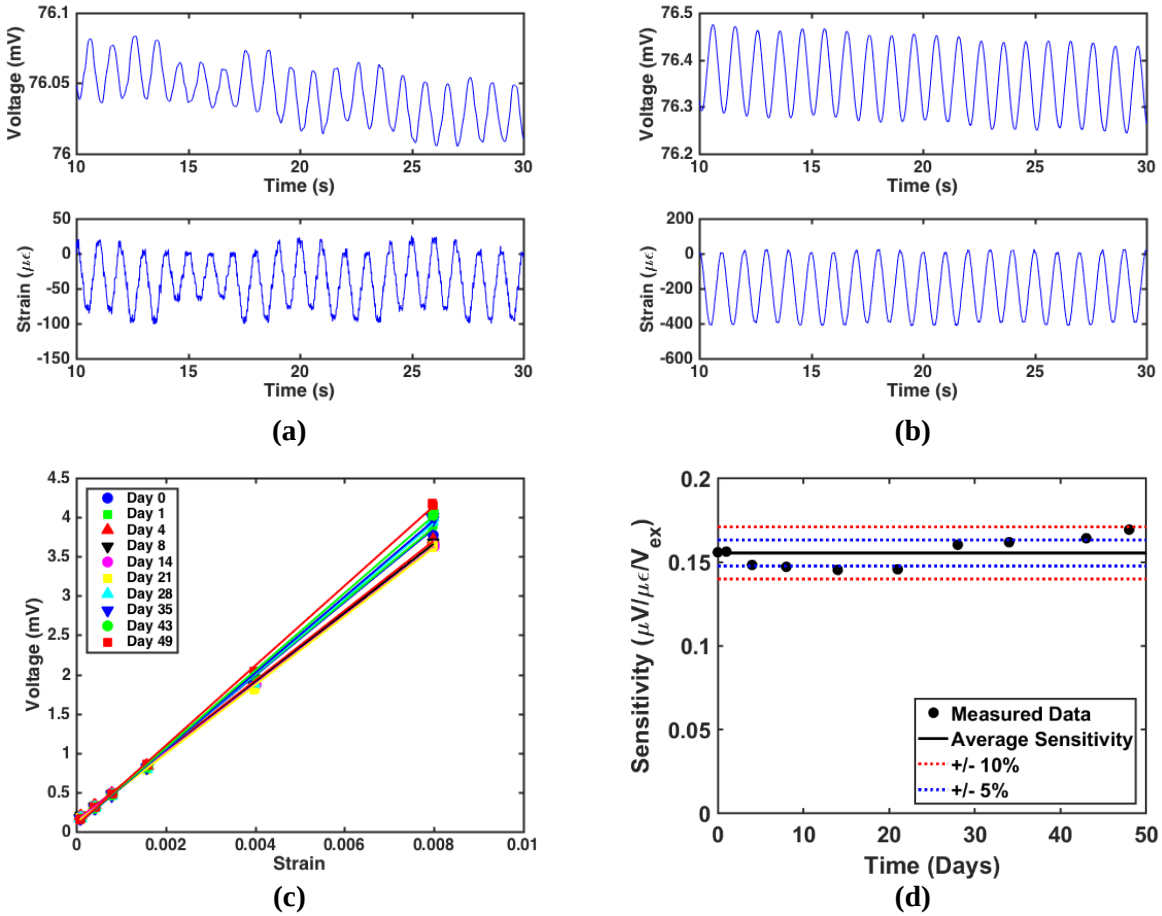

Figure 97 Strain sensor performance under physiological conditions in vitro. ***(a-b)*** *Voltage output of sensor in response to cyclic compressive strains at 75 με and 400 με amplitudes, respectively.* ***(c)*** *Long-term strain sensor performance under physiological conditions, evaluated from 75 με to 8000 με. Tests were conducted at a mechanical loading frequency of 1 Hz for 100 cycles each and tested in triplicate.* ***(d)*** *Strain sensor performance across an evaluation period of 7 weeks under physiological conditions.*

Device drift was monitored with a packaged sensor immersed in physiological solution at 37˚C, as shown in Figure 98. The device was powered and the voltage output was monitored for 10-minute intervals at various time points throughout the study. The observed sensor drift corresponded to a strain-referenced error of ±25 με/min within the functional lifetime of the device. This corresponded to approximately 250 με during each *in vivo* measurement. It is speculated that the observed drift magnitude will not severely impact strain measurements during the initial period of bone healing, as the anticipated strains are orders of magnitude larger.

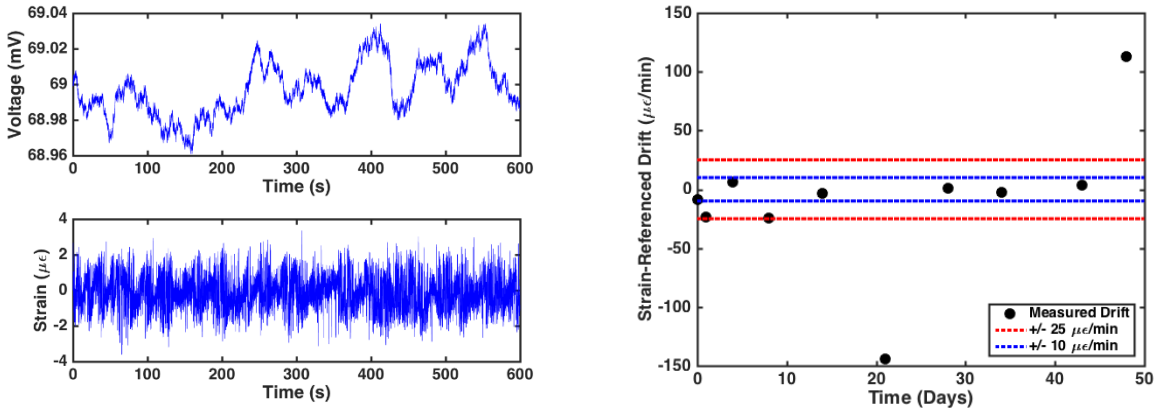

(a) **(b)**

Figure 98 Device drift under physiological conditions, presented as normalized change in nominal output voltage over time.

3.1.6. Off-Axis Mechanical Testing to Emulate Bone Regeneration

Figure 99 shows the strain sensor performance from off-axis mechanical loading, where the strain sensor was mounted onto two steel blocks separated by 10 mm to emulate the critically-sized bone defect. Data is summarized in Table 23. Testing was performed with either an empty defect or with materials of varying stiffness to emulate the different phases of load sharing between the healing bone and internal fixation plate. In the off-axis configuration, uniform strain distribution across the fixation plate cannot be assumed, especially at high loads (i.e., with an empty defect) because the fixation plate undergoes moderate buckling. Hence, laser extensometry was used to determine the local displacement of the sensor instead of using cross-head displacement data of the mechanical testing system to determine global strain. The strain sensors demonstrated similar sensitivity in the higher loading regimes (i.e., with empty and rubber defects), but lower sensitivity with a stiffer defect (i.e., Teflon). Given the linear strain response observed under direct loading conditions as small as 300 με, it is speculated that the lower strain sensitivity is attributed to the non-uniform strain distribution across the plate under off-axis loading. Given the consistent reduction in strain sensitivity, however, this may be accounted for when assessing mechanical loading during the acute inflammation and soft callus phase compared to the woven and lamellar bone phases of bone regeneration.

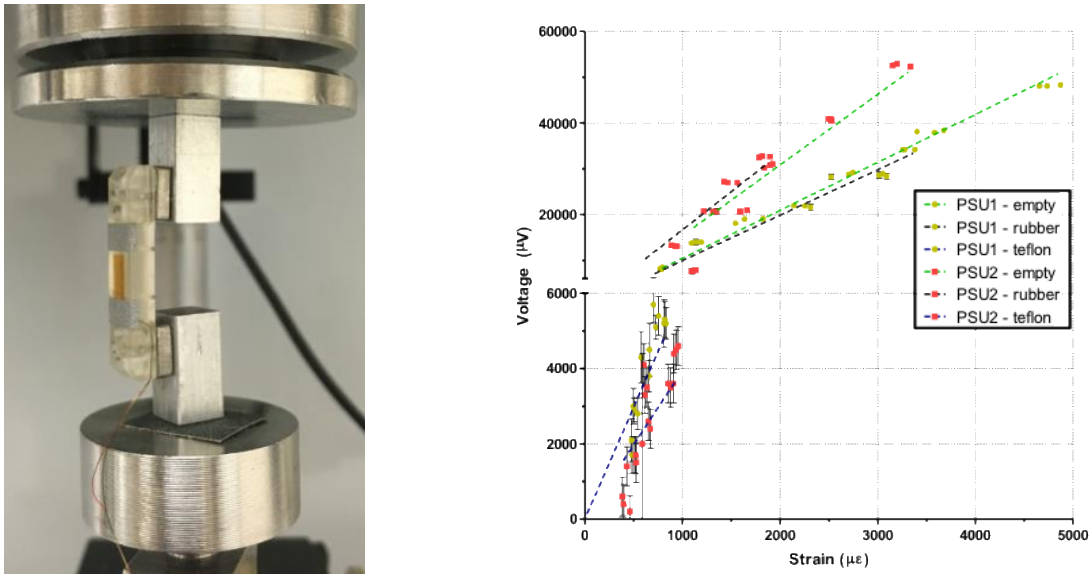

(a) **(b)**

Figure 99 Off-axis electromechanical testing of packaged sensor on fixation plate. ***(a)*** *optical image showing the off-axis test setup and* ***(b)*** *strain sensor performance during various emulated stages of bone healing, where callus formation, mineralization and remodeling occur in the inter-fragmentary space.*

Table 23 Sensor performance under off-axis loading, which captures the different extents of load sharing between the internal fixation plate and healing bone defect.

Defect Material	Device Sensitivity (μV/V/με)		Correlation (Pearson's R^2)	
	Sensor 1	Sensor 2	Sensor 1	Sensor 2
Empty	0.109	0.156	0.993	0.973
Rubber	0.103	0.169	0.967	0.976
Teflon	0.066	0.044	0.849	0.912

3.1.7. Fatigue Testing of Packaged Sensor

Fatigue testing of packaged strain sensors, as shown in Figure 100, indicated device failure at 7,500 cycles of high compressive loading (i.e., 4000-4400 με). Since high mechanical strain is only expected during the initial phases of bone regeneration, where load sharing is minimal and the fixation plate incurs the majority of the applied physiological load, the results suggested that the strain sensor is sufficiently robust for monitoring acute bone healing and long-term bone remodeling at lower strain magnitudes. Figure 100b shows that only intermittent failure was observed after 7500 cycles and when the sensor resumed

functionality, the voltage output approximated the device output during the initial 7000 cycles. This suggested that the sensor was not permanently damaged (e.g., broken traces in the sensing element and connection lines) because intermittent functionality with similar voltage outputs would not be possible with broken traces. These results also suggested that device delamination likely did not cause the observed device failure because the voltage response would decrease during intermittent functionality if this were the case. Altogether, it is speculated that the device failure was attributed to disrupted connection at the solder joints. Loose connections at the solder joint would cause device failure, but sufficient physical contact would support device operation. The higher contact resistance corresponding to the latter case would explain the slight fluctuations in sensor output during intermittent functionality. Solder joint failure may be attributed to the solder joint defects and mismatches between the thermal and mechanical properties of the solder joint and the surrounding medical-grade encapsulation. As the 40 AWG magnet wires were manually soldered onto the fine pitch contact pads of the sensor, suboptimal soldering may have contributed to weakened bond force. Further, the different coefficients of thermal expansion between solder and the polyurethane-based encapsulation may have caused unintended stress at the solder joint and expansion of the encapsulation due to Joule heating from continuous testing may have caused the solder joint to lift from the sensor contact pad. These common modes of failure at solder joints may potentially be resolved with the use of conductive polymer composites, such as with the Fe-PCL biodegradable interconnect demonstrated in Chapter 2.4. Interconnect micropatterning through a shadow mask would overcome the solder defects attributed to manual soldering of contact pads with fine pitch. Further, the thermal and mechanical properties of polymer composites better approximate that of polymeric encapsulants than bulk metal (e.g., solder), thereby relieving the stresses attributed to mismatches in coefficients in thermal expansion.

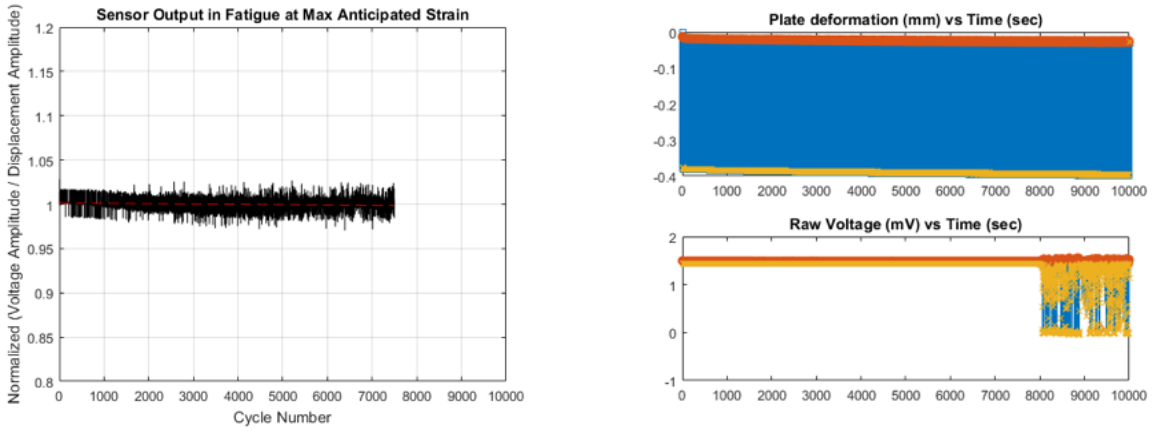

(a) **(b)**

Figure 100 Fatigue testing of non-degradable strain sensors. Devices were compressively strained under between 4000 με and 4400 με for 10,000 cycles. ***(a)*** *Normalized sensor output with respect to cycle count and* ***(b)*** *temporal data showing device failure after intermittent device failure after 7,500 cycles.*

3.1.8. Conclusions of Non-Degradable Strain Sensor

This study presented a MEMS-based strain sensor to monitor the mechanical environment across large bone defect in rodents. The demonstrated strain sensor provided local strain measurements longitudinally across time, enabling researchers to investigate the biomechanics of bone regeneration continuously within an animal. Electromechanical characterization at relevant physiological loads and ambulation frequencies, fatigue testing and long-term drift testing performed under physiological conditions confirmed that the strain sensor performance and packaging were sufficiently sensitive and robust for operation *in vivo*. The microfabricated strain sensor achieved the requisite device performance for the *in situ* monitoring of bone healing in a rodent femoral model and retained device functionality for 49 days. The study revealed that the functional lifetime of a non-degradable device is not necessarily permanent. Degradation by corrosion and/or fatigue can nonetheless render a non-degradable device non-functional even though its physical form remains relatively intact. The major distinction lies in the available material sets to protect against device degradation, as the library of materials and microfabrication schemes is much broader for traditional, non-degradable devices. Hence, the results provided an upper limit in the expected functional lifetime of an analogously biodegradable strain sensor. Going beyond strain

sensing, the environmental cues regulating bone healing are not only mechanical; the presented work serve as a stepping stone towards the design of multi-modal systems (e.g., with oxygen sensing) for quantitative *in vivo* monitoring and expand the measurement capability currently available in fundamental biological research.

3.2. Biodegradable Strain Sensors

3.2.1. Introduction

The following section explores the development of biodegradable strain sensors for implantable orthopedic applications. Specifically, the findings from the previous chapter on biodegradable materials and earlier section on non-degradable strain sensors culminate to inform the development of the current work. Given that a non-degradable strain sensor comprising polyimide and gold exhibited a functional lifetime of 7 weeks *in vitro*, the objective of this section was to demonstrate a biodegradable device whose functional lifetime was no more than 1-order of magnitude less than the corresponding non-degradable device (i.e., 7 weeks). The underlying goal was to improve biodegradable device functionality as a pathway towards developing clinical-viable therapies with biodegradable devices (e.g., biodegradable devices whose functional lifetime are clinically relevant). It was hypothesized that the material sets demonstrated in Chapter 2 would support the experimental objective; specifically, that electroplated magnesium and biodegradable passivation schemes were optimal for the design of a biodegradable strain sensor for monitoring bone healing and for achieving the functional lifetime goal.

It is hypothesized that the implementation of biodegradable passivation schemes will improve the performance of biodegradable sensors. This might correspond to a longer functional lifetime or more stable device performance within the functional lifetime of the sensor. For example, as demonstrated in the previous chapter, passivation schemes comprising pulse plated Zn (pp-Zn) reduced the corrosion rate of Mg by 3-4 orders of magnitude when tested in SBF at room temperature. However, when evaluated at 37^{o}C to emulate physiological conditions, the corrosion protection afforded by Zn coating reduced to only 1-2 orders of magnitude in improvement. More importantly, sample-to-sample variation increased and the maximum corrosion rate observed across samples was higher than that of bare Mg. This phenomenon indicated that the underlying Mg became exposed and galvanically coupled to the Zn coating and could have occurred due to pinholes during the Zn electrodeposition process or due to pitting or stress corrosion cracking after immersion in SBF. The former would correspond to a rapid onset in device deterioration,

whereas the latter would manifest as a delayed onset. It should also be noted that device fabrication entails more than the sequential electrodeposition of Mg and Zn, but must also encompass Mg micropatterning, device encapsulation and substrate release. Hence, it is imperative that the fabrication process preserves the functionality of the Mg sensor, but also the integrity of any passivation schemes.

3.2.2. Fabrication and Characterization

Figure 101 illustrates the fabrication scheme for a biodegradable strain sensor featuring electrodeposited Mg. To overcome the chemical and physical constraints of processing with biodegradable materials, a flexible polyimide film (75-µm-thickness; Dupont Kapton HN) was used as the substrate to support mechanical release of the fabricated structures. Whereas conventional substrates (e.g., silicon and glass wafers) require chemical or plasma-enhanced etching to undercut the device structures for substrate release, the use of a flexible substrate enables substrate release by simply peeling. However, thickness of the polyimide film and adhesion between the bottom-most surface of the device layer and top-most layer of the polyimide film must be considered in optimizing the fabrication process.

First, the polyimide substrates were prepared for the through-mold electrodeposition of Mg. The substrates were metallized with titanium and copper by sputter deposition (i.e., 25 nm Ti adhesion layer, 500 nm Cu seed layer and 25 nm Ti protection layer). Titanium was selected as the top protection layer because it can be removed by dry etching, avoiding exposure to moisture prior to Mg electrodeposition. Copper was selected as the conductive seed layer because Mg electroplates well on pristine Cu, but exhibits poor adhesion to oxidized copper. This enables the selected release of Mg structures from the copper-based substrates.

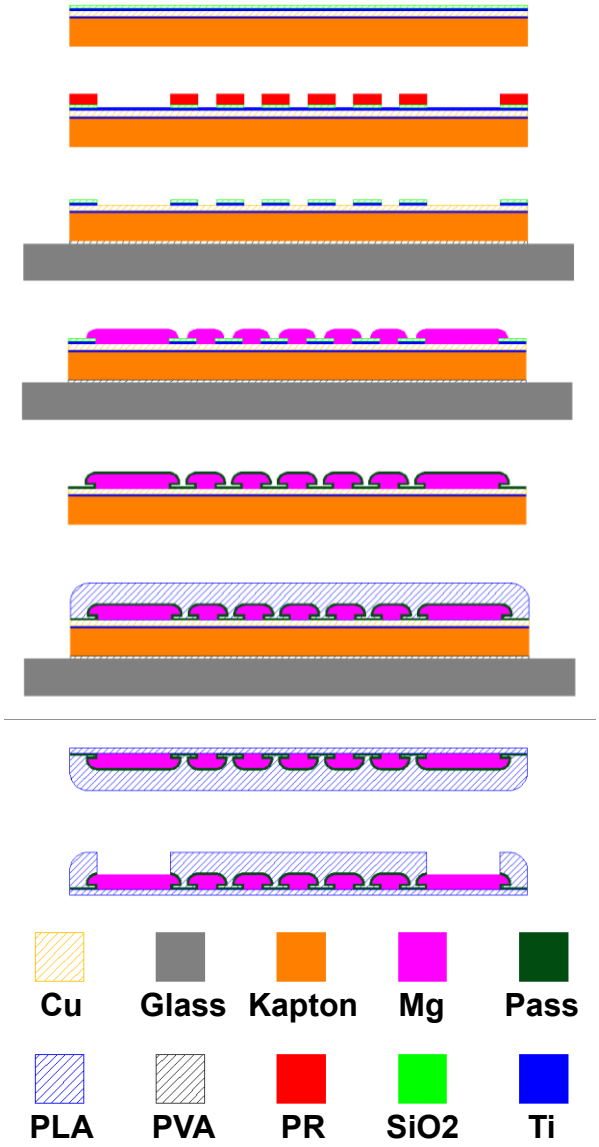

Figure 101 Fabrication scheme for biodegradable strain sensors featuring electroplated Mg conductors and passivation schemes, such as thin film barrier layers and electroplated coatings.

Next, the substrate was coated with a 500-nm-thick layer of silicon dioxide (SiO_2) by plasma-enhanced chemical vapor deposition (PECVD) at 175°C. The SiO_2 served as the electroplating mold for Mg deposition. In the previous chapter, this was achieved using PVA-based water-soluble molds that were patterned by negative molding with photoresist. The fabrication process supported the electrodeposition of Mg in the tens-of-microns thickness. While this thickness range might be useful for

certain applications (e.g., batteries, capacitive pressure sensors, antennas), thicknesses in the 1-10 μm range were more desirable for piezoresistive strain sensors in order to achieve gauge resistances in the tens or hundreds of Ohms. Although even thinner films (i.e., submicron thickness) can be achieve by physical vapor deposition techniques, the corresponding device lifetime due to degradation rendered these approaches less suitable. Hence, the targeted film thickness was 1-10 μm and a new type of Mg electroplating mold had to be considered. The oxide layer was patterned by reactive ion etching through a lithographically-defined etch mask (Shipley 1813 photoresist). The process proceeded at 150 W and 50 mTorr with 100 sccm of carbon trifluoride (CHF_3) and 4 sccm of oxygen (O_2) gas, corresponding to an etch rate of approximately 40 nm/min. The photoresist was then removed in a barrel asher with 100 sccm of oxygen at 300 W. The substrate was mounted onto a rigid substrate using SU-8 2005 as an adhesive on the edges of the polyimide film. Finally, the top Ti layer was removed by reactive ion etching in sulfur hexafluoride gas (50 sccm SF_6, 10 sccm O_2, 150 W and 50 mTorr) to avoid chemical processing in aqueous etchants before the sample was loaded into a moisture- and oxygen-free glovebox for Mg electrodeposition.

Magnesium electrodeposition was performed in a non-aqueous electrolyte in accordance with the deposition procedure discussed in the previous chapter. The electrolyte comprised a 6:1 molar ratio of methylmagnesium chloride and aluminum chloride in tetrahydrofuran. After the electrodeposition process, the sample was manually removed from the glass substrate, rinsed in THF to remove residual electrolyte on the sample surface and dried under inert nitrogen gas in the glove box overnight. Upon retrieval from the glove box, processing depends on the type of passivation scheme implemented.

For a bare Mg sensor (i.e., without passivation schemes), the oxide mask and underlying titanium was removed by reactive ion etching and the sample was returned to the glovebox for the solution casting of PLA (150 mg/mL in DCM; Purac PDL-05). This formulation of PLA was selected as the encapsulating polymer due to its balance of mechanical and degradation properties, as shown in Table 24. Since the targeted functional lifetime of the electroplated Mg strain sensor was less than 7 weeks, PL-38 and PLC-70 were less suitable because a better balance of functional and degradation lifetime (i.e., closer to unity) was

desired. However, lower molecular weight formulations of poly(DL-lactide) were too brittle after solution casting to the desired thickness. Even though PLC-70, a co-blend of PLLA and PCL, exhibits similar degradation time to PDL-05, the presence of PCL resulted in a much lower tensile modulus and plastic behavior. The solution-cast sample was dried under the ambient conditions of the glovebox overnight and degassed in a vacuum chamber for at least 12 hours. The encapsulated sample was then gradually heated to 145°C on a hot plate with an aluminum cover hovering 1 cm above the sample surface to maintain temperature at the polymer-air interface. The reflow, which planarized the polymer, removed residual solvent and eliminated any entrapped gas bubbles in the encapsulation, proceeded for 3 hours before the temperature was gradually ramped to room temperature.

Table 24 Material properties of various formulations of PLA and PLGA. Note that PDL, PL and PLC refer to poly(DL-lactide), poly(L-lactide), and L-lactide and ε-lactone co-polymers, respectively. In turn, IV, MW, t_{degrad}, T_g, T_m and E_T correspond to inherent viscosity, molecular weight, degradation time for complete mass loss, glass transition temperature, melting temperature and tensile modulus of elasticity, respectively.

	PDL-02	**PDL-04**	**PDL-05**	**PL-38**	**PLC-70**
IV (dL/g)	0.2	0.4	0.5	3.8	1.5
MW (kg/mol)	17	45	61		
t_{degrad} (mo.)	9-12	10-14	12-16	>24	12-24
T_g (°C)	50-55			60-65	15-25
T_m (°C)	Amorphous			185-195	110-120
E_T (GPa)	3.1-3.7			3.1-3.7	0.02-0.04

Individual sensors were singulated by laser ablation with a CO_2 laser and released from the substrate by peeling the polyimide backing from the sensor. The remaining Ti/Cu seed layer remained on the removed polyimide substrate due to selective adhesion. It is speculated that the copper surface is slightly oxidized during the fabrication process, hence weakening its adhesion to the electroplated Mg. This was suggested because the adhesion between electroplated Mg on pristine Cu (i.e., immediately after electrodeposition and without any subsequent processing) is robust and the Mg does not readily delaminate. The thickness of the PLA-encapsulated Mg structure is 100 microns. The sensor construct was then

embossed to a solution cast sheet of PLA (50 mg/mL PDL-05 in DCM) that was 40 microns in thickness. In order to achieve complete bonding and good adhesion between the bottom surface of the Mg structure and the bottom PLA film, a sequential embossing process with solvent bonding was employed. First, the PLA-encapsulated Mg structure and bottom PLA film were separately laminated at 80°C and 145 psi for 5 minutes. Next, the two halves were laminated together at 80°C and 145 psi for 5 minutes. A thin film of DCM was applied to the glass carrier substrate, onto which the now laminated Mg-PLA sensor was placed for embossing at 120°C and 290 psi for 5 minutes. The solvent on the glass substrate permeates the Mg-PLA construct so that both solvent bonding and lamination occur during the embossing process. This process was performed trice because improved bonding and Mg-PLA adhesion was observed with longer lamination times. The encapsulation above the contact pads was removed by laser ablation with an excimer laser under low fluence using multiple passes at 5.0-6.5 mJ and 85-95% attenuation.

In addition to electroplated Mg sensors encapsulated with PLA, sensors featuring passivation schemes were fabricated. For sensors coated with a thin barrier film, atomic layer deposition was performed after plasma removal of the oxide mask and remaining Ti layer (after Mg electrodeposition). Higher sensor yield was observed when the ALD was performed at 80°C than at 150°C, likely due to the CTE mismatch among the various materials present on the substrate. The remainder of the fabrication process was identical to that of bare Mg-PLA sensors (i.e., solvent casting of PLA, polymer reflow, substrate release, sensor bonding and laser ablation of contact pads). For sensors featuring PP-Zn passivation, the Zn electrodeposition was performed immediately after Mg electrodeposition. The Zn plating was conducted under the same parameters as described in the previous chapter. Due to the alkaline nature of the plating bath, Mg dissolution was not observed in spite of the thickness (<10 microns) of the Mg structures. Samples were rinsed in DI water and dried with nitrogen before proceeding with removal of the oxide mask and Ti seed layer. The remainder of the fabrication process, once again, followed that of bare Mg-PLA sensors.

Electromechanical performance was evaluated with a uniaxial mechanical testing system (Electroforce 3200, TA Instruments). Sensors were mounted onto acrylic rectangular blocks, which

served as test specimens during mechanical loading, using room temperature- curable epoxy. Commercial terminal pads were similarly mounted onto the test specimen below the sensor. Magnet wire (40 AWG) and room temperature-curable silver epoxy was used to electrically connect the contacts pads of the electroplated Mg strain sensors to the local terminal pads on the test specimen. Thicker 32 AWG magnet wire was soldered on one end to the terminal pads and connected to the experimental setup on the other. The two-stage wire connection provided strain relief to the mounted sensor and reduced line resistance through the use of lower gauge wiring. The circuitry of the experimental setup comprised a four-point configuration, where a DC current was applied across the sensing element with a commercial source measurement unit (Keithley 236). The output voltage was amplified in two stages: a non-inverting differential amplifier with a gain of unity to subtract 90% of the nominal voltage (i.e., voltage output in the unloaded, unstrained configuration) and a non-inverting amplifier with a gain of 33. The final voltage output of the two-stage amplification was measured and recorded with the Electroforce 3200 simultaneously with the time, strain and force data of the mechanical testing using a custom cable and modification to the Electroforce software.

The mechanical component of the electromechanical test was performed under direct loading (i.e., two-point loading). Cyclic compression was applied to the test specimen (pre-loaded to -10 N) at a frequency range of 50 mHz to 10 Hz and a strain amplitude range of -180 με to -3200 με. The upper limit in applied strain was established from the limits of the tool, which could not deliver compressive loads greater than -220 N; given the stiffness of the test specimen, the maximum strain of -3200 με corresponded to -190 N to -200 N (including the pre-load) and, hence, reached the 90% tolerance of the tool. Sampling frequency of all data was 100 Hz and exported data was analyzed in MATLAB for post-processing (i.e., digital FIR filtering) and analysis.

Since line and contact resistances are excluded in four-point electrical measurements, the theoretical sensitivity of quarter-bridge strain gauge under this configuration is shown below. Briefly, the normalized change in resistance ($\Delta R/R$) is proportional to the normalized output voltage ($\Delta V/V$) for a

constant excitation current (I_{ex}). For Mg-based piezoresistive strain gauges, the change in resistance under applied strain stems only from a change in the gauge geometry. Taken together, the theoretical sensitivity of electroplated Mg strain gauges is 1.67 μV/με/V_{ex}, where V_{ex} is the product of nominal gauge resistance and excitation current.

$$R + \Delta R = \frac{\rho l(1+\varepsilon)}{w\Gamma(1-\upsilon\varepsilon)^2} \tag{3.61}$$

$$\frac{\Delta R}{R} = \frac{\varepsilon(1+2\upsilon)}{(1-\upsilon\varepsilon)^2} \cong \frac{\varepsilon(1+2\upsilon)}{1-2\upsilon\varepsilon} \tag{3.62}$$

$$\frac{\Delta E}{E} = \frac{\Delta R}{R} \; where \; E = I_{ex}R \tag{3.63}$$

where R, ρ, e, n, w, Γ, l, E and I_{ex} correspond to the gauge resistance, electrical resistivity, strain, Poisson's ratio, feature width, thickness and effective length of the quarter-bridge strain gauge, voltage and excitation current, respectively.

3.2.3. Electroplated Magnesium Strain Sensors

Biodegradable strain sensors comprising electroplated Mg encapsulated in PLA were fabricated. Whole, half and quarter Wheatstone bridge configurations and of varying dimensions were examined to identify the optimal design for electroplated Mg-based biodegradable strain sensors. Figure 102 shows SEM and optical images of half bridge designs featuring serpentine resistors that are 7-9 μm in feature width and more than 100 turns. The Mg was electroplated through a lithographically-defined silicon dioxide mold (500 nm thickness) 3-μm-wide and 6-μm-wide so that the resulting Mg structure exhibits a hemispherical cross section due to lateral film growth. While the thinner electroplated mold was implemented to achieve thinner films and finer feature widths, it was speculated that the rounded cross-sectional structure is more beneficial in biodegradable applications because sharp edges might accelerate corrosion. Similar to chemical etching, this phenomenon can occur due to the exposure of multiple crystal planes at sharp edges and corners. The SEM images show that electrically-continuous structures can be

electroplated even with intricate serpentine designs on a flexible Kapton film. Continuity was achieved for a wide range of device dimensions (i.e., feature size and device footprint), as shown in the comparison of densely packed designs (Figure 102a-d) and sparse and longer lateral form factor design (Figure 102e).

However, electrical and structural continuity were difficult to maintain for all investigated designs during substrate release and pattern transfer to the encapsulating PLA film. This process was performed by solution casting PLA onto the sample and peeling the Kapton film away after the PLA film thorough dried (i.e., after solvent removal, degassing and thermal reflow). It was observed that the direction of peeling and, hence, the shear force imposed on the Mg structures impacted the quality of pattern transfer. Serpentine patterns aligned parallel to the direction of peeling exhibited better pattern transfer than elements oriented orthogonally. The results of the latter are shown in Figure 102f-g, where broken and missing traces populated the transferred PLA structure. This boded poorly for whole and half bridge Wheatstone bridge configurations, since strain-sensitive and strain-insensitive elements are oriented orthogonal to each other. Hence, one set of structures must be aligned perpendicular to the direction of peeling. These findings indicated that even though whole and half bridge strain gauges featuring micron-scale Mg features can successfully be electroplated, fabrication limits with substrate release and pattern transferred precluded their use in electroplated Mg strain sensors.

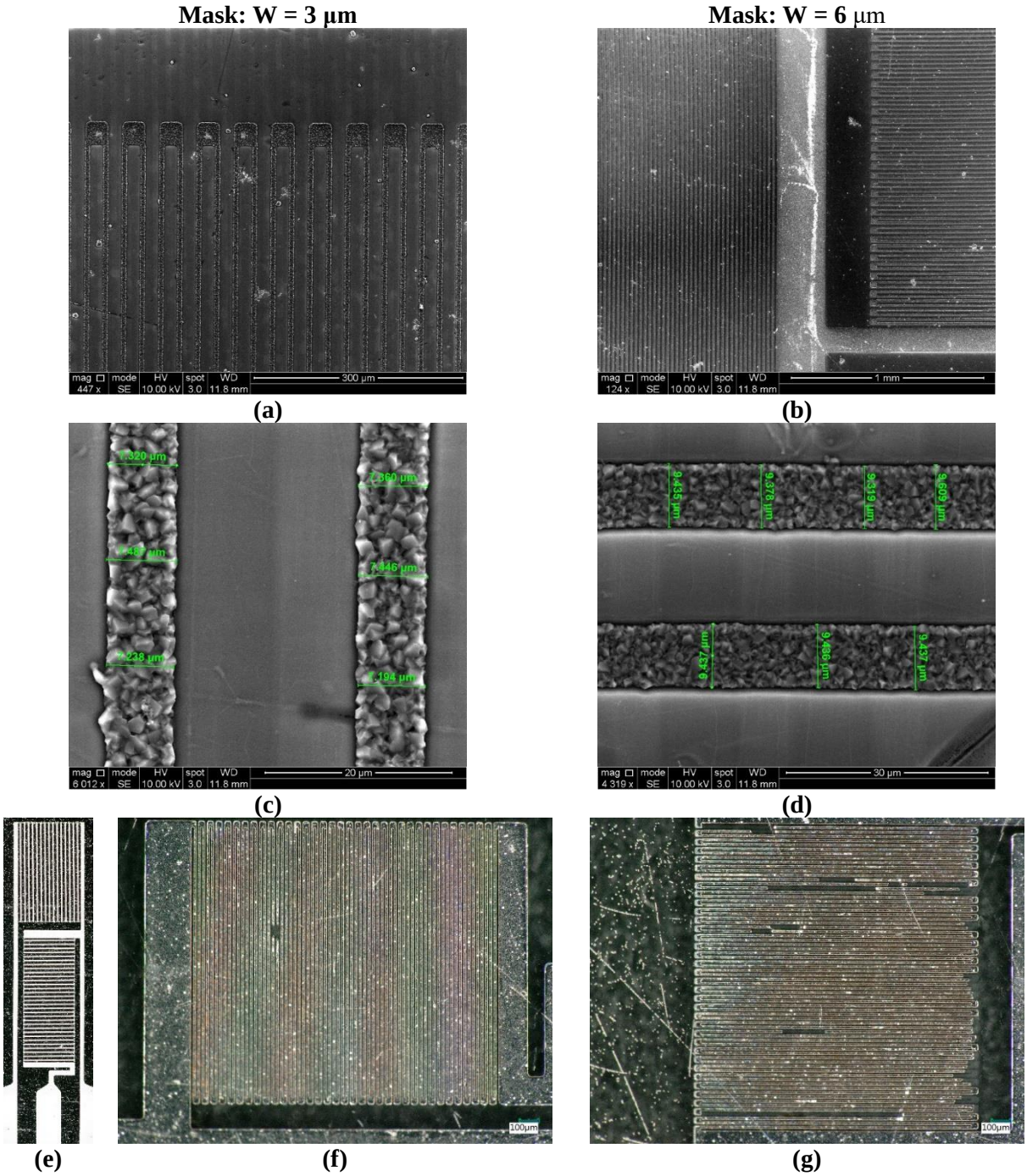

Figure 102 ***(a-d)*** *Scanning electron micrographs and* ***(e-g)*** *optical images of piezoresistive strain sensors (half bridge configuration) comprising electroplated Mg. Lateral plating enabled by the submicron-thick oxide mold corresponded to features wider than the mask design. Magnesium structures patterned through a mask with* ***(a, c)*** *3 µm and* ***(b, d, e)*** *6 µm, respectively, were imaged on the Kapton substrate, whereas* ***(f-g)*** *the optical images were taken of the Mg-PLA structure after substrate release and pattern transfer.*

Functional strain gauges comprising electroplated Mg in a quarter bridge configuration were fabricated and characterized. The transition to quarter bridge designs was guided by the fabrication limits previously observed. Gauges of varying feature widths and device footprints were explored optimize the balance between robust design and lower noise (i.e., higher resistance) sensors. Figure 103 shows optical images of Mg-PLA sensors in quarter bridge configurations. Based on feature width (15-40 μm) and serpentine length of the design, resistors ranging from 50 Ω to 300 Ω were successfully demonstrated. The thickness of the Mg structures was 6±1 μm and the corresponding surface roughness was approximately 1-2 μm. For reference, the sensor shown in Figure 103 exhibited a nominal resistance (i.e., under zero applied strain) of 50 Ω.

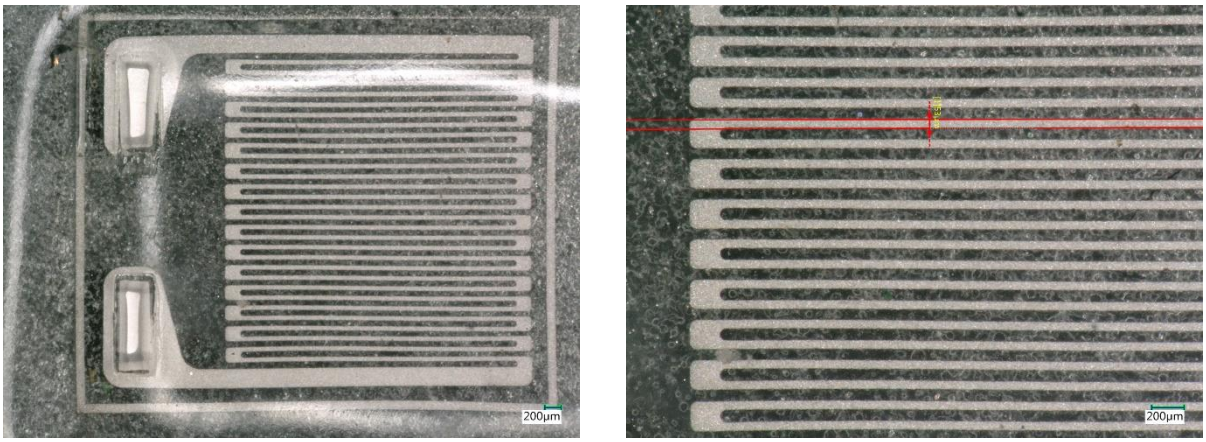

(a) **(b)**

Figure 103 Optical images of electroplated Mg strain sensor encapsulated in PLA.

Due to the disparity between the micron-scale roughness of the top surface and mirror finish of the bottom surface, it was hypothesized that sensors with the bottom surface mounted onto a substrate for mechanical testing would exhibit higher sensitivity because the bottom surface would be parallel to the substrate surface and the mirror finish would support more uniform strain transfer. Electroplated Mg strain sensors mounted in the top-down and bottom-down configuration were tested in order to evaluate this hypothesis. Figure 104 shows the electromechanical response of the Mg-PLA sensors to cyclic compressive strain ranging from 180 με to 3800 με in amplitude and loading frequencies from 100 mHz to 10 Hz. For

sensors loaded in the top-down configuration, strain sensitivity was maintained at loading frequencies as low as 250 mHz. The average strain sensitivity for tested frequencies greater than or equal to 250 mHz was 0.058 $\mu V/\mu\varepsilon/V_{ex}$, whereas the sensitivity decreased by more than 50% to 0.024 $\mu V/\mu\varepsilon/V_{ex}$ at a loading frequency of 100 mHz. Further, the correlation coefficient was greater than 0.99 for frequencies greater than 250 mHz and 0.93 at 100 mHz. The sensitivity loss at lower frequencies near DC was initially attributed to drift because quarter-bridge configurations do not compensate for thermal and environmental effects. However, bottom-down sensors retained strain sensitivity even at 100 mHz, indicating that poor strain transfer due to the micron-scale surface roughness also contributed to the sensitivity loss of top-down sensors. In the bottom-down configuration, the average strain sensitivity at 100 mHz to 10 Hz was 0.051 $\mu V/\mu\varepsilon/V_{ex}$. It should be noted that the data shown henceforth corresponds to sensors mounted in the bottom-down configuration, where the mirror finish faces the substrate surface. The observed strain sensitivity was approximately 25% that of non-degradable strain sensors encapsulated and evaluated under direct loading and far below the theoretical gauge factor of a Mg-based strain sensor. The attenuation in strain sensitivity is attributed to the differences in materials and geometry between the non-degradable and degradable strain sensors (e.g., PLA vs Kapton, micron-thick and surface rough Mg vs. thin film and mirror-finish titanium). However, the sensitivity and performance of the electroplated Mg strain gauges successfully monitored strain at the relevant strain and frequency ranges, as well as resolution, anticipated *in vivo* during bone healing.

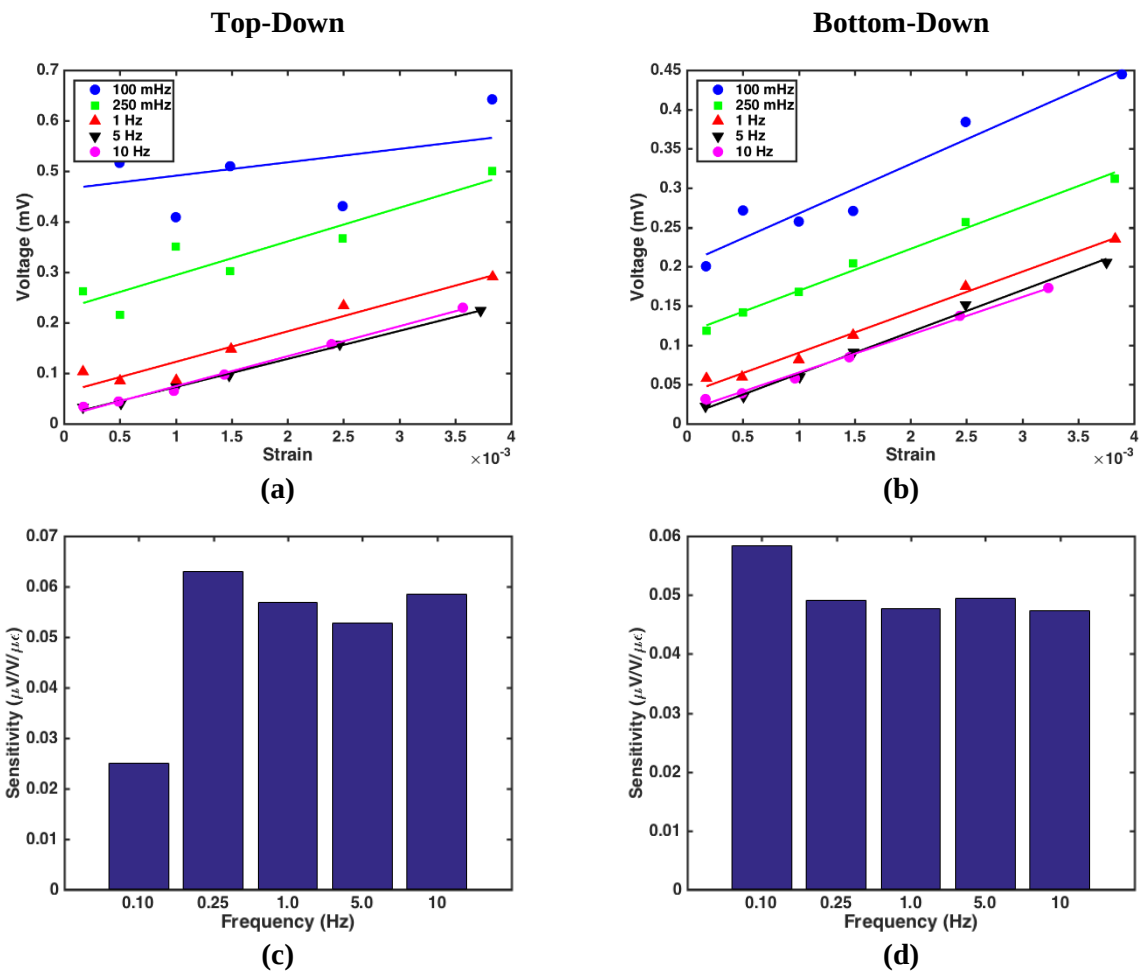

*Figure 104 Effect of electroplated Mg surface roughness on sensor performance. Voltage response of electroplated Mg strain sensors mounted with the **(a)** micron-rough electroplated surface and **(b)** mirror-finish Mg surface mounted on the testing substrate. Sensors were evaluated from 100 mHz to 10 Hz to encompass the physiological range of ambulation. Each data point is the result of cyclic testing (20-100 cycles) performed in triplicate. **(c-d)** Corresponding device sensitivities, determined by linear regression of electromechanical characterization.*

Figure 105 shows the device performance of an electroplated Mg strain sensor throughout the time course of degradation. This physiological conditioning was achieved by immersing the sensor in simulated body fluid maintained at 37°C. The nominal resistance of the sensor prior to degradation (i.e., at 0 h) was 50 Ω. Within 2 hours of physiological conditioning, the nominal resistance of the sensor increased to 52 Ω and remained consistent until the device neared its functional lifetime. The immediate increase and thereafter steady resistance value suggested electrolyte permeation into the PLA encapsulation and oxidation of the Mg surface. Although the $Mg(OH)_2$ formed in aqueous environments provides corrosion protection, its solubility typically renders it as an insufficient barrier layer. The PLA encapsulation,

however, may have hindered the dissolution of the surface magnesium hydroxide, providing temporary protection against further degradation. The sensor exhibited a functional lifetime of 90 hours. During this time, the average strain sensitivity was 0.049 $\mu V/\mu\varepsilon/V_{ex}$ for compressive strains of 180-3800 $\mu\varepsilon$. The average R^2 value from the strain sensitivity linear regression was 0.95, indicating that the functional lifetime not only corresponded to the duration in which electrical continuity in the sensor was observed (i.e., nominal resistance was not open circuit), but also corresponded to the retention of strain sensitivity. In other words, an electroplated Mg-based biodegradable strain sensor retained steady device performance up until the loss of functionality, rather than a gradual decline in sensitivity and performance. The average sensitivity throughout the functional lifetime fluctuated within +10% and -25% of the average value. The bias towards lower sensitivity is attributed to drift and noise, which obscures the strain-induced signal.

As expected, the non-degradable Au-polyimide strain sensor (discussed in the previous section) outperformed the biodegradable Mg-PLA sensor. The average sensitivity of the biodegradable Mg-PLA and non-degradable Au-PI strain sensors were 0.05 $\mu V/\mu\varepsilon/V_{ex}$ and 0.15 $\mu V/\mu\varepsilon/V_{ex}$, respectively. The lower strain sensitivity of the biodegradable strain sensors was attributed to increased noise (i.e., no cancellation of thermal or environmental noise from differential configurations), surface roughness of the electroplated Mg and poorer strain transfer from the test specimen to the sensor due to the thicker and stiffer design. Further, it is important to note that the non-degradable sensor was evaluated under 3-point bending, which supported cleaner mechanical testing (i.e., improved strain transfer, lower noise and the ability to examine lower strain amplitudes). Electroplated Mg-based strain sensors were tested under direct loading because the 3-point test fixture could not accommodate the larger test specimen used for the biodegradable sensors. Although both sensor types exhibited sensitivities below their corresponding theoretical values, this was expected due to the strong dependence of strain gauge performance on the test setup (e.g., interface and bond quality of the test specimen and sensor, strain transfer from the mechanical test platform to the sensor).

In turn, the functional lifetime was 4 days and 7 weeks, respectively. The data supported the experimental goal, wherein the functional lifetime of a biodegradable strain sensor would be no more than

1 order of magnitude shorter than that of a non-degradable analogue. The observed functional lifetime of the degradable and non-degradable sensors are 4 days and 49 days, respectively, and supported the goal. Although the strain sensitivity was of the degradable device was approximately 60% lower than that of the non-degradable sensor, the biodegradable device successfully detected physiological strain ranges and at relevant loading frequencies. The *in vitro* results supported the use of electroplated Mg devices as biodegradable strain sensors for monitoring bone healing.

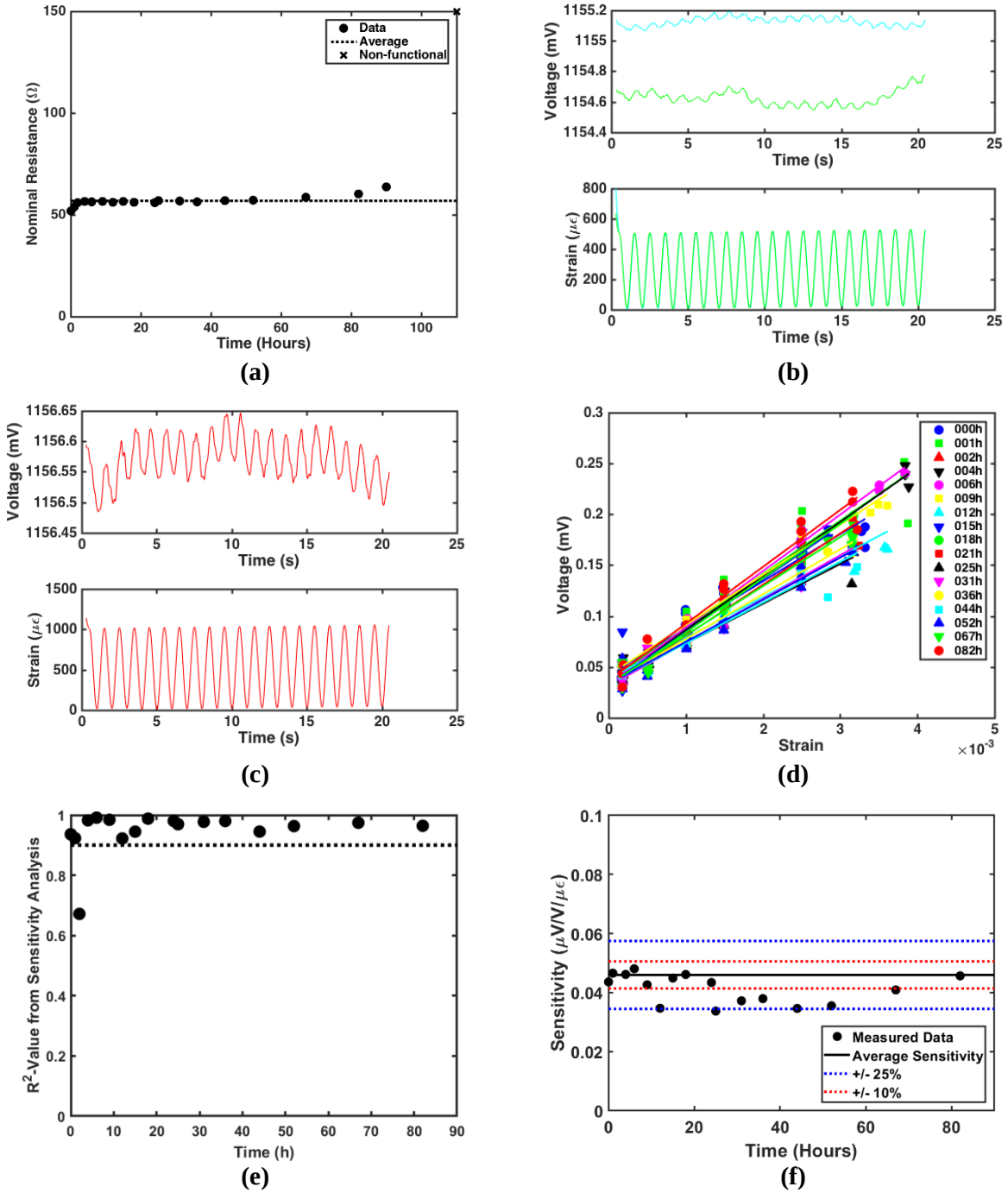

Figure 105 Electromechanical performance of electroplated Mg strain sensors (42 µm features) under degradation. ***(a)*** *Nominal resistance of an electroplated Mg strain sensor with 42-µm-wide features and encapsulated in PLA throughout the time course of physiological conditioning.* ***(b-c)*** *Temporal data of sensor voltage response to applied cyclic strain at amplitudes of 400 µε and 1000 µε, respectively.* ***(d)*** *Strain sensor performance under physiological degradation, evaluated across an applied compressive strain range of 180 µε to 3800 µε.* ***(e)*** *The correlation coefficient of device performance and* ***(f)*** *strain sensitivity of electroplated Mg sensor under physiological degradation.*

It was hypothesized that quarter-bridge sensors with higher nominal resistance would exhibit better strain sensor performance. To evaluate this, the electromechanical performance of an electroplated Mg strain sensor featuring a nominal resistance of 275 Ω was evaluated. The results, summarized in Figure 106, indicated a trade-off between performance and functional lifetime. The device exhibited a functional lifetime of 800 min or 13.3 h and an average strain sensitivity of 0.041 $\mu V/\mu\varepsilon/V_{ex}$. The shorter functional lifetime was attributed to the narrower features, since the resistor is more susceptibility losing electrical continuity due to localized pitting with narrower traces. Although neither metrics (i.e., lifetime or sensitivity) exceeded that of the 50 Ω device shown earlier, the strain sensitivity analysis exhibited an average R^2 value of 0.98 and fluctuations in strain sensitivity throughout the device functional lifetime ranged $\pm$10% of mean. These results reflect a tighter spread and more consistent device performance, confirming that higher device resistance overcomes noise and drift. For example, the noise contribution of electrical connections and contacts become less significant for higher device resistances. Further, the 275 Ω device exhibited a lower limit in strain detection than the 50 Ω sensor. The higher resistance device exhibited a lower limit of 180 με, as shown in Figure 106b, whereas the lowest strain amplitude robustly detected in the 50 Ω sensor was 400 με.

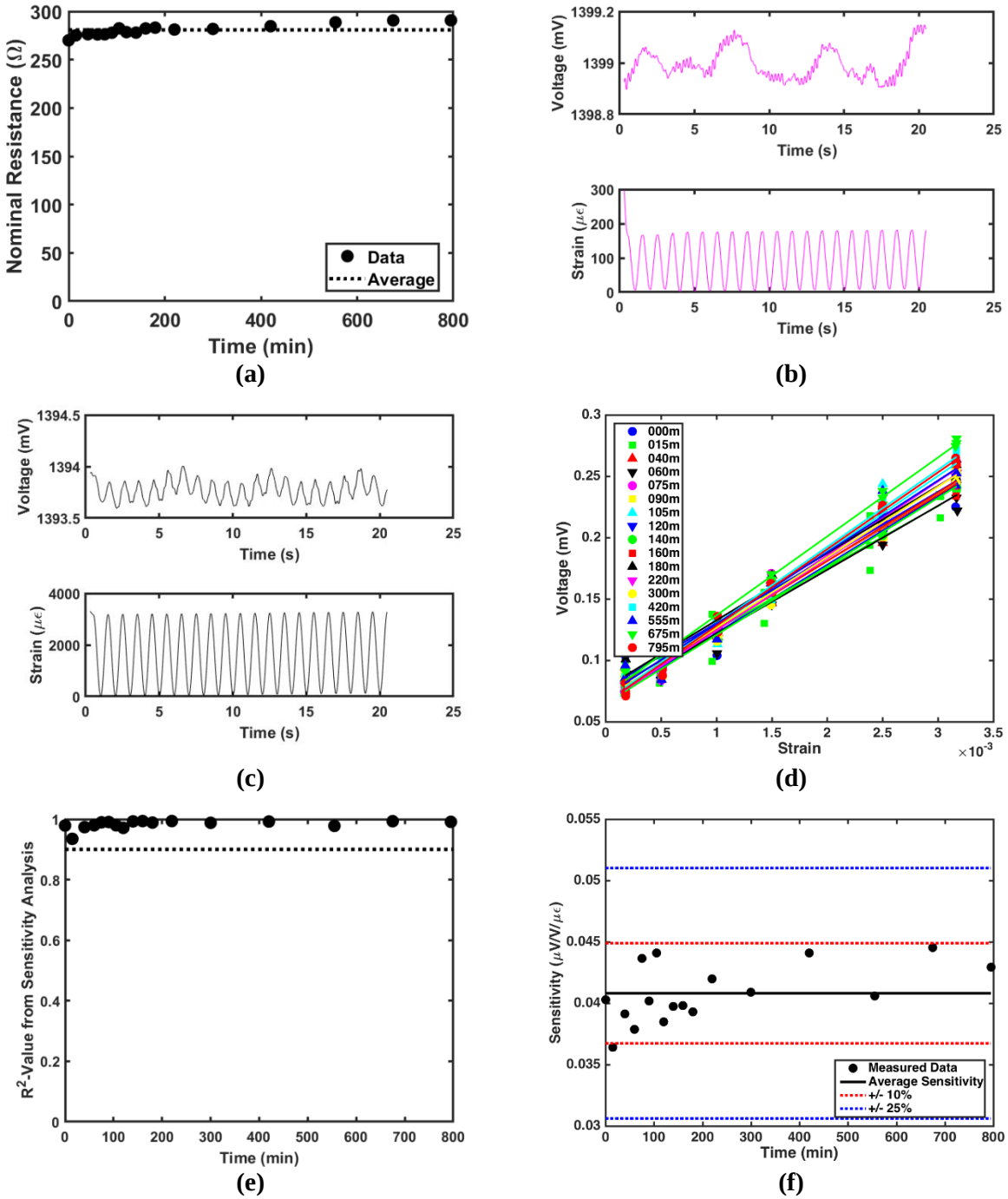

Figure 106 Electromechanical performance of electroplated Mg strain sensors (30 µm features) under degradation. ***(a)*** *Nominal resistance of an electroplated Mg strain sensor with 30-µm-wide features and encapsulated in PLA throughout the time course of physiological conditioning.* ***(b-c)*** *Temporal data of sensor voltage response to applied cyclic strain at amplitudes of 180 με and 3200 με.* ***(d)*** *Strain sensor performance,* ***(e)*** *The correlation coefficient of sensor performance and* ***(f)*** *strain sensitivity of device under physiological degradation, evaluated across an applied compressive strain range of 180 με to 3200 με.* ***(e)*** *Strain sensitivity of electroplated Mg sensor under physiological degradation.*

The effect of feature width on functional lifetime is summarized in Table 25and shown through optical images in Figure 107. As observed with the 275 Ω Mg strain gauge, narrower feature widths (and, hence, higher resistance) sensors exhibited shorter functional lifetimes. For a Mg film thickness of 6 μm, the observed functional lifetime of devices featuring 15 μm, 30 μm and 42 μm feature widths were 1-2 h, 12-24 h and 90-110 h, respectively. The optical images and data show a non-linear improvement in functional lifetime with increasing feature widths. Since the thickness of the Mg structures was less than the feature widths, it might have been expected that the functional lifetime of the electroplated Mg sensors would not depend on feature width; since the finest dimension (i.e., thickness) was constant among the designs, degradation might proceed uniformly in the thickness dimension. However, the electrochemical noise measurements shown in the previous chapter confirmed that Mg primarily degrades by pitting corrosion. A pitting index greater than 0.1 indicated that corrosion proceeded by pitting more than by uniform corrosion; magnesium exhibited a pitting index of 0.9-1. While the Weibull analysis of ECN data confirmed that two mechanisms of corrosion (i.e., pitting and uniform corrosion) nonetheless occur in Mg, the effect of uniform corrosion would be more pronounced in sub-micron-thick Mg structures, where uniform degradation can quickly corrode the entire thickness of the structure. For electroplated Mg sensors, however, this effect is mitigated. Since pitting corrosion determines functional lifetime in micron-thick electroplated Mg sensors, this suggests that, on the one hand, functional lifetime can be tuned by sensor design, but there still exists a degree of stochasticity to the sensor corrosion, establishing a distribution in functional lifetimes rather than a definitive target.

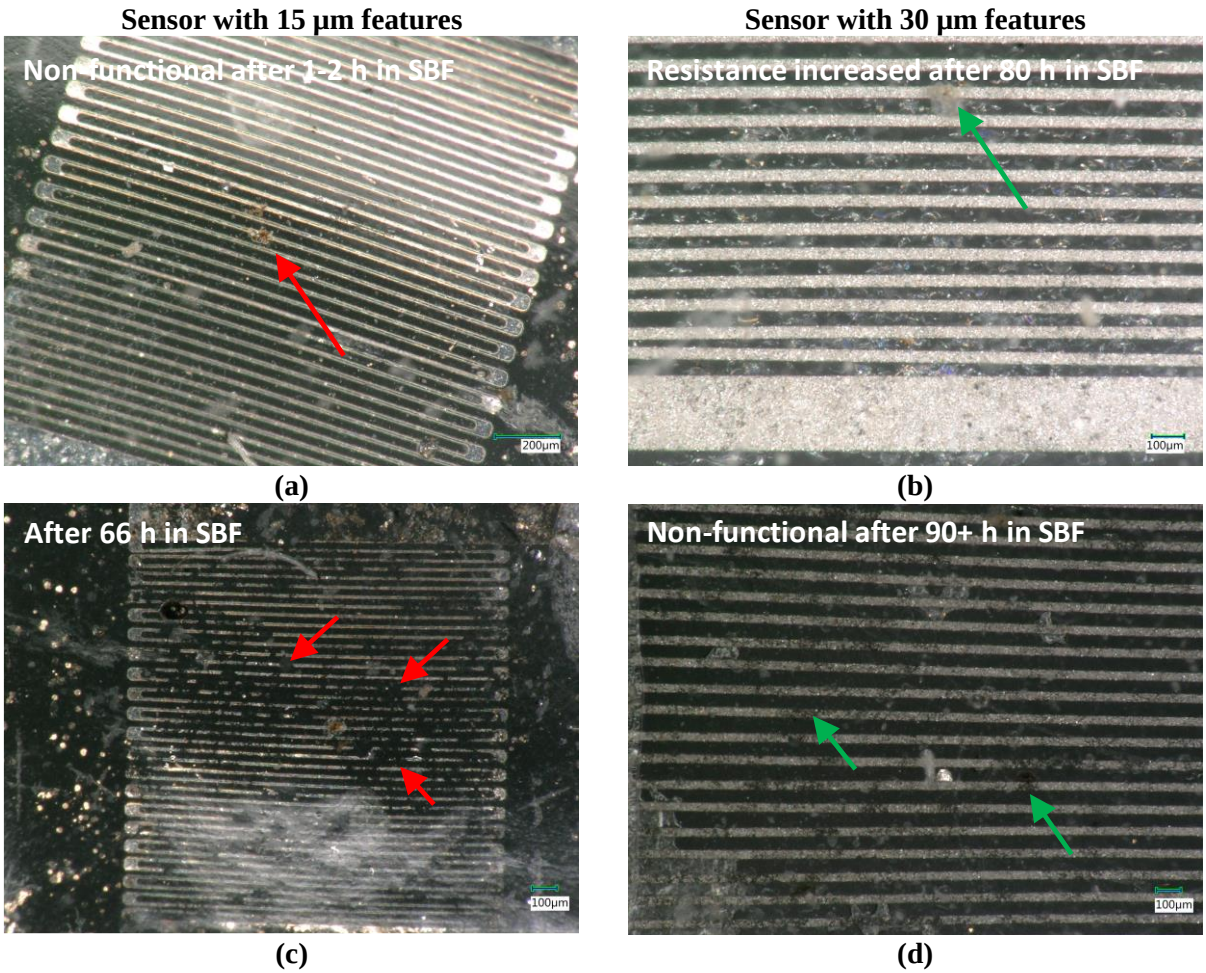

*Figure 107 Optical images of electroplated Mg sensors after loss of functionality for devices with **(a, c)** 15 µm and **(b, d)** 30 µm features.*

Table 25 Functional lifetime of electroplated Mg strain sensors encapsulated in PLA with respect of feature size.

Feature Size (µm)	Functional Lifetime (h)
15	1-2
30	12-24
42	90-110

3.2.4. Biodegradable Strain Sensors with Barrier Thin Film Passivation

Electroplated Mg strain sensors featuring barrier thin film passivation were fabricated with atomic layer deposition. The sensors were passivated with an ALD-deposited film of alumina, which served as a surrogate for magnesium fluoride. As shown in the previous chapter, protection against water ingress and subsequent corrosion depends more on the type of deposition process than on the material type for materials that do not readily solubilize in the testing environment. Alumina (40-nm-thickness) was implemented to understand how barrier passivation can improve the performance or lifetime of electroplated Mg-based biodegradable sensors. Figure 108 shows the results for an ALD-passivated Mg sensor with a nominal resistance of 127 Ω prior to physiological conditioning. The device exhibited a strain sensitivity of 0.071 $\mu V/\mu\varepsilon/V_{ex}$, which was 22% higher than that of bare Mg-PLA strain sensors. Robust strain detection was maintained for strain amplitudes ranging from 180 με to 3200 με. Higher and lower strain amplitudes were not explored due to limitations of the mechanical testing system paired with the testing substrate. Figure 108b-c shows that, in spite of the lower frequency noise, the strain-induced sensor output maintains constant amplitude throughout each test. However, the device exhibited a functional lifetime of less than 1 h. Optical imaging revealed accelerated corrosion at the contact pads, where wire connections were made. It is speculated that the low pinhole density barrier film successfully protects the Mg sensor from exposure to SBF and, consequently, the only region where Mg was exposed was at the contact pads. The wired contact also served as a galvanic couple that accelerated localized corrosion at the contact pad and, in this manner, prematurely terminated the functionality of the ALD-passivated Mg sensor. Although the contacts were passivated with medical-grade urethane encapsulation, 75% of the fabricated ALD-passivated Mg sensors demonstrated a short functional lifetime. These results underscored the importance of future work in developing biodegradable packaging and interconnects, as a trajectory towards a fully biodegradable, implantable system.

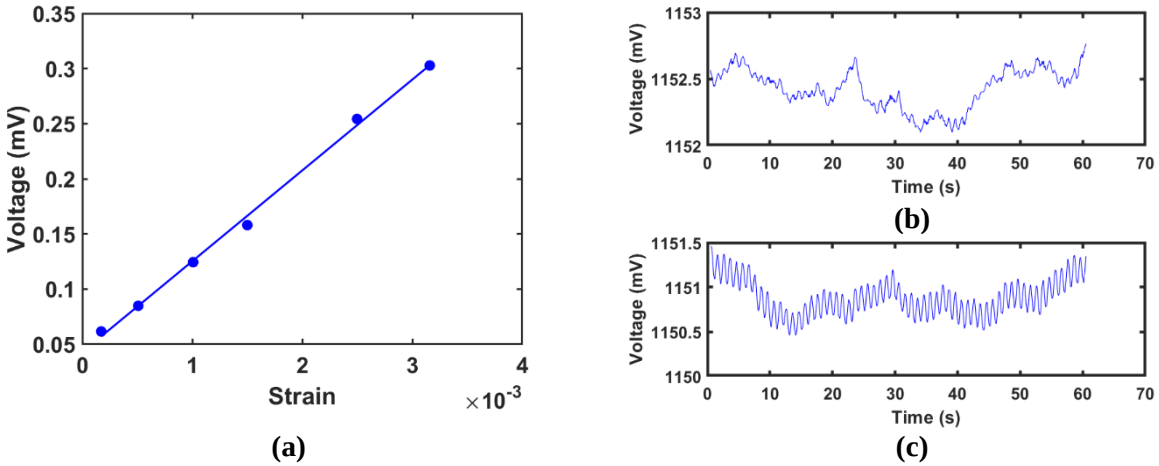

Figure 108 Device performance of electroplated Mg strain sensors passivated with atomic layer deposited alumina, which serves as a surrogate for magnesium fluoride. The ALD-deposited film represents a barrier thin film approach to passivated electroplated Mg. ***(a)*** *Strain sensor performance of an ALD-coated device featuring a nominal resistance of 127 Ω and tested with an excitation current of 9 mA.* ***(b-c)*** *Temporal response of device to cyclic compressive strain at amplitudes of 500 με and 3200 με, respectively.*

Figure 109 shows the performance of a 44 Ω ALD-passivated Mg sensor that did not prematurely lose functionality. Performance evaluated from 50 mHz to 10Hz revealed that the ALD passivation did not improve the lower frequency limit in strain detection, as strains applied at frequencies lower than 250 mHz could not be detected and attenuated sensitivity was observed even at 250 mHz. This is, in part, due to limitations of the mechanical test setup (i.e., direct loading on the Bose test system), as attenuated sensitivity at low frequency was also observed with the non-degradable strain sensor evaluated under direct loading (as opposed to under 3-point bending). However, the attenuated frequency may also be attributed to the single gauge configuration, which offers no cancellation of thermal or environmental effects. Hence, drift attributed to device heating, evaporation of SBF within the bulk PLA and general environmental fluctuations will limit the sensor's ability to detect at lower frequencies. Further testing with modified waveforms (e.g., step functions in applied strain) would provide greater clarity in identifying the principle reason underlying the sensitivity attenuation. Overall, the average sensitivity from 1 Hz to 10 Hz was 0.035 $\mu V/\mu\varepsilon/V_{ex}$, which is half of what was observed with ALD sensors that prematurely lost functionality.

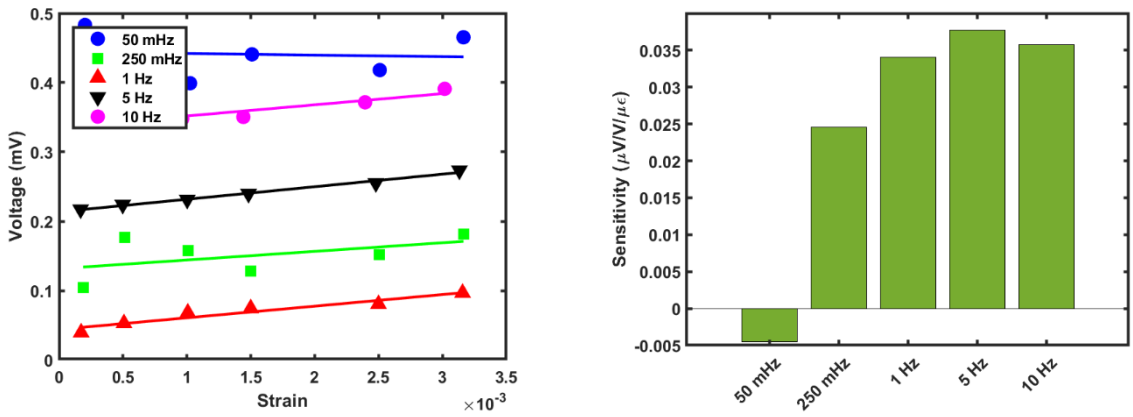

(a) **(b)**

Figure 109 Device performance of electroplated Mg strain sensors passivated featuring an ALD coating of 40 nm thickness. The device geometry corresponded to a nominal resistance of 44 Ω and was tested at an excitation current of 20 mA. ***(a)*** *Strain sensor performance and* ***(b)*** *strain sensitivity of sensor under ambient conditions, evaluated from 50 mHz to 10 Hz to capture the frequency range of ambulation.*

The performance of ALD-passivated electroplated Mg strain sensors was examined as physiological degradation progressed. The results, shown in Figure 110, significantly differed from the performance of bare Mg-PLA sensors. The increase in nominal resistance of the sensor occurred over the course of 8 hours, as opposed to the 2 hours observed with bare Mg-PLA sensors. The slower increase in nominal resistance suggested that electrolyte ingress and subsequent surface corrosion was hindered by the ALD barrier film. The slower stabilization time is unfavorable in the given strain sensing application, where acute measurements are desired. Further, the average strain sensitivity across a functional lifetime of 18 hours was 0.018 $\mu V/\mu\varepsilon/V_{ex}$ and the average correlation coefficient was 0.81. Although the fluctuations in strain sensitivity resembled that of bare Mg-PLA sensors (i.e., +10% to -25%), device sensitivity was more than 69% lower than that of bare Mg-PLA sensors and the lower R^2 value suggests that sensing accuracy based on initial calibration would be low. Optical images monitoring device degradation after loss of functionality (Figure 111) revealed pits that corroded through the thickness of the Mg structure by day 3 in SBF and corrosion progressing along the width of the Mg features by day 6. The results overall indicated

that even though barrier passivation successfully hinders electrolyte ingress, the localized corrosion at pinholes renders the device less stable and predictable; ALD passivation did not improve electroplated Mg strain sensor performance.

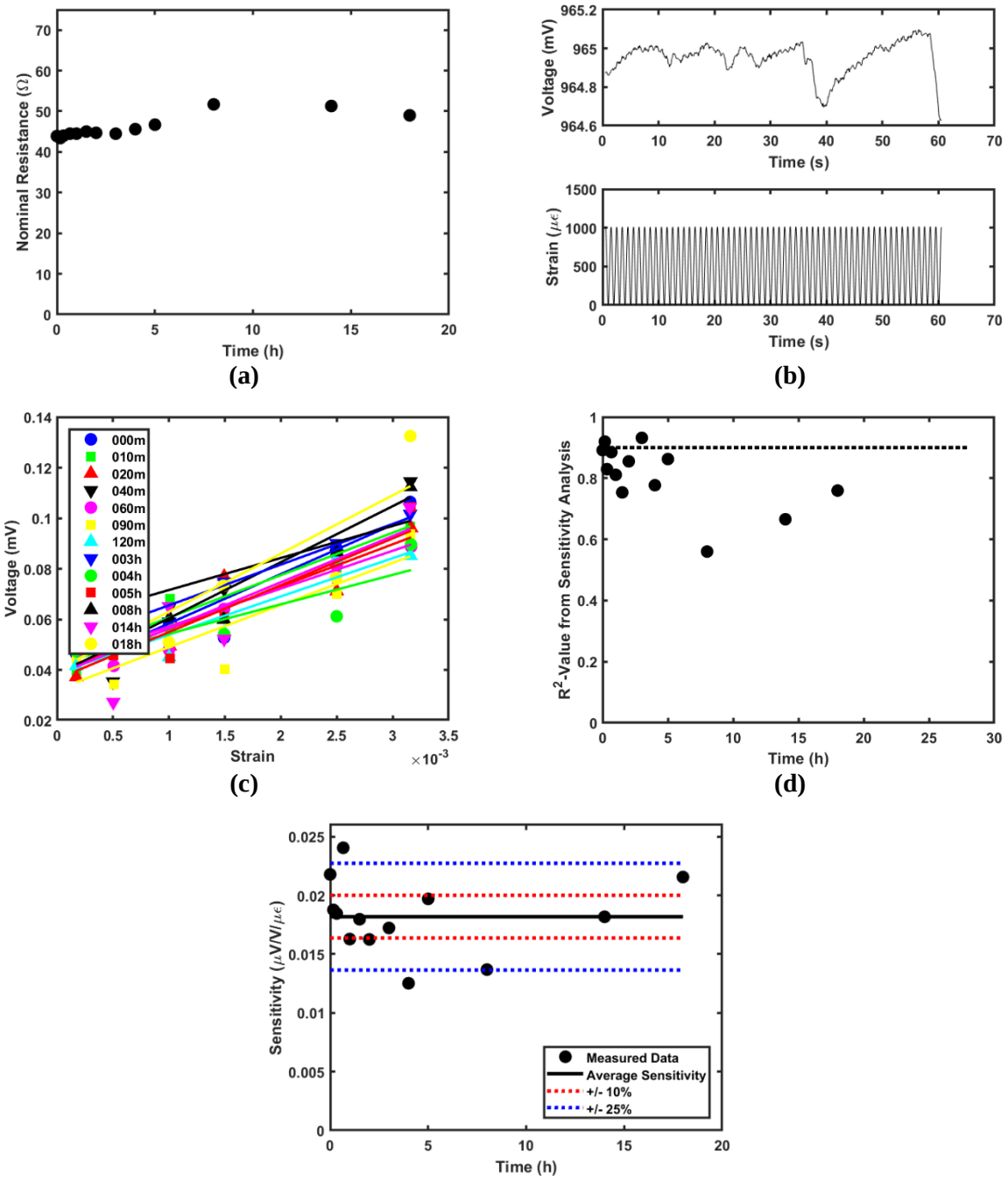

Figure 110 Electromechanical performance of ALD-passivated electroplated Mg strain sensors under degradation. ***(a)*** *Nominal resistance of an electroplated Mg strain sensor with ALD passivation under physiological degradation.* ***(b)*** *Temporal response of device to compressive cyclic strains at amplitudes of 1000 με.* ***(c)*** *Strain sensor performance,* ***(d)*** *The correlation coefficient analysis and* ***(e)*** *strain sensitivity of ALD-passivated sensor under physiological conditioning. Data was evaluated at a loading frequency of 1 Hz.*

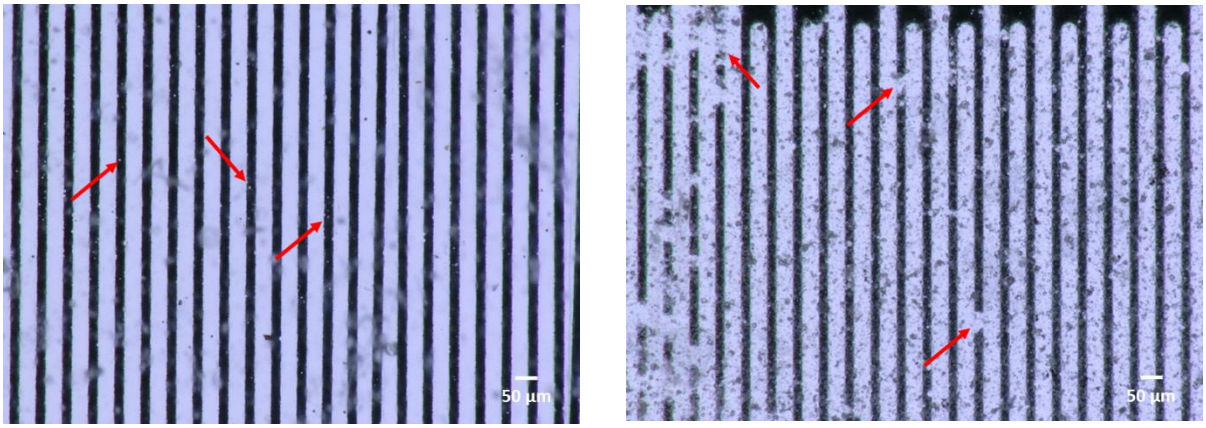

(a) **(b)**

*Figure 111 Optical images of ALD-passivated Mg sensor after **(a)** 3 days and **(b)** 6 days of physiological conditioning.*

3.2.5. Biodegradable Strain Sensors with Electroplated Zinc Passivation

Pulse plated Zn coatings were explored as a passivation scheme to improve the performance of electroplated Mg strain gauges. Figure 112 shows the electromechanical performance of PP Zn-coated Mg sensors evaluated from 50 mHz to 10 Hz. Consistent with previous data on Mg-based sensors, 50 mHz was below the threshold for reliable strain detection. Unlike bare and ALD-passivated Mg sensors, however, Zn-coated sensors maintained strain sensitivity at 50 mHz. The observed sensitivity was higher than the average strain sensitivity of ALD-passivated Mg sensors subjected to degradation. However, the strain sensitivity at 50 mHz (i.e., 0.2 $\mu V/\mu\varepsilon/V_{ex}$) was less than 90% of the sensitivity observed at higher frequencies. Hence, even though the sensor was sensitivity at near-DC frequencies, readings would be unreliable in an *in vivo*, uncontrolled environment (i.e., where the actual loading frequency is unknown). Above this limit of detection, Zn-coated Mg sensors exhibited the highest sensitivity; the sensitivity monotonically increased, however, with loading frequency for the physiological range of interest. Strain sensitivity was 0.073 $\mu V/\mu\varepsilon/V_{ex}$ at 250 mHz, but increased by 26% to 0.093 $\mu V/\mu\varepsilon/V_{ex}$ at 10 Hz. Higher strain sensitivity with Zn-coated Mg sensors was observed even though the nominal resistance of the Zn-coated sensor was less than half that of bare and ALD-passivated Mg sensors. This was

attributed to the reduced surface roughness of the electroplated Mg strain gauge with the Zn coating. As shown in earlier results, the micron-scale surface roughness detracts from sensor performance due to non-uniform strain distributions. Scanning electron micrographs of PP Zn-coated electroplated Mg (shown in the previous chapter) revealed a refinement in the surface roughness and gross change in surface morphology.

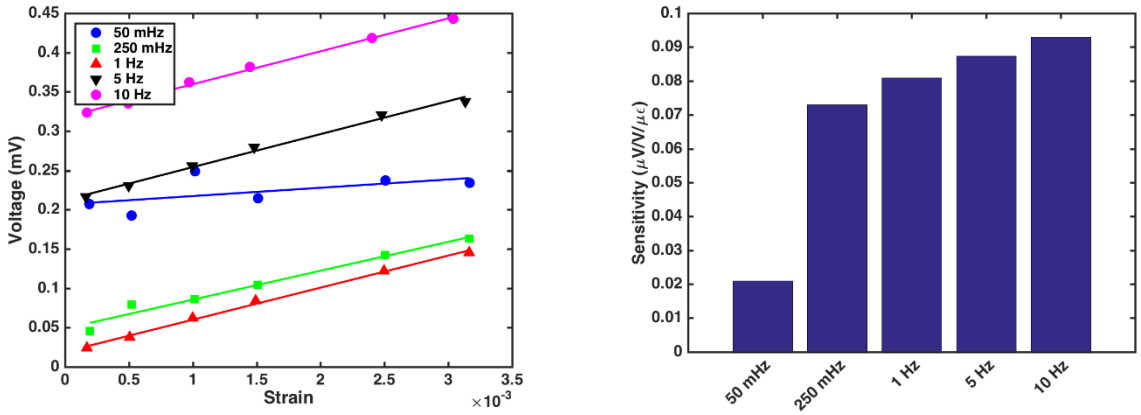

(a) **(b)**

Figure 112 Device performance of electroplated Mg strain sensors passivated with Zn deposited by pulse electrodeposition in an alkaline electrolyte and encapsulated with PLA. ***(a)*** *Strain sensor performance and* ***(b)*** *strain sensitivity of Zn-coated Mg sensor under ambient conditions, evaluated from 50 mHz to 10 Hz to capture the frequency range of ambulation.*

The effect of physiological degradation on PP Zn-coated Mg strain sensors was examined. As shown in Figure 113, Zn-coated sensors exhibited improved performance over bare Mg-PLA and ALD-passivated Mg sensors. The nominal resistance of the sensor remained stable during the initial 24 hours of degradation and did not exhibit any stabilization period. This further confirmed the theory that the initial resistance increase is attributed to surface corrosion of the sensor following electrolyte ingress. Since the corrosion rate of Zn is more than 3 orders of magnitude less than that of bare Mg, the impact of surface corrosion on the initial stabilization was negligible. It should be noted, however, that after 24 hours, nominal resistance of the Zn-coated sensor increased 200% and reached a steady value at 40 hours. At the

elevated nominal resistance, the sensor remained stable for another 30 hours before loss of functionality. The more stable device performance can also be observed in tests conducted at the lower range of strain amplitudes. Figure 113b shows the voltage response to a cyclic strain with an amplitude of 180 με. The voltage output showed lower frequency noise, but the amplitude of the output remained consistent in the test. At the maximum strain evaluated (i.e., 3800 με), negligible baseline drift and low frequency oscillations were observed.

The Zn-coated sensors also showed the highest sensitivity among electroplated Mg sensors. The average sensitivity was 0.105 $\mu V/\mu\varepsilon/V_{ex}$ and corresponded to an average R^2 value of 0.96. The sensitivity was nearly 50% higher than that of bare Mg-PLA sensors and nearly fivefold higher than that of ALD-passivated Mg strain sensors evaluated under physiological conditioning. Further, the average sensitivity was 70% that of non-degradable Au-polyimide strain sensors, which feature full Wheatstone bridge configurations for higher strain sensitivity and elimination of thermal and environmental noise. It can be seen in Figure 113f that noise and drift of the quarter bridge configuration nonetheless impacts the Zn-coated sensor; the majority of data points collected over the device's functional lifetime are distributed below the mean. Optical images of the sensor after 60 hours of physiological conditioning in SBF (Figure 114) show the formation of 2 pits in the Zn-coated Mg sensor, one of which showed more extensive corrosion along the length of the feature. This aligned well with the subsequent loss of functionality after 64 hours. Even though the functional lifetime of the PP Zn-coated Mg strain sensor did not exceed that of bare Mg-PLA sensors (i.e., 64 hours compared to 90 hours), the more stable performance and higher strain sensitivity support the use of PP Zn as a passivation scheme for electroplated Mg-based biodegradable devices.

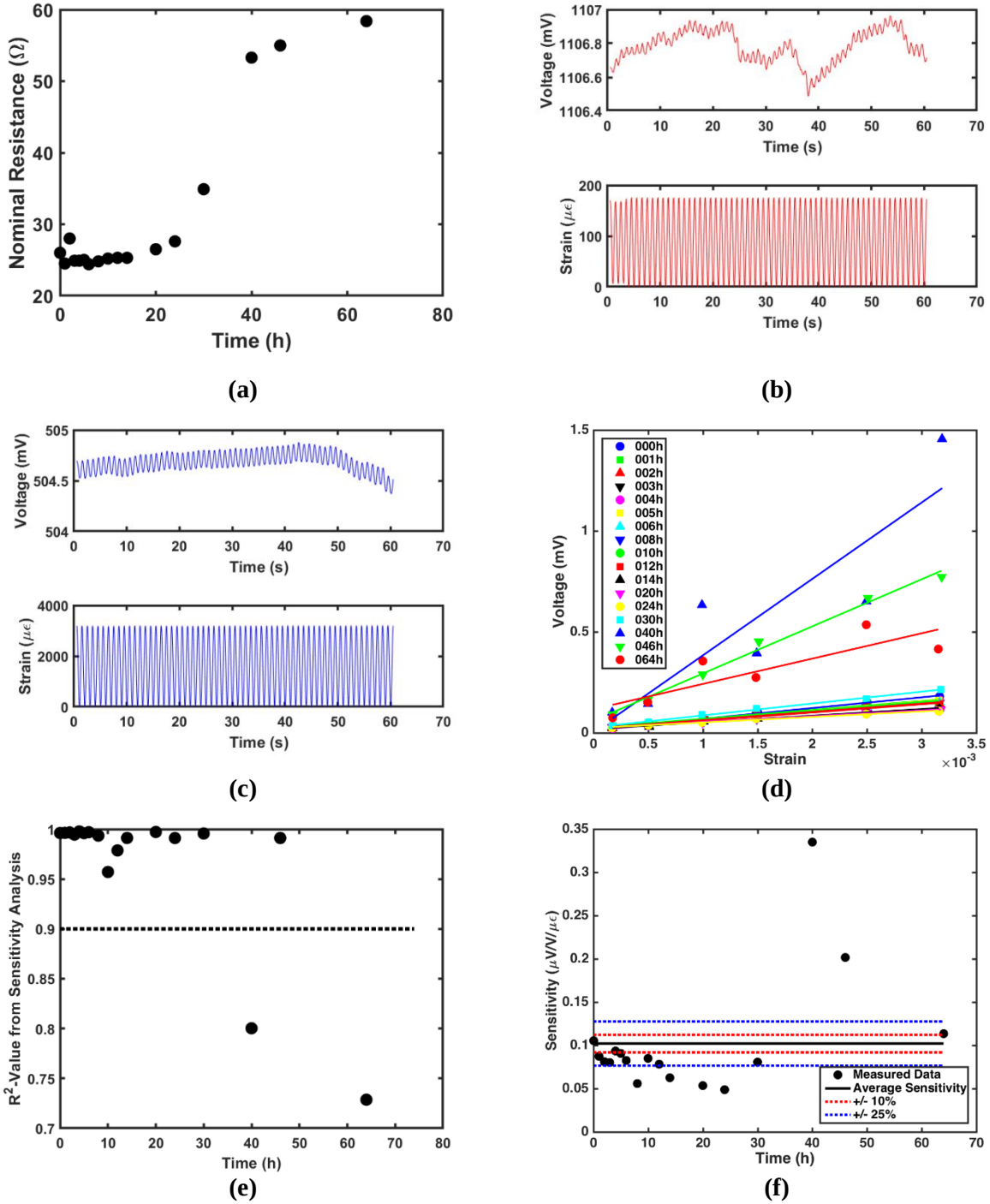

Figure 113 Electromechanical performance of Zn-coated electroplated Mg strain sensors under degradation. ***(a)*** *Nominal resistance of Zn-coated Mg strain sensor throughout physiological degradation.* ***(b-c)*** *Temporal response of device to compressive cyclic strains at amplitudes of 180 με and 3200 με, respectively.* ***(d)*** *Strain sensor performance,* ***(e)*** *The correlation coefficient analysis of strain sensitivity, and* ***(f)*** *strain sensitivity of Zn-coated Mg sensor under physiological conditioning. Data was evaluated at a loading frequency of 1 Hz.*

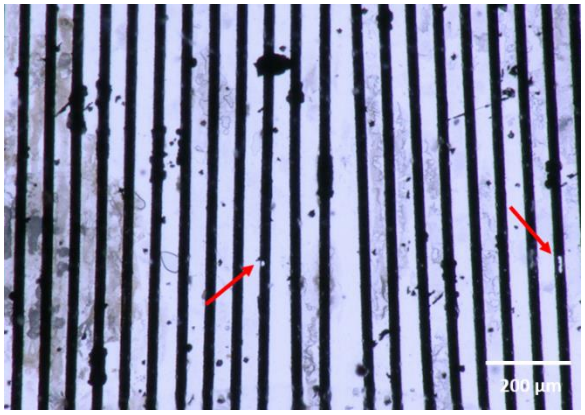

Figure 114 Optical image of PP Zn-coated Mg sensor after 60 hours of physiological conditioning.

3.2.6. Comparison of Biodegradable and Non-Degradable Sensors

Electroplated Mg-based strain sensors were fabricated and characterized as biodegradable devices to monitor bone healing. The examined range in compressive strain and loading frequency were guided by the physiological ranges observed in rodents. Figure 115 summarizes the performance of electroplated Mg strain sensors under physiological degradation. Electroplated Mg sensors, bare and with either ALD or PP Zn passivation, were examined in quarter bridge strain gauge configurations featuring various nominal resistances. For sensors featuring the same encapsulation and passivation schemes (or lack thereof), gauges with higher nominal resistance showed more stable performance at lower loading frequencies (i.e., <100 mHz) and higher linearity to applied strains from 180 με to 3800 με. The tradeoff, however, was a shorter functional lifetime, as observed with both bare and ALD-passivated Mg strain gauges. Further, higher strain sensitivity was not unilaterally observed with higher resistance gauges, as only ALD-passivated sensors showed a near three-fold increase in strain sensitivity; other sensor types showed no dependence between nominal gauge resistance and strain sensitivity.

Bare electroplated Mg, without any passivation schemes, exhibited a functional lifetime of more than 90 hours. Results from ALD and PP Zn passivation indicated that additional passivation schemes do

not guarantee longer functional lifetimes, but can improve device performance. It was speculated that the shorter functional lifetimes observed with ALD and PP Zn coatings were attributed to acute, localized corrosion at pinholes or damaged areas (e.g., cracks) in the coating. This was particularly true with ALD passivation, where localized pitting corrosion rendered the device less stable and, hence, less accurate at lower strains and frequencies. Since Zn-coated Mg strain sensors showed the highest strain sensitivity, linearity and minimum detectable loading frequency, PP Zn coatings did successfully improve the performance of electroplated Mg strain sensors, albeit not in functional lifetime.

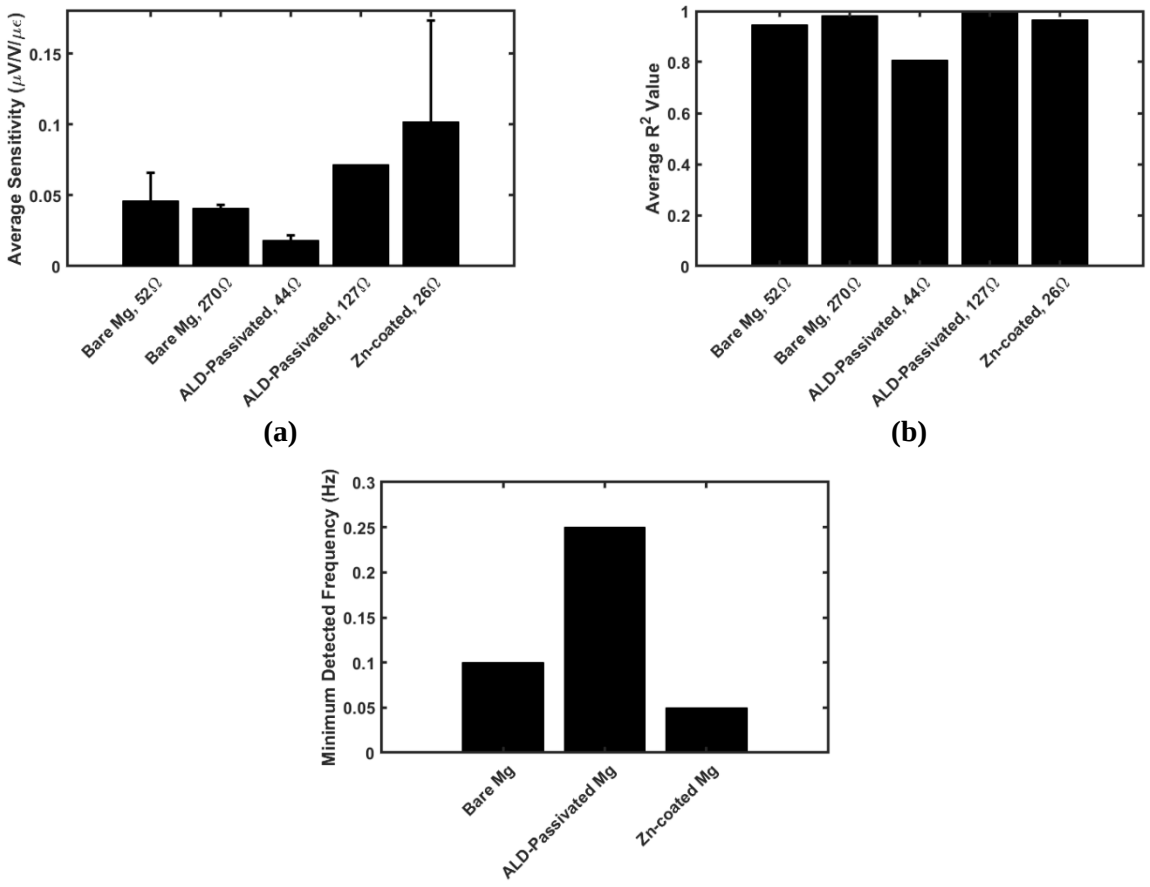

Figure 115 ***(a)*** *Average strain sensitivity,* ***(b)*** *average R^2 value and* ***(c)*** *the minimum detectable frequency of electroplated Mg strain sensors, featuring various passivation schemes and nominal resistances, subjected to physiological conditioning in SBF at 37°C.*

This section implemented and integrated the biodegradable materials previously developed in Chapter 2 towards the demonstration of MEMS-based biodegradable strain sensors and energy sources. To better understand the intended biomedical application, the design, fabrication and characterization of a non-degradable strain sensor preceded developments of corresponding biodegradable analogues (Chapter 3.1); the iterative design cycle and findings from the non-degradable sensor helped to quantitatively define the femoral segmental bone defect model, an *in vivo* bone healing platform for device deployment. Further, the study provided a more realistic baseline for comparing the functionality and longevity of biodegradable and non-degradable devices; even though non-degradable devices are theoretically permanent and can perform indefinitely, device degradation can nonetheless occur under physiological conditions.

Although non-degradable devices will not entirely break down into non-toxic byproducts, device degradation can still cause device failure. The objective of this study was to demonstrate a biodegradable device whose functional lifetime was no more than 1 order of magnitude less than a corresponding non-degradable device; in this manner, the goal was to develop biodegradable devices with improved device functionality as, ultimately, a trajectory towards clinically-relevant technology. It was hypothesized that the implementation of biodegradable passivation schemes aimed to prolong device functionality. Herein, the biodegradable strain sensors fabricated from electroplated magnesium exhibited a functional lifetime of up to 4 days, as compared to 49 days with the non-degradable sensor. The functional lifetime was only 1 order of magnitude less, supporting the experimental goal of prolong functional lifetime in biodegradable devices while underscoring the utility of electroplated Mg for biodegradable applications.

Passivation with PP Zn and multi-layer barriers did not extend functional lifetime. However, such passivation schemes enhanced device performance by improving strain sensitivity and expanding the detection range, both in strain and frequency. For example, the minimum strain detected by PP Zn-coated Mg sensors was 180 με and strain sensing was preserved even at near-DC frequencies (i.e., 50 mHz). This compared favorably with the non-degradable thin film strain sensor, which supported a minimum strain detection of 80-100 με and a minimum frequency detection of 50 mHz. Further, the strain sensitivity of PP Zn-coated and non-degradable strain sensors were 0.07 $\mu V/\mu\varepsilon/V_{ex}$ and 0.19 $\mu V/\mu\varepsilon/V_{ex}$, respectively. Since whole bridge configurations of a Wheatstone bridge doubles device sensitivity compared to quarter bridge configurations, the results suggested that the limitations associated with biodegradable devices and electroplated Mg (e.g., corrosion and surface roughness, respectively) detracted from device sensitivity by 25% compared to non-degradable thin film strain sensors.

3.2.7. Future Work

Biodegradable strain sensors featuring electroplated Mg and biodegradable passivation schemes were successfully demonstrated. The devices exhibited a functional lifetime of up to 4 days and possessed a linear strain response across the physiological range in applied strain and loading frequency. Future work

should explore alternative substrate release strategies to support the fabrication of functional full bridge strain gauges. It is hypothesized that drift compensation of full bridge Wheatstone bridges will improve sensor performance at low frequencies and small strains. It should be noted, however, that the effect of degradation will likely not be negated in a Wheatstone bridge, since Mg is prone to pitting corrosion, which is a stochastic process. In addition, future work should examine the effect of combination passivation schemes (e.g., ALD and Zn coatings) to evaluate whether such combinations possess a synergistic effect on sensor performance.

3.2.8. Conclusions

Biodegradable strain sensors featuring electroplated Mg were successfully demonstrated. The fabricated sensors exhibited a functional lifetime of 4 days and stable strain sensitivity across the physiological range of strain and frequency. The results confirmed that, in spite of the rapid degradation rate of Mg (i.e., 9 mm/day), robust sensors for short-term sensing can be achieved through proper design; feature dimensions that balanced the tradeoff between mechanical stiffness and degradation lifetime supported the use of micron-scale electroplated Mg for biodegradable strain sensors. Since devices were subject to both cyclic mechanical loading and physiological degradation, crack formations, corrosion and stress corrosion cracking were all plausible mechanisms that limited the functional lifetime of a biodegradable strain sensor. Mixed performance was observed with additional passivation schemes. In the case of sensors featuring ALD passivation, it was speculated that focused, accelerated corrosion manifested at pinholes or damaged zones in the passivation (incurred either during the fabrication process, mechanical testing or physiological conditioning). Hence, even though ALD passivation exhibited superior barrier properties to water ingress, imperfect ALD films exacerbated device corrosion by concentrating corrosion in localized regions. In contrast, Zn coatings successfully improved device performance by resolving the limitations of electroplated Mg—surface roughness. As observed with bare Mg-PLA sensors, the micron-scale surface roughness of Mg detracted from its sensitivity and limits of detection as a strain sensor.

Zinc-coated Mg sensors, which reduced the surface roughness and irregularity of electroplated Mg, exhibited the highest sensitivity and linearity, as well as the lowest frequency limit of detection. The findings altogether support the use of electroplated Mg for acute strain sensing applications and emphasize the importance of passivation for achieving enhanced performance and longer lifetimes with biodegradable devices.

3.3. Biodegradable Batteries based on Galvanic Corrosion

3.3.1. Introduction

Biodegradable electronics have garnered increasing interest as an emerging technology spanning biomedicine and MEMS [111], [264], [265]. Specifically, transient implantable medical devices (TIMDs) have been demonstrated, which either entirely or partially dissolve under physiological conditions after completing a sensor task [116], [264]. The use of TIMDs would be advantageous in the monitoring and treatment of transient diseases, such as wound healing, bone fracture, traumatic brain injury, and drug delivery systems, where the device is only needed for a transient period. In this manner, TIMDs eliminate the need for revision surgery to remove the device and chronic inflammatory response observed with permanent implanted devices. From a cost-benefit perspective, the short duration of functional need required for transient disease applications may not merit the long term implications associated with permanent implants [266]. Current demonstrations of TIMDs have been limited to either electrically passive designs or wireless powering [124]. Hwang *et al.* reported a transient implantable system featuring magnesium (Mg) and silicon nano-membranes (Si-NM).[111] The device was inductively powered and exhibited complete dissolution in 10 minutes. Additional passivation schemes with magnesium oxide (MgO) and silk were implemented and extended the degradation lifetime to 10 hours. Luo *et al.* demonstrated a wireless radio frequency (RF) pressure sensor comprising micropatterned zinc (Zn) and iron (Fe) bilayers as the conducting material and poly-L-lactide (PLLA) and polycaprolactone (PCL) as the insulating and structural material, respectively [264]. The device implemented the galvanic coupling of Zn and Fe to control the conductor degradation rate. Telemetry by inductive coupling, however, is limited to short-range distances (i.e., tens of

centimeters) and typically implemented at low frequencies (i.e., less than 100 MHz) with output power between 10-250 mW and data rates of 1-2 $Mb \cdot s^{-1}$ [116].

To realize biodegradable devices with higher performance and more advanced functions, appropriately biodegradable energy sources must be developed to provide onboard powering [124]. The development of biodegradable energy sources would support the design of self-powered electronics with greater functionality and permit sensing and actuation over longer time intervals. The global design constraints of a biodegradable energy source are compactness, energy content, stability of performance, shelf life, biodegradability, and biocompatibility. The biodegradable energy source should satisfy the power requirements of the target device utilizing biodegradable chemistries in its operation and degrade into non-toxic products after serving its discharge lifetime. While transient implantable electronics have not yet reached the commercial market, energy requirements may be estimated based on the power consumption of reported permanent IMDs and the desired functional lifetime of biodegradable analogues. For example, flow rate and pressure sensors may find transient applications in the early detection of vascular graft failure and urodynamic bladder diagnostics. Low power (LP) and ultralow power (ULP) sensors and telemetry systems have been reported to support implantable medical applications [267]–[269]. Xue *et al.* reported a blood flow rate sensing system that consumes a total power of 21.6 µW [270]. Majerus *et al.* demonstrated a wireless implantable micromanometer system that required 32.4 µW of power [271]. In addition, the biodegradable energy source should support current and voltage requirements amenable to microelectronics operation. Ultralow power circuitry is commercially available with current requirements as low as 45 $\mu A \cdot MHz^{-1}$ during active mode and operating voltages of 0.5 V [272]. As biodegradable materials spontaneously break down into their respective principal components in the presence of

an aqueous environment (i.e., metals degrade into ionic species and polymers hydrolytically break down into monomers), the design of a biodegradable battery should also emphasize chemistries that support a stable shelf life [95], [96], [102], [107]. In addition to minimizing exposure to environmental moisture, this also requires minimizing parasitic corrosion of the electrode materials, defined as dissolution not attributed to energy draw from the battery, in the battery electrolyte, and initiation of the battery prior to intended use [124], [265], [273].

3.3.2. Fabrication and Characterization of a MEMS-Enabled Mg/Fe Battery

This study presents the design, fabrication and testing of a biodegradable Mg/Fe battery for the powering of transient IMDs. Because biodegradation may be defined as the electrochemical corrosion of materials within a physiological environment, a natural extension of biodegradable electronics is to harness the energy released from the metallic corrosion reactions in the form of a biodegradable battery [128], [274]–[276]**.** The battery features a Mg anode and Fe cathode in a 0.1 M magnesium chloride ($MgCl_2$) electrolyte solution. Magnesium was selected as the anode due to its attractive electrochemical, mechanical, and physiological properties [115], [265]. Magnesium exhibits a theoretical specific capacity of 2200 $mAh \cdot g^{-1}$ and a standard electrode potential of 2.34 V vs. SHE, which is over 1.5 V more electronegative than Zn and Fe [94], [99], [265], [276]. In addition, Mg features a high modulus-to-density ratio and a Young's modulus (45 GPa) that approximates that of cortical bone (20 GPa) better than titanium or stainless steel (Table 26) [84], [98], [99]. Both Mg and Fe have been demonstrated in biodegradable, structural implants (e.g., bone screws and fixation plates, cardiovascular stents) with confirmed biocompatibility *in vivo* [96], [110], [277]. Further, Mg is the fourth-most abundant cation found in the body and an essential mineral nutrient [92], [93]. As the anode is consumed in the battery discharge reaction, the high physiological tolerance of Mg supports its use as the sacrificial anode material [278]. In turn, Fe was chosen as the cathode material because it exhibits the more noble electrochemical potential

and a lower hydrogen overpotential than that of Zn, providing a more efficient cathode for hydrogen reduction to occur [96], [275].

Table 26 Comparison of electrochemical, mechanical, and physiological properties of Mg, Zn, and Fe. The electrochemical properties are based on half-cell reactions with a valence of two.

	Mg	Zn	Fe
Standard Electrode Potential (V vs. SHE)	-2.34	-0.76	-0.44
Theoretical Specific Capacity (mAh/g)	2200	820	960
Young's Modulus (GPa)	45	108	210
Density (g/cm^3)	1.74	7.14	7.87
Corrosion Rate (mil/y)	22.3	1.97	7.48
Daily Tolerance (mg)	700	15	15

The governing chemistry of the battery is the cathodic protection of the Fe electrode through the oxidation of Mg and, thus, reduction of hydrogen on the Fe cathode surface (Figure 116). In addition to these discharge reactions, Mg naturally degrades in aqueous solutions. This effect, or parasitic corrosion of the Mg, would detract from the capacity and energy of the battery. To hinder this effect, the Mg surface was protected with either polycaprolactone (PCL) or poly(glycerol-sebacate) (PGS), both biodegradable and biocompatible polymers [6]. As the thickness and permeability of the polymeric coating may contribute to mass transfer resistance and impact discharge performance of the battery, PCL and PGS were compared at varying thicknesses to determine the relevant parameters for achieving a high coulombic efficiency and discharge potential. The timescale of PCL and PGS degradation (i.e., months) exceeds the lifetime of the battery, and the thickness of the polymer coating does not appreciably change during discharge of the battery. The electrolyte was selected as $MgCl_2$ because Mg^{2+} and Cl^- ions are constituents of physiological solutions [7].

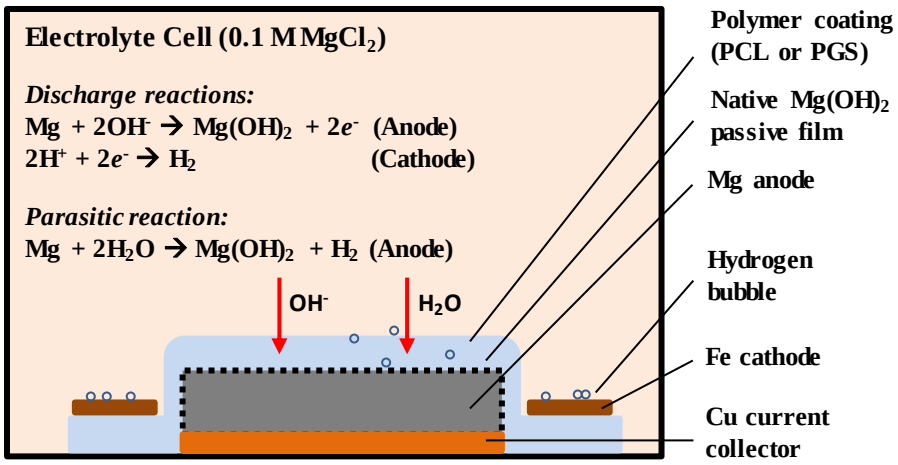

Figure 116 Schematic of the Mg/Fe biodegradable battery. Electrolyte diffuses across the polymer coating and native magnesium hydroxide ($Mg(OH)_2$) film to reach the Mg surface, where oxidation reactions that supply electrons for the battery and generate hydrogen occur. The $Mg(OH)_2$ formation is countered by mechanical disruption of this passive film from the discharge current. Hydrogen is reduced on the Fe cathode surface.

Fabrication of the biodegradable battery began with through-mold electrodeposition of Mg to form the anode (Figure 117). Silicon dioxide (500 µm thickness) and metallic seed layers (50 nm Ti/ 500 nm Cu/ 50 nm Ti) were deposited onto a silicon wafer by plasma-enhanced chemical vapor deposition (PECVD) and sputter deposition, respectively. To achieve a mesh seed layer, the Ti and Cu were chemically-etched through a photomask. Next, an electroplating mold was patterned using polyvinyl alcohol (PVA), a water-soluble polymer with low solubility in solvent solutions. The negative image of the electroplating mold was patterned with NR-21 photoresist (Futurrex), and PVA (33 w/v%) was spin-coated onto the wafer and cured. A brief oxygen plasma treatment removed any PVA coating the edges of the photoresist. The sample was sonicated in acetone to achieve a micropatterned water-soluble mold.

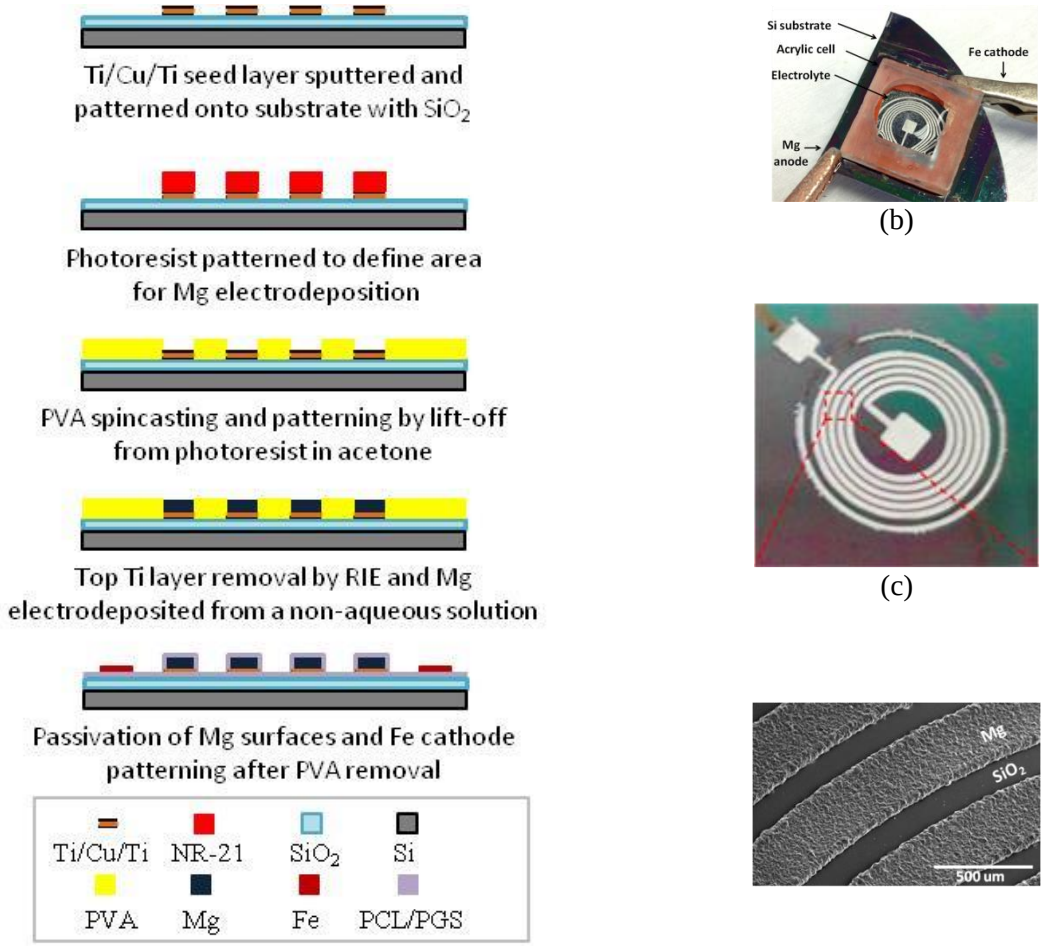

Figure 117 (a) Fabrication process and (b) testing setup of the Mg/Fe battery, and (c) optical and (d) SEM images of the electroplated Mg anode.

Magnesium was electroplated from a non-aqueous solution of methylmagnesium chloride and aluminum chloride at a 6:1 molar ratio in tetrahydrofuran (THF). The electrodeposition was performed in a moisture-free glove box under inert nitrogen atmosphere. Pulse plating was conducted with an average current density of 10 mA/cm^2 at 20% duty cycle to a thickness of 35 µm. The electroplating mold was removed by solubilizing in water. The Mg anode was coated with either PCL or PGS. Commercial 80 kDa PCL pellets were solubilized in trifluoroethanol at a concentration of 100 mg/mL. PGS was synthesized by a polycondensation reaction of sebacic acid and glycerol, as described in [6], and diluted in

THF (33 w/v%). PCL or PGS was spin-coated onto the Mg anode at varying thicknesses, and cured at room temperature and at 120ºC under vacuum, respectively. The Fe cathode was patterned by e-beam evaporation through a Kapton (DuPont) shadow mask to a thickness of 300 nm. Both the shadow mask and electrolyte cell were fabricated by laser micromachining with a CO_2 laser.

The surface morphology and elemental composition of the Mg and Fe electrodes were characterized by SEM/EDX (Hitachi S-3700N). Potentiodynamic polarization tests were performed between -1.7 and -1.2 V at a scan rate of 1 mV/s to characterize the corrosion behavior of electroplated Mg and the effect of polymeric coatings. A three-electrode setup was implemented with Mg, Pt, and Ag/AgCl as the working, counter, and reference electrodes, respectively. Tests were conducted in 0.1 M aqueous $MgCl_2$ solution with a potentiostat (WaveDriver 10, Pine Instruments).

A two-electrode-cell configuration, where Mg and Fe serve as anode and cathode, respectively, was utilized to test the performance of the batteries with a potentiostat (Model 263, EG&G Princeton Applied Research). The electrolyte was selected as 0.1 M aqueous $MgCl_2$ solution, which provided a conductivity of 0.9 mS/cm. Tests were performed under galvanostatic conditions at a discharge current of 25 µA.

3.3.3. Characterization of Battery Components

Figure 117c-d shows optical and SEM images of the microfabricated Mg anode. Surface elemental analysis confirmed the atomic composition of the electroplated metal as 95% Mg and 5% O (data not shown). While the theoretical standard electrode potential of Mg is -2.34 V, this value is not observed in practice due to a native $Mg(OH)_2$ film that forms on the Mg surface. Electrolyte must first diffuse across the passive film to react with the Mg. The film is further disrupted mechanically during current draw to expose more active material to the electrolyte [8]. Figure 118 shows the polarization curves of uncoated Mg and Mg coated with either PCL or PGS in the proposed electrolyte. Uncoated Mg demonstrated a

corrosion potential of -1.32 V *vs.* SHE. This agrees with literature values for Mg in dilute chloride solutions [9]. In contrast, Mg coated with 15 µm of PCL or PGS exhibited corrosion potentials of -1.292 V and -1.165 V, respectively. The corrosion potential shifted towards the noble direction with PCL and PGS coatings, suggesting that the polymer coatings reduced the parasitic corrosion of Mg in the electrolyte solution [9-10]. The higher corrosion potentials observed with PGS coatings than PCL coatings further suggested that Mg coated with PGS may be more corrosion resistant. The fluctuations observed in the anodic curves were attributed to the pitting nature of Mg corrosion, with repeated breakdown and formation of the passivating film [9].

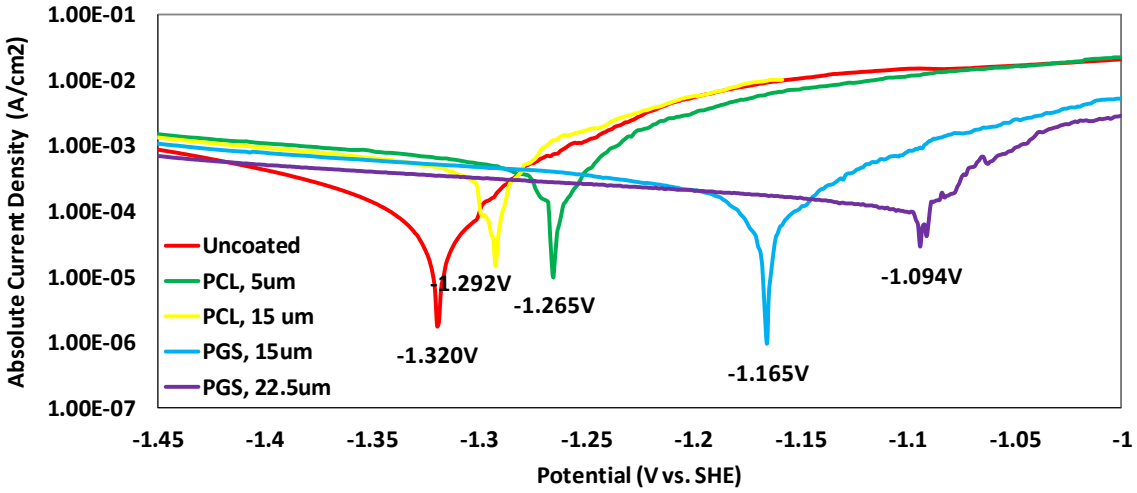

Figure 118 Polarization curves of the Mg anode coated with PCL and PGS at varying thicknesses, compared against uncoated Mg, in a 0.1M $MgCl_2$.

As a first step towards understanding ion transport across the biodegradable polymers, water permeability tests were conducted to evaluate the diffusion properties of the polymers (Chapter 2). As discussed in Chapter 2, the rate of water transport across the 300-µm-thick PCL and PGS membranes were 0.08 mg/cm^2/h and 0.19 mg/cm^2/h, respectively. These findings confirmed that the polymer coatings would not eliminate water transport to the Mg anode surface.

3.3.4. Electrochemical Characterization of MEMS-Enabled Mg/Fe Battery

Figure 119 demonstrates the effect of polymer coatings on the discharge profile and capacity of the

Mg/Fe batteries. The results are summarized in Table 27. Uncoated batteries delivered the shortest service life and power, at 2.9 h and 15.5 µW, respectively. It was speculated that the hydrogen evolution, as well as the continuous breakdown and formation of the native passive film on the Mg surface, induced stress to the Mg film. The stressing may have been the cause of Mg delaminating from the substrate and consequently causing loss of electrical connection to the current collector. Hence, the polymer coating may provide a secondary purpose of mechanically stabilizing the Mg anode on the substrate.

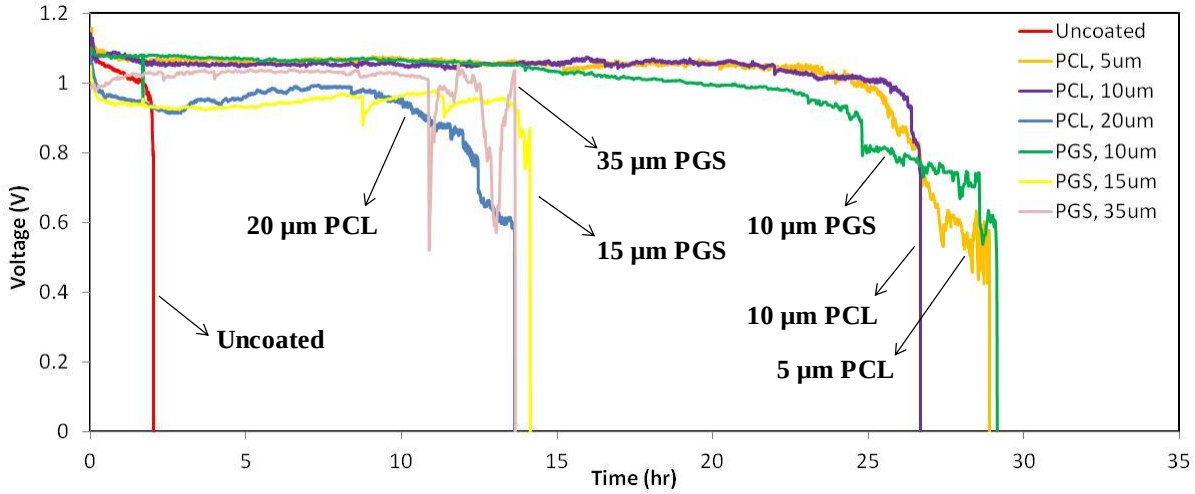

Figure 119 Galvanostatic discharge profiles at a current of 25 µA. The cutoff potential was 400 mV.

Table 27 Summary of MEMS-enabled Mg/Fe battery performance at a discharge current of 25 µA.

		PCL			PGS		
Passivation	**Uncoated**	**5um**	**10um**	**20um**	**10um**	**15um**	**35um**
Discharge time (h)	2.9	28.9	26.7	13.6	29.1	14.1	13.6
Capacity (µAh)	73	722	667	341	729	353	341
Power (µW)	15.5	25.3	26.2	22.9	24.8	23.5	25
Energy (J)	0.2	2.6	2.5	1.1	2.6	1.2	1.2
Coulombic efficiency (%)	1.0	13.0	12.0	6.3	13.5	6.6	6.3

Batteries coated with 5 and 10 µm of PCL showed higher discharge potentials than uncoated batteries. As expected, electrodes with thicker PCL coatings exhibited increased resistance to charge

transfer and provided lower discharge potentials. With increasing polymer thickness, it becomes more difficult for OH^- ions to travel to the Mg surface. This effect also governed the lifetime of the battery because with thicker polymer films, reaction products accumulated at the PCL-Mg interface with prolonged discharge and corresponded to a decline in discharge potential. This can be observed from batteries coated with 20-µm-thick PCL. Further, hydrogen formation at the Mg anode caused a buildup of internal pressure with thicker PCL membranes. This weakened the adhesion of the PCL film to the substrate and, in some instances, resulted in film delamination.

PGS-coated batteries delivered longer discharge lifetimes than the uncoated batteries. As PGS exhibited higher water permeability and PGS-coated Mg demonstrated lower corrosion potential, it was expected that batteries coated with PGS would also demonstrate better performance than those coated with PCL. This was observed with 10-µm-thick PGS, which showed the highest capacity and coulombic efficiency of 0.7 mA/h and 13.5%, respectively. This discharge lifetime was similar to that of PCL-coated batteries at 5 and 10 µm thickness. PGS also provided greater mechanical stability, as thicker PGS films did not delaminate during discharge, as with thicker PCL films. The lower average potential and less stable discharge profile obtained with PGS-coated batteries, especially with increasing polymer thickness, suggested an accumulation of reaction products at the PGS-Mg interface. This was confirmed with X-ray photoelectron spectroscopy (XPS) of PGS-coated batteries after discharge, which showed $Mg(OH)_2$ in regions where Mg was consumed (data not shown). As such, PGS-coated batteries provided slightly lower power at 25 µA discharge, and the highest power and energy were obtained from PCL-coated batteries. PCL-coated batteries showed a maximum of 26.2 µW of power and 2.6 J of energy. As these results fall within the range in power requirements for commercial IMDs, the presented battery chemistries show a promising direction towards providing viable energy sources for powering transient implantable electronics. The range in average discharge potential obtained with batteries coated with PGS and PCL, which exceeded the average discharge potential of the uncoated battery, suggested that there exists an optimum coating and thickness for maximizing the power and performance of Mg/Fe batteries. The coating

should hinder parasitic corrosion at the Mg anode without appreciably increasing resistance to mass transfer. Further, the coating should be mechanically robust to accommodate for hydrogen evolution at the polymer-Mg interface. Future work may further optimize the use of biodegradable polymer coatings or consider alternative means of enhancing corrosion resistance of the Mg anode. Biodegradable material sets should also be considered for the substrate and packaging. Further design constraints should be governed by the design requirements for a targeted transient disease state.

This study demonstrated the viability of a biodegradable battery that harnesses the galvanic corrosion of Mg and Fe as an energy source. A spiral anode design and polymeric coatings were implemented to achieve a candle-inspired consumption of the Mg anode and, in this manner, govern the discharge lifetime of the battery. The present design, however, was unable to achieve a candle-like discharge because the thick polymeric encapsulation was insufficient in retarding electrolyte ingress and promoted the buildup of corrosion products that further hindered the candle-like discharge. The PGS and PCL coatings did hinder parasitic corrosion of the Mg anode and increased the coulombic efficiency of the system by improving the mechanical robustness of the structures; thinner coatings corresponded to higher energy densities, but showed no appreciable effect on power densities. Taken together, these findings not only confirmed the viability of biodegradable energy sources, but further underscore the need for an extensive characterization of Mg/Fe galvanic couples as energy sources. The findings further emphasize the need for more sophisticated barrier coatings in order to achieve a candle-like discharge profile. Specifically, the barrier coating should exhibit orders of magnitude lower water transport rates and be sufficiently thin and brittle to break down at the discharge zone to reduce the mass transfer limitations imposed by the buildup of corrosion products underneath the coating.

3.3.5. Design and Operation of Mg/Fe Batteries with Polycaprolactone Encapsulation

The previously reported biodegradable battery comprised micropatterned Mg and Fe as the anode and cathode, respectively, and 0.1 M magnesium chloride as the electrolyte solution [124]· While the battery demonstrated a stable discharge potential of 1.1 V at a discharge rate of 125 $\mu A \cdot cm^{-2}$, the candle-like

consumption of the Mg anode was unsuccessful. In addition, the electrodes were packaged on bulk silicon, which is not biodegradable, and the study did not demonstrate encapsulation of the proposed electrolyte. Yin *et al.* subsequently demonstrated a series of biodegradable batteries featuring Mg as the anode, Fe, molybdenum (Mo), or tungsten (W) as the cathode, and phosphate-buffered saline (PBS) as the electrolyte [81]. The bulk Mg/Mo cells achieved stable discharge potentials of up to 1.6 V with the use of four cells connected in series at a discharge rate of up to 100 $\mu A \cdot cm^{-2}$. Kim *et al.* reported an ingestible sodium ion electrochemical cell, which comprised manganese oxide (MnO_2) and activated carbon (AC) as the electrode components. The packaged electrochemical cell achieved discharge potentials of up to 0.6 V at discharge currents of 5-20 µA.[86] These demonstrations underscore the prospects of biodegradable batteries for achieving power schemes capable of powering similarly biodegradable devices.

The present study reports a microfabricated PCL-encapsulated Mg/Fe biodegradable battery featuring a total cell volume of less than 0.02 cm^3 and stable performance at higher discharge rates than previously reported. In addition, this study systematically examines the effect of various design criteria (i.e., electrolyte selection, functional material design, and geometry) on Mg-based batteries and proposes the underlying phenomena governing battery performance. The objective of the present study was two-fold: (1) to demonstrate a biodegradable battery with improved discharge performance and (2) to provide a fundamental study on Mg-based battery chemistries to support future efforts on biodegradable batteries.

Following a functional rather than an electrochemical definition, the devices fabricated in this work will be referred to as PCL-coated Mg/Fe batteries, even though they are more accurately termed electrochemical cells. The PCL-coated Mg/Fe battery features a two-electrode-cell configuration with Mg as the sacrificial anode and Fe as the cathode. The principle of operation is the galvanic protection of Fe through the anodic oxidation of Mg. As shown in Figure 120a, the electrodes are separated by and encapsulated in a thin PCL film (5 µm thickness) that dually serves as the packaging for the battery and a semipermeable membrane for infiltration of the battery

electrolyte. Microfabrication and assembly of the battery are presented in Figure 120b. To overcome challenges with electrolyte encapsulation, which requires isolation of the Mg anode from the electrolyte solution prior to desired activation of the battery, the present study utilizes physiological fluid as the battery electrolyte. In testing, phosphate buffered saline was used as an *in vitro* surrogate of physiological fluid.

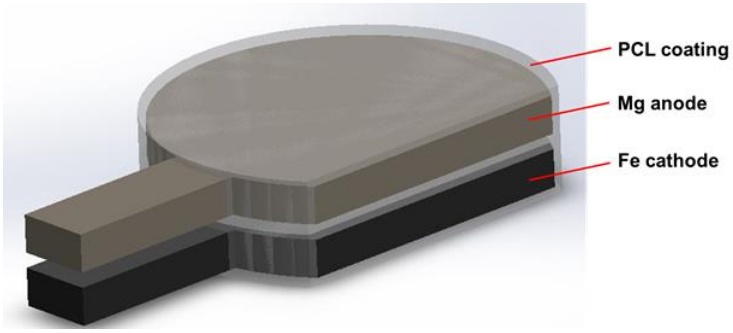

(a)

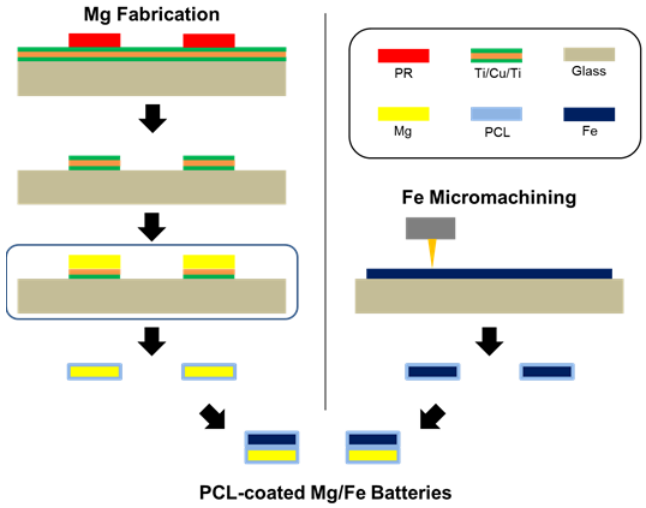

(b)

Figure 120 Schematic and fabrication of the PCL-coated Mg/Fe battery. (a) PCL-coated Mg/Fe batteries that harness physiological solution as the electrolyte; and (b) Fabrication of PCL dip-coated Mg/Fe batteries comprises three stages: Mg fabrication, Fe micromachining, and battery assembly. Chemical etching through a lithographically-defined photomask is performed on a metalized glass substrate to yield a micropatterned seed layer. Magnesium is electrodeposited onto the substrate under nitrogen atmosphere after removal of the top Ti layer and sample cleaning. Magnesium anodes are then delaminated from the substrate and dip-coated in a PCL solution. Iron cathodes are micromachined from commercial Fe foil with an infrared laser. Samples are removed from the rigid substrate, cleaned, dip-coated into PCL solution and laminated against the PCL-coated Mg anode to form the assembled battery.

Three electrolytes (0.1 M $MgCl_2$, 0.9 wt.% NaCl, and 1x PBS) were investigated because the ionic constituents of the electrolytes are similarly found in the human body.[124], [264], [265] Further, the design of a biodegradable battery may either utilize the body's physiological solution as the electrolyte, where PBS is proposed as a suitable analog for *in vitro* studies, or feature encapsulation of the electrolyte cell within biodegradable packaging. While utilizing physiological solution presents a simpler battery design and facilitates initial battery demonstrations, an investigation of battery performance in alternative electrolytes may support future research on biodegradable batteries with more advanced battery activation and electrolyte isolation mechanisms.

The discharge reactions of the Mg/Fe battery in an aqueous electrolyte are given by:

Overall:	$Mg + 2H_2O \rightarrow Mg(OH)_2 + H_2$	$\Delta E = 1.51$ V
Anodic:	$Mg + 2OH^- \rightarrow Mg(OH)_2 + 2e^-$	$E^\circ = -2.34$ V
Cathodic:	$2H_2O + 2e^- \rightarrow H_2 + 2OH^-$	$E^\circ = -0.83$ V

As discussed, the oxidation of Mg takes places on the anode surface and reduction of either water or hydrogen occurs on the cathode surface. Hydrogen gas and magnesium hydroxide ($Mg(OH)_2$) are formed from the discharge reactions.[95], [265], [275] However, additional reactions with electrolyte constituents must also be considered. For example, chloride ions at concentrations greater than 30 mM support the following reactions with Mg:

$$Mg + 2Cl^- \rightarrow MgCl_2 + 2e^-$$

$$Mg(OH)_2 + 2Cl^- \rightarrow MgCl_2 + 2OH^-$$

Both magnesium and magnesium hydroxide react with the reducing chloride environment to form magnesium chloride ($MgCl_2$), a soluble product. The effect is an increased Mg corrosion rate. The following reaction has also been observed with Mg in a phosphate-containing solution:

$$3Mg + 2PO_4^{3-} \rightarrow Mg_3(PO_4)_2 + 6e^-$$

The reaction product, $Mg_3(PO_4)_2$, is less soluble than $MgCl_2$ and manifests as a passivation layer on the Mg surface, with an observed reduction in corrosion rate and pitting behavior.[128] The cumulative effect of Mg in a multi-ionic species must be considered when understanding the performance of Mg-based battery chemistries.

3.3.6. Fabrication and Characterization of PCL-Encapsulated Mg/Fe Batteries

Magnesium and iron electrodes were fabricated by non-aqueous electrodeposition and laser micromachining, respectively (Figure 120b). Fabrication of Mg anodes began with metallization of glass substrates by DC sputtering (CVC) with 100 nm Ti, 500 nm Cu, and 100 nm Ti. A lithographically defined etch mask was deposited onto the substrate using a positive tone photoresist (Shipley S-1813). The photoresist was spun at 3000 rpm at a rate of 500 rpm s^{-1} for 30 s and baked at 110 °C for 3.5 minutes before UV exposure and development in tetramethylammonium hydroxide (TMAH)-based aqueous solution (MF-319, Microposit). The exposure dosage was set to 150 mJ cm^{-2} at 365 nm wavelength. The Ti and Cu seed layers were chemically-etched in dilute hydrofluoric acid (1:50 v/v HF) and ferric chloride ($FeCl_3$) solutions, respectively, to obtain a mesh seed layer featuring the anode geometry and appropriate electrical connections for electroplating. The photoresist and topmost Ti layer were removed by sonication in acetone and with dilute HF, respectively. Electrical connection lines were protected by applying a thin coating of polyvinyl alcohol (1:5 w/v PVA; 2 kDa), which exhibited poor solubility in the electroplating solvent. The samples were dried at room temperature and loaded into a glovebox under dry nitrogen for Mg electroplating. Prior to electroplating, samples were cleaned in a salicylic acid solution (10 g L^{-1} in tetrahydrofuran (THF)) and rinsed in THF. [115] Magnesium electroplating was performed in a 6:1 molar ratio of methylmagnesium chloride (CH_3MgCl) and aluminum chloride ($AlCl_3$) in THF under pulse plating conditions (i_{av} = 10 mA cm^{-2}, t_{on} = 1 ms, t_{off} = 4 ms, k_{dep} = 7 µm min^{-1}) to the desired thickness. [265] The electroplated samples were then rinsed in THF and dried.

Iron cathodes were micropatterned from commercial Fe foil (Sigma Aldrich, purity > 99.95%) using an infrared laser (Resonetics, Nd:YLF, 1047 nm) operating at 180 ns pulses and a power density of

$18x10^{12}$ Wm^{-2}. Prior to laser micromachining, the Fe foil was thoroughly degreased with acetone and laminated onto a glass substrate with adhesive. Following the laser micromachining, the samples were immersed in acetone to remove the adhesive, thereby releasing the micromachined Fe cathodes.

Figure 120b shows the assembly and packaging of microfabricated Mg and Fe electrodes with PCL. The electroplated Mg anodes were delaminated from the glass substrate and dip-coated in a PCL solution (50 mg mL^{-1} in THF). The mass of the Mg anodes was measured by a high-precision balance before and after dip-coating. PCL-coated Mg anodes were stored under inert nitrogen atmosphere until battery assembly. Iron cathodes were similarly dip-coated in PCL (50mg mL^{-1} in THF) and laminated with corresponding PCL-coated Mg anodes.

Electrochemical testing comprised two phases, beginning with the corrosion assessment of Mg electrodes in various electrolytes. Next, Mg/Fe half-cells were galvanostatically discharged to investigate the effect of electrode size, electrolyte selection, and polymeric passivation. The results were implemented in PCL-coated Mg/Fe full-cell batteries, which were characterized and compared with previous studies in the literature. The corrosion properties of electroplated Mg anodes in the select electrolytes were investigated by potentiodynamic polarization using a potentiostat (WaveDriver 10, Pine Instruments). A three-electrode-cell configuration was implemented with Mg sample, saturated silver/silver chloride (Ag/AgCl), and a platinum (Pt) mesh as the working, reference, and counter electrodes, respectively. Samples were immersed in the solution for five minutes to reach equilibrium prior to testing. Open circuit potentials (OCP) were recorded, and linear sweep voltammetry was conducted for a 1 V range centered about the measured OCP with a scan rate of 1 $mV \cdot s^{-1}$. Corrosion currents were determined from Tafel approximations and polarization resistance in accordance with ASTM G102-89 and corresponding corrosion rates were determined based on Faraday's law.[279] Electrical conductivity of the electrolyte was measured using a conductivity meter (Bench 700 Series, Oakton Instruments), and each sample was measured in triplicate.

The electrochemical performance of the Mg/Fe half-cells and PCL-coated Mg/Fe full-cells was characterized by performing galvanostatic discharge tests in a two-electrode-cell configuration at discharge rates of up to 400 μA cm^{-2} using a potentiostat (Model 263, EG&G Princeton Applied Research). The electrolyte solutions investigated were 0.1 M $MgCl_2$, 0.9 wt.% NaCl, and 1x PBS, and the electrolyte volume was 50 mL. The cut-off potential for the discharge tests was selected as 200 mV. From the discharge data, the specific capacity (C_s) and the power (Po) of the cells were calculated using Equation 1 and 2, where m, I, t, and E_{av} refer to the mass (g), discharge current (mA), discharge time (h), and average discharge potential (V) of the cells, respectively.

$$C_s = \frac{I \cdot t}{m} \tag{3.64}$$

$$Po = E_{av} \cdot I \tag{3.65}$$

Optical degradation studies were conducted in 1x PBS at 37˚C and agitated at 50 rpm using PCL-coated Mg/Fe full-cells without prior discharge. Media was exchanged to maintain a pH deviation of less than 0.5 of initial measurements at day 0.

3.3.7. Electrolyte Selection based on Electrode Corrosion

Magnesium corrodes naturally in aqueous solutions and serves as a sacrificial anode when galvanically coupled with more noble metals (e.g., Fe and Zn).[124], [275] Consumption of the Mg due to natural corrosion (i.e., parasitic corrosion) would reduce the amount of electrochemically active anode material available for battery discharge. Therefore, the assessment of the natural corrosion of the Mg anodes is essential for the battery design. As observed in Figure 121, the corrosion potentials of the Mg electrodes were -1.30 V, -1.35 V, and -1.55 V (vs. SHE) in 0.1 M $MgCl_2$, 0.9 wt.% NaCl, and 1x PBS, respectively. Fluctuations were observed in the anodic portions of the Mg polarization curves, and they were most pronounced in 0.1 M $MgCl_2$. Corresponding corrosion current, corrosion rate and polarization resistance are summarized in Table 28. Electroplated Mg electrodes demonstrated corrosion current densities of

53.8 µA·cm^{-2}, 102 µA·cm^{-2}, and 24.4 µA·cm^{-2} in 0.1 M $MgCl_2$, 0.9 wt.% NaCl, and 1x PBS, which corresponded to corrosion rates of 49 mil·yr^{-1}, 93 mil·yr^{-1}, and 22 mil·yr^{-1}, respectively. Polarization resistance was obtained from the linear region within 10 mV of the corrosion potential based on Stern-Geary equations, and corresponded to 1930 Ω·cm^{-2}, 666 Ω·cm^{-2}, and 1930 Ω·cm^{-2} in 0.1 M $MgCl_2$, 0.9 wt.% NaCl, and 1x PBS, respectively. Corrosion currents calculated from polarization resistance measurements and were in good agreement with Tafel approximations, confirming that the reactions are activation limited. The measured electrolyte conductivity was 0.905 mS·cm^{-1}, 7.40 mS·cm^{-1}, and 15.9 mS·cm^{-1} for 0.1 M $MgCl_2$, 0.9 wt.% NaCl, and 1x PBS, respectively, following the same increasing trend as the corrosion potentials.

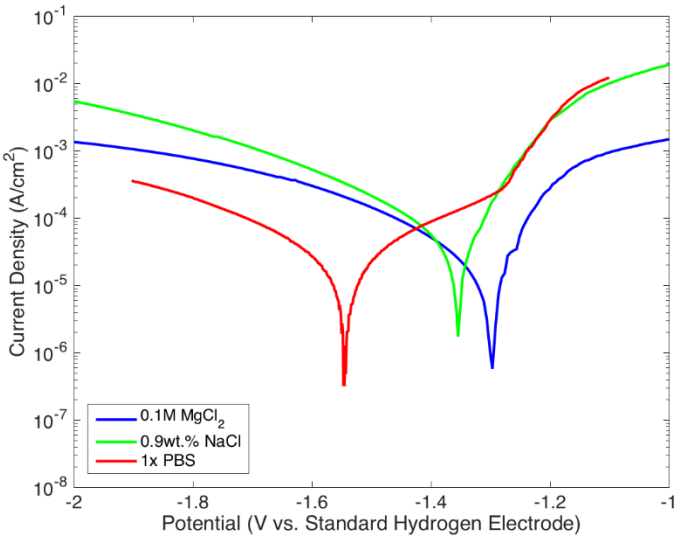

Figure 121 Corrosion behavior of electroplated Mg in physiological solutions. (A) Potentiodynamic sweeps of electroplated Mg in 0.1M $MgCl_2$, 0.9wt.% NaCl, and 1x PBS showing corresponding corrosion potentials. Tests were performed in 0.1M $MgCl_2$ using a potentiostat at a sweep rate of 1mV·s^{-1}.

Table 28 Comparison of Mg corrosion properties in physiological electrolytes. Conductivity values show the arithmetic mean of three measurements. Corrosion data was obtained from linear sweep voltammetry of electroplated Mg samples against a saturated Ag/AgCl reference electrode and Pt counter-electrode.

	0.1 M $MgCl_2$	**0.9 wt.% NaCl**	**1x PBS**
Electrolyte Conductivity (mS/cm)	0.905	7.40	15.9
Electrolyte pH	6.09	5.95	7.41
Corrosion Potential (V vs. SHE)	-1.3	-1.35	-1.55
Corrosion Current ($\mu A/cm^2$)	53.8	102	24.4
Corrosion Rate (mil/y)	49.2	93.1	22.3
Polarization Resistance (Ω/cm^2)	1926	666	1932

As observed in Figure 121, Mg exhibited the most noble corrosion potential in 0.1 M $MgCl_2$ and least noble in 1x PBS. The fluctuations observed in the anodic curves are indicative of the pitting corrosion characteristic of Mg.[90], [265] However, Mg demonstrated the highest corrosion rate in 0.9 wt.% NaCl, which was two-fold and four-fold greater than corrosion rates observed in 0.1 M $MgCl_2$ and 1x PBS, respectively. This behavior may be attributed to ionic composition of the electrolytes. It has been reported that the critical chloride concentration for Mg to undergo pitting corrosion is approximately 30 mM.[84] The chloride concentrations in the physiological electrolytes exceed the critical concentration and are 200 mM, 154 mM, and 140 mM for 0.1 M $MgCl_2$, 0.9 wt.% NaCl, and 1x PBS, respectively. Chloride ions react with the $Mg(OH)_2$ passive film on the Mg surface to form a more soluble product, $MgCl_2$. Dissolution of the $Mg(OH)_2$ film reduces the protected surface area and exposes a larger active Mg surface to the electrolyte.[273], [280] While this suggests that the highest Mg corrosion rate corresponds to the electrolyte with the highest chloride concentration, Mg interaction with the remaining electrolyte constituents should also be considered. Although 0.9 wt.% NaCl and 1x PBS exhibit similar concentrations of chloride ions compared to 0.1 M $MgCl_2$, the Mg corrosion rate in PBS was approximately four-fold less than what was observed in 0.9 wt% NaCl. The presence of phosphate ions may explain the reduced corrosion rate of Mg in 1x PBS. Phosphate ions react with Mg to form a poorly soluble $Mg_3(PO_4)_2$ product that passivates the Mg electrode surface.[128] It should be noted that a lower corrosion rate is not absolutely desired, as the discharge chemistry relies on the continuous formation and breakdown of passivation on the Mg.

Consequently, formation of a poorly soluble $Mg_3(PO_4)_2$ film may hinder the anodic reaction on the Mg surface. In contrast, the presence of magnesium ions in 0.1 M $MgCl_2$ may have hindered the dissolution of Mg into the electrolyte solution, as a 50% reduction in corrosion rate was observed with Mg in 0.1 M $MgCl_2$ compared to 0.9 wt.% NaCl. However, the measured electrical conductivity, which contributes to the total internal resistance of the electrochemical cell, was highest for 1x PBS and lowest for 0.1M $MgCl_2$, indicating a lower potential drop across the cell when the former electrolyte is utilized. This suggests that there exists a design tradeoff between solution conductivity and corrosion behavior in electrolyte selection.

3.3.8. Electrochemical Performance of Uncoated Mg Half-Cells

Figure 122a-d shows the discharge performance of Mg/Fe half-cells in 0.1 M $MgCl_2$. The effect of discharge current density and electrode size was investigated. The Mg electrodes exhibited stable discharge profiles at discharge rates greater than 80 $\mu A \cdot cm^{-2}$ (i.e., 15 µA in Figure 122a). The specific capacity and power of the Mg electrodes showed a parabolic relationship with discharge rate for 0 to 300 $\mu A \cdot cm^{-2}$ (Figure 122b). At the maximum performance, which corresponded to 45 µA (230 $\mu A \cdot cm^{-2}$), the Mg electrodes demonstrated a specific capacity of 770 mAh g^{-1}, an average power of 39 µW, and a Coulombic efficiency of 35%. Coulombic efficiency of the electrodes was calculated by dividing the mass of the discharged Mg electrode by the mass of the electroplated Mg. Figure 122c-d compares the specific capacity and power of the Mg electrodes for two different anode sizes (i.e., 5 mm and 10 mm diameter). While the parabolic trend was preserved with increasing anode size, the increase in specific capacity with the larger anodes did not scale with the four-fold increase in anode surface area. At 230 $\mu A \cdot cm^{-2}$, the larger anodes showed a 13% increase in specific capacity. However, increasing the anodic surface area supported higher average powers (Figure 122d) with a maximal power gain observed at 280 $\mu A \cdot cm^{-2}$, which corresponded to average powers of 36 µW and 108 µW for 5 mm and 10 mm diameter Mg anodes.

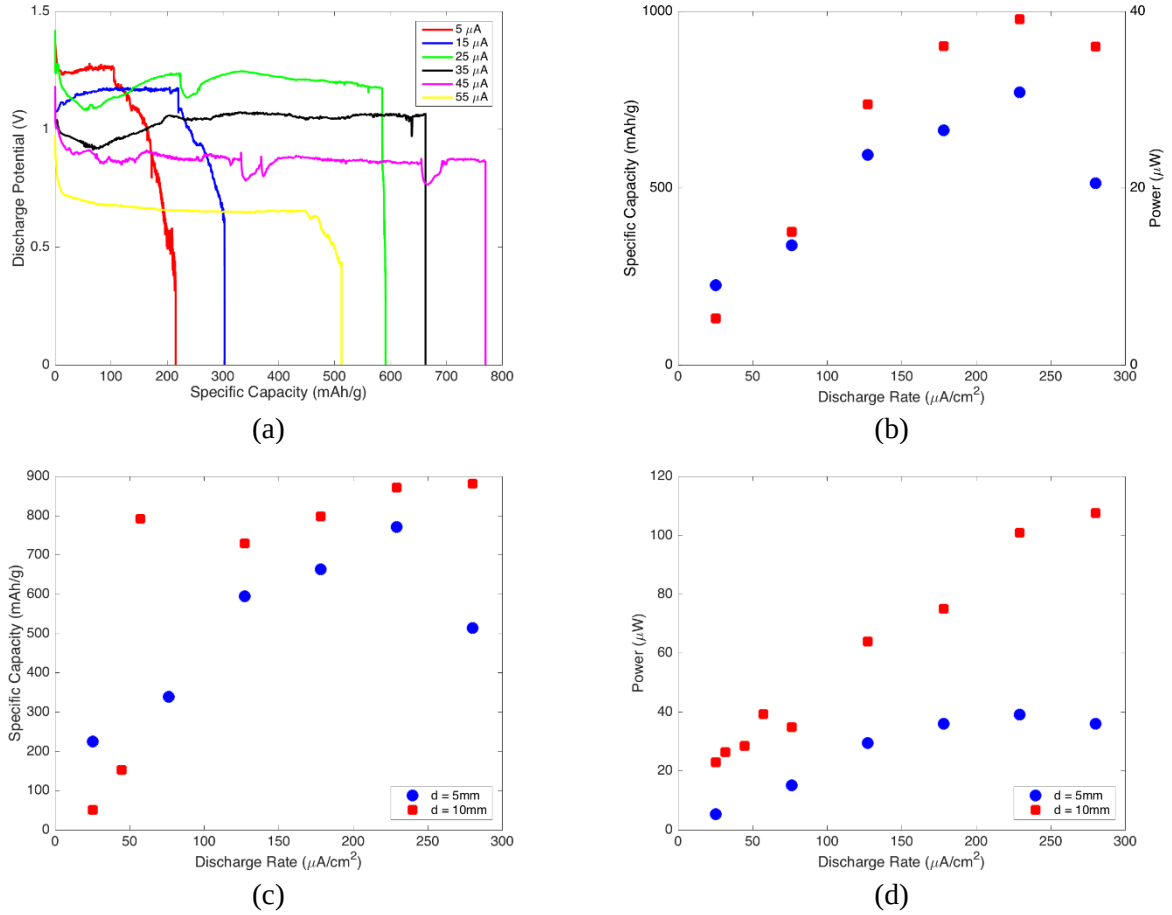

Figure 122 Performance of Mg/Fe half-cells under galvanostatic discharge in 0.1M $MgCl_2$. (a) Discharge profiles of Mg/Fe half-cells at various discharge currents in 0.1M $MgCl_2$. (b) Specific capacity and power with discharge rate for 5-mm-diameter electrodes and comparison of (c) specific capacity and (d) with anode size.

In contrast to conventional battery systems, where the specific capacity generally increases as the discharge rate is reduced, the Mg electrodes exhibited a parabolic relationship between their discharge rate and specific capacity. The reduced performance at lower discharge rates may be attributed to the pitting nature of Mg. A surface passive film comprising $Mg(OH)_2$ forms when Mg is immersed in an aqueous solution. Pitting corrosion occurs when the $Mg(OH)_2$ film is locally disrupted, exposing active Mg surface. As $Mg(OH)_2$ is formed as a reaction product of Mg corrosion, the surface passivation is continually broken down and reformed in pitting zones.[273] When current is drawn from the Mg-based batteries, the native passivation is disrupted to initiate the battery, as well as corrosion of the anodic material. However, at

sufficiently low currents, the rate of $Mg(OH)_2$ reformation is postulated to exceed the rate of film breakdown, resulting in premature termination of the battery. This was experimentally observed by discharging a terminated battery, which had previously been discharged at low current (i.e., 5 µA), at elevated current to rupture the reformed passive film and initiate a second interval of discharge (data not shown). In contrast, when high current is drawn from the Mg-based batteries, excessive breakdown of the surface film enhances surface corrosion of the Mg. It is speculated that the parabolic relationship observed between discharge rate and power is attributed to the increased charge transfer resistance and corresponding voltage decline presented by the accumulation and film formation of $Mg(OH)_2$ (Figure 122b). Further, reduced capacity and power have been observed in batteries under high discharge rates due to the limitations pertaining to ion transport, as well as kinetics.[265], [273]

The scalability in performance was investigated with Mg anodes of two sizes. Results indicated that the specific capacity scaled with increasing anodic material, preserving the parabolic trend observed with specific capacity at increasing discharge rates. However, the average discharge power did not scale with increasing anode size due to an observed voltage drop with larger Mg anodes at higher discharge rates. These findings regarding the scalability of various performance parameters suggested that surface-area-to-volume ratio may be a critical factor in Mg/Fe battery design.

3.3.9. Improved Performance with Thin PCL Coating

The effect of a protective thin film of PCL was investigated in the half-cell configuration (Figure 123). The PCL dip-coated cells demonstrated smooth discharge profiles, but less stable potentials during the tail end of the discharge lifetime. Comparing the discharge profile to uncoated electrodes, (Figure 123Figure 122b), PCL dip-coated half-cells discharged galvanostatically at 55 $\mu A \cdot cm^{-2}$ demonstrated approximately 400 $mAh \cdot g^{-1}$ increase in specific capacity with the additional polymeric coating (5 µm thick PCL). Figure 123Figure 122c further shows that PCL dip-coated Mg electrodes shifted the parabolic trend towards higher discharge rates and higher specific capacities (i.e., to the upper right of the graph) compared to uncoated Mg electrodes. As such, PCL dip-coated Mg electrodes showed lower specific capacity at 180

$\mu A \cdot cm^{-2}$ than uncoated cells, but a 70% increase at 280 $\mu A \cdot cm^{-2}$ and a maximal specific capacity of 930 $mAh \cdot g^{-1}$ at 330 $\mu A \cdot cm^{-2}$. Similarly, implementation of the PCL coating shifted the parabolic curve towards higher discharge rates (Figure 123Figure 122d). Specifically, a maximal average power of 41 µW and Coulombic efficiency of 42% were observed at 330 $\mu A \cdot cm^{-2}$.

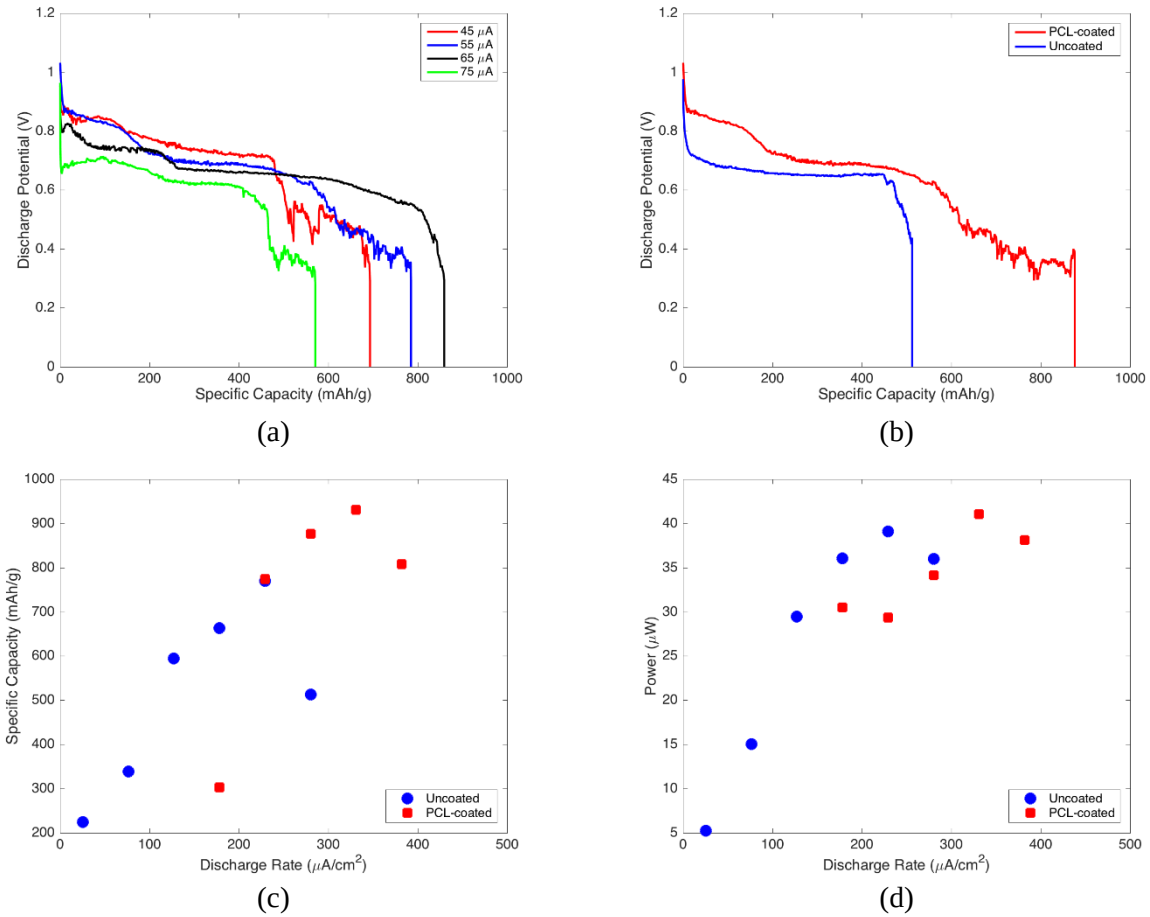

Figure 123 Performance of Mg/Fe half-cells under galvanostatic discharge with PCL coating. (a) Discharge profiles of Mg/Fe half-cells with PCL coating in 0.1M $MgCl_2$, (b) effect of PCL at 55 µA and comparison of PCL-coated and bare electrodes on (c) specific capacity and (d) power.

It was hypothesized that a thin protective coating of a biodegradable polymer (e.g., PCL) may enhance performance of Mg-based batteries by increasing the mechanical integrity of the surface $Mg(OH)_2$ film and, in this manner, enable discharge at higher current densities. This was experimentally confirmed with PCL dip-coated electrodes in the half-cell configuration. Although the PCL-coated electrodes supported smooth discharge profiles, the less stable behavior observed during the tail end of the

discharge lifetime may be due to steady accumulation of $Mg(OH)_2$, as the polymeric coating may hinder or slow down transport of discharge products from the anode surface. Comparing the parabolic trend in specific capacity and discharge rate supported the proposed hypothesis (Figure 123c). Implementation of the PCL coating shifted the parabolic trend towards higher discharge rates. This reflects the additional charge transfer resistance imposed by the PCL coating, wherein higher current densities were required to break through the PCL-enforced surface passivation. The thin PCL coating improved specific capacity and Coulombic efficiency of the Mg/Fe electrochemical cells without sacrificing performance with discharge power or potential. As PCL is an FDA-approved biodegradable polymer, these findings suggested that PCL coatings can be exploited for Mg-based biodegradable batteries.[102], [105], [116]

3.3.10. Design Trade-offs with Electrolyte Selection

Figure 124 shows the discharge performance of Mg/Fe half-cells in PBS. The discharge potential in 1x PBS was less stable and showed a linear decline throughout the lifetime of the battery than corresponding performance in 0.1 M $MgCl_2$ (Figure 124b). However, the average discharge potential and average power of the Mg electrodes discharged in 1x PBS approximated values obtained in 0.1 M $MgCl_2$. Figure 124b-c compares the performance of the Mg electrodes in 1x PBS and in 0.1 M $MgCl_2$. Representative profiles of galvanostatic discharge at 45 µA are shown in Figure 124b, where PBS demonstrated a higher average discharge potential and specific capacity than 0.1 M $MgCl_2$. As shown in Figure 124c, both electrolytes demonstrated a parabolic trend in specific capacity and average power with respect to discharge rate, with maximum performance centered at 230 $\mu A \cdot cm^{-2}$. However, for a given discharge rate, uncoated Mg electrodes demonstrated higher specific capacities in 1x PBS as compared to in 0.1 M $MgCl_2$. At 230 $\mu A \cdot cm^{-2}$, Mg electrodes in 1x PBS exhibited a specific capacity of 1110 $mAh \cdot g^{-1}$, 44% greater than in 0.1 M $MgCl_2$.

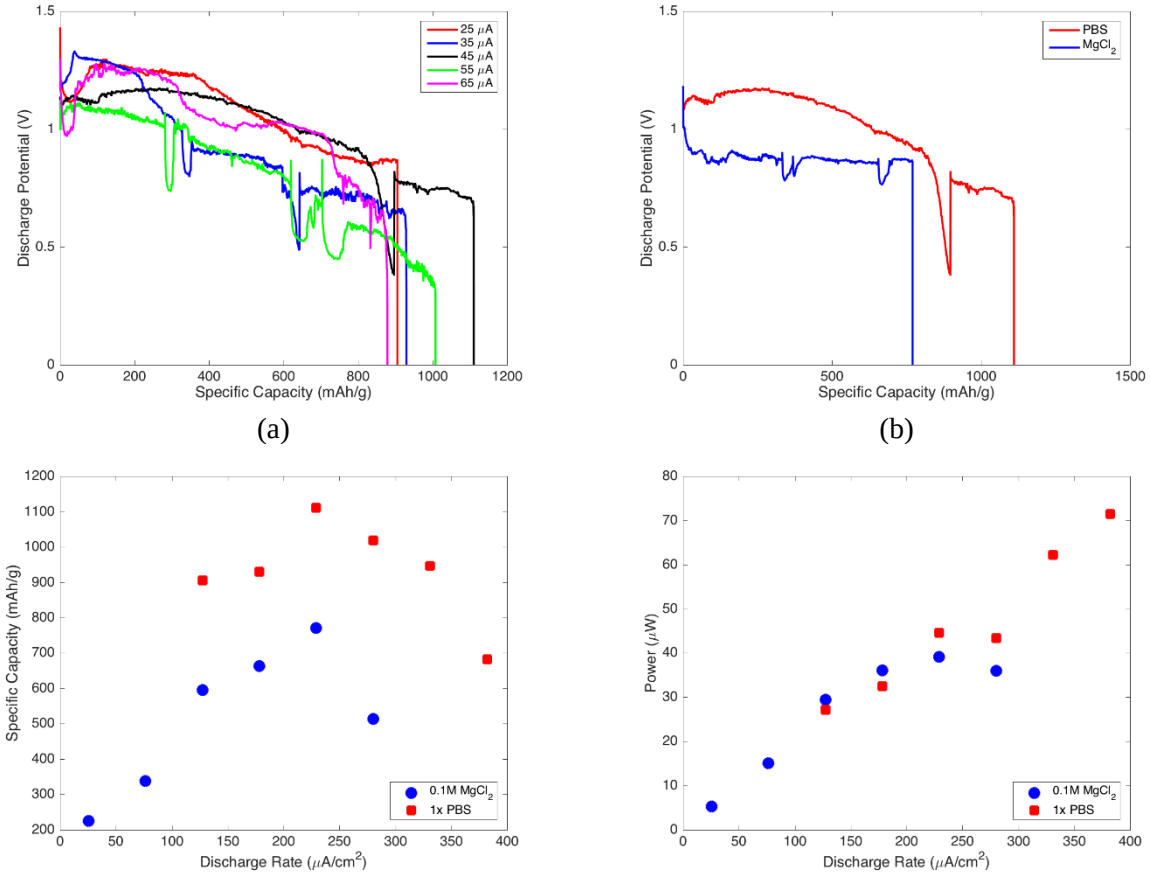

Figure 124 Performance of Mg/Fe half-cells under galvanostatic discharge in 1x PBS. (a) Discharge profiles of Mg/Fe half-cells at various discharge currents in in 1x PBS and comparison of PBS with 0.1M $MgCl_2$ (b) at 45 µA, (c) with specific capacity and (d) with power.

As discussed previously, the design of a biodegradable battery may comprise two general approaches in terms of the electrolyte utilization: (i) a specified biocompatible electrolyte contained within a biodegradable electrolyte cell, or (ii) the harnessing of human physiological fluid as the electrolyte. Whereas electrochemical testing in 0.1 M $MgCl_2$ supports the former approach, 1x PBS was used to investigate battery performance with physiological solution as the electrolyte. Figure 124b compares the discharge profile in 0.1 M $MgCl_2$ and 1x PBS, where the discharge potential decreased linearly with discharge in PBS. This phenomenon may be attributed to the presence of phosphate ions in PBS, which

serves as a pH buffering agent, but also reacts with the Mg anode to form a $Mg_3(PO_4)_2$ passivation layer. The passivation presents additional mass transfer resistance on the anode surface. However, the average discharge potential and average power were comparable between 0.1 M $MgCl_2$ and 1x PBS. In fact, Figure 124c indicated that PBS supports higher specific capacities. Consequently, whereas 0.1 M $MgCl_2$ supports more stable discharge potentials, 1x PBS promoted higher specific capacities and lifetime of the Mg/Fe half-cells. Figure 124d shows the average powers obtained in 1x PBS and 0.1 M $MgCl_2$, which were comparable for a given discharge rate.

It is speculated that the buffering capacity of PBS promoted the lifetime and specific capacity of Mg-based battery chemistries because Mg is resistant to breakdown in alkaline environments. Studies have reported the accumulation of a thick white film of precipitated $Mg(OH)_2$ when the pH exceeds 9. Magnesium becomes resistant to corrosion when the pH exceeds 10.5, as this corresponds to the pH of saturated $Mg(OH)_2$.[275], [281] Given that $Mg(OH)_2$ is a product formed from the oxidation of Mg and its accumulation increases the local pH, this suggested that the performance of Mg-based batteries may deteriorate or terminate once the electrolyte pH exceeds a critical value indicative of excessive $Mg(OH)_2$ accumulation. Consequently, the buffering system observed in PBS and physiologically in the body may support enhanced battery performance by stabilizing the electrolyte pH as Mg breaks down due to both battery discharge and parasitic corrosion. The buffering capacity of the 1x PBS was experimentally confirmed. It was hypothesized that higher discharge potentials would be attained in 1x PBS due to its higher electrical conductivity. As shown in Table 2, the conductivity of 1x PBS was two orders of magnitude greater than that of 0.1M $MgCl_2$, thus reducing solution resistance. However, the average power attained in 1x PBS approximated that in 0.1 M $MgCl_2$, as the Mg/Fe half-cells demonstrated similar discharge potentials in both electrolytes. Further, the average power significantly increased at higher current densities (i.e., $>330 \mu A \cdot cm^{-2}$) due to disintegration of the Mg anode at the electrolyte-air interface. This was another indication, as confirmed by corrosion testing (Figure 121), that Mg is more corrosive in PBS.

3.3.11. Electrochemical Performance of PCL-Encapsulated Mg/Fe Batteries

Fully assembled, PCL dip-coated Mg/Fe batteries were discharged in 0.1 M $MgCl_2$, 0.9 wt.% NaCl, and 1x PBS (Figure 125a). The batteries were discharged galvanostatically at 45 µA in 50 mL of electrolyte. The discharge profiles were less stable in 0.1 M $MgCl_2$ and 0.9 wt.% NaCl than in 1x PBS. The electrochemical performance of the batteries is summarized in Table 2. The discharge lifetimes were reported to be 49 h, 90 h, and 99 h in 0.1 M $MgCl_2$, 0.9 wt.% NaCl, and 1x PBS, respectively. The average discharge potential in 1x PBS was 200 mV and 300 mV greater than in 0.1 M $MgCl_2$ and 0.9 wt.% NaCl, respectively. Further, 0.9 wt.% NaCl and 1x PBS demonstrated similar performance in specific capacity and Coulombic efficiency, but more than a two-fold increase compared to 0.1 M $MgCl_2$. The presented PCL dip-coated batteries achieved energies of 3.7 J, 6.2 J, and 11 J in 0.1M $MgCl_2$, 0.9wt.% NaCl, and 1x PBS, respectively. Optical images of the PCL dip-coated batteries before and after discharge demonstrate the breakdown of the battery from discharge and natural corrosion (Figure 125c-d). The remainder of the Mg anode after discharge is covered with a white MgO film and the PCL coating is ruptured.

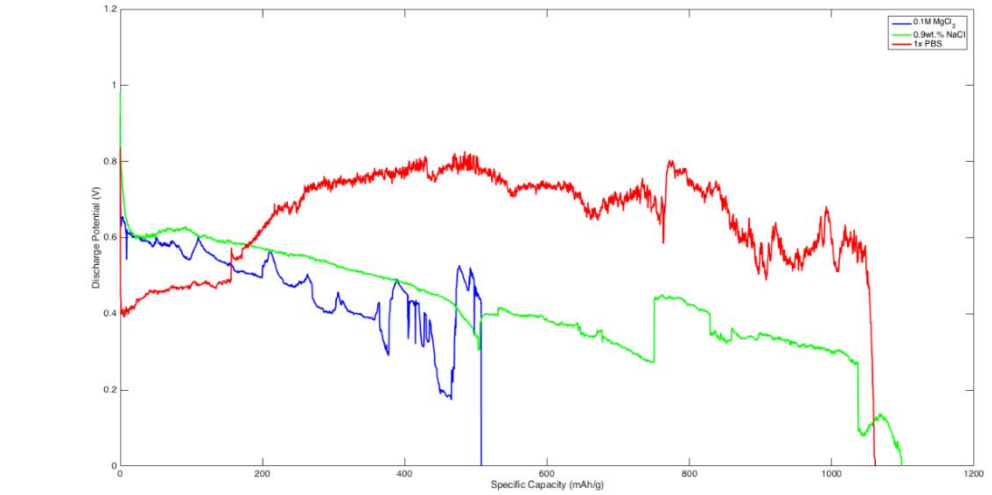

(a)

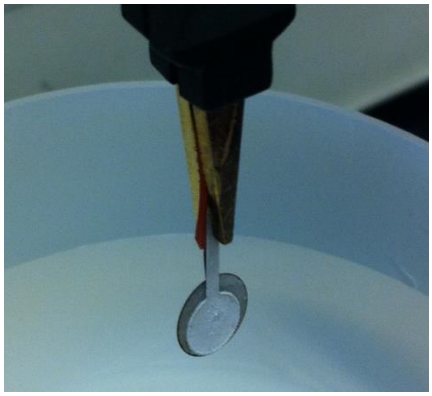

(b)

(c)

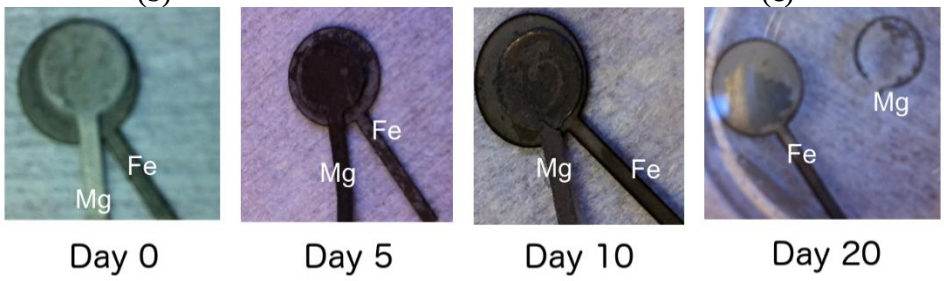

(d)

Figure 125 Evaluation of PCL dip-coated Mg/Fe batteries. (A) Discharge profiles of PCL dip-coated batteries under galvanostatic discharge at 45µA in 0.1M $MgCl_2$, 0.9wt.% NaCl, and 1x PBS. Optical images of assembled PCL dip-coated Mg/Fe battery (B) before and (C) after discharge at 45µA. (D) Degradation tests were performed in 1x PBS at 37°C and samples were not discharged prior to testing to demonstrate the complete dissolution of the biodegradable battery within physiological solution. The near complete dissolution of the Mg anode is observed by day 20.

Table 29 Discharge performance of PCL dip-coated Mg/Fe batteries in physiological electrolyte solutions.

	0.1 M $MgCl_2$	**0.9 wt.% NaCl**	**1x PBS**
Discharge Time (h)	49	90	99
Average Discharge Potential (V)	0.5	0.4	0.7
Specific Capacity (mAh/g)	509	1100	1060
Energy (J)	3.7	6.2	11
Power (μW)	21	19	29
Coulombic Efficiency (%)	23	50	48
Change in Electrolyte pH	2.11	3.05	0.41

A separate study of the degradation of the assembled, PCL dip-coated Mg/Fe batteries is shown in Figure 125d. The study examined the degradation of the battery assembly in 1x PBS stored at 37 ºC and agitated at 50 rpm, in order to mimic the body conditions and to assess the lifetime of the implanted battery components. The detachment from the assembly and nearly complete dissolution of the Mg anode was observed by day 20. As the degradation rate of Fe is well-documented in the literature and occurs on the order of months to years, the time scale of the *in vitro* test did not capture the complete cathode degradation.[99]

Figure 125 demonstrates the superior performance of PCL-coated Mg/Fe batteries in PBS, which sustained a higher and more stable discharge potential than batteries discharged in 0.1 M $MgCl_2$ and 0.9 wt.% NaCl. Interestingly, a linear reduction in discharge potential was shown with PCL-coated batteries in the 0.1 M $MgCl_2$ and 0.9 wt.% NaCl, which was not observed in corresponding half-cell experiments with uncoated electrodes. In addition, PCL-coated batteries in PBS achieved the longest discharge lifetime and the highest energy, average power, and Coulombic efficiency. These results suggested that the application of the PCL coating in the full-cell configuration, which imposes additional mass transfer resistance attributed to the transport of $Mg(OH)_2$, favored PBS as the electrolyte. As mentioned previously, accumulation of the $Mg(OH)_2$ discharge product is mass transfer- and pH-dependent. Due to the additional mass transfer resistance of the PCL-coated full-cells, the pH buffer system provided by PBS promoted its superior performance as the battery electrolyte. This was experimentally confirmed by the measurements

of electrolyte pH prior and after battery discharge (Table 29). As shown, the pH deviated by less than 0.5 throughout the discharge lifetime of the PCL-coated battery in PBS, whereas the changes in electrolyte pH for batteries discharged in 0.1 M $MgCl_2$ and 0.9 wt.% NaCl were over five- and seven-fold higher, respectively. It is speculated that the buffering capacity of PBS hindered the precipitation of $Mg(OH)_2$, whereas its accumulation during discharge of the PCL-coated full-cells in 0.1 M $MgCl_2$ and 0.9 wt.% NaCl may have gradually increased charge transfer resistance, accounting for the linear decline in discharge potential.

The discharge performance of the PCL-coated batteries demonstrated promising results of biodegradable batteries for powering TIMDs. As discussed earlier, the range in power required for commercial permanent devices are from 10-1000 μW.[282] The power achieved with the PCL-coated batteries satisfies the lower range in IMD power requirements. Specifically, PCL-coated Mg/Fe batteries discharged in PBS achieved an average discharge power and lifetime of approximately 30 μW and 100 h, respectively. This suggested that the battery may provide onboard powering of a low-power neurostimulators for over 4 days.[282] Alternatively, the PCL-coated Mg/Fe batteries may power flow rate sensing systems featuring ULP circuitry for up to 6 days.[270]

3.3.12. Comparison of Biodegradable Batteries to State-of-the-Art

The PCL-coated batteries demonstrated improved performance and increased compactness than previously reported biodegradable batteries. Figure 126 compares the energy density and volume of state-of-the-art biodegradable batteries and two commercial lithium-ion (Li-ion) batteries used for medical devices. The fully packaged PCL-coated batteries presented in this study featured a footprint of 0.2 cm^2 and a total volume of less than 0.02 cm^3. This corresponded to an over 75 times reduction in volume than the Mg/Mo biodegradable battery packaged in polyanhydride (Mg/Mo/PAH) reported by Yin *et al.* in the single cell configuration (i.e., 3.9 cm^2 and ≈4 mm electrode spacing). Further, the energy density achieved with PCL-coated Mg/Fe batteries in PBS (694 $Wh \cdot kg^{-1}$) was two orders of magnitude larger than that of the Mg/Mo/PAH battery (4-cell series connection) [81]. The reported battery also featured smaller volume

and increased energy density compared to the edible sodium-ion electrochemical cells reported by Kim *et al.*, which featured activated carbon and manganese dioxide electrodes (AC/MnO2) on a conductive polymer film (i.e., silver nanowires dispersed in polyglycerol sebacate).[86] Although Kim *et al.* subsequently presented a melanin-based (Mel/MnO2) sodium ion cell, which demonstrated improved performance with an energy density of 16.6 Wh·kg-1, results did not feature full-cell design and packaging [87]. Comparing against commercial primary Li-ion batteries, the reported PCL-coated Mg/Fe batteries exhibited greater compactness by harnessing physiological solution as the electrolyte and a low-density element as the sacrificial anode material. The PCL-coated battery also featured a higher energy density than the lithium-manganese dioxide (Li-MDX) and lithium-carbon monofluoride (Li-CFx) batteries, which demonstrated 149 Wh·kg-1 and 200 Wh·kg-1, respectively [283], [284].

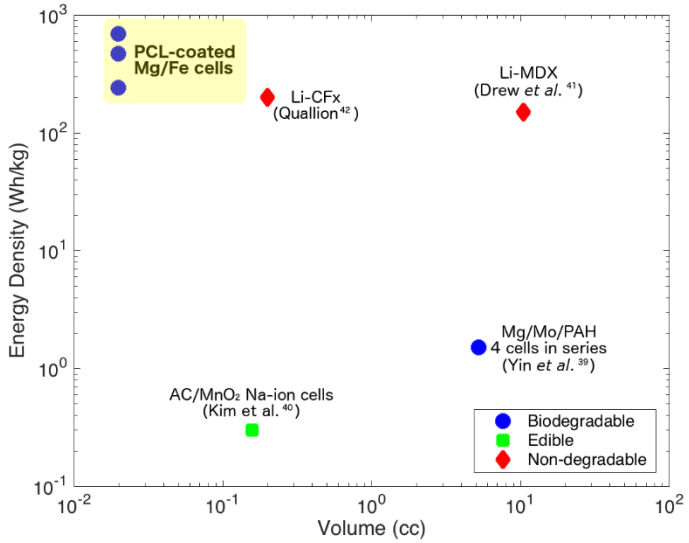

Figure 126 Energy density vs. volume of reported biodegradable and edible energy sources. To evaluate the design constraints of battery performance and compactness, energy density and volume of biodegradable and edible energy sources are compared against commercial primary batteries (i.e., Li-CFx and Li-MDX). (denotes data without packaging).*

In addition, the reported PCL-coated Mg/Fe batteries maintained stable discharge performance at higher discharge rates and longer discharge times than previously reported biodegradable batteries. Yin *et al.* implemented a series of 4 cells in order to obtain an average potential of 1.6 V for a discharge lifetime

of 6 h [81]. Here, the PCL-coated batteries achieved an average potential of 0.7 V in the single cell configuration, and the microfabrication process (Figure 117) supports batch scale production and modifications for series configuration. The PCL-coated batteries further demonstrated an over 16-fold improvement in battery lifetime. Through the implementation of a thin PCL-coating dually as packaging and for passivation-enhancement, the reported PCL-coated Mg/Fe cells supported higher discharge rates than alternative galvanic-based biodegradable batteries. Yin *et al.* observed a limiting current density of 100 $\mu A \cdot cm^{-2}$ in the Mg/Mo/PAH galvanic cell, above which the discharge potential significantly deteriorates. Consequently, the multi-cell Mg/Mo battery featured an electrode area of 10.5 cm^2 to attain an output current of 700 µA, corresponding to a current density of 66.7 $\mu A \cdot cm^{-2}$ [81]. In the present study, stable battery discharge was achieved at up to 400 $\mu A \cdot cm^{-2}$. This facilitated miniaturization of the biodegradable battery over previous demonstrations while improving performance. The PCL-coated batteries achieved a Coulombic efficiency of 50% and energy efficiency of 22.5%. More broadly, the trajectory of improvement demonstrated by these results suggested that biodegradable batteries present a viable strategy for achieving self-powered TIMDs at clinically relevant time scales and device power schemes.

This study presented an extensive characterization of Mg/Fe couples for use as galvanic energy sources and demonstrated the enhanced performance of biodegradable PCL-coated Mg/Fe batteries. Specifically, the systematic investigation of discharge rate, electrolyte selection and electrode size on discharge performance establishes a foundation for future work in this area and will support the development of an equivalent circuit model of Mg/Fe-based energy sources. Results indicated that the use of physiological fluid as the electrolyte, where PBS served as an *in vitro* surrogate, may enhance battery performance over alternative electrolytes due to its pH buffering abilities. It was further observed that the surface passivation of $Mg(OH)_2$ on the Mg anode largely governs battery performance, where enhancing the mechanical integrity of the passivation with a thin polymeric coating supported higher discharge rates and specific capacities. Further, the maximum lifetime achieved with the current geometry, where the entire

surface of the Mg is exposed at all times, presents a lower limit in the design of future, candle-inspired batteries because the primary motivation behind the candle design is controlling and extending the discharge lifetime of galvanic energy sources. The PCL-coated Mg/Fe biodegradable batteries exhibited improved performance compared to previous works on biodegradable batteries through the use of physiological fluid as the electrolyte and thin PCL coatings for packaging. This design ultimately reduced the battery mass, extended discharge lifetime and supported higher discharge rates. The PCL-coated batteries sustained an average power of approximately 30 μW for 100 h, which is sufficient for powering a commercial pacemaker for up to four days. Further, the battery design satisfies the design constraint of compactness, occupying less than 0.02 cm^3 in volume. The promising discharge performance and verified biodegradation of the PCL-coated Mg/Fe batteries support their consideration as potential energy sources for powering transient implantable medical devices.

3.3.13. Candle-Inspired Mg/Fe Battery Featuring Barrier Film Technology

This section examines the effect of barrier passivation and a candle-based geometry for improving the performance of biodegradable Mg/Fe batteries. As a proof-of-concept, the study focuses on Mg half cells to isolate the effect of passivation and anode design on electrochemical performance, especially since the microfabrication and assembly of a full electrochemical cell has already been demonstrated in previous sections. The objective of this study was to improve the electrochemical performance of biodegradable Mg/Fe batteries, whose operating principle is galvanic corrosion of the anode and hydrogen reduction of the cathode. The approach undertaken was to improve the anode design. The Mg anode would feature a compact cross section (i.e., narrow and thin) so that the length of the anode would be at least 1-2 orders of magnitude larger than its cross-sectional dimensions. Thin film barrier passivation would coat all surfaces of the anode exposed to the electrolyte except for an opening at one end of the anode. In this manner, the anode resembles that of a candle; since only a small cross-section of Mg at one end of the anode would be exposed to the electrolyte, discharge of the battery would proceed along the length of the anode.

Two stages of experiments were conducted to evaluate this design based on the two underlying hypotheses motivating the design. First, it was hypothesized that the performance of biodegradable Mg batteries improves as the discharge current density exceeds the corrosion current density of Mg in the given electrolyte. Second, it was hypothesized that barrier thin films will improve the Coulombic efficiency of Mg-based batteries. The first hypothesis was assessed by characterizing the discharge performance of bare Mg half cells, as shown in Figure 127. Tests were conducted in simulated body fluid at 37°C. For a fixed anode size, the data showed that increasing the discharge current density corresponded to higher specific capacity and a parabolic effect in power. The latter is due to the lower discharge voltage observed at higher current densities, consistent with data shown in previous sections. The range of current density examined was expanded to 2 orders of magnitude to capture the electrochemical performance at current densities both above and below the corrosion current density. For reference, the corrosion current density of bare Mg in 37°C SBF was obtained by LSV and was 1867 μA/cm^2, as shown in Figure 128 and summarized in Table 30.

Interestingly, even though the specific capacity exhibited a parabolic behavior at low discharge rates (i.e., below 1000 μA/cm^2), the specific capacity of Mg half cells sharply increased thereafter as the discharge rate approached the corrosion current density; the maximum specific capacity at discharge rates below 1000 μA/cm^2 was 0.2 mAh/g, whereas the specific capacity was 1.25 mAh/g when the discharge rate equaled the corrosion current density. The increase in specific capacity hastened as the discharge rate exceeded the corrosion current density, but increased nonetheless. At the highest discharge rate examined, which was approximately 3 times that of the corrosion current density, the observed specific capacity was 1.55 mAh/g. Further, the relationship between power and discharge rate was parabolic with the inflection point centered near the corrosion current density. This corresponded to a maximum power of approximately 2.25 mW. The electrochemical performance of bare Mg half cells examined across the large span of discharge rates supported the first hypothesis. Specifically, the data suggests that the performance of Mg-based biodegradable batteries improves as the discharge rate exceeds the corrosion current density.

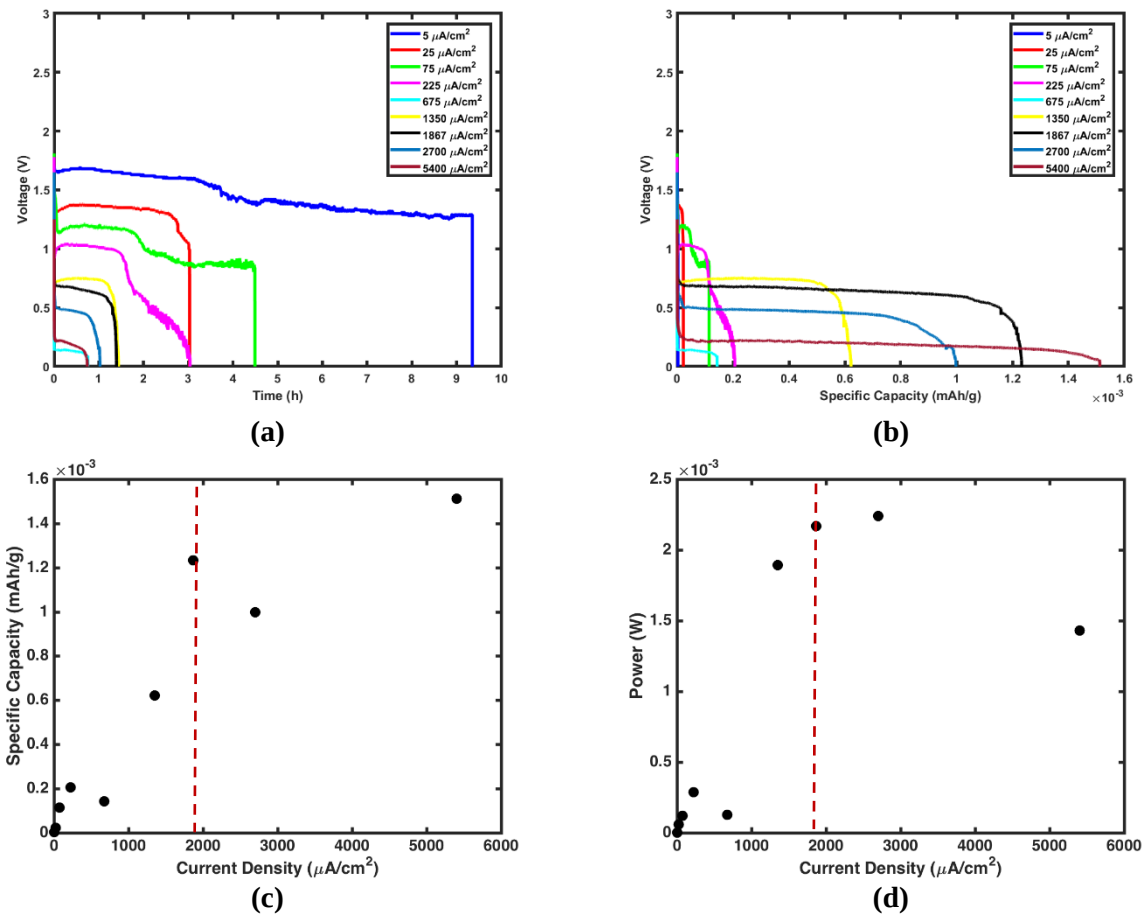

*Figure 127 Half-cell discharge results of bare Mg performed in SBF at 37°C. The dotted line in **(c-d)** indicates the corrosion current density of bare Mg, as determined by LSV.*

Recall that the second hypothesis supporting the candle design of Mg anodes is that barrier coatings will improve Coulombic efficiency. Of the various passivation schemes explored in the previous chapter, barrier thin films (e.g., ALD-deposited coatings) was identified as the optimal passivation for candle designs due to its ultralow water transport rate, conformal coating of samples and desirable mechanical properties. Specifically, it was speculated that the stress of the corrosion reaction would damage the nanoscale thick and mechanically brittle ceramic coating. In this manner, the coating would continuously break off as the candle-design anode was consumed and overcome the mass transfer limitations previously observed with PGS encapsulation. To confirm that the WTR of ALD-deposited alumina does reduce the

corrosion rate of Mg, linear sweep voltammetry was performed with Mg samples coated with 40-nm-thick alumina. As expected, ALD-passivated Mg exhibited a more noble corrosion potential and reduced the corrosion current density by more than 2 orders of magnitude compared to bare Mg. The corrosion current density of ALD-passivated Mg was 12.3 µA/cm^2, which corresponded to a corrosion rate of 0.77 µm/day. (For reference, the corrosion rate of ALD-passivated Mg is higher than suggested by previous water permeation studies because the measurements were performed without additional polymeric coating, which protects the mechanical integrity of the barrier coating, and SBF was used as the electrolyte instead of water.)

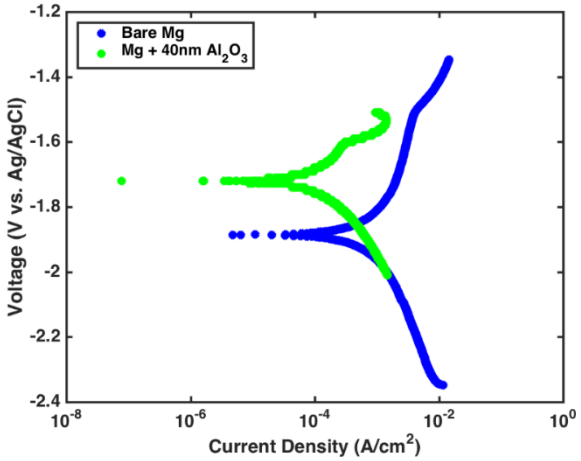

Figure 128 Potentiodynamic polarization curves obtained by linear sweep voltammetry of Mg samples (i.e., bare and coated with ALD-deposited alumina). Characterization was performed in SBF at 37°C.

Table 30 Summary of LSV results with and without barrier thin film passivation on Mg.

Sample	E_{corr} (V vs. Ag/AgCl)	i_{corr} (µA/cm^2)	C.R. (µm/day)
Uncoated Mg	-1.89	1867	9130
Mg + 40 nm Al_2O_3	-1.72	12.3	0.77

The second hypothesis can be represented by an equivalent circuit model, as shown in Figure 129a. The circuit shows two pathways for electrolyte ingress and, hence, discharge or corrosion: permeation through the ALD passivation or reaction at the propagating front (i.e., the open end) of the Mg candle. A Randles circuit and Warburg circuit connected in parallel represent direct electrolyte access to the Mg anode and electrolyte permeation through the passivation scheme, respectively. A Randles circuit comprises of only a charge transfer resistance and double layer capacitance connected in parallel, which correspond to an electrode-electrolyte interface. It should be noted that direct electrolyte access can occur through a user-defined opening or through pinholes in the barrier film, however. A Warburg circuit comprises a Randles circuit with a second Randles circuit serially connected to the resistor of the first. The capacitor and resistor of the first (i.e., outer) Randles circuit denote the membrane capacitance and pore resistance of the passivation, whereas the passive components of the inner circuit again correspond to the charge transfer resistance and double layer capacitance.

If the second hypothesis is true, the EIS spectra should also support the described equivalent circuit. Specifically, the impedance of the coated pathway should exceed that of the exposed Mg. The calculated and modeled parameters (based on experimental EIS data) are summarized in Table 31. The modeled parameters were calculated assuming the double layer capacitance is approximately 20-60 $\mu F/cm^2$ and the electrical properties of ALD-deposited alumina resembles that of the bulk material. Bode plots (shown in Figure 129b) exhibited excellent correspondence in the impedance magnitude between the experimental data and circuit fit. The phase exhibited better correspondence at low frequencies (i.e., >100 Hz), but the overall goodness of fit supported the equivalent circuit as an acceptable first order representation of the ALD-passivated candle design. Further, the fitted parameters (e.g., double layer capacitance, membrane resistance, membrane capacitance and solution resistance) were within range of calculated values. It should be noted that fitted values that approximated that of calculated values within 1 order of magnitude was considered acceptable because calculated values were based on literature and bulk material properties. The charge transfer resistance of bare versus ALD-passivated Mg, however, was unexpected. The charge

transfer resistance of bare Mg was orders of magnitude higher than that of ALD-passivated Mg, suggesting that once electrolyte permeated the ALD coating, charge transfer at the Mg-electrolyte interface was more facile. Initial modeling suggested that electrolyte access and reaction with ALD-passivated Mg does proceed along two pathways. The minor deviations in the experimental data might suggest additional passives in the circuit that would manifest at higher frequencies in the EIS spectra, such as inductive elements associated with pitting corrosion.

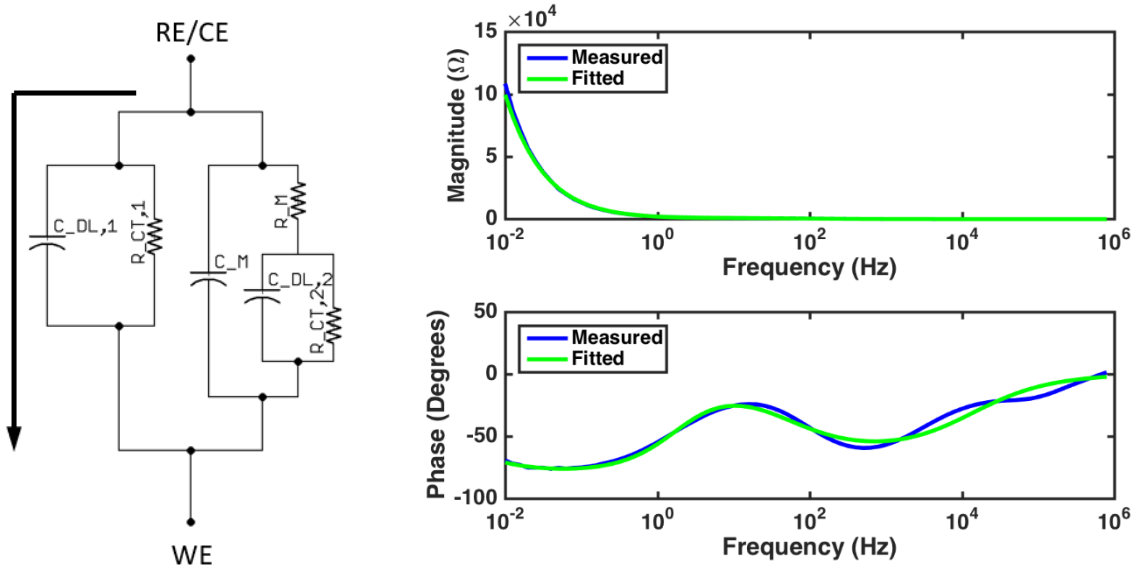

(a) **(b)**

Figure 129 ***(a)*** *The equivalent circuit model and* ***(b)*** *the impedance spectra obtained by experimental results (with EIS) and circuit model fitting for ALD-coated Mg in a candle geometry.*

Table 31 Comparison of experimental EIS and equivalent circuit fitting results for ALD-coated Mg candle designs.

Parameter	Physical Meaning	Calculated	Fitted
Rs	Solution resistance	10-50 Ω	15 Ω
Rct, 1	Charge transfer resistance of exposed Mg	n/a	850 kΩ
Rm	Membrane resistance of coating	2-200 MΩ	6.8 MΩ
Rct, 2	Charge transfer resistance of ALD-coated Mg	n/a	1 kΩ
Cdl, 1	Double layer capacitance of exposed Mg	30-100 nF	2.1 nF
Cm	Membrane capacitance of coating	0.4 μF	16 μF
Cdl, 2	Double layer capacitance of ALD-coated Mg	35-110 μF	97 μF

Half-cell studies with ALD-passivated Mg were conducted to complete the evaluation of the second hypothesis. The results, shown in Figure 130, show an extended discharge time compared to bare Mg. For example, the discharge times of bare and ALD-passivated Mg discharged at 225 $\mu A/cm^2$ were 3 hours and 125 hours, respectively. This suggests that the surface area exposed to electrochemical reactions (i.e., for discharge or parasitic corrosion) was drastically reduced with ALD passivation. Capacity is shown rather than specific capacity because reaction products and residual SBF remained inside the ALD coating; the fragility of the structure rendered it difficult to rinse. The Coulombic capacity monotonically and sharply increased as the discharge rate exceeded that of the corrosion current density. It was visually observed, however, that less than 20% of the Mg had been consumed at the end of discharge, which occurred due to loss of electrical contact due to corrosion at the electrolyte-air interface. The power was linear with respect to discharge rate and, as expected, was significantly lower than that of bare Mg because the sizably smaller exposed Mg area corresponded to a significantly lower discharge current.

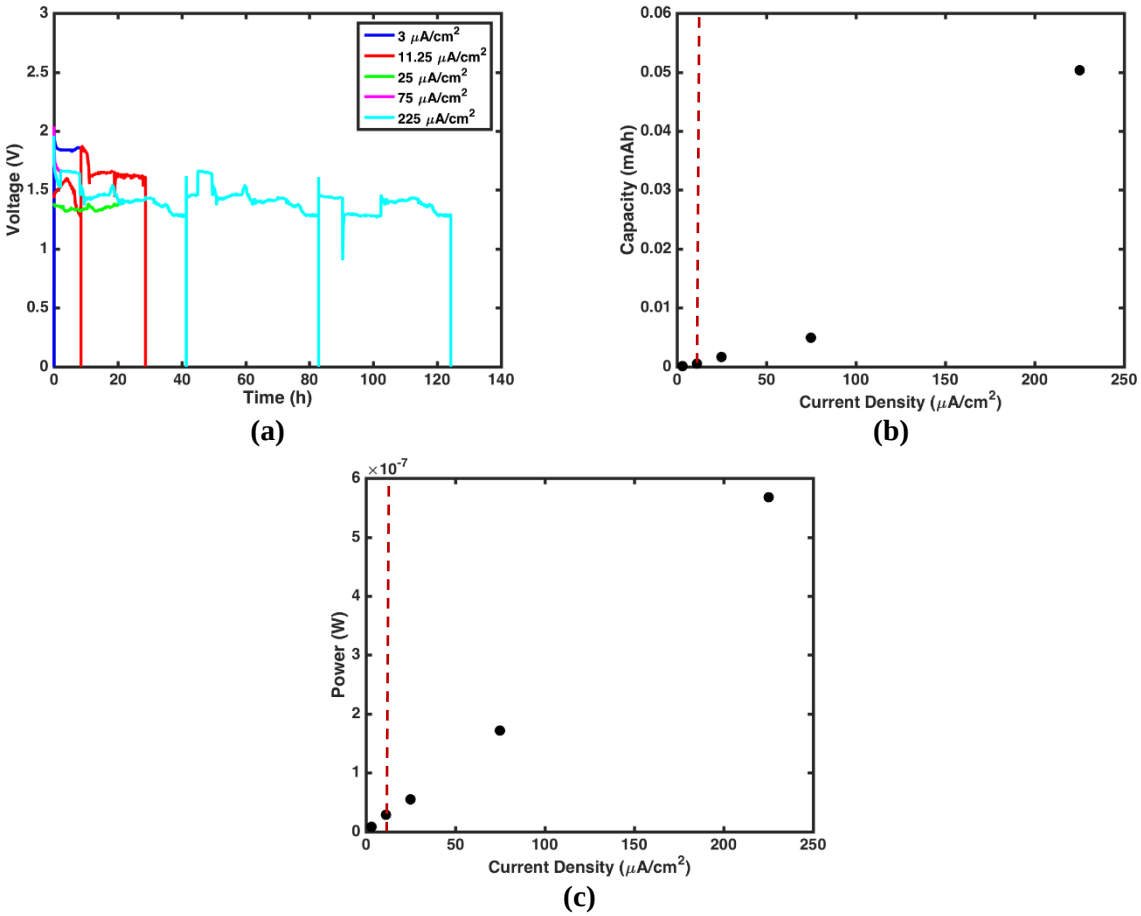

Figure 130 Half-cell discharge profiles of Mg candles conducted in SBF at 37°C.

The results confirmed that ALD passivation indeed improves the electrochemical performance of Mg candle-based anodes, but the reality of pinhole formation and fragility of the structure requires additional design improvements in order to fully harness the performance advantages of Mg candle-based biodegradable batteries. Future work should integrate the Mg candle-based anode into a full electrochemical cell and battery, such as with the configurations shown in earlier sections or with a supersaturated solid NaCl-PCL electrolyte [285].

3.4. Summary of MEMS-Based Strain Sensors and Energy Sources

This chapter demonstrated MEMS-based strain sensors and energy sources in biodegradable and degradable forms. Non-degradable strain sensors were developed to better understand the intended biomedical application—bone healing, as well as to provide a standard of comparison for biodegradable sensors. In turn, biodegradable strain sensors were demonstrated through implementation and integration of the biodegradable materials previously developed and characterized in Chapter 2. Given the non-permanence of even a non-degradable device, the endeavor was to demonstrate comparable device performance and achieve a functional lifetime of no more than 1 order of magnitude less than that of a corresponding non-degradable device under the same testing conditions. Biodegradable strain sensors comprising electroplated Mg and passivation schemes featuring PP Zn and multi-layer barriers successfully achieved the experimental objective. The utility of electroplated Mg was further demonstrated in various incarnations of biodegradable batteries and electrochemical cells. Ultimately, PCL-coated Mg/Fe cells achieved an energy density comparable to commercial lithium-based batteries use in medical devices while retaining a compact footprint. The results of this chapter highlight the successful demonstration of MEMS-based biodegradable strain sensors and energy sources towards bone healing applications.

CHAPTER 4

ASSESSMENT OF DEVICES AND MATERIALS FOR IMPLANTABLE USE

This chapter aims to bridge the gap between the bench top demonstrations of non-degradable and biodegradable MEMS devices (as elaborated in Chapter 3) and the proposed biomedical applications. Animal deployment and cytotoxicity studies were respectively performed to further the demonstrations of the corresponding technology for use in clinical and/or fundamental science arenas. As the fabrication, integration and application of biodegradable materials in MEMS technology remain in the incipient stages of a developing field, assessment of the biodegradable strain sensors introduced in Chapter 3 were conducted by evaluating cytotoxicity in accordance with international and FDA-recommended standard. Non-degradable strain sensors were, in turn, deployed in a rodent model of femoral segmental bone defect to demonstrate proof-of-concept functionality *in vivo*. The system integration and animal deployment demonstrated in this chapter were made possible through an interdisciplinary collaboration with Dr. Robert Guldberg's Musculoskeletal Research Laboratory at Georgia Institute of Technology and Dr. Mark Allen's MicroSensors and MicroActuators Research Group at the University of Pennsylvania. Specifically, the author would like to acknowledge the graduate students involved in this collaboration: Brett Klosterhoff, Didi She and Lin Du. Longer-term animal investigations are beyond the scope of this work, as this entails further developments in circuitry and pertain to the larger scope of the collaboration. The following section details the wireless telemetry, end-to-end testing and, ultimately, device deployment *in vivo*. The cytotoxicity of biodegradable analogues is subsequently discussed.

4.1. In vivo *Deployment of Non-Degradable Strain Sensing System*

4.1.1 Telemetry for Wireless Communication *In vivo*

System integration with wireless telemetry was integral to the successful *in vivo* deployment of implantable sensors. The use of transcutaneous wires to power and communicate with implantable sensors would limit the mobility of animal subjects, as well as increase the risk of infection and wire damage (inflicted by the animal). The development of wireless telemetry, as well as device implantation in animal, was accomplished through an interdisciplinary collaboration between two labs, as well as collaboration amongst several members of each lab. Briefly, wireless transmission was achieved with a baseboard and satellite board, which were respectively located external to and implanted in the animal, as shown in Figure 131. A custom satellite board (Figure 131b) transmitted from a subcutaneous pocket within the rodent; the commercial base board receives the transmitted signal and couples to a laptop for data acquisition and storage. The satellite PCB comprised a two-stage analog amplifier, MSP 430 microcontroller, quarter wave antenna (433 MHz) and matching network. Supply and reference voltages were stabilized by linear voltage regulators. In addition, peripheral circuits were included for decoupling and stabilization. The circuitry was either powered by a lithium coin cell (CR 2032) or rechargeable lithium polymer battery, which featured a discharge voltage of 4.2 V and integrated 2.8 V voltage regulator (Figure 131c). The size of the lithium polymer battery (20 mm by 30 mm by 4 mm) further supported its use for the compact PCB design. For reference, the subcutaneous pocket in which the satellite circuit is implanted can accommodate a circuit footprint of up to 1 in by 1.5 in and the footprint of the satellite PCB was, in turn, 30 mm by 20 mm by 8 mm. The battery was connected to the backside of the satellite board.

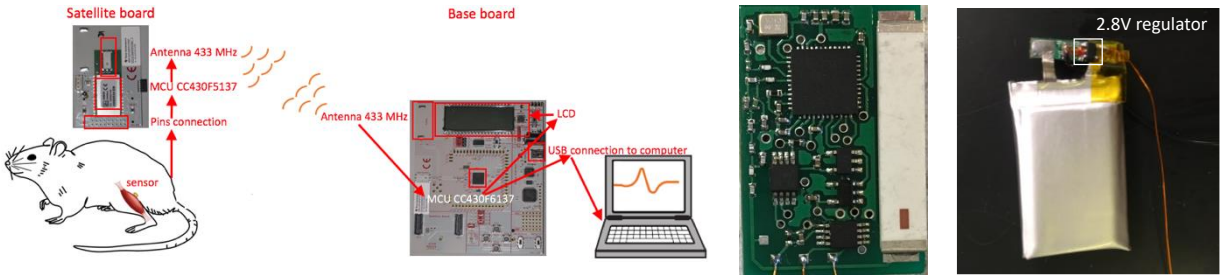

(a) **(b)** **(c)**

Figure 131 ***(a)*** *Schematic illustrating wireless communication between a satellite board, implanted subcutaneously within the rodent model, and an external base board. Optical images of* ***(a)*** *the top side of the satellite PCB designed for wireless transmission from within the rodent model and* ***(b)*** *commercial battery with integrated 2.8 V regulator used for the satellite PCB.*

Figure 132a shows a schematic of the satellite PCB circuit. The circuit supports the operation of both a piezoresistive strain sensor and electrochemical oxygen sensor. The analog frontend of the strain sensor is shown in Figure 132b. Since the sensor output comprised an initial voltage offset and strain-referenced voltage signal, the analog frontend served to remove the strain-independent voltage contribution (i.e., initial voltage offset) and amplify the strain-dependent signal prior to analog-to-digital conversion. The initial voltage offset stems from imperfect balance in the resistive elements of the Wheatstone bridge. For example, a $\pm$1% variation in the resistances of the Wheatstone bridge elements can correspond to an initial voltage offset of 25 mV, whereas the strain-dependent signal ranges from 0-3 mV for 0-5000 με at 2.5 V excitation. The sensor output voltage was, ultimately, amplified 100-300 prior to digital conversion. Connected to a reference voltage of 1.2 V, the 12-bit ADC provided a resolution of 0.29 mV. Frontend amplification ensured that the sensor output was sufficiently amplified to sustain the desired resolution in strain resolution (i.e., <5 με).

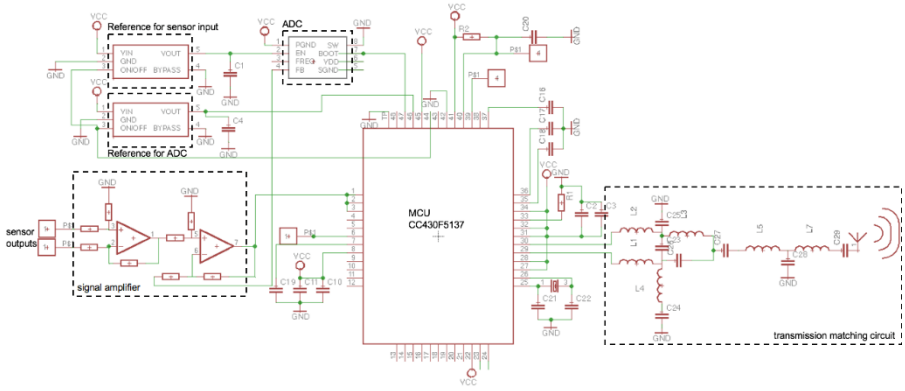

(a)

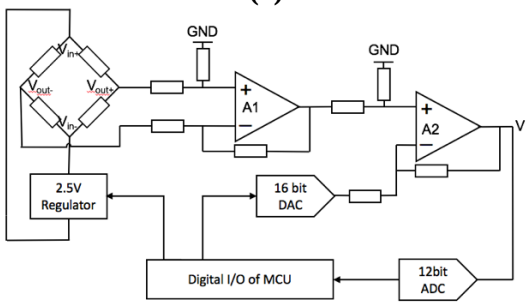

(b)

Figure 132 ***(a)*** *Circuit schematic of satellite board for wireless transmission in vivo and* ***(b)*** *schematic of analog front-end that interfaces with the Wheatstone bridge-configured strain sensor.*

The baseboard, a commercial experimental board (TI MSP-EXPCC430RF4), comprised a microcontroller (TI CC430F6137), an onboard emulator, a liquid crystal display screen, a transmission circuit, an antenna (433 MHz) and peripheral circuits. The commercial board was selected because it featured an integrated sub-GHz radio core (CC1101) and supported low power operation. The baseboard can be connected via USB to UART (i.e., Universal Asynchronous Receiver/Transmitter) for powering and data communication with a computer, respectively. The data received on the computer was, in turn, recorded and displayed with a custom Python program. With the onboard antenna and matching network, the transmission distance between the satellite and base boards was approximately 60 m.

To conserve battery power, the satellite board was programmed to wake-on-radio (WOR) mode. The radio core periodically wakes up based on the WOR timer to listen for incoming data packets. The radio registers transmitted one packet every second and, during each cycle, the radio core remained active (i.e., when it

can either receive or transmit) at a 12.5% duty cycle; it remained in sleep mode for the remainder of each cycle. Figure 133 illustrates the transmission process between the satellite and base boards. After initiation of the modules, the base board begins checking for user prompts (administered via the onboard push button); the satellite board enters WOR mode to periodically check the receiving status. If the 'start' button is activated, the base board transmits a 'start' packet. Once the satellite board receives the 'start' command, it responds 'ok'. Reception of the 'ok' packet by the base board completes the identification process and launches data transmission from the satellite board to the base board. When an 'end' command is initiated from the base board, the satellite board resumes the WOR mode and, again, periodically checks for 'start' commands.

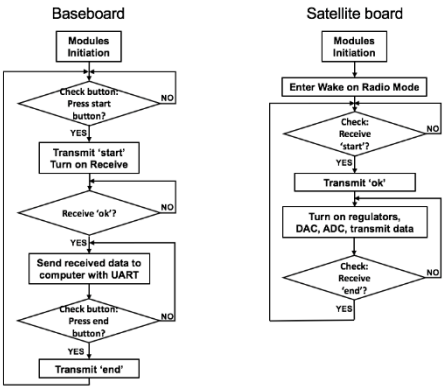

Figure 133 Flow chart illustrating the Python program for receiving information from the implantable satellite board to the base board.

4.1.2. End-to-End Validation of Implantable System

End-to-end testing was performed with the strain sensor packaged within a fixation plate and connected to the satellite PCB for wireless data transmission. As shown in Figure 134, strain detection was maintained across the test range of 10 N to 100 N, which corresponded to a strain range of 650 με to 6500 με. Linear regression indicated a strain sensitivity of 0.14 $\mu V/\mu\varepsilon/V_{ex}$, which agreed with previous

strain sensor analysis. Specifically, electromechanical characterization of the strain sensor alone (as shown in Chapter 3) revealed a strain sensitivity of 0.15 ± 0.01 μV/με/V_{ex}. The results confirmed that strain detection and data transmission of the packaged strain sensor and wireless telemetry was respectively preserved to the accuracy and strain resolution observed from singular component testing. The fidelity and stability of the voltage output degraded under applied cyclic loading of 25 N or less, as seen in Figure 134b. Since this had previously been observed with the mechanical testing system paired with direct loading of the fixation plate (e.g., due to substrate rotation and movement), end-to-end testing was transferred to a 3-point bending platform.

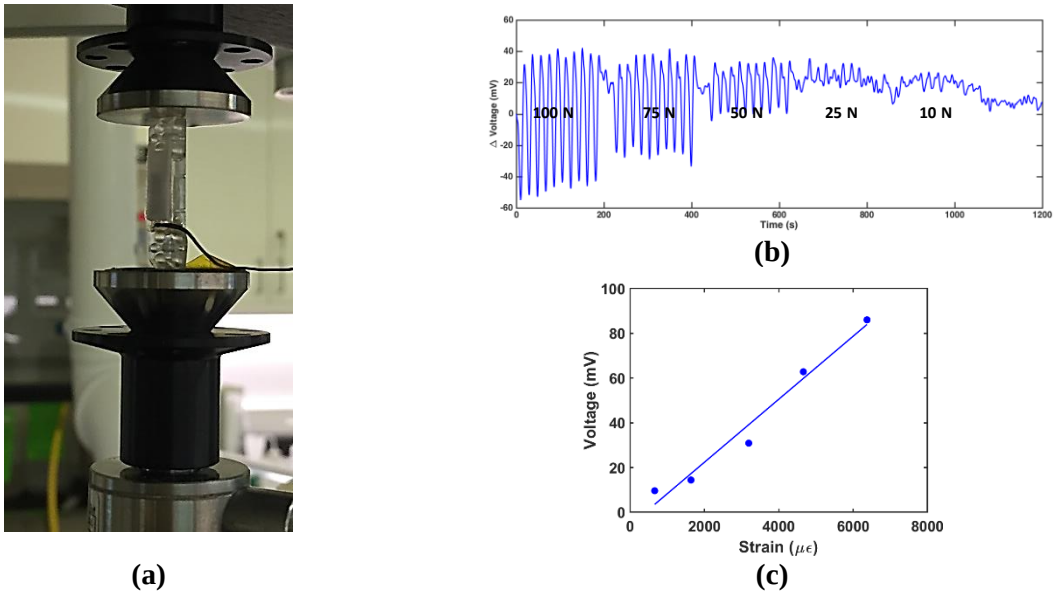

(a) **(b)** **(c)**

Figure 134 End-to-end testing with non-degradable strain sensor, custom satellite board and commercial base board under cyclic compressive loading. ***(a)*** *Optical image of packaged fixation plate and strain sensor under direct loading and* ***(b)*** *voltage output and* ***(c)*** *sensitivity of strain sensing system under load-controlled mechanical testing.*

Figure 135 shows the results of end-to-end testing with the fixation plate under 3-point bending. Specifically, 3-point bending was performed at displacement amplitudes of -100 μm, -10 μm and -1 μm, which corresponded to an applied strain of -8000 με, -800 με and -80 με, respectively. However, the lowest applied strain corresponds to the limit of detection of the mechanical testing system and, hence, strain

amplitudes varied between by 20-50 με. Stable and consistent strain cycles were detected under applied cyclic strain of -800 με under 3-point bending, as compared to the results at -25 N (i.e., -1600 με) under direct loading. Further, the strain sensing system successfully detected compressive strains of less than 100 με in amplitude and captured the strain fluctuations of the mechanical testing system, similar to what was previously observed with component testing of the strain sensor. This suggested that the voltage waveforms observed under applied loading of -25 N or less (Figure 134b) stemmed from the direct loading test setup, not due to limitations of the strain sensing system. Together, the end-to-end testing demonstrated that design of the strain sensor and wireless telemetry performed in unison to support strain detection and wireless communication for *in vivo* applications of the fixation plate to bridge large bone defects.

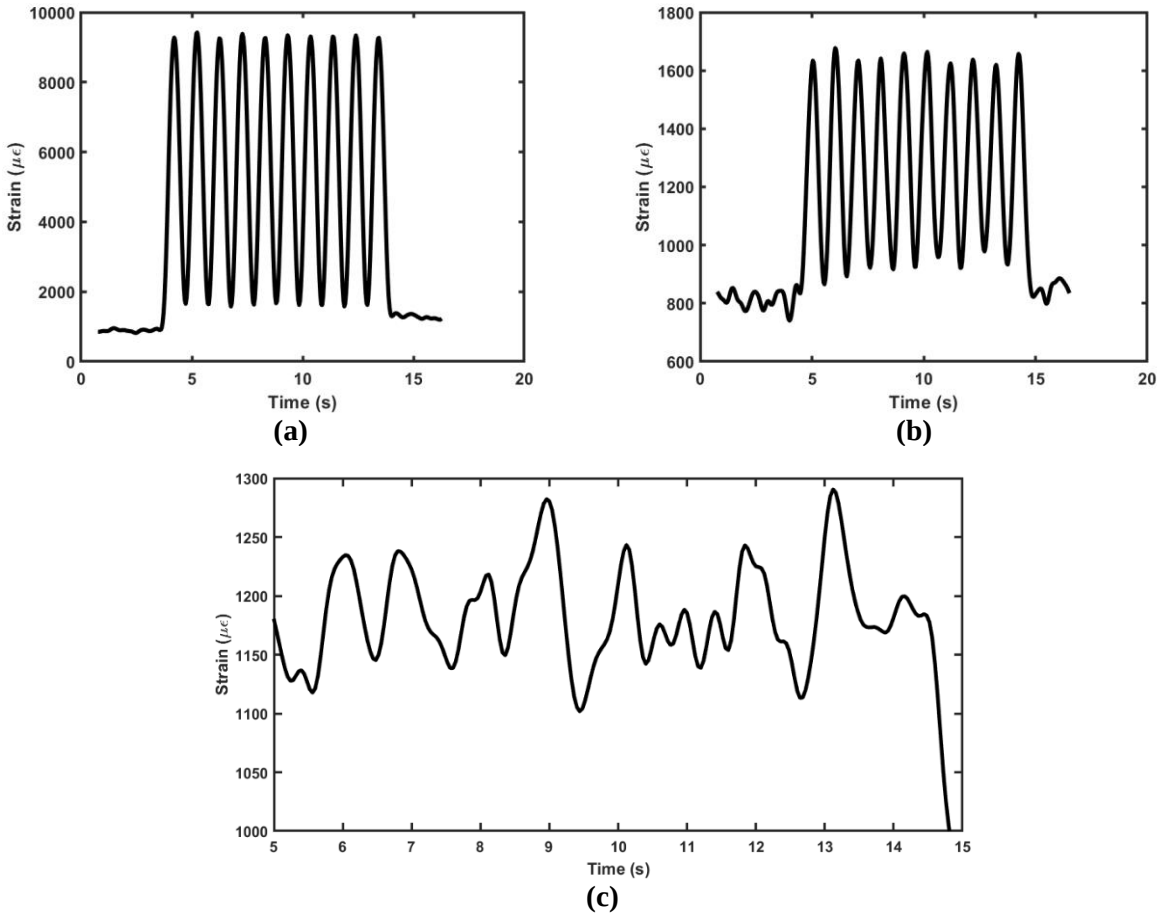

Figure 135 Measured strain from end-to-end testing under 3-point bending. Applied compressive strains from the mechanical testing system were -8000 με, -800 με and -80-100 με, respectively.

4.1.3. Sensor Deployment in Animal

Animal deployment of the strain sensing system was conducted as part of an interdisciplinary collaboration effort (Figure 136). Briefly, the fixation plate was implanted to bridge a 6 mm femoral segmental bone defect in a rodent model. The satellite PCB was packaged in custom housing and implanted within a subcutaneous pocket in the abdomen. Wired connections between the packaged strain sensor and circuitry was routed subcutaneously, as well, from the femoral defect to the abdomen. All implants were sterilized with ethylene oxide and degassed for a minimum of 2 days prior to *in vivo* use. All procedures were performed in accordance with IACUC protocol. Upon recovery from the surgery, wireless strain monitoring was evaluated by provoking movement of the rodent. Figure 137 shows the results of the ambulation study, wherein the recovering rodent instituted a single step and several postural movements during the duration of recording. (For reference, compressive loading corresponds to positive strain in the figures shown.) These movements resulted in load transfer across the implanted fixation plate and corresponding strain measurements. During a recording window of 400 s, a maximum strain of 835 με was observed and occurred when the animal took a single step forward. The mechanical strain observed during ambulation was two large amplitude waveforms, as highlighted in Figure 137b. The waveforms were characteristic of ambulation, as previously demonstrated in literature (Figure 138); the applied strain resembled a non-ideal square wave, where the peak strains (i.e., >100 με) are not constant within each period, but rather oscillate based on gait pattern. The magnitude of the peak strain and oscillations depend on the extent of load sharing between the femoral defect and fixation plate. A key distinction, however, is that the movements were recorded immediately after the surgical implant and when residual effects of analgesia persisted. Consequently, the animal's movements were much slower and more cautious than normal daily activities. This can be observed with the timescale of a single ambulation step, which manifested over 2 peaks that were approximately 10 s and 6 s in length, respectively. Further the maximum

amplitude of the peaks reflected a reluctance to place weight onto the newly formed defect. The characteristics of the waveform, nonetheless, agree with literature results reflect ambulation

In addition, postural movements observed in the rodent were also captured by the strain sensing system and are depicted by the green arrows in Figure 137b. The magnitude of postural strains was in the 100-200 με range except for the postural loading immediately preceding ambulation, which indicated greater loading across the femoral defect. Overall, the animal implant demonstrated that design and performance of the non-degradable strain sensor successfully satisfied the intended application of monitoring bone healing within a rodent femoral defect model. The range of detection, strain and physical design to accommodate the animal host, fixation plate geometry, as well as power budget of the custom circuitry, supported strain measurements and system functionality *in vivo*. Further, the results indicate that the non-degradable strain sensor boasts the resolution and range to capture minor movements and reduced loading associated with postural movements and cautious post-implant movements, respectively. These findings positively support the use of the current strain sensing system for monitoring bone fracture healing over longer time periods in future studies.

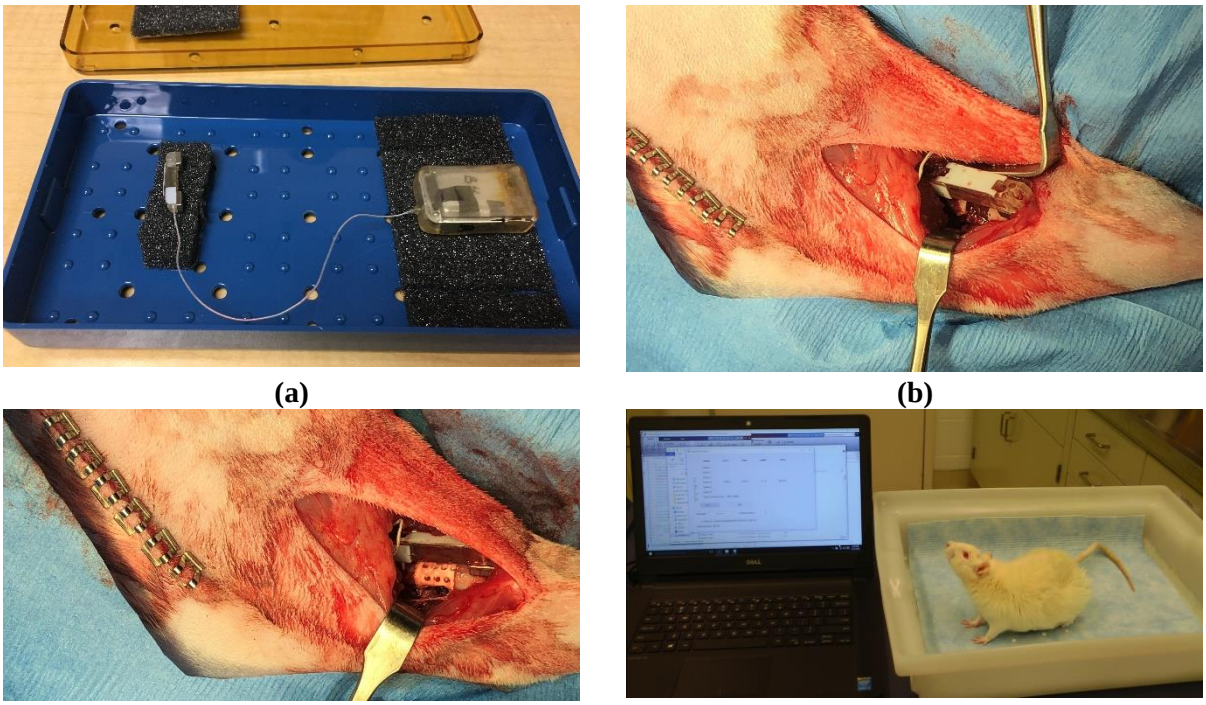

(a) **(b)**

(c) **(d)**

*Figure 136 Optical images of the **(a)** the sterilized strain sensor packaged within a fixation plate and satellite PCB packaged in hermetic housing, **(b-c)** the fixation plate implanted into a femoral segmental bone defect during surgery and **(d)** animal recording.*

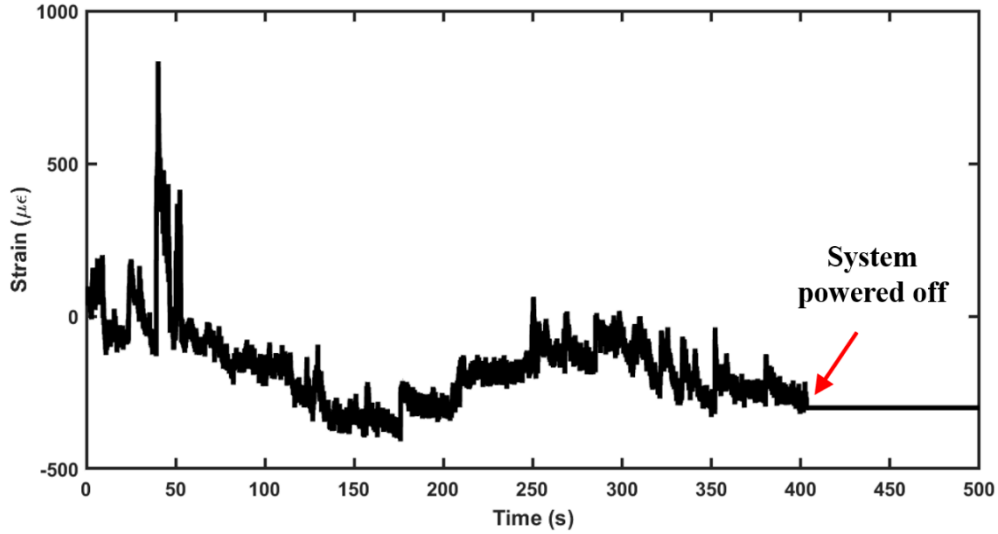

(a)

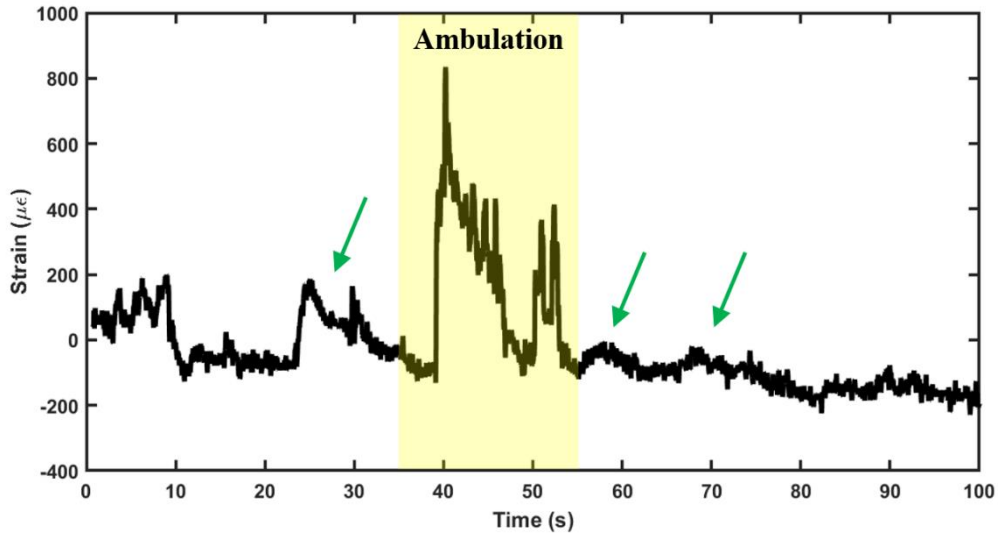

(b)

Figure 137 Mechanical strain across fixation plate during physiological loading. ***(a)*** *Strain output throughout 400 s duration of sensor operation and data transmission and* ***(b)*** *a zoomed-in segment illustrating a single step and postural shifts in the rodent. Red and green arrows correspond to the strain sensing system powered off and postural movements in the rodent, respectively.*

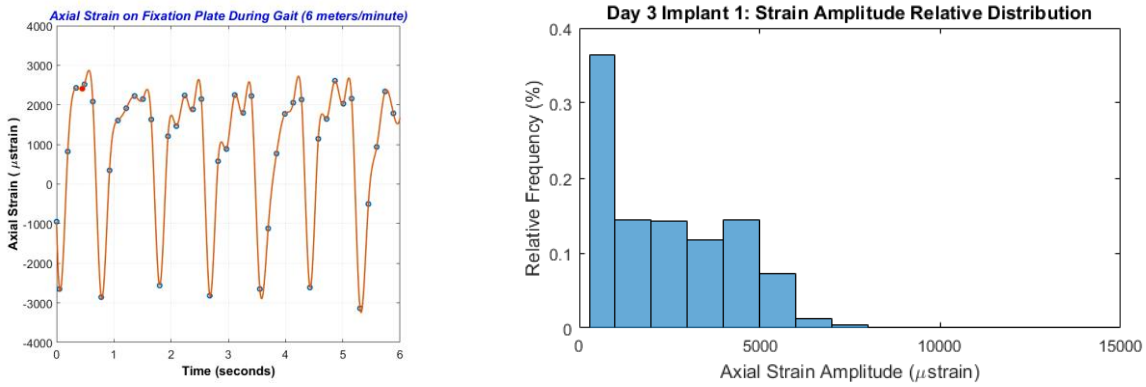

(a) **(b)**

Figure 138 Gait analysis based on measured strain and high-speed biplanar fluoroscopy. Rodent was placed on a treadmill to control ambulation speed (1 Hz) [286].

The results of the *in vivo* testing confirmed the functionality of the strain sensor for the intended use of providing *in situ* measurements during bone healing. The study further confirmed the validity of MEMS-based sensors for implantable applications that entail physiological monitoring. Future work should focus on longitudinal studies to gather strain data throughout the time course of bone regeneration and remodeling, as the results would support stronger strain analysis of gait pattern and the biomechanics of bone healing. However, these studies are premised on robust circuitry to power the sensor and wirelessly transmit the data. As part of a larger group endeavors, these efforts remain in progress with attention focused on battery consumption, microcontroller programming and robust PCB design.

4.2. Cytotoxicity of Biodegradable Materials for Implantable Use

4.2.1. Introduction

As a preamble to the *in vivo* deployment of biodegradable devices, the cellular toxicity of the constituent biodegradable materials was examined. The ISO 10993 is an internationally recognized protocol for evaluating the cytotoxicity of implantable medical materials and devices; the standard has also been recognized by the FDA as an acceptable *in vitro* assessment of toxicity [83], [287], [288]. The standard states that the cell line selected should represent the intended physiological environment of the implant.

Medical implants are immersed in the cell culture media and incubated at 37°C for a specified amount of time (e.g., 1-7 days). After this time, the extracted media is introduced to cells that have previously been seeded and allowed to adhere and proliferate in the cell culture container (e.g., a 96-well plate) for 24 hours. In this manner, the extract, which might contain leeched products from the implant, is exposed to the cell culture. Pure media that hasn't been exposed to any implant serves as the positive control. After a designated period of incubation, cellular viability is quantified using a colorimetric assay (e.g., MTT, MTS). The ISO standard defines the biosafety level as 70%; medical implants are non-toxic if the measured cell viability is equal to or greater than 70% that of the positive control [287], [288].

The utility of the ISO standard lies in its ease of implementation and prevalence in literature, providing many published data to compare against. However, the relevance of the cytotoxicity data depends on the appropriate selection of experimental parameters, such as the extraction period, cell incubation period and extraction ratio [83], [214], [289]–[293]. The last parameter is a surface area- or mass-to-volume ratio that standardizes how much of the implant should be immersed in a given volume of media during extract preparation. The recommended guideline, summarized in Table 32, depends on implant geometry. If the implant thickness is uniform, then the recommended extraction ratio is segregated into 3 groups: below 0.5 mm, between 0.5 mm and 1.0 mm, and greater than 1.0 mm thickness. As implant thickness increases, the implant surface area per unit volume decreases. For irregularly-shaped implants, a mass-based ratio of 0.1-0.2 g/mL is recommended, depending likely on the effective surface area. For MEMS-based devices, whose thickness likely does not exceed 0.5 mm, the recommended extraction ratio is 6 cm^2/mL [287], [288].

Table 32 A summary of the ISO-recommended extraction ratio for medical implants based on geometry and composition [287].

Implant Thickness (mm)	Extraction Ratio (±10% tolerance)	Examples of Materials
≤0.5	6 cm^2/mL	Metal, synthetic polymer, ceramic, composites, tubing walls
>0.5	3 cm^2/mL	Metal, synthetic polymer, ceramic, composites, tubing, molded items
>1.0	1.25 cm^2/mL	Natural elastomer
Irregular	0.1-0.2 g/mL 6 cm^2/mL	Pellets

Despite the prevalence of ISO 10993, drafting of the standard did not take biodegradable materials and devices into consideration [287], [288]. In general, the cell lines cultured for *in vitro* studies may exhibit different ion sensitivities than their *in vivo* analogue. Specifically, the protocol does not consider the clearance of biodegradable ions via physiological circulation *in vivo*. In addition, the protocol assumes that leeching or degradation occurs uniformly with time. However, many biodegradable polymers exhibit slower degradation initially, as the induction period precedes hydrolysis and cleavage of the polymer chains [83]. Further, literature and the results discussed in previous chapters both indicated that not all biodegradable metals degrade uniformly either; magnesium, in particular, favors localized pitting corrosion, which not only introduces non-uniformity, but also an element of stochasticity (and, hence, statistical spread) in the observed degradation rate [90], [113], [180].

These limitations demand an amendment to the current ISO 10993 standard for evaluating the cellular toxicity of biodegradable implants. Wang *et al.* identified a dilution ratio for biodegradable implants based on a rigorous comparison of *in vitro* cellular toxicity and *in vivo* testing in rabbits and rats. The study also examined the osmolality, ion concentration and pH of test extracts to verify whether observed results are due to intrinsic toxicity to the material or due to changes to the media conditions. The results supported a dilution ratio of 6- to 10-fold for the ISO-10993 evaluation of biodegradable materials. In addition, the study showed large pH shifts towards alkalinity for extracts with biodegradable metals [83].

This emphasized the use of negative controls (i.e., extract only; no cells) for all investigated test specimens in order to subtract elevated background signals due to pH effects.

The objective of this section is to evaluate the cellular toxicity of electroplated magnesium, both alone and with additional passivation and encapsulation schemes. Though largely based on the ISO 10993 standard, the assessment considers dilution ratio and pH effects in the experimental design. In addition to media-only positive controls, commercial magnesium will be examined as a comparator.

4.2.2. Experimental Design

The cellular toxicity of electroplated magnesium was quantified using a commercial cell viability assay. Briefly, the assay contains a tetrazolium-based dye that is reduced by metabolic enzymes (e.g., NADPH-dependent oxidoreductase) into formazan (Figure 139). Since formazan is water-insoluble, traditional assays (e.g., MTT) requires the addition of DMSO to solubilize the DMSO. However, the tetrazolium compound found in the newer MTS assay, which is used in this study, forms a soluble formazan product in tissue culture medium [294].

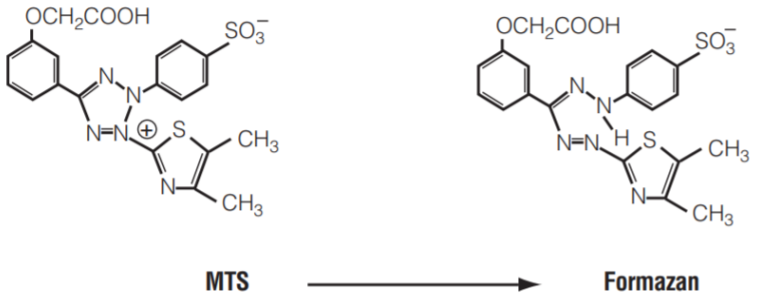

Figure 139 Molecular schematic illustrating the conversion of MTS tetrazolium to formazan by cellular reduction [294].

Extract preparation began with sample fabrication and sterilization. Cytotoxicity of commercial and electroplated Mg, bare and encapsulated with PLA, were first evaluated separately. In a second study, electroplated Mg baring various passivation schemes (e.g., FHA, PP Zn, ALD alumina and sputtered multi-layers of MgF_2 and PCL) were examined. For both studies, samples were UV sterilized for 1 hour prior to extract preparation. An extraction ratio of 1.5 cm^2/mL (i.e., dilution ratio of four-fold) was selected because, even though biodegradable materials merit a diluted extraction ratio, fluid exchange is poorer in bone that in the circulatory system. Samples were immersed in Dulbecco's minimum essential media (DMEM) fortified with 10% fetal bovine serum (FBS) for 72 hours under standard cell culture conditions (i.e., 37°C and 5% CO_2). It should be noted that DMEM without phenol red was used, as the compound interferes with spectrophotometric readings.

Murine fibroblasts (L-929) were cultured in 96-well cell culture plates. Briefly cells were seeded at 500 cells/well and incubated with DMEM + 10% FBS for 24 hours to establish cell adhesion. The culture media was then removed and replaced with sample extract (150 µL/well). Each sample type featured 4 positive (i.e., with cells) and 4 negative (i.e., without cells) wells. Incubation proceeded for 72 hours under standard cell culture conditions, after which the MTS assay (Promega CellTiter 96 AQ_{eous} One Solution Cell Proliferation Assay) was performed in accordance to manufacturer's protocol to quantify cell viability. Absorbance was measured at 490 nm wavelength. The results shown in this section represent the mean and standard deviation of the data.

4.2.3. Results & Discussion

The cellular toxicity of electroplated Mg and biodegradable passivation schemes was evaluated in accordance with the ISO 10993 standard. The extraction ratio was 1.0 cm^2/mL, representing a 6-fold dilution as recommended from literature for biodegradable materials. Figure 140 shows the cytotoxicity results for electroplated and commercial Mg. Pure media served as the positive control. Magnesium samples

were encapsulated in PLA following the same fabrication procedure, composition and thicknesses as described in the previous chapter on biodegradable strain sensors. This was maintained to ensure the validity and relevance of the obtained data in evaluating electroplated Mg for biodegradable strain sensor applications. Electroplated and commercial Mg encapsulated in PLA exhibited 89% and 96% cell viability compared to positive controls, respectively, indicating that both forms of encapsulated Mg are non-toxic based on the ISO 10993 standard. The lower cell viability observed with electroplated Mg, compared to commercial Mg, was attributed to increased surface roughness of the electroplated material; this increases the effective surface area and, since corrosion is a surface reaction, corresponded to increased Mg ions released into the extract media.

As expected, bare Mg (i.e., without any encapsulation) did not meet ISO standards for cytotoxicity. Specifically, cell viability was only 1% of positive control for bare Mg. The rapid, unhindered degradation of bare Mg resulted in the complete dissolution of the bare Mg sample into the extract media. This not only corresponded to a high Mg-ion concentration, but also a marked increase in solution pH. As observed from the Pourbaix diagram, pH increases due to Mg corrosion (and the formation of $Mg(OH)_2$) does not exceed approximately 8.2. The high Mg-ion concentration and elevated pH rendered bare Mg cytotoxic to fibroblast cultures. These findings suggest that encapsulation is critical for medical implants comprising Mg. For reference, Mg degradation with and without the demonstrated PLA encapsulation are 0.69 μm/day and 9.1 mm/day, respectively.

The results further suggested that bulk polymeric encapsulation (i.e., 25-50 μm PLA) was sufficient in overcoming cytotoxicity concerns. Specifically, all PLA-encapsulated samples satisfied the biosafety limits prescribed by ISO 10993 and corresponding FDA guidelines. Additional, biocompatible passivation schemes might further improve cell viability (i.e., to better approximate or even exceed the cell viability of positive controls). Further, additional passivation schemes may be necessary from the perspective of device performance and functional lifetime.

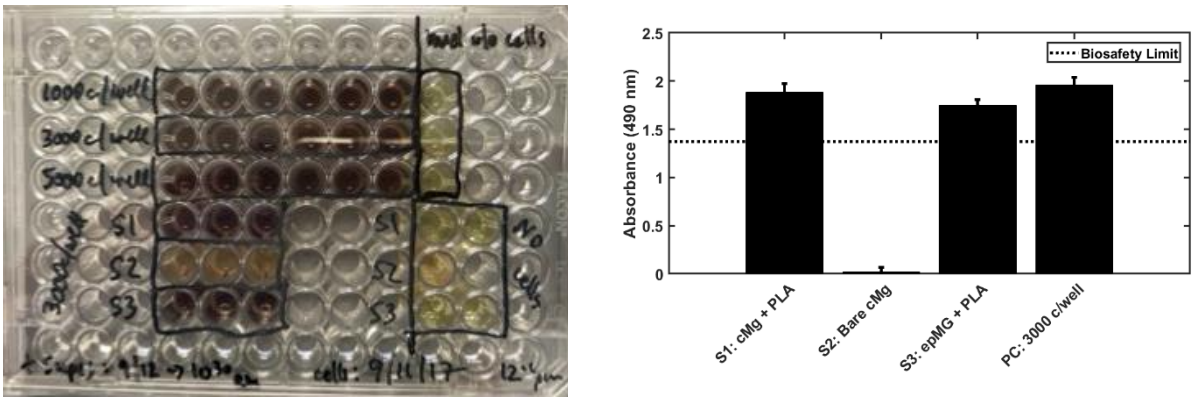

(a) **(b)**

Figure 140 ***(a)*** *Optical image and* ***(b)*** *absorbance results from MTS assay on cells cultured in extract containing degradation products from commercial Mg and electroplated Mg, compared against positive controls cultured without extract and negative controls containing extract only and zero cells. Dashed line corresponds to the biosafety level defined by ISO 10993, or 70% cell viability of positive control.*

Since results indicated that electroplated Mg encapsulated in PLA was non-toxic, a second study was conducted to evaluate the effect of additional passivation schemes (Figure 141). Specifically, pulse-plated Zn (PP Zn), fluorinated hydroxyapatite (FHA), and multi-layers comprising sputter deposited MgF_2 and PCL were examined. Pure media and commercial Mg encapsulated in PLA were also evaluated as the positive control and comparator. For reference, fibroblasts were seeded at a lower cell density in this study than previously implemented in order to remain within the recommended linear regime of the commercial MTS assay. In addition, the extraction ratio was modified to 1.5 cm^2/mL. Recall that Wang *et al.* had recommended a dilution ratio of 6-10 in order to account for the physiological clearance achieved with circulation [83]. Although vascular perfusion occurs at a fracture site, especially in the acute stages of bone regeneration, circulation is generally lower in bone than in the vascular system. Further, higher concentrations of both magnesium and hydroxyapatite-derivatives are found in bone and the materials have been shown to promote osseointegration. Given these experimental modifications, electroplated and commercial Mg encapsulated in PLA showed 80% and 89% cell viability compared to positive controls, respectively. This trend of non-toxicity and higher cell viability with commercial than electroplated Mg agreed with earlier results.

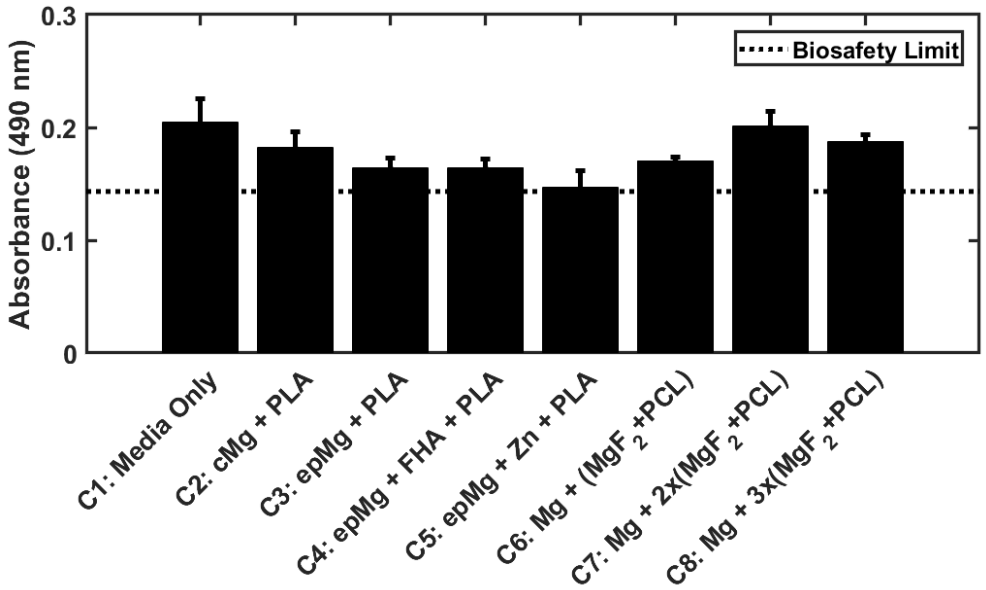

Figure 141 Cytotoxicity results of fibroblasts cultured in media containing degradation products of Mg and various passivation and encapsulation schemes. Absorbance results were obtained with a colorimetric assay that quantifies cell viability. Dashed line corresponds to the biosafety level defined by ISO 10993, or 70% cell viability of positive control.

Overall, all evaluated passivation schemes satisfied the biosafety limit for cellular toxicity. Passivation with PP Zn and electroplated FHA corresponded to cell viabilities of 72% and 80%, respectively. For reference, the corrosion rate of Mg features the examined passivation schemes were 0.3 μm/day and 0.18 mm/day, respectively. The results indicated that FHA is more biocompatible than PP Zn in spite of its higher corrosion rate. This might be attributed to the bioactivity and native presence of FHA in bone. In addition, the formation of pinholes in the PP Zn coating over time, such as due to film defects or pitting, would result in galvanic coupling of Mg and Zn. This would, in turn, accelerate Mg corrosion. Hence, while ideal Zn coatings would significantly reduce the corrosion rate of Mg and introduce only dissolved Zn into the physiological environment, non-perfect PP Zn coatings will likely introduce both Zn and Mg ions into solution, as well as potentially enhance the Mg ion concentration if galvanic coupling occurs. Test samples of PP Zn-coated Mg revealed partial corrosion of the underlying Mg through a few

pinholes in the Zn coating. This likely explains the reduced cell viability compared to that of Mg encapsulated with PLA alone.

Multi-layer passivation with sputtered barrier films (33-nm-thick MgF_2) and PCL also satisfied biosafety requirements. Atomic layer deposited alumina-based multi-layers were not examined in the present cytotoxicity study because previous characterization and use of ALD alumina assumed the material served as a surrogate for ALD-deposited MgF_2. (Recall that water permeation through barrier thin films depends mainly on deposition technique and, hence, ALD alumina was a surrogated for ALD MgF_2.) However, cytotoxicity studies depend on both water permeation (i.e., Mg protection), as well as the intrinsic biocompatibility of the materials. Further, ALD-deposited MgF_2-based multi-layers would only exhibit better performance than that of sputtered MgF_2. For these reasons, only sputtered MgF_2-based multi-layers were examined for cytotoxicity, as it represented the worst-case scenario. The observed cell viabilities of MgF_2 and PCL multi-layers were 83%, 99% and 92% for one-, two- and three-layers of passivation. These results indicated that multi-layer passivation was most effective in preserving cellular viability compared to positive controls. Material characterization from Chapter 2 revealed that 1x, 2x and 3x multi-layers of MgF_2 and PCL corresponded to water permeation rates of 8.74 e-3 $g/m^2/day$, 2.44 e-3 $g/m^2/day$ and 1.95 e-3 $g/m^2/day$, respectively. The corresponding Mg degradation rate are 3.4 nm/day, 0.9 nm/day and 0.8 nm/day, respectively. This assumed that Mg corrosion is diffusion limited due to the rapid reaction rate of Mg corrosion in aqueous solutions; hence, water that permeates the multi-layer barrier films was assumed to instantly react with Mg. Further, this calculation assumes linear, uniform corrosion, which is intrinsic to measurements obtained by linear sweep voltammetry and, hence, supports fair comparison amongst the samples. Taking the cytotoxicity and water permeation results together, the data suggested that multi-layer passivation with MgF_2 and PCL boasted higher cell viability than PP Zn and FHA coatings due to the orders of magnitude lower Mg corrosion rate, as well as the biocompatible nature of the constituent materials (i.e., MgF_2 and PCL). Specifically, 2 layers of MgF_2 and PCL exhibited 99% cell viability compared to positive controls, which was 27% and 19% higher than that of PP Zn and FHA, respectively. Interestingly,

three layers showed lower cell viability than two layers, reminiscent of the higher WTR observed when additional layers corresponded to damage incurred from additional process. This suggested that the deposition of additional layers may have inflicted damage to the multi-layer passivation and render more pinholes and damage with excess multi-layers; in the case of MgF_2 and PCL multi-layers, this was occasionally observed during polymeric spin casting, where the solvent in the PCL solution can attack the underlying PCL layers through defects in the film.

The overall findings from the cytotoxicity studies indicated that, even though PLA encapsulation alone eliminated cytotoxicity concerns with Mg, the selection of passivation schemes may provide additional benefits, such as improved performance with PP Zn and enhanced cell viability with multi-layer passivation. The synergistic effects of multiple passivation schemes on electroplated Mg is recommended in future work. In addition, future work should build upon the preliminary biocompatibility demonstrated by cytotoxicity studies. For example, since it is speculated that the toxicity results were mainly attributed to the reduced degradation rate imparted by the corrosion passivation schemes (assuming no gross toxicity results are introduced by the passivation itself), a second study might map out this design space by directly correlating corrosion rate with cell toxicity. This can be achieved either by producing passivation schemes that span a spectrum of corrosion rate and evaluating their corresponding cell viability or by measuring the Mg ion concentration in the extract and, in this manner, correlate Mg release with cell toxicity. In addition, future studies can directly evaluate toxicity *in vivo* by implanting non-functional devices, which feature the materials and relevant device dimensions, into the proposed rodent femoral bone defect model. The inflammatory response, as well as hyper-sensitivity (i.e., allergic reaction), can be evaluated by histology.

4.2.4. Conclusion

The ISO 10993 standard was implemented to evaluate the cellular toxicity of electroplated Mg and various passivation and encapsulation schemes. The objective to validate the use of these materials for biodegradable, implantable devices in bone healing applications. Although Mg degrades rapidly under

physiological conditions, the findings confirmed that electroplated Mg is non-toxic even with the addition of simple polymeric encapsulation (i.e., PLA). Passivation with ALD barriers, electroplated Zn or FHA, and multi-layer passivation also satisfied biosafety limits prescribed by ISO and the FDA. Higher cell viability with MgF_2 and PCL multi-layers suggested that the passivation schemes not only present beneficial effects from the perspective of device performance (i.e., stability and functional lifetime), but also in terms of biocompatibility. The results of these studies support the use of electroplated Mg and the examined passivation schemes for use in biodegradable, implantable devices.

4.3. Conclusions on the Use of MEMS-Based Devices for Biomedical Applications

The objective of this thesis was to expand the material sets available for constructing biodegradable MEMS devices and to further the path of biomedical MEMS through more application-specific testing, both on the bench top and in animal. The culmination of these efforts was demonstrated in this chapter. Specifically, this chapter demonstrated the *in vivo* deployment of a non-degradable strain sensor and confirmed the biocompatibility of the investigated biodegradable materials. The results validated the use of MEMS-based devices for not only clinical therapies, but also for interrogating questions in fundamental biology. Although biodegradable strain sensors and energy sources were not directly evaluated in animal, the positive results observed with non-degradable analogues and the demonstrated biocompatibility of the biodegradable materials suggest that, by extension, MEMS devices that contemplate the proposed biodegradable material schemes can likewise perform their intended function *in vivo* within the fabrication, performance and cytotoxicity guidelines identified in this thesis. With future developments in biodegradable circuitry and packaging, it is the hope that a fully biodegradable strain sensing system will be deployed in a similar rodent model for the transient application of bone healing.

CHAPTER 5

CONCLUSIONS

A sensor that lasts forever isn't always desirable. Yet, designing a sensor with a limited lifetime isn't so simple. This thesis has explored the development of biodegradable strain sensors and energy sources, beginning with the identification, microfabrication and characterization of biodegradable materials. A review of the biodegradable literature revealed that biodegradable MEMS devices are currently limited by the availability of biodegradable materials. Many devices comprise physical vapor deposited Mg, Zn or Fe encapsulated by commercial polymers, such as PCL, PLA and PLGA. Some studies have extended this library to include traditional CMOS materials (e.g., silicon, silicon dioxide and silicon nitride) by arguing that the materials boast a very slow degradation rate and, thereby, justifies their use as thin films.

The present dissertation aimed to expand the library of biodegradable materials available to MEMS. Specifically, Chapter 2 explored thicker film Mg fabrication techniques (e.g., electroplating), passivation schemes comprising metallic and ceramic coatings (i.e., PP Zn and FHA, respectively), barrier thin film multi-layers and conductive polymer composites. Electroplated Mg supported the use of thicker (i.e., 1-100 μm thickness) Mg while overcoming the limitations associated with subtractive fabrication techniques from commercial Mg foil. The fabrication and integration of PP Zn, FHA and MgF_2-PCL multi-layers supported their use as passivation schemes to hinder Mg degradation and, ultimately, their use in MEMS-based biodegradable devices. Each passivation scheme boasted their respective advantages and limitations. Zinc coatings reduced the physiological corrosion rate of Mg to 1-10 μm/day (as compared to 9.1 mm/day for bare Mg), but accelerated Mg corrosion through galvanic coupling if pits and pinholes were present in the coating. Zinc coatings, being conductive, also reduced the resistance of corresponding Mg features. In turn, FHA is a calcium phosphate-derivative that is naturally found in bone and bioactive. Corrosion studies revealed that the corrosion rate of FHA-coated Mg decreased with time under

physiological conditions, corresponding to an observed degradation rate of approximately 20 μm/day. The ceramic nature of FHA rendered the coating more brittle and the acidic electrolyte presented limitations on the Mg substrate. Finally, biodegradable barrier thin films achieved with MgF_2-PCL multi-layers exhibited reduced water permeation to 1.95e-3 g/m^2/day, compared to bulk polymeric encapsulation (e.g., 200 g/m^2/day with 200-μm-thick PLLA). The barrier thin films offer conformal passivation, but require sequential deposition techniques with each additional layer, during which film defects may be introduced. All examined materials demonstrated biocompatibility, as evaluated by ISO 10993 cytotoxicity studies. Overall, the metallic, ceramic, and multi-layer passivation schemes examined in this thesis have reduced Mg corrosion by 3-4 orders of magnitude and hindered water permeation by 5 orders of magnitude compared to bulk polymeric strategies observed in literature.

It is speculated that a combination of passivation schemes will further improve corrosion protection and barrier encapsulation. As observed with barrier multi-layers, the addition of PCL to MgF_2, even with a single dyad, reduced WTR by 1 order of magnitude, indicating that the synergistic effect was more than additive. The extent of improvement with FHA and MgF_2-PCL multi-layers will need to be experimentally confirmed, but initial calculations suggest that the combination can introduce further appreciable improvements. Based on water permeation data, the corresponding corrosion rate of MgF_2-PCL in an aqueous environment at room temperature is approximately 1 nm/day with 2 dyads, assuming Mg corrosion occurs instantly once water permeates the barrier and reaches the Mg surface (given the fast kinetics of Mg corrosion). This assumes uniform corrosion, intentional because FHA and PP Zn corrosion obtained by LSV characterization possess the same assumptions. If the extent of corrosion protection afforded by passivation is taken as a ratio of the corrosion rates with and without the coating, then the extent of improvement provided by FHA coatings on electroplated Mg corresponds to a ratio of 0.002 (i.e., corrosion with an FHA coating is 0.002 that of bare Mg). Taken together, and assuming that the corrosion rate of MgF_2-PCL follows Arrhenius relations with temperature, then the corrosion rate of an FHA and MgF_2-PCL combination passivation would be 4 pm/day. These findings present the best-case scenario of the

combinatorial passivation scheme, whereas purely additive effects (and, hence, negligible differences with and without the additional of FHA) present the worst-case scenario. Limitations presented by fabrication of the passivation schemes must also be identified. The spectrum of potential improvements to Mg corrosion warrants a deeper, experimental dive into the synergistic effects of combinatorial passivation schemes.

Biodegradable strain sensors and energy sources were demonstrated with electroplated Mg as the active material of the device (i.e., sensing element and galvanic anode, respectively). The results confirmed the successful micropatterning and integration of the examined biodegradable materials towards MEMS-based biodegradable devices. Electroplated Mg strain sensors exhibited a maximum strain sensitivity and functional lifetime of 0.11 $\mu V/\mu\varepsilon/V_{ex}$ and 4 days, respectively. The sensors were sensitive across strain and frequency range of 180-3800 $\mu\varepsilon$ and 0.05-10 Hz, respectively. The performance of the biodegradable strain sensors supported their use in the proposed application of monitoring bone healing in rodent femoral models. Further, the electroplated Mg-based devices successfully achieved the targeted functional lifetime; the objective was to achieve a functional lifetime of no more than 1 order of magnitude less than that of an analogous non-degradable strain sensor through the use of thicker Mg films and clever passivation schemes. For reference, microfabricated gold and polyimide strain sensors exhibited a functional lifetime of 49 days under the same physiological conditions and an average strain sensitivity of 0.19 $\mu V/\mu\varepsilon/V_{ex}$. Although thicker Mg films did support the target functional lifetime, the passivation schemes (e.g., PP Zn and barrier thin films) did not; instead, they improved the performance of the device, such as with strain sensitivity and minimum frequency of operation. The limitations of the passivation schemes in prolonging device functionality was attributed to the fabrication challenges of not only patterning, but also integrating the materials and MEMS-relevant dimensions. For example, the implemented device fabrication scheme entailed a mechanical release of the device layer by peeling off the flexible polyimide substrate and subsequently lamination to fully encapsulate the device. While this approach avoids chemical exposure and minimizes thermal processing, the devices are exposed to bending

and applied pressure throughout processing. It is envisioned that the functional lifetime of passivated Mg-based strain sensors will exceed that of unpassivated devices through future research on improving device fabrication and even implementing combinatorial passivation schemes.

Biodegradable energy sources featuring energy densities comparable to that of commercial batteries used in medical implants were developed with electroplated Mg as the galvanic anode. Electrochemical cells that harnessed physiological solution as the electrolyte achieved an energy density 694 Wh/kg, as compared to 150-200 Wh/kg for commercial lithium-based batteries. Further, the PCL-coated Mg/Fe cells offered a compact footprint and comprised a volume of 0.02 cm^3, more than 2 orders of magnitude smaller than biodegradable energy sources previously demonstrated in literature. Since the electrolyte is not packaged within the system, the shelf life of the PCL-coated Mg/Fe cells is not limited by the biodegradable nature of its constituents. Even though galvanic corrosion of Mg occurs has a parasitic reaction, the Coulombic efficiency of the PCL-coated Mg/Fe cells was 48%. The performance characteristics of the electroplated Mg-based energy sources (e.g., discharge current, average potential, capacity and power) support their use with commercial circuitry, especially given the developments in low-power components (e.g., microcontrollers).

Passivation schemes were implemented to guide the anodic reaction and, hence, consumption of the Mg anode along a given direction (i.e., candle configuration). Initial designs comprising bulk polymeric encapsulation were, ultimately, unsuccessful due to the high water permeation rate of polymers and a build of up reaction products underneath the bulk encapsulation due to mass transfer limitations. Half-cell studies featuring barrier thin films demonstrated, however, that candle-like configurations can be achieved to preferentially promote Mg consumption (i.e., via the discharge reaction or parasitic corrosion) if the passivation is sufficient. The findings supported two hypotheses about galvanic corrosion-based energy sources. It was first hypothesized that the electrochemical performance would improve at discharge current densities greater than the corrosion current density of the anode. The second hypothesis was represented by an equivalent circuit model of the electrochemical system, where electrolyte permeation can proceed via

two pathways: through a designed opening where Mg is exposed and/or through the passivation scheme; electrolyte ingress preferentially occurs via the path of lower impedance. The results supported the two hypotheses, where the specific capacity and power of bare and ALD-coated Mg half cells significantly increased at discharge rates greater than their corresponding corrosion rates. Further, data gathered from EIS characterization supported the electrochemical circuit model, as well as supported the use of barrier thin films for achieving the preferential candle design.

The research trajectory of the biodegradable passivation schemes, strain sensors and energy sources developed in this thesis are analogous to the non-degradable technology demonstrated—an implantable strain sensing system. The performance and degradation characteristics of electroplated Mg-based strain sensors and energy sources can be integrated in future works towards this goal. The PCL-coated Mg/Fe electrochemical cells demonstrated a maximum specific capacity of 770 mAh/g at a discharge rate of 230 $\mu A/cm^2$. For a Mg anode that is the footprint of a commercial CR1220 coin cell (i.e., 1.25 cm diameter) and 100 μm thickness, dimensions that be achieved with the microfabrication technologies introduced in this dissertation, the projected electrochemical performance corresponds to a discharge current, capacity and projected lifetime of 564 μA, 16.4 mAh and 116 h, respectively. Based on the PCL-coated Mg/Fe design presented in Chapter 3.3, the average discharge potential at this current range is 0.7 V. The suggests that the equivalent resistance in a Wheatstone bridge and, hence, the nominal resistance of each element in a balanced bridge design must be 1.24 kΩ. The corresponding feature size and design can be achieved with the fabrication process developed for electroplated Mg strain gauges, but only for individual elements of the Wheatstone bridge. The gauge elements can then be integrated, along with the PCL-coated Mg/Fe energy source, via wire connection. (For reference, half and whole bridge configurations are presently difficult to fabricate due to the mechanical peeling entailed in substrate release, wherein meandering designs that run perpendicular to the direction of peeling do not retain mechanical integrity and electrical continuity. The limitation to fabricating half and whole bridge strain gauges is not attributed to patterning limitations with electroplated Mg, but rather the present approach to releasing the device layer from the substrate.)

While such higher-resistance strain gauges can be fabricated with electroplated Mg, passivation schemes (e.g., FHA coatings and/or MgF_2-PCL multi-layers) must be implemented to ensure that the device functional lifetime is similar to that of the energy source (i.e., 116 h) because narrower feature sizes generally correspond to shorter functional lifetimes (as shown in Chapter 3.2). A device lifetime of 90-100 h was previously demonstrated with electroplated Mg that comprised wider features, but no additional passivation beyond polymeric encapsulation. These results, together with the extent of Mg protection afforded by the passivation schemes examined in this thesis, suggest that a comparable functional lifetime can be achieved with higher-resistance electroplated Mg strain gauges with the implementation of FHA coatings and/or MgF_2-PCL multi-layers. Further, the addition of passivation schemes has been shown to improve strain sensor performance. A half bridge configuration would provide a strain sensitivity of -0.675 $\mu V/\mu\varepsilon/V_{ex}$, as well as compensation for thermal and environmental noise. By integrating the biodegradable passivation schemes, strain sensor and energy sources pursued in this thesis, a biodegradable strain sensing system can be achieved (excluding circuitry) that supports system functionality on the timescale of at least 4 days and with higher device sensitivity than individual strain sensors alone.

This thesis has focused on the development of biodegradable strain sensors and energy sources with the trajectory towards *in vivo* applications in monitoring bone healing. While the transient nature of the biodegradable devices has been fundamentally and experimentally detailed, it is less accepted that non-degradable devices might similarly boast a transient lifetime. Specifically, Chapter 3.1 revealed that the functional lifetime of a non-degradable strain sensor is not necessarily permanent, as convention and reason might assume. Electrolyte permeation and component degradation can still occur, particularly with active devices, to render the device non-functional even though a majority of its constituent materials remain. While the material sets available to minimize or hinder this effect is broader than that of biodegradable devices, the results presented a reasonable upper limit to the anticipated functional lifetime of an analogous biodegradable device under the same testing conditions. For these reasons, a target functional lifetime of no more than 1 order of magnitude less than that of the non-degradable strain sensor

(i.e., 49 days) was imposed and, ultimately, achieved with electroplated Mg-based strain sensors and energy sources.

In addition, the non-degradable strain sensor research confirmed that the system design (i.e., rodent femoral defect model, implantable fixation plate design and strain sensing system) supported *in situ* strain monitoring during bone healing. End-to-end testing and *in vivo* deployment showed that the strain sensing system enabled the real time monitoring of mechanical strain applied across a fixation plate-assisted segmental bone defect within a rodent during movement. The microfabricated strain sensor was sensitive to both large amplitude strains applied during ambulation and smaller signals during postural adjustments of the animal. Since the strain sensing system comprised a microfabricated strain sensor and commercial coin cell battery, it is argued that, by extension, a MEMS-based biodegradable strain sensor and energy source that satisfies the same performance and application design constraints can similarly support *in vivo* strain monitoring in the proposed rodent femoral defect model. Electroplated Mg strain sensors and energy sources, enabled by the microfabrication techniques and fortified by the passivation schemes discussed in Chapter 2, successfully demonstrated the strain sensor performance and power requirements to support system integration towards these goals.

This dissertation has developed MEMS-based strain sensors and energy sources that intentionally do not last forever. The transience in functionality and in physical form of the microfabricated biodegradable devices support their use in similarly short-term applications, such as with monitoring or treating acute disease states (e.g., bone healing) and minimizing environmental waste with disposable electronics. The research in this thesis addressed the direct application of monitoring mechanical strain across a rodent femoral bone defect, but also serves the general field of biodegradable MEMS research. The microfabrication technologies and passivation schemes developed for the implementation and integration of biodegradable materials into MEMS can be applied to a broad class of devices and to achieve a spectrum of functional lifetimes. Beyond sensors and energy sources, future work should further

developments in biodegradable circuitry and packaging, to, ultimately, complete the trajectory towards an entirely biodegradable and clinically-relevant strain sensing system.

REFERENCES

[1] H. M. Frost, “Bone’s mechanostat: a 2003 update.,” *Anat. Rec. A. Discov. Mol. Cell. Evol. Biol.*, vol. 275, no. 2, pp. 1081–101, Dec. 2003.

[2] E. Schoenau, “From mechanostat theory to development of the ‘ Functional Muscle-Bone-Unit ,’” vol. 5, no. 3, pp. 232–238, 2005.

[3] J. D. Boerckel, “Effects of in vivo mechanical loading on bone,” Georgia Institute of Technology, 2011.

[4] R. T. Whales and P. Alto, “Trabecular bone density and loading history: Regulation of connection tissue biology by mechanical energy,” no. December, 1986.

[5] B. S. Klosterhoff *et al.*, “Implantable Sensors for Regenerative Medicine,” *J. Biomech. Eng.*, vol. 139, no. 2, p. 21009, 2017.

[6] P. C. LaStayo, K. M. Winters, and M. Hardy, “Fracture healing: Bone healing, fracture management, and current concepts related to the hand,” *J. Hand Ther.*, vol. 16, no. 2, pp. 81–93, Apr. 2003.

[7] L. C. Y. Wong, W. K. Chiu, M. Russ, and S. Liew, “Review of techniques for monitoring the healing fracture of bones for implementation in an internally fixated pelvis.,” *Med. Eng. Phys.*, vol. 34, no. 2, pp. 140–52, Mar. 2012.

[8] P. Augat, K. Margevicius, J. Simon, S. Wolf, G. Suger, and L. Claes, “Local tissue properties in bone healing: influence of size and stability of the osteotomy gap.,” *J. Orthop. Res.*, vol. 16, no. 4, pp. 475–81, Jul. 1998.

[9] C. B. Machado, W. C. D. a Pereira, M. Granke, M. Talmant, F. Padilla, and P. Laugier, “Experimental and simulation results on the effect of cortical bone mineralization in ultrasound axial transmission measurements: a model for fracture healing ultrasound monitoring.,” *Bone*, vol. 48, no. 5, pp. 1202–9, May 2011.

[10] M. D. Jr and A. N. D. J. Malcolm, “X-Ray Diagnosis of Healing Fractures in Rabbits,” pp. 1978–1980, 1978.

[11] J. J. Tiedeman, D. Ph, and J. F. Connolly, “Quantitative Roentgenographic Densitometry for Assessing Fracture Healing,” pp. 279–286.

[12] “Tibial shaft fractures assessment by CT - Schnarkowski 1995.pdf.” .

[13] S. Shelton, A. Guedes, R. Przybyla, R. Krigel, B. Boser, and D. A. Horsley, “Aluminum nitride piezoelectric micromachined ultrasound transducer arrays,” *Solid-State Sensors, Actuators, Microsystems Work.*, pp. 291–294, 2012.

[14] V. C. Protopappas, M. G. Vavva, S. Member, D. I. Fotiadis, S. Member, and K. N. Malizos, “Ultrasonic Monitoring of Bone Fracture Healing,” vol. 55, no. 6, 2008.

[15] J. D. Boerckel, Y. M. Kolambkar, H. Y. Stevens, A. S. P. Lin, K. M. Dupont, and R. E. Guldberg, “Effects of in vivo mechanical loading on large bone defect regeneration.,” *J. Orthop. Res.*, vol. 30, no. 7, pp. 1067–75, Jul. 2012.

[16] C. Laurencin, Y. Khan, and S. F. El-amin, “Bone graft substitutes,” pp. 49–57, 2006.

[17] E. Schneider, M. C. Michel, M. Genge, K. Zuber, R. Ganz, and S. M. Perren, “Loads acting in an

intramedullary nail during fracture healing in the human femur.," *J. Biomech.*, vol. 34, no. 7, pp. 849–57, Jul. 2001.

[18] C. H. Turner, I. Owan, and Y. Takano, "Mechanotransduction in bone : role of strain rate," *Am. J. Physiol. Endocrinol. Metab.*, vol. 32, no. 3, pp. E438–E442.

[19] C. H. Turner, M. R. Forwood, J.-Y. Rho, and T. Yoshikawa, "Mechanical loading thresholds for lamellar and woven bone formation," *J. bone Miner. Res.*, vol. 9, no. 1, pp. 87–97.

[20] W. E. Caler and D. R. Carter, "Bone creep-fatigue damage accumulation," *J. Biomech.*, vol. 22, no. 6, 1989.

[21] L. E. Claes and C. a Heigele, "Magnitudes of local stress and strain along bony surfaces predict the course and type of fracture healing.," *J. Biomech.*, vol. 32, no. 3, pp. 255–66, Mar. 1999.

[22] B. Derbyshire, "Comment on 'Static vs dynamic loads as an influence on bone remodelling'.," *J. Biomech.*, vol. 18, no. 9, p. 729, Jan. 1985.

[23] C. T. Rubin and L. E. Lanyon, "Regulation of Bone Mass by Mechanical Strain Magnitude," pp. 411–417, 1985.

[24] C. H. Turner, "Three Rules for Bone Adaptation to Mechanical Stimuli," vol. 23, no. 5, pp. 399–407, 1998.

[25] L. E. Lanyona and C. T. Rubina, "Static vs dynamic loads as an influence on bone remodelling.," *J. Biomech.*, vol. 17, no. 9, pp. 897–905, 1984.

[26] S. Nagaraja, "Microstructure stresses and strains associated with trabecular bone microdamage," *Georgi*, no. December, 2006.

[27] K. C. McGilvray *et al.*, "Implantable microelectromechanical sensors for diagnostic monitoring and post-surgical prediction of bone fracture healing.," *J. Orthop. Res.*, vol. 33, no. 10, pp. 1439–46, Oct. 2015.

[28] L. C. Y. Wong, W. K. Chiu, M. Russ, and S. Liew, "Review of techniques for monitoring the healing fracture of bones for implementation in an internally fixated pelvis," *Med. Eng. Phys.*, vol. 34, no. 2, pp. 140–152, 2012.

[29] J. D. Boerckel, K. M. Dupont, Y. M. Kolambkar, A. S. P. Lin, and R. E. Guldberg, "In vivo model for evaluating the effects of mechanical stimulation on tissue-engineered bone repair.," *J. Biomech. Eng.*, vol. 131, no. 8, p. 84502, 2009.

[30] D. J. Chew *et al.*, "A Microchannel Neuroprosthesis for Bladder Control After Spinal Cord Injury in Rat," *Sci. Transl. Med.*, vol. 5, no. 210, p. 210ra155-210ra155, 2013.

[31] E. Y. Chow, A. L. Chlebowski, S. Chakraborty, W. J. Chappell, and P. P. Irazoqui, "Fully wireless implantable cardiovascular pressure monitor integrated with a medical stent," *IEEE Trans. Biomed. Eng.*, vol. 57, no. 6, pp. 1487–1496, 2010.

[32] P. Griss, P. Enoksson, H. K. Tolvanen-Laakso, P. Meriläinen, S. Ollmar, and G. Stemme, "Micromachined electrodes for biopotential measurements," *J. Microelectromechanical Syst.*, vol. 10, no. 1, pp. 10–16, 2001.

[33] H. Cao *et al.*, "An implantable, batteryless, and wireless capsule with integrated impedance and pH sensors for gastroesophageal reflux monitoring," *IEEE Trans. Biomed. Eng.*, vol. 59, no. 12 PART2, pp. 3131–3139, 2012.

[34] R. W. Troughton *et al.*, “Direct left atrial pressure monitoring in severe heart failure: Long-term sensor performance,” *J. Cardiovasc. Transl. Res.*, vol. 4, no. 1, pp. 3–13, 2011.

[35] K. Totsu, Y. Haga, and M. Esashi, “Vacuum sealed ultra miniature fiber-optic pressure sensor using white light interferometry,” *TRANSDUCERS 2003 - 12th Int. Conf. Solid-State Sensors, Actuators Microsystems, Dig. Tech. Pap.*, vol. 1, pp. 931–934, 2003.

[36] A. Lal, “Integrated pressure and flow sensor in silicon-based ultrasonic surgical actuator,” in *2001 IEEE Ultrasonics Symposium. Proceedings. An International Symposium (Cat. No.01CH37263)*, 2001, vol. 2, pp. 1373–1376.

[37] M. K. Hong *et al.*, “Can coronary flow parameters after stent placement predict restenosis?,” *Cathet. Cardiovasc. Diagn.*, vol. 36, no. 3, pp. 278–282, 1995.

[38] F. Umbrecht, M. Wendlandt, D. Juncker, C. Hierold, and J. Neuenschwander, “A wireless implantable passive strain sensor system,” in *Proceedings of IEEE Sensors*, 2005, vol. 2005, pp. 20–23.

[39] C. K. Mahutte, “On-line arterial blood gas analysis with optodes: current status.,” *Clin. Biochem.*, vol. 31, no. 3, pp. 119–30, 1998.

[40] Y. T. Kim, Y.-Y. Kim, and C.-H. Jun, “Needle-shaped glucose sensor with multi-cell electrode fabricated by surface micromachining,” vol. 3680, no. II, pp. 924–930, 1999.

[41] J. J. Mastrototaro, K. W. Cooper, G. Soundararajan, J. B. Sanders, and R. V. Shah, “Clinical experience with an integrated continuous glucose sensor/insulin pump platform: A feasibility study,” *Adv. Ther.*, vol. 23, no. 5, pp. 725–732, 2006.

[42] Y. Ling, T. Pong, C. C. Vassiliou, P. L. Huang, and M. J. Cima, “Implantable magnetic relaxation sensors measure cumulative exposure to cardiac biomarkers.,” *Nat. Biotechnol.*, vol. 29, no. 3, pp. 273–277, 2011.

[43] A. D. DeHennis and K. D. Wise, “A fully integrated multisite pressure sensor for wireless arterial flow characterization,” *J. Microelectromechanical Syst.*, vol. 15, no. 3, pp. 678–685, 2006.

[44] J. L. T. Ritzema-Carter *et al.*, “Dynamic myocardial ischemia caused by circumflex artery stenosis detected by a new implantable left atrial pressure monitoring device,” *Circulation*, vol. 113, no. 15, pp. 705–707, 2006.

[45] U. Schnakenberg *et al.*, “Intravascular pressure monitoring system,” *Sensors Actuators, A Phys.*, vol. 110, no. 1–3, pp. 61–67, 2004.

[46] M. D. Twa, C. J. Roberts, H. J. Karol, A. M. Mahmoud, P. a Weber, and R. H. Small, “Evaluation of a contact lens-embedded sensor for intraocular pressure measurement.,” *J. Glaucoma*, vol. 19, no. 6, pp. 382–390, 2010.

[47] H. Miyake, T. Ohta, Y. Kajimoto, and M. Matsukawa, “A new ventriculoperitoneal shunt with a telemetric intracranial pressure sensor: Clinical experience in 94 patients with hydrocephalus,” *Neurosurgery*, vol. 40, no. 5, pp. 931–935, 1997.

[48] D. F. Signorini, a Shad, I. R. Piper, and P. F. Statham, “A clinical evaluation of the Codman MicroSensor for intracranial pressure monitoring.,” *Br. J. Neurosurg.*, vol. 12, no. 3, pp. 223–7, 1998.

[49] C. Story, “Remote Pressure Sensing for Thoracic Endografts,” *Surgery*, no. February, pp. 1–3, 2006.

[50] K. Takahata, A. DeHennis, K. D. Wise, and Y. B. Gianchandani, “A wireless microsensor for monitoring flow and pressure in a blood vessel utilizing a dual-inductor antenna stent and two pressure sensors,” *17th IEEE Int. Conf. Micro Electro Mech. Syst. Maastricht MEMS 2004 Tech. Dig.*, pp. 216–219, 2004.

[51] A. Magalski *et al.*, “Continuous ambulatory right heart pressure measurements with an implantable hemodynamic monitor: A multicenter, 12-month follow-up study of patients with chronic heart failure,” *J. Card. Fail.*, vol. 8, no. 2, pp. 63–70, 2002.

[52] Renard, “Implantable glucose sensors for diabetes monitoring.,” *Minim. Invasive Ther. Allied Technol.*, vol. 13, no. 2, pp. 78–86, 2004.

[53] R. A. M. Receveur, C. R. Marxer, R. Woering, V. C. M. H. Larik, and N. F. de Rooij, “Laterally moving bistable MEMS DC switch for biomedical applications,” *J. Microelectromechanical Syst.*, vol. 14, no. 5, pp. 1089–1098, 2005.

[54] M. Schwarz *et al.*, “Single chip CMOS imagers and flexible microelectronic stimulators for a retina implant system,” *Sensors Actuators, A Phys.*, vol. 83, no. 1, pp. 40–46, 2000.

[55] E. Siwapornsathain, A. Lal, and J. Binard, “A telemetry and sensor platform for ambulatory urodynamics,” *2nd Annu. Int. IEEE-EMBS Spec. Top. Conf. Microtechnologies Med. Biol. - Proc.*, pp. 283–287, 2002.

[56] L. E. Claes and J. L. Cunningham, “Monitoring the mechanical properties of healing bone.,” *Clin. Orthop. Relat. Res.*, vol. 467, no. 8, pp. 1964–71, Aug. 2009.

[57] D. D. D’Lima, B. J. Fregly, and C. W. Colwell, “Implantable sensor technology: measuring bone and joint biomechanics of daily life in vivo.,” *Arthritis Res. Ther.*, vol. 15, no. 1, p. 203, 2013.

[58] K. Seide *et al.*, “Telemetric assessment of bone healing with an instrumented internal fixator: a preliminary study.,” *J. Bone Joint Surg. Br.*, vol. 94, no. 3, pp. 398–404, 2012.

[59] C. T. Brighton and A. G. Krebs, “Oxygen tension of healing fractures in the rabbit.,” *J. Bone Joint Surg. Am.*, vol. 54, no. 2, pp. 323–32, Mar. 1972.

[60] D. R. Epari, J. Lienau, H. Schell, F. Witt, and G. N. Duda, “Pressure, oxygen tension and temperature in the periosteal callus during bone healing-An in vivo study in sheep,” *Bone*, vol. 43, no. 4, pp. 734–739, 2008.

[61] M. C. Frost and M. E. Meyerhoff, “Implantable chemical sensors for real-time clinical monitoring: Progress and challenges,” *Current Opinion in Chemical Biology*, vol. 6, no. 5. pp. 633–641, 2002.

[62] R. Langer, “Drug delivery and targeting,” *Nature*, vol. 392, no. 6679, pp. 5–10, 1998.

[63] A. Azagury, L. Khoury, G. Enden, and J. Kost, “Ultrasound mediated transdermal drug delivery,” *Advanced Drug Delivery Reviews*, vol. 72. pp. 127–143, 2014.

[64] W. Gao, J. Chan, and O. C. Farokhzad, “pH-Responsive Nanoparticles for Drug Delivery,” *Mol. Pharm.*, vol. 7, no. 6, pp. 1913–1920, 2010.

[65] J. Liu *et al.*, “PH-Sensitive nano-systems for drug delivery in cancer therapy,” *Biotechnology Advances*, vol. 32, no. 4. pp. 693–710, 2014.

[66] M. Bikram, A. M. Gobin, R. E. Whitmire, and J. L. West, “Temperature-sensitive hydrogels with SiO2-Au nanoshells for controlled drug delivery,” *J. Control. Release*, vol. 123, no. 3, pp. 219–227, 2007.

[67] A. N. Koo *et al.*, “Disulfide-cross-linked PEG-poly(amino acid)s copolymer micelles for glutathione-mediated intracellular drug delivery.,” *Chem. Commun. (Camb).*, no. 48, pp. 6570–2, 2008.

[68] J. Banerjee *et al.*, “Release of liposomal contents by cell-secreted matrix metalloproteinase-9,” *Bioconjug. Chem.*, vol. 20, no. 7, pp. 1332–1339, 2009.

[69] J. Ge, E. Neofytou, T. J. Cahill, R. E. Beygui, and R. N. Zare, “Drug release from electric-field-responsive nanoparticles,” *ACS Nano*, vol. 6, no. 1, pp. 227–233, 2012.

[70] K. Cai *et al.*, “Magnetically triggered reversible controlled drug delivery from microfabricated polymeric multireservoir devices,” *Adv. Mater.*, vol. 21, no. 40, pp. 4045–4049, 2009.

[71] D. J. H. Tng, R. Hu, P. Song, I. Roy, and K. T. Yong, “Approaches and challenges of engineering implantable microelectromechanical systems (MEMS) drug delivery systems for in vitro and in vivo applications,” *Micromachines*, vol. 3, no. 4, pp. 615–631, 2012.

[72] and N. A. P. Steichen, Stephanie D., Mary Caldorera-Moore, “A review of current nanoparticle and targeting moieties for the delivery of cancer therapeutics,” *Off. J. Eur. Fed. Pharm. Sci.*, vol. 48(3), pp. 416–427, 2013.

[73] G. A. Salvatore *et al.*, “Biodegradable and Highly Deformable Temperature Sensors for the Internet of Things,” *Adv. Funct. Mater.*, vol. 27, no. 35, pp. 1–10, 2017.

[74] Q. Zheng *et al.*, “Biodegradable triboelectric nanogenerator as a life-time designed implantable power source,” *Sci. Adv.*, vol. 2, no. 3, p. e1501478, 2016.

[75] R. K. Pal, A. A. Farghaly, C. Wang, M. M. Collinson, S. C. Kundu, and V. K. Yadavalli, “Conducting polymer-silk biocomposites for flexible and biodegradable electrochemical sensors,” *Biosens. Bioelectron.*, vol. 81, pp. 294–302, 2016.

[76] J.-K. Chang, H. Fang, C. A. Bower, E. Song, X. Yu, and J. A. Rogers, “Materials and processing approaches for foundry-compatible transient electronics,” *Proc. Natl. Acad. Sci.*, vol. 114, no. 28, pp. E5522–E5529, 2017.

[77] S. K. Kang *et al.*, “Bioresorbable silicon electronic sensors for the brain,” *Nature*, vol. 530, no. 7588, pp. 71–76, 2016.

[78] A. Tamayol *et al.*, “Biodegradable elastic nanofibrous platforms with integrated flexible heaters for on-demand drug delivery,” *Sci. Rep.*, vol. 7, no. 1, pp. 1–10, 2017.

[79] M. Luo, W. Shen, Y. Wang, and M. G. Allen, “IN VITRO DEGRADATION OF BIODEGRADABLE METAL ZN AND ZN / FE-COUPLES AND University of Pennsylvania , Philadelphia , PA , USA The recorded potential dynamic polarization diagrams,” pp. 1370–1373, 2015.

[80] M. Luo, “Materials and Microfabrication Approaches for Completely Biodegradable Wireless Micromachined Sensors,” Georgia Institute of Technology, 2014.

[81] L. Yin *et al.*, “Materials, designs, and operational characteristics for fully biodegradable primary batteries,” *Adv. Mater.*, vol. 26, no. 23, pp. 3879–3884, 2014.

[82] F. Witte *et al.*, “In vitro and in vivo corrosion measurements of magnesium alloys,” *Biomaterials*, vol. 27, no. 7, pp. 1013–1018, 2006.

[83] J. Wang *et al.*, “Recommendation for modifying current cytotoxicity testing standards for biodegradable magnesium-based materials,” *Acta Biomater.*, vol. 21, pp. 237–249, 2015.

[84] F. Witte *et al.*, *Degradable biomaterials based on magnesium corrosion*, vol. 12, no. 5–6. 2008.

[85] S. Hwang *et al.*, "A Physically Transient Form of Silicon Electronics," *Science (80-.).*, vol. 337, no. 6102, pp. 1640–1644, 2013.

[86] Y. J. Kim, S.-E. Chun, J. Whitacre, and C. J. Bettinger, "Self-deployable current sources fabricated from edible materials," *J. Mater. Chem. B*, vol. 1, no. 31, p. 3781, 2013.

[87] Y. J. Kim, W. Wu, S.-E. Chun, J. F. Whitacre, and C. J. Bettinger, "Biologically derived melanin electrodes in aqueous sodium-ion energy storage devices.," *Proc. Natl. Acad. Sci. U. S. A.*, vol. 110, no. 52, pp. 20912–7, 2013.

[88] B. Finamore *et al.*, "Development of an Implantable Biodegradable Electrical Stimulator for Bone Repair," p. 15213.

[89] J. E. Gray and B. Luan, "Protective coatings on magnesium and its alloys — a critical review," *J. Alloys Compd.*, vol. 336, pp. 88–113, 2002.

[90] R. Walter and M. B. Kannan, "Influence of surface roughness on the corrosion behaviour of magnesium alloy," *Mater. Des.*, vol. 32, no. 4, pp. 2350–2354, 2011.

[91] M. H. Lee, I. Y. Bae, K. J. Kim, K. M. Moon, and T. Oki, "Formation mechanism of new corrosion resistance magnesium thin films by PVD method," *Surf. Coatings Technol.*, vol. 169–170, pp. 670–674, 2003.

[92] W. J. Fawcett, E. J. Haxby, and D. a Male, "Magnesium: physiology and pharmacology.," *Br. J. Anaesth.*, vol. 83, no. 2, pp. 302–20, Aug. 1999.

[93] N. E. Saris, E. Mervaala, H. Karppanen, J. a Khawaja, and a Lewenstam, "Magnesium. An update on physiological, clinical and analytical aspects.," *Clin. Chim. Acta.*, vol. 294, no. 1–2, pp. 1–26, Apr. 2000.

[94] D. Aurbach, A. Schechter, M. Moshkovich, and Y. Cohen, "On the Mechanisms of Reversible Magnesium Deposition Processes," *J. Electrochem. Soc.*, vol. 148, no. 9, p. A1004, 2001.

[95] Y. Yun *et al.*, "Revolutionizing biodegradable metals," *Mater. Today*, vol. 12, no. 10, pp. 22–32, 2009.

[96] M. Moravej and D. Mantovani, "Biodegradable metals for cardiovascular stent application: Interests and new opportunities," *Int. J. Mol. Sci.*, vol. 12, no. 7, pp. 4250–4270, 2011.

[97] G. Y. Yang, V. J. Bailey, G. Lin, W. C. Tang, and J. H. Keyak, "Design of microfabricated strain gauge array to monitor bone deformation in vitro and in vivo," *Proc. - Fourth IEEE Symp. Bioinforma. Bioeng. BIBE 2004*, no. Bibe, pp. 30–37, 2004.

[98] V. Correia, V. Sencadas, M. S. Martins, C. Ribeiro, P. Alpuim, and J. G. Rocha, "Sensors and Actuators A : Physical Piezoresistive sensors for force mapping of hip-prostheses," *Sensors Actuators A. Phys.*, vol. 195, pp. 133–138, 2013.

[99] H. Hermawan, M. Moravej, D. Dubé, M. Fiset, and D. Mantovani, "Degradation Behaviour of Metallic Biomaterials for Degradable Stents," *Adv. Mater. Res.*, vol. 15–17, pp. 113–118, 2007.

[100] M. Moravej, S. Amira, F. Prima, A. Rahem, M. Fiset, and D. Mantovani, "Effect of electrodeposition current density on the microstructure and the degradation of electroformed iron for degradable stents," *Mater. Sci. Eng. B Solid-State Mater. Adv. Technol.*, vol. 176, no. 20, pp. 1812–1822, 2011.

[101] N. Hirai, H. Ishikawa, and Y. Ohki, “Electrical Conduction Properties of Several Biode- gradable Polymers,” pp. 592–595, 2007.

[102] S. Izwan, A. Razak, N. Fadzliana, A. Sharif, W. Aizan, and W. Abdul, “Biodegradable Polymers and their Bone Applications : A Review,” *Int. J. Basic Appl. Sci.*, vol. 12, no. 1, pp. 31–49, 2012.

[103] R. Shogren, “Water Vapor Permeability of Biodegradable Polymers,” vol. 5, no. 2, pp. 4–8, 1997.

[104] S. Eshraghi and S. Das, “Mechanical and microstructural properties of polycaprolactone scaffolds with one-dimensional, two-dimensional, and three-dimensional orthogonally oriented porous architectures produced by selective laser sintering,” *Acta Biomater.*, vol. 6, no. 7, pp. 2467–2476, 2010.

[105] J. M. Williams *et al.*, “Bone tissue engineering using polycaprolactone scaffolds fabricated via selective laser sintering.,” *Biomaterials*, vol. 26, no. 23, pp. 4817–27, Aug. 2005.

[106] Y. Gao, T. Chen, X. Wang, and J. Tang, “Influence of hot embossed process parameters on biodegradable polymer microstructure for drug delivery,” *NEMS 2011 - 6th IEEE Int. Conf. Nano/Micro Eng. Mol. Syst.*, pp. 1246–1249, 2011.

[107] P. Gentile, V. Chiono, I. Carmagnola, and P. V Hatton, “An overview of poly(lactic-co-glycolic) acid (PLGA)-based biomaterials for bone tissue engineering.,” *Int. J. Mol. Sci.*, vol. 15, no. 3, pp. 3640–59, Jan. 2014.

[108] J. S. Lewis and M. S. Weaver, “Thin-Film Permeation-Barrier Technology for Flexible Organic Light-Emitting Devices,” vol. 10, no. 1, pp. 45–57, 2004.

[109] F. Witte *et al.*, “In vivo corrosion of four magnesium alloys and the associated bone response,” *Biomaterials*, vol. 26, no. 17, pp. 3557–3563, 2005.

[110] F. Witte, “The history of biodegradable magnesium implants: a review.,” *Acta Biomater.*, vol. 6, no. 5, pp. 1680–92, May 2010.

[111] S.-W. Hwang *et al.*, “A physically transient form of silicon electronics.,” *Science*, vol. 337, no. 6102, pp. 1640–4, Sep. 2012.

[112] C. M. Boutry, H. Chandrahalim, and C. Hierold, “Characterization of RF resonators made of biodegradable materials for biosensing applications,” *Procedia Eng.*, vol. 25, pp. 1529–1532, 2011.

[113] K. Schlüter, C. Zamponi, A. Piorra, and E. Quandt, “Comparison of the corrosion behaviour of bulk and thin film magnesium alloys,” *Corros. Sci.*, vol. 52, no. 12, pp. 3973–3977, 2010.

[114] D. M. Allen, M. Simpkins, and H. Almond, “A novel photochemical machining process for magnesium aerospace and biomedical microengineering applications,” *J. Micromechanics Microengineering*, vol. 20, no. 10, 2010.

[115] M. Tsang, F. Herrault, R. H. Shafer, and M. G. Allen, “Methods for the microfabrication of magnesium,” *2013 IEEE 26th Int. Conf. Micro Electro Mech. Syst.*, pp. 347–350, Jan. 2013.

[116] C. M. Boutry, H. Chandrahalim, P. Streit, M. Schinhammer, A. C. Hänzi, and C. Hierold, “Towards biodegradable wireless implants.,” *Philos. Trans. A. Math. Phys. Eng. Sci.*, vol. 370, no. 1967, pp. 2418–32, May 2012.

[117] R. J. Gummow and Y. He, “Morphology and Preferred Orientation of Pulse Electrodeposited Magnesium,” *J. Electrochem. Soc.*, vol. 157, no. 4, p. E45, 2010.

[118] N. Amir, Y. Vestfrid, O. Chusid, Y. Gofer, and D. Aurbach, “Progress in nonaqueous magnesium electrochemistry,” *J. Power Sources*, vol. 174, no. 2, pp. 1234–1240, 2007.

[119] C. Liebenow, Z. Yang, P. Lobitz, E. Moritz, and A. Uniõersitat, “The electrodeposition of magnesium using solutions of organomagnesium halides , amidomagnesium halides and magnesium organoborates,” pp. 1–5, 2000.

[120] C. Liebenow, “Reversibility of electrochemical magnesium deposition from Grignard solutions,” *J. Appl. Electrochem.*, vol. 27, no. 2, pp. 221–225, 1997.

[121] P. Wang, Y. NuLi, J. Yang, and Z. Feng, “Mixed ionic liquids as electrolyte for reversible deposition and dissolution of magnesium,” *Surf. Coatings Technol.*, vol. 201, no. 6, pp. 3783–3787, 2006.

[122] R. D. Rieke and S. E. Bales, “Activated Metals. IV. Preparation and Reactions of Highly Reactive Magnesium Metal’,” no. 26, pp. 1775–1781, 1972.

[123] S. Ben Hassen, L. Bousselmi, E. M. Rezrazi, P. Berçot, and E. Triki, “Comparative study of protective magnesium deposit behaviour obtained by continuous and pulsed currents from methylmagnesium chloride solution,” *Surf. Coatings Technol.*, vol. 202, no. 15, pp. 3579–3584, 2008.

[124] M. Tsang, A. Armutlulu, A. Martinez, F. Herrault, S. A. Bidstrup-Allen, and M. G. Allen, “A MEMS-enabled biodegradable battery for powering transient implantable devices,” *Proc. 2014 IEEE 27th Int. Conf. Microelectromechanical Syst. (MEMS)*, 2014.

[125] a. B. Frazier and M. G. Allen, “Uses of electroplated aluminum for the development of microstructures and micromachining processes,” *J. Microelectromechanical Syst.*, vol. 6, no. 2, pp. 91–98, Jun. 1997.

[126] T. D. Gregory, “Nonaqueous Electrochemistry of Magnesium,” *J. Electrochem. Soc.*, vol. 137, no. 3, p. 775, 1990.

[127] P. Gunde, “Biodegradable magnesium alloys for osteosynthesis - Alloy development and surface modifications,” *Thesis Diss. from ETH Zurich*, vol. No. 19171, no. 19171, 2010.

[128] Y. Xin, “Corrosion behavior of biomedical AZ91 magnesium alloy in simulated body fluids,” *J. Mater. Res.*, vol. 22, no. 7, pp. 2004–2011, 2007.

[129] T. Assessment, “Polyvinyl Alcohol (Pva),” *Int. J. Toxicol.*, vol. 1, no. 3, pp. 3–5, 2004.

[130] M. Luo, C. Song, F. Herrault, M. G. Allen, and M. Science, “A MICROFABRICATED WIRELESS RF PRESSURE SENSOR MADE COMPLETELY OF BIODEGRADABLE MATERIALS,” *Conf. Proc. from 2012 Solid-State Sensors, Actuators, Microsystems Work.*, pp. 2–5.

[131] P. M. Dentinger, W. M. Clift, and S. H. Goods, “Removal of SU-8 photoresist for thick film applications,” *Microelectron. Eng.*, vol. 61–62, pp. 993–1000, 2002.

[132] A. Kono, Y. Arai, Y. Goto, and H. Horibe, “<title>Removal of SU-8 resists using hydrogen radicals generated by tungsten hot-wire catalyzer</title>,” vol. 8328, p. 83280R–83280R–10, 2012.

[133] J. Tang, S. R. Green, and Y. B. Gianchandani, “Miniature wireless resonant rotary motor actuated by litographically micromachined magnetoelastic foil,” *Conf. Proc. from 2012 Solid-State Sensors, Actuators, Microsystems Work.*, pp. 86–89, 2012.

[134] C. Blawert, W. Dietzel, E. Ghali, and G. Song, “Anodizing Treatments for Magnesium Alloys and Their Effect on Corrosion Resistance in Various Environments,” *Adv. Eng. Mater.*, vol. 8, no. 6, pp. 511–533, Jun. 2006.

[135] X. N. Gu and Y. F. Zheng, “A review on magnesium alloys as biodegradable materials,” *Front. Mater. Sci. China*, vol. 4, no. 2, pp. 111–115, 2010.

[136] F. Witte, “Reprint of: The history of biodegradable magnesium implants: A review,” *Acta Biomater.*, vol. 23, no. S, pp. S28–S40, 2015.

[137] F. El-Taib Heakal, N. S. Tantawy, and O. S. Shehata, “Impact of chloride and fluoride additions on surface reactivity and passivity of AM60 magnesium alloy in buffer solution,” *Corros. Sci.*, vol. 64, pp. 153–163, 2012.

[138] S. Y. Zhang, Q. Li, B. Chen, S. Q. Xu, J. M. Fan, and F. Luo, “Electrodeposition of zinc on AZ91D magnesium alloy pre-treated by stannate conversion coatings,” *Mater. Corros.*, vol. 61, no. 10, pp. 860–865, 2010.

[139] C. S. Lin, H. C. Lin, K. M. Lin, and W. C. Lai, “Formation and properties of stannate conversion coatings on AZ61 magnesium alloys,” *Corros. Sci.*, vol. 48, no. 1, pp. 93–109, 2006.

[140] H. Huo, Y. Li, and F. Wang, “Corrosion of AZ91D magnesium alloy with a chemical conversion coating and electroless nickel layer,” *Corros. Sci.*, vol. 46, no. 6, pp. 1467–1477, 2004.

[141] C. Blawert, W. Dietzel, E. Ghali, and G. Song, “Anodizing treatments for magnesium alloys and their effect on corrosion resistance in various environments,” *Adv. Eng. Mater.*, vol. 8, no. 6, pp. 511–533, 2006.

[142] Y. Zhang, C. Yan, F. Wang, H. Lou, and C. Cao, “Study on the environmentally friendly anodizing of AZ91D magnesium alloy,” *Surf. Coatings Technol.*, vol. 161, no. 1, pp. 36–43, 2002.

[143] Y. Mizutani, S. J. Kim, R. Ichino, and M. Okido, “Anodizing of Mg alloys in alkaline solutions,” *Surf. Coatings Technol.*, vol. 169–170, pp. 143–146, 2003.

[144] Y. Song, S. Zhang, J. Li, C. Zhao, and X. Zhang, “Electrodeposition of Ca-P coatings on biodegradable Mg alloy: In vitro biomineralization behavior,” *Acta Biomater.*, vol. 6, no. 5, pp. 1736–1742, 2010.

[145] I. S. Roncˇevic, Z. Grubacˇ, and M. Metikosˇ-Hukovic´, “Electrodeposition of hydroxyapatite coating on AZ91D alloy for biodegradable implant application,” *Int. J. Electrochem. Sci.*, vol. 9, no. 11, pp. 5907–5923, 2014.

[146] S. T. Jiang, J. Zhang, S. Z. Shun, and M. F. Chen, “The formation of FHA coating on biodegradable Mg-Zn-Zr alloy using a two-step chemical treatment method,” *Appl. Surf. Sci.*, vol. 388, no. 3, pp. 424–430, 2016.

[147] L. Jiang, M. Li, W. Zhang, and J. Shen, “Electrochemical corrosion behavior of nanocrystalline zinc coatings in 3.5% NaCl solution,” *J. Chinese Soc. Corros. Prot.*, vol. 28, no. 5, pp. 303–306, 2008.

[148] M. Mouanga, L. Ricq, J. Douglade, and P. Berçot, “Effects of some additives on the corrosion behaviour and preferred orientations of zinc obtained by continuous current deposition,” *J. Appl. Electrochem.*, vol. 37, no. 2, pp. 283–289, 2007.

[149] G. Katarivas Levy, J. Goldman, and E. Aghion, “The Prospects of Zinc as a Structural Material for Biodegradable Implants—A Review Paper,” *Metals (Basel).*, vol. 7, no. 10, p. 402, 2017.

[150] P. K. Bowen *et al.*, "Biodegradable metlas for cardiovascular stents: from clinical concerns to recent Zn - alloys," *Adv. Healthc. Mater.*, vol. 5, no. 10, pp. 1121–1140, 2017.

[151] W. Simka, D. Puszczyk, and G. Nawrat, "Electrodeposition of metals from non-aqueous solutions," *Electrochim. Acta*, vol. 54, no. 23, pp. 5307–5319, 2009.

[152] A. Bakkar and V. Neubert, "Electrodeposition onto magnesium in air and water stable ionic liquids: From corrosion to successful plating," *Electrochem. commun.*, vol. 9, no. 9, pp. 2428–2435, 2007.

[153] C. J. Park, M. M. Lohrengel, T. Hamelmann, M. Pilaski, and H. S. Kwon, "Grain-dependent passivation of surfaces of polycrystalline zinc," *Electrochim. Acta*, vol. 47, no. 21, pp. 3395–3399, 2002.

[154] S. Hiromoto and A. Yamamoto, "High corrosion resistance of magnesium coated with hydroxyapatite directly synthesized in an aqueous solution," *Electrochim. Acta*, vol. 54, no. 27, pp. 7085–7093, 2009.

[155] M. Wei, A. J. Ruys, M. V. Swain, S. H. Kim, B. K. Milthorpe, and C. C. Sorrell, "Interfacial bond strength of electrophoretically deposited hydroxyapatite coatings on metals," *J. Mater. Sci. Mater. Med.*, vol. 10, no. 7, pp. 401–409, 1999.

[156] Y. Su, G. Li, and J. Lian, "A chemical conversion hydroxyapatite coating on AZ60 magnesium alloy and its electrochemical corrosion behaviour," *Int. J. Electrochem. Sci.*, vol. 7, no. 11, pp. 11497–11511, 2012.

[157] H. X. Wang, S. K. Guan, X. Wang, C. X. Ren, and L. G. Wang, "In vitro degradation and mechanical integrity of Mg-Zn-Ca alloy coated with Ca-deficient hydroxyapatite by the pulse electrodeposition process," *Acta Biomater.*, vol. 6, no. 5, pp. 1743–1748, 2010.

[158] M. Jamesh, S. Kumar, and T. S. N. S. Narayanan, "Electrodeposition of hydroxyapatite coating on magnesium for biomedical applications," *J. Coatings Technol. Res.*, vol. 9, no. 4, pp. 495–502, 2012.

[159] C.-C. Yang, C.-Y. Huang, C.-C. Lin, and S.-K. Yen, "Electrolytic Deposition of Collagen/HA Composite on Post HA/TiO[sub 2] Coated Ti6Al4V Implant Alloy," *J. Electrochem. Soc.*, vol. 158, no. 2, p. E13, 2011.

[160] T. Laonapakul, A. Rakngarm Nimkerdphol, Y. Otsuka, and Y. Mutoh, "Failure behavior of plasma-sprayed HAp coating on commercially pure titanium substrate in simulated body fluid (SBF) under bending load," *J. Mech. Behav. Biomed. Mater.*, vol. 15, pp. 153–166, 2012.

[161] C. Benaqqa, J. Chevalier, M. Saädaoui, and G. Fantozzi, "Slow crack growth behaviour of hydroxyapatite ceramics," *Biomaterials*, vol. 26, no. 31, pp. 6106–6112, 2005.

[162] J. Li *et al.*, "In vitro responses of human bone marrow stromal cells to a fluoridated hydroxyapatite coated biodegradable Mg-Zn alloy," *Biomaterials*, vol. 31, no. 22, pp. 5782–5788, 2010.

[163] S. Miao *et al.*, "Sol-gel preparation of Zn-doped fluoridated hydroxyapatite films," *Surf. Coatings Technol.*, vol. 198, no. 1–3 SPEC. ISS., pp. 223–226, 2005.

[164] E. C. Meng *et al.*, "Effect of electrodeposition modes on surface characteristics and corrosion properties of fluorine-doped hydroxyapatite coatings on Mg-Zn-Ca alloy," *Appl. Surf. Sci.*, vol. 257, no. 11, pp. 4811–4816, 2011.

[165] N. Rameshbabu, T. S. Sampath Kumar, and K. Prasad Rao, "Synthesis of nanocrystalline

fluorinated hydroxyapatite by microwave processing and its in vitro dissolution study," *Bull. Mater. Sci.*, vol. 29, no. 6, pp. 611–615, 2006.

[166] C. C. Wu, S. Te Huang, T. W. Tseng, Q. L. Rao, and H. C. Lin, "FT-IR and XRD investigations on sintered fluoridated hydroxyapatite composites," *J. Mol. Struct.*, vol. 979, no. 1–3, pp. 72–76, 2010.

[167] Y. Chen and X. Miao, "Effect of fluorine addition on the corrosion resistance of hydroxyapatite ceramics," *Ceram. Int.*, vol. 30, no. 7, pp. 1961–1965, 2004.

[168] K. Rezwan, Q. Z. Chen, J. J. Blaker, and A. R. Boccaccini, "Biodegradable and bioactive porous polymer/inorganic composite scaffolds for bone tissue engineering," *Biomaterials*, vol. 27, no. 18, pp. 3413–3431, 2006.

[169] C. Cuevas-Arteaga and J. Porcayo-Calderón, "Electrochemical noise analysis in the frequency domain and determination of corrosion rates for SS-304 stainless steel," *Mater. Sci. Eng. A*, vol. 435–436, pp. 439–446, 2006.

[170] J. J. Perdomo and P. M. Singh, "Electrochemical Noise (Ecn) Measurements as a Corrosion Monitoring Tool: A Review," *Corros. Rev.*, vol. 20, no. 4, pp. 359–378, 2002.

[171] Y. Xin, C. Liu, X. Zhang, G. Tang, X. Tian, and P. K. Chu, "Corrosion behavior of biomedical AZ91 magnesium alloy in simulated body fluids," *J. Mater. Res.*, vol. 22, no. 7, pp. 2004–2011, 2007.

[172] S. H. E. Rt and A. Estimate, "Chapter 3: Electrochemical Kinetics of Corrosion," *Corros. Eng.*, pp. 651–665, 2015.

[173] A. J. Bard and L. R. Faulkner, *Electrochemical Methods: Fundamentals and Applications*, 2nd ed. John Wiley & Sons, Inc, 2001.

[174] Y. Xin, J. Jiang, K. Huo, G. Tang, X. Tian, and P. K. Chu, "Corrosion resistance and cytocompatibility of biodegradable surgical magnesium alloy coated with hydrogenated amorphous silicon," *J. Biomed. Mater. Res. - Part A*, vol. 89, no. 3, pp. 717–726, 2009.

[175] N. Winzer *et al.*, "A critical review of the Stress Corrosion Cracking (SCC) of magnesium alloys," *Adv. Eng. Mater.*, vol. 7, no. 8, pp. 659–693, 2005.

[176] R. a. Cottis and S. Turgoose, "Electrochemical Noise Measurements - A Theoretical Basis," *Materials Science Forum*, vol. 192–194. pp. 663–672, 1995.

[177] R. A. Cottis, "Interpretation of Electrochemical Noise Data," vol. 57, no. 3, pp. 265–285, 2001.

[178] C. A. . b Loto, "Electrochemical noise measurement technique in corrosion research," *Int. J. Electrochem. Sci.*, vol. 7, no. 10, pp. 9248–9270, 2012.

[179] G199-09, "Standard Guide for Electrochemical Noise Measurement," *ASTM Int.*, vol. 9, no. Reapproved, pp. 1–9, 2014.

[180] T. Zhang, X. Liu, Y. Shao, G. Meng, and F. Wang, "Electrochemical noise analysis on the pit corrosion susceptibility of Mg-10Gd-2Y-0.5Zr, AZ91D alloy and pure magnesium using stochastic model," *Corros. Sci.*, vol. 50, no. 12, pp. 3500–3507, 2008.

[181] M. K. Cavanaugh, N. Birbilis, and R. G. Buchheit, "Modeling pit initiation rate as a function of environment for Aluminum alloy 7075-T651," *Electrochim. Acta*, vol. 59, pp. 336–345, 2012.

[182] A. R. Trueman, "Determining the probability of stable pit initiation on aluminium alloys using

potentiostatic electrochemical measurements," *Corros. Sci.*, vol. 47, no. 9, pp. 2240–2256, 2005.

[183] G. Engelhardt and D. D. Macdonald, "Unification of the deterministic and statistical approaches for predicting localized corrosion damage. I. Theoretical foundation," *Corros. Sci.*, vol. 46, no. 11, pp. 2755–2780, 2004.

[184] T. Shibata, "Application of extreme-value statistics to corrosion," *J. Res. Natl. Inst. Stand. Technol.*, vol. 99, no. 4, p. 327, 1994.

[185] H. Klumbies *et al.*, "Thickness dependent barrier performance of permeation barriers made from atomic layer deposited alumina for organic devices," *Org. Electron. physics, Mater. Appl.*, vol. 17, pp. 138–143, 2015.

[186] A. B. Chwang *et al.*, "Thin film encapsulated flexible organic electroluminescent displays," *Appl. Phys. Lett.*, vol. 83, no. 3, pp. 413–415, 2003.

[187] E. Kim, Y. Han, W. Kim, K. C. Choi, H. G. Im, and B. S. Bae, "Thin film encapsulation for organic light emitting diodes using a multi-barrier composed of MgO prepared by atomic layer deposition and hybrid materials," *Org. Electron. physics, Mater. Appl.*, vol. 14, no. 7, pp. 1737–1743, 2013.

[188] G. L. Graff, R. E. Williford, and P. E. Burrows, "Mechanisms of vapor permeation through multilayer barrier films: Lag time versus equilibrium permeation," *J. Appl. Phys.*, vol. 96, no. 4, pp. 1840–1849, 2004.

[189] H. Klumbies, "Encapsulations for Organic Devices and their Evaluation using Calcium Corrosion Tests," *Dissertation*, 2013.

[190] C. T. Pan, Y. C. Chen, M. F. Chen, and Y. C. Hsu, "Fabrication and design of various dimensions of multi-step ashperical microlens arrays for OLED package," *Opt. Commun.*, vol. 284, no. 13, pp. 3323–3330, 2011.

[191] G. H. Kim, J. Oh, Y. S. Yang, L. M. Do, and K. S. Suh, "Lamination process encapsulation for longevity of plastic-based organic light-emitting devices," *Thin Solid Films*, vol. 467, no. 1–2, pp. 1–3, 2004.

[192] K. M. Kim, B. J. Jang, W. S. Cho, and S. H. Ju, "The property of encapsulation using thin film multi layer for application to organic light emitting device," *Curr. Appl. Phys.*, vol. 5, no. 1, pp. 64–66, 2005.

[193] H. Klumbies *et al.*, "Water ingress into and climate dependent lifetime of organic photovoltaic cells investigated by calcium corrosion tests," *Sol. Energy Mater. Sol. Cells*, vol. 120, no. PART B, pp. 685–690, 2014.

[194] H. Chatham, "Review Oxygen diffusion barrier properties of transparent oxide coatings on polymeric substrates," *Surf. Coatings Technol.*, vol. 78, pp. 1–9, 1996.

[195] G. L. Siparsky, K. J. Voorhees, J. R. Dorgan, and K. Schilling, "Water transport in polylactic acid (PLA), PLA/polycaprolactone copolymers, and PLA/polyethylene glycol blends," *J. Environ. Polym. Degrad.*, vol. 5, no. 3, pp. 125–136, 1997.

[196] G. Nisato *et al.*, "Experimental comparison of high-performance water vapor permeation measurement methods," *Org. Electron. physics, Mater. Appl.*, vol. 15, no. 12, pp. 3746–3755, 2014.

[197] A. S. da Silva Sobrinho, G. Czeremuszkin, M. Latrèche, and M. R. Wertheimer, "Defect-

permeation correlation for ultrathin transparent barrier coatings on polymers," *J. Vac. Sci. Technol. A Vacuum, Surfaces, Film.*, vol. 18, no. 1, pp. 149–157, 2000.

[198] S. Schubert, H. Klumbies, L. Müller-Meskamp, and K. Leo, "Electrical calcium test for moisture barrier evaluation for organic devices," *Rev. Sci. Instrum.*, vol. 82, no. 9, 2011.

[199] H. Kim, A. K. Singh, C. Y. Wang, C. Fuentes-Hernandez, B. Kippelen, and S. Graham, "Experimental investigation of defect-assisted and intrinsic water vapor permeation through ultrabarrier films," *Rev. Sci. Instrum.*, vol. 87, no. 3, 2016.

[200] N. Kim, "Fabrication and Characterization of Thin-Film Encapsulation for Organic Electronics," *Georg. Inst. Technol. Thesis*, no. December, 2009.

[201] J. Greener, K. Ng, K. Vaeth, and T. Smith, "Effects of expandable graphite and modified ammonium polyphosphate on the flame-retardant and mechanical properties of wood flour-polypropylene composites," *Polym. Polym. Compos.*, vol. 21, no. 7, pp. 449–456, 2013.

[202] P. E. Burrows *et al.*, "Ultra barrier flexible substrates for flat panel displays," *Displays*, vol. 22, pp. 65–69, 2001.

[203] M. Madou, *Fundamentals of Microfabrication*. CRC Press LLC, 1997.

[204] S. D. Senturia, *Microsystem Design*. Springer Science+Businss Media LLC, 2001.

[205] J. Hennessy, A. D. Jewell, F. Greer, M. C. Lee, and S. Nikzad, "Atomic layer deposition of magnesium fluoride via bis(ethylcyclopentadienyl)magnesium and anhydrous hydrogen fluoride," *J. Vac. Sci. Technol. A*, vol. 33, no. 1, p. 01A125, 2015.

[206] T. Pilvi, E. Puukilainen, U. Kreissig, M. Leskelä, and M. Ritala, "Atomic Layer Deposition of MgF 2 Thin Films Using TaF 5 as a Novel Fluorine Source," *Chem. Mater.*, vol. 20, no. 15, pp. 5023–5028, 2008.

[207] C. P. Fonseca, F. C. Jr, F. a Amaral, C. a Z. Souza, and S. Neves, "Thermal and Conduction Properties of a PCL-biodegradable," vol. 2, pp. 52–63, 2007.

[208] M. A. Woodruff and D. W. Hutmacher, "The return of a forgotten polymer - Polycaprolactone in the 21st century," *Prog. Polym. Sci.*, vol. 35, no. 10, pp. 1217–1256, 2010.

[209] Y. Zhu, C. Gao, X. Liu, and J. Shen, "Surface modification of polycaprolactone membrane via aminolysis and biomacromolecule immobilization for promoting cytocompatibility of human endothelial cells," *Biomacromolecules*, vol. 3, no. 6, pp. 1312–1319, 2002.

[210] Z. G. Tang, R. A. Black, J. M. Curran, J. A. Hunt, N. P. Rhodes, and D. F. Williams, "Surface properties and biocompatibility of solvent-cast poly[ε-caprolactone] films," *Biomaterials*, vol. 25, no. 19, pp. 4741–4748, 2004.

[211] Q. Z. Chen, S. L. Liang, J. Wang, and G. P. Simon, "Manipulation of mechanical compliance of elastomeric PGS by incorporation of halloysite nanotubes for soft tissue engineering applications," *J. Mech. Behav. Biomed. Mater.*, vol. 4, no. 8, pp. 1805–1818, 2011.

[212] S. L. Liang, X. Y. Yang, X. Y. Fang, W. D. Cook, G. A. Thouas, and Q. Z. Chen, "In Vitro enzymatic degradation of poly (glycerol sebacate)-based materials," *Biomaterials*, vol. 32, no. 33, pp. 8486–8496, 2011.

[213] C. A. Sundback *et al.*, "Biocompatibility analysis of poly(glycerol sebacate) as a nerve guide material," *Biomaterials*, vol. 26, no. 27, pp. 5454–5464, 2005.

[214] S. L. Liang, W. D. Cook, G. A. Thouas, and Q. Z. Chen, “The mechanical characteristics and in vitro biocompatibility of poly(glycerol sebacate)-Bioglass®elastomeric composites,” *Biomaterials*, vol. 31, no. 33, pp. 8516–8529, 2010.

[215] W. Cai and L. Liu, “Shape-memory effect of poly (glycerol-sebacate) elastomer,” *Mater. Lett.*, vol. 62, no. 14, pp. 2175–2177, 2008.

[216] H. T. Nguyen *et al.*, “Electric field stimulation through a biodegradable polypyrrole-co-polycaprolactone substrate enhances neural cell growth,” *J. Biomed. Mater. Res. - Part A*, vol. 102, no. 8, pp. 2554–2564, 2014.

[217] H. Liu, R. Wang, H. K. Chu, and D. Sun, “Design and characterization of a conductive nanostructured polypyrrole-polycaprolactone coated magnesium/PLGA composite for tissue engineering scaffolds,” *J. Biomed. Mater. Res. - Part A*, vol. 103, no. 9, pp. 2966–2973, 2015.

[218] J. Nagstrup, S. Keller, K. Almdal, and A. Boisen, “3D microstructuring of biodegradable polymers,” *Microelectron. Eng.*, vol. 88, no. 8, pp. 2342–2344, 2011.

[219] G. Y. Yang, G. Johnson, W. C. Tang, and J. H. Keyak, “Parylene-based strain sensors for bone,” *IEEE Sens. J.*, vol. 7, no. 12, pp. 1693–1697, 2007.

[220] R. N. Das, F. D. Egitto, and V. R. Markovich, “Nano- and micro-filled conducting adhesives for z -axis interconnections: new direction for high-speed, high-density, organic microelectronics packaging,” *Circuit World*, vol. 34, no. 1, pp. 3–12, 2008.

[221] J. Liu, A. Tolvgârd, J. Malmodin, and Z. Lai, “A reliable and environmentally friendly packaging technology-flip - chip joining using anisotropically conductive adhesive,” *IEEE Trans. Components Packag. Technol.*, vol. 22, no. 2, pp. 186–190, 1999.

[222] M. Zwolinski *et al.*, “Electrically conductive adhesives for surface mount solder replacement,” *IEEE Trans. components, Packag. Manuf. Technol. Part C. Manuf.*, vol. 19, no. 4, pp. 241–250, 1996.

[223] N. Jackson and J. Muthuswamy, “Flexible chip-scale package and interconnect for implantable MEMS movable microelectrodes for the brain,” *J. Microelectromechanical Syst.*, vol. 18, no. 2, pp. 396–404, 2009.

[224] R. Tummala, *Fundamentals of Microsystems Packaging*. THe McGraw-Hill Companies, Inc., 2001.

[225] R. Tummala and M. Swaminathan, *Introduction to System-on-Package (SOP): Miniaturization of the Entire System*. THe McGraw-Hill Companies, Inc., 2008.

[226] S. Nurmi, J. Sundelin, E. Ristolainen, and T. Lepistö, “The effect of solder paste composition on the reliability of SnAgCu joints,” *Microelectron. Reliab.*, vol. 44, no. 3, pp. 485–494, 2004.

[227] M. J. Yim *et al.*, “Flip Chip Interconnection With Anisotropic Conductive Adhesives for RF and High-Frequency Applications,” *IEEE Trans. Components Packag. Manuf. Technol. Part B*, vol. 28, no. 4, pp. 789–796, 2005.

[228] L. Tongxiang, G. Wenli, Y. Yinghui, and T. Chunhe, “Electroless plating of silver on graphite powders and the study of its conductive adhesive,” *Int. J. Adhes. Adhes.*, vol. 28, no. 1–2, pp. 55–58, 2008.

[229] A. M. Lyons, E. Hall, Y. Wong, and G. Adams, “A New Approach to Using Anisotropicallv Conductive Adhesives for Flip-Chip Assembly,” *IEEE Trans. Components Packag. Technol. A*,

vol. 19, no. 1, pp. 5–11, 1996.

[230] L. Li, C. Lizzul, H. Kim, I. Sacolick, and J. E. Morris, “Electrical, Structural and Processing Properties of Electrically Conductive Adhesives,” *IEEE Trans. Components, Hybrids, Manuf. Technol.*, vol. 16, no. 8, pp. 843–851, 1993.

[231] R. Zhang, W. Lin, K. Lawrence, and C. P. Wong, “Highly reliable, low cost, isotropically conductive adhesives filled with Ag-coated Cu flakes for electronic packaging applications,” *Int. J. Adhes. Adhes.*, vol. 30, no. 6, pp. 403–407, 2010.

[232] R. Zhang, Y. Duan, W. Lin, K. S. Moon, and C. P. Wong, “New Electrically Conductive Adhesives (ECAs) for flexible interconnect applications,” *Proc. - Electron. Components Technol. Conf.*, pp. 1356–1360, 2009.

[233] J. B. Nysæther, Z. Lai, and J. Liu, “Thermal cycling lifetime of flip chip on board circuits with solder bumps and isotropically conductive adhesive joints,” *IEEE Trans. Adv. Packag.*, vol. 23, no. 4, pp. 743–749, 2000.

[234] Y. Zhang, S. Qi, X. Wu, and G. Duan, “Electrically conductive adhesive based on acrylate resin filled with silver plating graphite nanosheet,” *Synth. Met.*, vol. 161, no. 5–6, pp. 516–522, 2011.

[235] Y. Oh *et al.*, “Silver-plated carbon nanotubes for silver/conducting polymer composites,” *Nanotechnology*, vol. 19, no. 49, 2008.

[236] M. Knite, V. Teteris, A. Kiploka, and J. Kaupuzs, “Polyisoprene-carbon black nanocomposites as tensile strain and pressure sensor materials,” *Sensors Actuators, A Phys.*, vol. 110, no. 1–3, pp. 142–149, 2004.

[237] G. T. Pham, Y. Bin Park, Z. Liang, C. Zhang, and B. Wang, “Processing and modeling of conductive thermoplastic/carbon nanotube films for strain sensing,” *Compos. Part B Eng.*, vol. 39, no. 1, pp. 209–216, 2008.

[238] J. S. Leng, W. M. Huang, X. Lan, Y. J. Liu, and S. Y. Du, “Significantly reducing electrical resistivity by forming conductive Ni chains in a polyurethane shape-memory polymer/carbon-black composite,” *Appl. Phys. Lett.*, vol. 92, no. 20, 2008.

[239] G. R. Ruschau, S. Yoshikawa, and R. E. Newnham, “Resistivities of conductive composites,” *J. Appl. Phys.*, vol. 72, no. 3, pp. 953–959, 1992.

[240] A. Bunde and J. W. Kantelhardt, “Introduction to Percolation Theory (Part A),” in *Diffusion in Condensed Matter*, no. 0, 1998, pp. 340–352.

[241] S. Kamalesh, P. Tan, J. Wang, T. Lee, E. T. Kang, and C. H. Wang, “Biocompatibility of electroactive polymers in tissues.,” *J. Biomed. Mater. Res.*, vol. 52, no. 3, pp. 467–78, Dec. 2000.

[242] M. Weber and M. R. Kamal, “Estimation of the Volume Resistivity of Electrically Conductive Composites,” *Annu. Tech. Conf. - ANTEC, Conf. Proc.*, vol. 18, no. 6, 1997.

[243] E. Thommerel, J. C. Valmalette, J. Musso, S. Villain, J. R. Gavarri, and D. Spada, “Relations between microstructure, electrical percolation and corrosion in metal - Insulator composites,” *Mater. Sci. Eng. A*, vol. 328, no. 1, pp. 67–79, 2002.

[244] M. C. Lonergan, E. J. Severin, B. J. Doleman, S. A. Beaber, R. H. Grubbs, and N. S. Lewis, “Array-Based Vapor Sensing Using Chemically Sensitive , Carbon Black - Polymer Resistors,” vol. 4756, no. 14, pp. 2298–2312, 1996.

[245] H. Li, H. Xiao, and J. Ou, “Effect of compressive strain on electrical resistivity of carbon black-

filled cement-based composites," *Cem. Concr. Compos.*, vol. 28, no. 9, pp. 824–828, Oct. 2006.

[246] J. Sánchez-González, A. MacÍas-García, M. F. Alexandre-Franco, and V. Gómez-Serrano, "Electrical conductivity of carbon blacks under compression," *Carbon N. Y.*, vol. 43, no. 4, pp. 741–747, 2005.

[247] P. Fernberg, G. Nilsson, and R. Joffe, "Piezoresistive Performance of Long-Fiber Composites with Carbon Nanotube Doped Matrix," *J. Intell. Mater. Syst. Struct.*, vol. 20, no. 9, pp. 1017–1023, Nov. 2008.

[248] S. Wen and D. D. . Chung, "Piezoresistivity in continuous carbon fiber cement-matrix composite," *Cem. Concr. Res.*, vol. 29, no. 3, pp. 445–449, Mar. 1999.

[249] J. G. Simmons, "Generalized Formula for the Electric Tunnel Effect between Similar Electrodes Separated by a Thin Insulating Film," *J. Appl. Phys.*, vol. 34, no. 6, pp. 1793–1803, 1963.

[250] E. Mengi and Yu-Chong Tai, "Parylene etching techniques for microfluidics and biomems," *18th IEEE Int. Conf. Micro Electro Mech. Syst. 2005. MEMS 2005.*, pp. 568–571, 2005.

[251] M. G. Allen, "MICROFABRICATED IMPLANTABLE WIRELESS MICROSYSTEMS : PERMANENT AND BIODEGRADABLE IMPLEMENTATIONS Department of Electrical and Systems Engineering School of Engineering and Applied Science University of Pennsylvania , Philadelphia , PA USA CHRONIC CONDITION," *Proc. IEEE Conf. Microelectromechanical Syst.*, pp. 3–6, 2014.

[252] W. Shen *et al.*, "Extracellular matrix-based intracortical microelectrodes: Toward a microfabricated neural interface based on natural materials," *Nat. Microsystems Nanoeng.*, vol. 1, 2015.

[253] M. ~J. Silva and L. ~J. Gibson, "Modeling the mechanical behaviour of vertebal trabecular bone: {E}ffects of age-related changes in microstructure," *Bone*, vol. 21, no. 2, pp. 191–199, 1997.

[254] P. Alpuim, V. Correia, E. S. Marins, J. G. Rocha, I. G. Trindade, and S. Lanceros-Mendez, "Piezoresistive silicon thin film sensor array for biomedical applications," *Thin Solid Films*, vol. 519, no. 14, pp. 4574–4577, 2011.

[255] N. Van Toan, H. Miyashita, M. Toda, Y. Kawai, and T. Ono, "Fabrication and packaging process of silicon resonators capable of the integration of LSI for application of timing device," *2013 IEEE 26th Int. Conf. Micro Electro Mech. Syst.*, vol. 1, pp. 377–380, Jan. 2013.

[256] D. J. Lichtenwalner, A. E. Hydrick, and A. I. Kingon, "Flexible thin film temperature and strain sensor array utilizing a novel sensing concept," *Sensors Actuators, A Phys.*, vol. 135, no. 2, pp. 593–597, 2007.

[257] Omega, "Transducer Quality Strain Gage Full Wheatstone Bridge , Bending or Axial Tension or Compression Perpendicular Grids."

[258] F. Burny *et al.*, "Concept, design and fabrication of smart orthopedic implants," *Med. Eng. Phys.*, vol. 22, no. 7, pp. 469–479, 2000.

[259] R. L. Parker and A. Krinsky, "Electrical resistance-strain characteristics of thin evaporated metal films," *J. Appl. Phys.*, vol. 34, no. 9, pp. 2700–2708, 1963.

[260] G. R. Witt, "The electromechanical properties of thin films and the thin film strain gauge," *Thin Solid Films*, vol. 22, no. 2, pp. 133–156, 1974.

[261] P. L. Rossiter, *The Electrical Resisitivity of Metals and Alloys*. Cambridge, UK: Cambridge

University Press, 1991.

[262] A. C. Guyton, *Textbook of Medical Physiology*, 9th ed. W B Saunders, Co, 1996.

[263] W. E. Caler and D. R. Carter, “Bone creep-fatigue damage accumulation,” *J. Biomech.*, vol. 22, no. 6–7, pp. 625–635, 1989.

[264] M. Luo, A. W. Martinez, C. Song, F. Herrault, and M. G. Allen, “A Microfabricated Wireless RF Pressure Sensor Made Completely of Biodegradable Materials,” *J. micro*, vol. 23, no. 1, pp. 4–13, 2014.

[265] M. Tsang *et al.*, “Development of Electroplated Magnesium Microstructures for Biodegradable Devices and Energy Sources,” *J. Microelectromechanical Syst.*, vol. 23, no. 6, pp. 1281–1289, 2014.

[266] M. G. Allen, “Microfabricated implantable wireless microsystems: Permanent and biodegradable implementations,” in *IEEE MEMS 2014 Conference Proceedings, San Francisco, CA*, 2014.

[267] G. Kilian, H. Petkov, and R. Psiuk, “Improved Coverage for Low-Power Telemetry Systems using Telegram Splitting,” in *IEEE Smart SysTech 2013 Conference Proceedings, Nuremberg, Germany*, 2013.

[268] P. Turcza, “An Ultra Low Power 2 Mbps RF-telemetry System for Neural Recording Applications,” *Procedia Eng.*, vol. 47, pp. 813–816, 2012.

[269] T. Bautista and F. Santana-martfnt, “Low-Power MEMS Pressure Sensor for Wireless Biomedical Applications,” in *2011 IEEE 54th International Midwest Symposium on Circuits and Systems (MWSCAS)*, 2011, pp. 1–4.

[270] R.-F. Xue *et al.*, “Ultra-low-power wireless implantable blood flow sensing microsystem for vascular graft applications,” *2011 Int. Symp. Integr. Circuits*, pp. 224–229, Dec. 2011.

[271] S. J. a. Majerus, S. L. Garverick, M. a. Suster, P. C. Fletter, and M. S. Damaser, “Wireless, Ultra-Low-Power Implantable Sensor for Chronic Bladder Pressure Monitoring,” *ACM J. Emerg. Technol. Comput. Syst.*, vol. 8, no. 2, pp. 1–13, Jun. 2012.

[272] Texas Instruments, “MSP430 Ultra-Low-Power Microcontrollers,” Dallas, Texas, 2014.

[273] S. Santhanagopalan and R. E. White, “Linden’ s Handbook of Batteries,” *Linden’s Handb. Batter.*, pp. 146–173, 2014.

[274] P. Gill, “Corrosionand Biocompatibility Assessment of Magnesium Alloys,” *J. Biomater. Nanobiotechnol.*, vol. 3, no. 1, pp. 10–13, 2012.

[275] B. Guang, L. Song, and A. Atrens, “Corrosion Mechanisms of Magnesium Alloys **,” no. 1, pp. 11–33, 2000.

[276] D. Vojtěch, J. Kubásek, J. Šerák, and P. Novák, “Mechanical and corrosion properties of newly developed biodegradable Zn-based alloys for bone fixation,” *Acta Biomater.*, vol. 7, no. 9, pp. 3515–3522, 2011.

[277] D. Xue, Y. Yun, Z. Tan, Z. Dong, and M. J. Schulz, “In Vivo and In Vitro Degradation Behavior of Magnesium Alloys as Biomaterials,” *J. Mater. Sci. Technol.*, vol. 28, no. 3, pp. 261–267, 2012.

[278] X.-N. Gu and Y.-F. Zheng, “A review on magnesium alloys as biodegradable materials,” *Front. Mater. Sci. China*, vol. 4, no. 2, pp. 111–115, May 2010.

[279] ASTM International, “Standard Practice for from Electrochemical Measurements 1,” 2010.

[280] B. Guang, L. Song, and A. Atrens, “Corrosion Mechanisms of Magnesium Alloys,” *Adv. Eng. Mater.*, vol. 1, no. 1, pp. 11–33, 2000.

[281] M. Pourbaix, “Electrochemical corrosion of metallic biomaterials.,” *Biomaterials*, vol. 5, no. 3, pp. 122–34, May 1984.

[282] X. Wei and J. Liu, “Power sources and electrical recharging strategies for implantable medical devices,” *Front. Energy Power Eng. China*, vol. 2, no. 1, pp. 1–13, 2008.

[283] J. Drews, G. Fehrmann, R. Staub, and R. Wolf, “Primary batteries for implantable pacemakers and defibrillators,” *J. Power Sources*, vol. 98, no. June 2000, pp. 2000–2002, 2001.

[284] Quallion LLC, “Non-Rechargeable Litium-ion Battery: QL0025C,” Sylmar, CA, 2003.

[285] D. She, M. Tsang, J. K. Kim, and M. G. Allen, “Immobilized Electrolyte Biodegradable Batteries For Implantable MEMS,” in *TRANSDUCERS 2015 - 18th International Conference on Solid-State Sensors, Actuators and Microsystems, Digest of Technical Papers*, 2015.

[286] B. S. Klosterhoff *et al.*, “Wireless Implantable Sensor for Noninvasive, Longitudinal Quantification of Axial Strain Across Rodent Long Bone Defects,” *J. Biomech. Eng.*, vol. 139, no. 11, 2017.

[287] Mddiadmin, “A Practical Guide to ISO 10993-12: Sample Preparation and Reference Materials,” *MDDI Med. Device Diagnostic Ind. News Prod. Suppliers*, pp. 10–13, 1998.

[288] L. Kux, “Use of International Standard ISO 10993-1, ‘Biological evaluation of medical devices – Part 1: Evaluation and testing within a risk management process’, Guidance for Industry and Food and Drug Administration Staff; Availability,” vol. 81, no. 116, pp. 39269–39271, 2016.

[289] Y. Yun *et al.*, “Biodegradable Mg corrosion and osteoblast cell culture studies,” *Mater. Sci. Eng. C*, vol. 29, no. 6, pp. 1814–1821, 2009.

[290] Z. Li, X. Gu, S. Lou, and Y. Zheng, “The development of binary Mg-Ca alloys for use as biodegradable materials within bone,” *Biomaterials*, vol. 29, no. 10, pp. 1329–1344, 2008.

[291] X. Gu, Y. Zheng, Y. Cheng, S. Zhong, and T. Xi, “In vitro corrosion and biocompatibility of binary magnesium alloys,” *Biomaterials*, vol. 30, no. 4, pp. 484–498, 2009.

[292] B. Liu and Y. F. Zheng, “Effects of alloying elements (Mn, Co, Al, W, Sn, B, C and S) on biodegradability and in vitro biocompatibility of pure iron,” *Acta Biomater.*, vol. 7, no. 3, pp. 1407–1420, 2011.

[293] F. Witte *et al.*, “Biodegradable magnesium-hydroxyapatite metal matrix composites,” *Biomaterials*, vol. 28, no. 13, pp. 2163–2174, 2007.

[294] Promega Corporation, “CellTiter 96 ® AQueous One Solution Cell Proliferation Assay,” *Www.Promega.Com/Protocols/*, pp. 2014-12–15, 2012.